CARe

CENTRE FOR ADVANCED RESEARCH ON ENERGY
Universiti Teknikal Malaysia Melaka

Proceedings of MERD'15

Mechanical Engineering Research Day

First published 2015

ISBN: 978-967-0257-51-8 (online)

Published and Printed in Malaysia by:
Centre for Advanced Research on Energy (CARe)
Faculty of Mechanical Engineering, Universiti Teknikal Malaysia Melaka,
Hang Tuah Jaya, 76100 Durian Tunggal, Melaka, MALAYSIA.
Tel: +606 234 6891 | Fax: +606 234 6884 | E-mail: care@utem.edu.my
www.utem.edu.my/care

FOREWORD BY THE CHAIRMAN

Assalamu'alaikum wrt. wbt, and Salam Sejahtera,

I would like to express warmest welcome to all participants to the Mechanical Engineering Research Day 2015 (MERD'15) held at Kampus Teknologi, Universiti Teknikal Malaysia Melaka (UTeM) - Melaka, Malaysia. Alhamdulillah, all praise to Allah, this is the second event after successful responds at the first event in 2011. The current event is jointly organized by the Faculty of Mechanical Engineering and Centre for Advanced Research on Energy (CARe), UTeM with the theme '*Pioneering Future Discovery*'.

The aim of MERD'15 is to foster a broad range of sustainable collaboration among researchers, expert, educators and participants, thus promoting new opportunities for research activities enhancement. This is in line with the increasing demand for innovative research ideas, design, optimizing, modeling, processing and solutions involving real engineering problems which advocate the provision of rigorous study among distinct communities.

Pioneering future discovery can gives big impact to the organization, human development and nation. Given '*Pioneering Future Discovery*' as a theme, MERD'15 is a perfect and excellent platform for academicians, engineers and researchers in broad ranges of sustainable collaborations to share their knowledge of innovation, creativity and latest approaches in various research activities.

I would like to take this opportunity to convey my special thanks to those who are involved in organizing MERD'15, especially from the Faculty staffs and CARe members for successfully organizing this event. Finally, I would like to express our deepest gratitude to the sponsors for the support given in ensuring the success of this event.

Thank you.

Associate Professor Dr. Noreffendy Bin Tamaldin

Chairman, MERD'15
Universiti Teknikal Malaysia Melaka, Malaysia.

FOREWORD BY THE DIRECTOR

Assalamu'alaikum wrt. wbt, and Salam Sejahtera,

Welcome to Mechanical Engineering Research Day 2015 (MERD'15)!

As the organizing director of MERD'15, it is my great pleasure to welcome all participants to the event, jointly organized by the Faculty of Mechanical Engineering (FKM) and Centre for Advanced Research on Energy (CARe) of Universiti Teknikal Malaysia Melaka (UTeM). This is much anticipated event which allows UTeM's researchers to share and promote their research as well as a chance to extend their network in the mechanical engineering field.

MERD'15 is aimed to be a platform for researchers, academicians and practitioners to seal advancement of engineering and finding through knowledge sharing and discussion related to current practices, innovations and trends. It is hoped that this event will catalyze and increase academic and research collaborations between other institutions and respective industries involved. I sincerely believe this will spur further advancement of scientific research and fruitful co-operation between organizations.

Last but not least, I would also like to take this opportunity to express my utmost appreciation and many thanks to all members of the organizing committee and all others who have either directly or indirectly contributed towards the success of MERD'15. I wish all the best to the participants and hopefully, this event will provide new heights of research accomplishment for UTeM's researchers.

Thank you.

Dr. Mohd Fadzli Bin Abdollah

Director, MERD'15
Universiti Teknikal Malaysia Melaka, Malaysia.

FOREWORD BY THE EDITOR-IN-CHIEF

This Open Access e-Proceeding contains 74 selected papers from the Mechanical Engineering Research Day 2015 (MERD'15) event, which is held in Kampus Teknologi, Universiti Teknikal Malaysia Melaka (UTeM) - Melaka, Malaysia, on 31 March 2015. The theme chosen for this event is '*Pioneering Future Discovery*'.

The response for MERD'15 is overwhelming as the technical committees have received more than 90 papers from various areas of mechanical engineering. From the total number of submissions, the technical committees have selected 74 papers to be included in this proceeding. The selected papers are grouped into 12 categories: Advanced Materials Processing; Automotive Engineering; Computational Modeling and Analysis & CAD/CAE; Energy Management & Fuels and Lubricants; Hydraulics and Pneumatics & Mechanical Control; Mechanical Design and Optimization; Noise, Vibration and Harshness; Non-Destructive Testing & Structural Mechanics; Surface Engineering and Coatings; Others Related Topic.

With the large number of submissions from the researchers in other faculties, the event has achieved its main objective which is to bring together educators, researchers and practitioners to share their findings and perhaps sustaining the research culture in the university. The topics of MERD'15 are based on a combination of advanced research methodologies, application technologies and review approaches.

As the editor-in-chief, we would like to express our gratitude to the editorial board members for their tireless effort in compiling and reviewing the selected papers for this proceeding. We would also like to extend our great appreciation to the members of the Publication Committee and Secretariat for their excellent cooperation in preparing the proceedings of MERD'15.

Thank you.

Dr. Mohd Zulkefli Bin Selamat

Dr. Reduan Bin Mat Dan

Editor-in-Chief

Universiti Teknikal Malaysia Melaka, Malaysia.

EDITORIAL BOARD

Editor-in-Chief

Mohd Zulkefli Bin Selamat (FKM, UTeM, Malaysia)

Reduan Bin Mat Dan (FKM, UTeM, Malaysia)

Editors

Abd Rahman Bin Dullah (FKM, UTeM, Malaysia)

Abd Salam Bin Md Tahir (FKM, UTeM, Malaysia)

Abdul Munir Hidayat Syah Lubis (FKM, UTeM, Malaysia)

Abdul Talib Bin Din (FKM, UTeM, Malaysia)

Ahmad Anas Bin Yusof (FKM, UTeM, Malaysia)

Ahmad Kamal Bin Mat Yamin (FKM, UTeM, Malaysia)

Ahmad Rivai (FKM, UTeM, Malaysia)

Aliza Binti Che Amran (FKE, UTeM, Malaysia)

Azma Putra (FKM, UTeM, Malaysia)

Cheng See Yuan (FKE, UTeM, Malaysia)

Chong Shin Horng (FKE, UTeM, Malaysia)

Faiz Redza Bin Ramli (FKM, UTeM, Malaysia)

Fatimah Al-Zahrah Binti Mohd Sa'at (FKM, UTeM, Malaysia)

Herdy Rusnandi (FKM, UTeM, Malaysia)

Hilmi Bin Amiruddin (FKM, UTeM, Malaysia)

Imran Syakir Bin Mohamad (FKM, UTeM, Malaysia)

Mariam Binti Md Ghazaly (FKE, UTeM, Malaysia)

Md Isa Bin Ali (FKM, UTeM, Malaysia)

Md. Fahmi Bin Abd. Samad @ Mahmood (FKM, UTeM, Malaysia)

Md Radzai Bin Said (FKM, UTeM, Malaysia)

Mohd Ahadlin Bin Mohd Daud (FKM, UTeM, Malaysia)

Mohd Asri Bin Yusuff (FKM, UTeM, Malaysia)

Mohd Azli Bin Salim (FKM, UTeM, Malaysia)

Mohd Azman Bin Abdullah (FKM, UTeM, Malaysia)

Mohd Fadzli Bin Abdollah (FKM, UTeM, Malaysia)

Mohd Haizal Bin Mohd Husin (FKM, UTeM, Malaysia)

Mohd Juzaila Bin Abd. Latif (FKM, UTeM, Malaysia)

Mohd Khairi Bin Mohamad Nor (FKM, UTeM, Malaysia)

Mohd Nizam Bin Sudin (FKM, UTeM, Malaysia)

Mohd Rizal Bin Alkahari (FKM, UTeM, Malaysia)

Mohd Zaid Bin Akop (FKM, UTeM, Malaysia)

Mohd Zulkefli Bin Selamat (FKM, UTeM, Malaysia)

Nona Merry Merpati Mitan (FKM, UTeM, Malaysia)

Nor Azmmi Bin Masripan (FKM, UTeM, Malaysia)

Norasra Binti A.Rahman (FKM, UTeM, Malaysia)

Noreffendy Bin Tamaldin (FKM, UTeM, Malaysia)

Nur Rashid Bin Mat Nuri @ Md Din (FTK, UTeM, Malaysia)

Omar Bin Bapokutty (FKM, UTeM, Malaysia)

Rafidah Binti Hasan (FKM, UTeM, Malaysia)

Rainah Binti Ismail (FKM, UTeM, Malaysia)

Roszaidi Bin Ramlan (FKM, UTeM, Malaysia)

Safarudin Gazali Herawan (FKM, UTeM, Malaysia)

Shamsul Anuar Bin Shamsudin (FKM, UTeM, Malaysia)

Siti Hajar Binti Sheikh Md. Fadzullah (FKM, UTeM, Malaysia)

Siti Nurhaida Binti Khalil (FKM, UTeM, Malaysia)

Sivakumar A/L Dhar Malingam (FKM, UTeM, Malaysia)

Sushella Edayu Binti Mat Kamal (FKM, UTeM, Malaysia)

Tan Chee Fai (FKM, UTeM, Malaysia)

Tee Boon Tuan (FKM, UTeM, Malaysia)

Umar Al-Amani Bin Haji Azlan (FTK, UTeM, Malaysia)

Zairulazha Bin Zainal (FKM, UTeM, Malaysia)

Zakiah Binti Halim (FKM, UTeM, Malaysia)

ORGANIZING COMMITTEE

Chairman
Assoc. Prof. Dr. Noreffendy Bin Tamaldin

Deputy Chairman
Dr. Abd Rahman Bin Dullah

Director
Dr. Mohd Fadzli Bin Abdollah

Deputy Director
Dr. Tee Boon Tuan

Secretary
Dr. Umar Al-Amani Bin Haji Azlan
Mrs. Suhaila Binti Mohd Yusof

Publication
Dr. Mohd Zulkefli Bin Selamat
Dr. Reduan Bin Mat Dan

Submission
Dr. Rainah Binti Ismail
Mr. Hilmi Bin Amiruddin
Mrs. Sushella Edayu Binti Mat Kamal

Registration
Dr. Shamsul Anuar Bin Shamsudin
Mr. Muhammad Zulfattah Bin Zakaria

Evaluation Panel
Prof. Dr. Md. Radzai Bin Said
Assoc. Prof. Ir. Dr. Abdul Talib Bin Din
Assoc. Prof. Ahmad Rivai

Logistic and Technical
Dr. Mohd Azman Bin Abdullah
Dr. Faiz Redza Bin Ramli

Publicity
Ir. Dr. Mohd Rizal Bin Alkahari

Certificate and Souvenir
Dr. Siti Nurhaida Binti Khalil
Mrs. Norasra Binti A. Rahman

Special Tasks
Dr. Nor Azmmi Bin Masripan
Dr. Sivakumar A/L Dhar Malingam

TABLE OF CONTENTS

Theme 2: Automotive Engineering

Theme 3: Computational Modeling and Analysis & CAD / CAE

Theme 4: Energy Management & Fuels and Lubricants

Theme 5: Hydraulics and Pneumatics & Mechanical Control

Theme 6: Mechanical Design and Optimization

Theme 7: Mechatronics Engineering

Theme 8: Noise, Vibration and Harshness

Theme 11: Surface Engineering and Coatings

Theme 12: Others Related Topic

Preliminary study of KNN thin films doped by rare-earths for sensor applications

M.H. Maziati Akmal[1], A.U. Al-Amani[2,*], A.R. Mohd Warikh[1], A. Nurul Azuwa[1]

[1)] Faculty of Manufacturing Engineering, UniversitiTeknikal Malaysia Melaka, Hang Tuah Jaya, 76100 Durian Tunggal, Melaka, Malaysia.
[2)] Faculty of Engineering Technology, UniversitiTeknikal Malaysia Melaka, Hang Tuah Jaya, 76100 Durian Tunggal, Melaka, Malaysia.

[*]Corresponding e-mail: umar@utem.edu.my

Keywords: KNN; doping; rare-earths; yttrium

ABSTRACT – Among ferroelectrics systems, potassium sodium niobate (KNN) has drawn much attention due to a clear-cut advantage of high piezoelectric and ferroelectric performances. The volatility of alkaline element (K,Na) is detrimental to the stoichiometry of KNN, contributing to the formation of intrinsic defects. Thus, the primary goal of this study is to design a solution to overcome the volatility issue of KNN. Introduction of rare-earth cations in the host KNN could reduce the vacancies in KNN. Currently, three arrays of dopants were integrated into KNN. In this preliminary work, a sol-gel technique was employed to produce a thin film that can be utilized later in the sensor applications. The structural and electrical properties were characterized using Raman spectroscopy and 2-point probe equipment, respectively. The typical Raman spectra of KNN thin films were shifted towards lower or higher wavenumbers depending on the cations deficiencies or redundancies. The conductivity of thin films was found to be increased as the dopant concentration was increased.

1. INTRODUCTION

Alkaline niobate, in particular, potassium sodium niobate, (K_xNa_{1-x}) NbO_3 (KNN) is derived from a combination of simple perovskite structure of $KNbO_3$ (KN) and $NaNbO_3$ (NN). It has a high Curie temperature (420 °C) and exhibits good ferroelectric and piezoelectric properties. However, the proportion of K, Na, and Nb is likely to deviate from stoichiometry due to the evaporation of K and Na at high temperature. Theoretically, the formation of intrinsic defects in the perovskite structure results in reduced ferroelectric and piezoelectric properties [1].

Substitutions of several cations in KNN structure would improve the properties of KNN-based ceramics. Improvement of properties is believed due to the coexistence of orthorhombic-tetragonal phases at room temperature. This occurrence allows a better electrical poling process because of the existence of more crystallographic directions for the polarization [2-4]. Rare-earth elements (i.e. Ce, La, Nd) are dominant dopants to be substituted for KNN-based materials. It was stated that rare-earth elements are known to demonstrate useful functions of stabilizing and lowering dissipation factor in dielectric ceramics [5]. In previous work on lead-free barium titanate (BT), it was found that the appropriate amount of rare-earth in KNN could enhance the electrical properties of BT [3]. A similar idea could be addressed to compensate the volatility of K and Na in KNN. For this reason, the present study is concentrated on the doping elements in KNN materials in response to having excellent properties. Different content of dopants were used in this study.

2. METHODOLOGY

There are several stages to fabricate rare-earths doped KNN. Two alkali precursors that are potassium acetate and sodium acetate were used as starting solutions. The precursors were mixed with rare-earth nitrate-based, i.e., and yttrium nitrate hexahydrate. Different content of rare-earth were used in this work (Y = 0, 0.25, 0.5). These chemicals were dissolved in a polar organic solvent, 2-methyoxyethanol with constant stirring at room temperature. Then, niobium ethoxide was added to the mixture solution. To retain the stability of the niobium ethoxide, acetylacetone was introduced to the prepared solution.

The solution was then deposited on the Si substrate to produce the thin films. The films were spun onto the wafer at 2000-3000 rpm for 60 seconds. After spinning, the wet films were heated at 200°C for 5 minutes. Then, the thin films were annealed for 30 minutes at 650°C in the furnace.

Subsequently, Raman microprobe measurements were used to study the changes in the Raman scattering modes of KNN thin films prepared with different yttrium contents. Later, the electrical properties were observed using I-V measurement by 2-point probe equipment.

3. EXPECTED RESULTS AND DISCUSSION

Raman spectra of KNN thin films with different yttrium content are depicted in Figure 1. The Raman-active mode v_1, v_2 and v_3 correspond to the stretching modes of NbO_6 octahedra [6]. The peak position shifted toward the higher wavenumber side (619 to 621 cm^{-1}) as the yttrium (Y) concentration increase up to 0.5%. According to Hardcastle and co-worker, the peak shifting to a higher wavenumber was due to an increase in the binding strength [7]. This change was attributed to the shortening distance between Nb^{5+} and a

coordinate of the oxygen atom. Additionally, the peak shift occurs when the A-site in the ABO_3 crystal structure was integrated with a smaller ion.

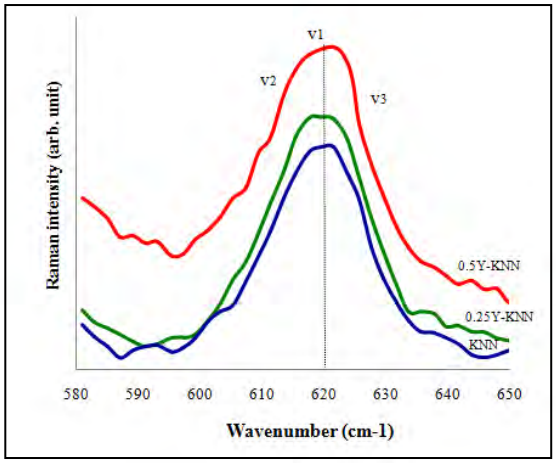

Figure 1 Magnified Raman spectra with vibration changes of stretching mode v_1.

The I-V characteristics of the KNN thin films recorded at room temperature are shown in Figure 2. Current increase as more yttrium dopant was introduced in KNN thin films. From the graph, it presented that the most conductive sample is 0.5% Y-KNN and the least conductive is undoped KNN. The increase in conductivity is due to more free electrons were generated by integrating Y ions which increase the carrier concentration in thin film [8].

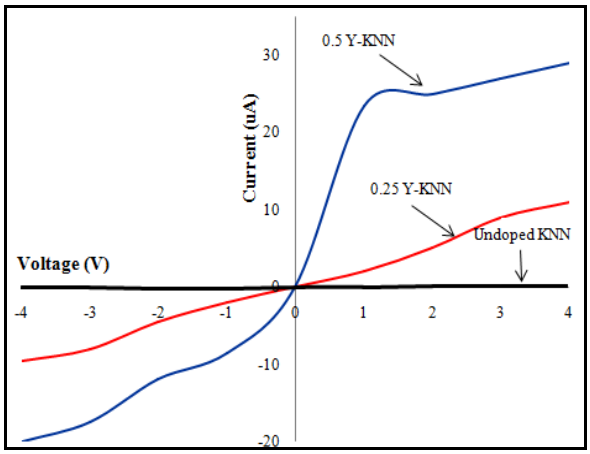

Figure 2 I-V characteristics of KNN thin films at various dopant concentration

4. CONCLUSIONS

The KNN thin films were successfully fabricated by sol-gel method. Raman spectra indicate that the variation of peak shifting around 619 cm^{-1} attributed to the enhancement of binding strength dominated by dopant concentration. Meanwhile, the I-V measurements show that the thin film conductivity was high at 0.5% Y-doped KNN. Hence, the encouraging results could contribute to the incorporation of these thin films in sensor devices.

5. ACKNOWLEDGMENT

The authors would like to thank the Ministry of Higher Education, Malaysia for funding our research. (FRGS/1/2014/TK04/UTEM/02/3)

6. REFERENCES

[1] P. K. Panda, "Review: environmental friendly lead-free piezoelectric materials," *Journal of Materials Science*, vol. 44, no. 19, pp. 5049–5062, Jul. 2009.

[2] S. Qian, K. Zhu, X. Pang, J. Liu, J. Qiu, and J. Du, "Phase transition , microstructure , and dielectric properties of Li / Ta / Sb co-doped (K , Na) NbO 3 lead-free ceramics," *Ceramics International*, vol. 40, no. 3, pp. 4389–4394, 2014.

[3] X. Huang, R. Xing, C. Gao, and Z. Chen, "Influence of CeO2 doping amount on the property of BCTZ lead-free piezoelectric ceramics sintered at low temperature," *Journal of Rare Earths*, vol. 32, no. 8, pp. 733–737, Aug. 2014.

[4] E. M. Alkoy, "Effect of Cu and Li Addition on the Electrical Properties of KNN Ceramics," pp. 1–4, 2010.

[5] C.-H. Kim, K.-J. Park, Y.-J. Yoon, M.-H. Hong, J.-O. Hong, and K.-H. Hur, "Role of yttrium and magnesium in the formation of core-shell structure of BaTiO3 grains in MLCC," *Journal of the European Ceramic Society*, vol. 28, no. 6, pp. 1213–1219, Jan. 2008.

[6] K. Kakimoto, K. Akao, Y. Guo, and H. Ohsato, "Raman scattering study of piezoelectric $(Na0.5K0.5)NbO_3$-$LiNbO_3$ Ceramics," *J. Phys. Soc. Jpn*, vol. 44, pp. 7064-7067, 2005.

[7] F. D. Hardcastle and I. Wachs, "Determination of niobium-oxygen bond distances and bond orders by Raman spectroscopy," *Solid State Ion.*, vol. 45, no. 3–4, pp. 201–213, April 1991.

[8] M. H. Mamat, M. Z. Sahdan, Z. Khusaimi, A. Z. Ahmed, S. Abdullah, and M. Rusop, "Influence of doping concentrations on the aluminum doped zinc oxide thin films properties for ultraviolet photoconductive sensor applications," *Optical Materials*, vol. 32, no. 6, pp. 696–699, 2010.

Effect of pineapple leaf fiber loading on the properties of pineapple leaf fiber – polypropylene composite

A.N. Kasim[1,2,*], M.Z. Selamat[1,2,*], N. Aznan[1], S.N. Sahadan[1,2], M.A.M. Daud[1,2], S. Salleh[1,2], R. Jumaidin[1,2]

[1)] Faculty of Mechanical Engineering, UniversitiTeknikal Malaysia Melaka,
Hang Tuah Jaya, 76100 Durian Tunggal, Melaka, Malaysia.
[2)] Centre for Advanced Research on Energy, UniversitiTeknikal Malaysia Melaka,
Hang Tuah Jaya, 76100 Durian Tunggal, Melaka, Malaysia.

[*]Corresponding e-mail: ayunatasyakasim@yahoo.com, zulkeflis@utem.edu.my

Keywords: Pineapple Leaf Fiber (PLF); Polypropylene (PP); Fiber Reinforced Polymer (FRP)

ABSTRACT – Nowadays, the natural fibers are widely used in FRP composite especially as automotive interior parts because it is much cheaper and natural availability compare to glass fiber and carbon fiber. This paper discusses the effects of pineapple leaf fiber (PLF) loading on the mechanical properties of pineapple leaf fiber/polypropylene (PLF/PP) composite. An alkaline treatment was conducted to enhance the PLF properties before the formation process of PLF/PP composite. The mechanical properties of PLF/PP composite were determined using tensile test, hardness test, density measurement and microstructure analysis. The result of PLF/PP composite with a composition of 30/70 showed the best mechanical properties comparable to others composition ratios.

1. INTRODUCTION

Natural fiber is an alternative to glass fiber in FRP composite materials industry, especially in automotive application. Natural fibers composite give a combination of excellent mechanical property, dielectric property, and environmental advantages such as recyclable, biodegradable and renewability [1-2,7]. Pineapple leaf fiber is one of the most attractive materials as a strengthening natural fiber, and the mechanical properties of PLF are listed in Table 1. Mohamad et al [6], states that in Malaysia the pineapple industry is markable but only the fruit is used and other part such as leaf is thrown away, thus causing pollution and wasting the best potential sources of fiber. Furthermore, this study aims to investigate the effect of PLF loading on the properties of PLF/PP composite and to explore the potential of this composite. The mechanical properties such as tensile stress, hardness, bulk density and microstructure are observed.

Table 1 Properties of pineapple leaf fiber: [5]

Property	Value
Density (g/cm^3)	1.526
Softening Point (°C)	104
Tensile Strength (MPa)	170
Young's Modulus (MPa)	6260
Specific Modulus (MPa)	4070
Elongation at Break (%)	3
Moisture regain (%)	12

2. METHODOLOGY

The materials used in the fabrication of FRP composites are PLF and PP. Figure 1 (a) and (b) shows the image of PLF and PP. Meanwhile, the composition of this composite is listed in Table 2.

(a) (b)

Figure 1 Photograph image: (a) PLF ; (b) PP

Before the PLF can be used as filler, an alkaline treatment was done. The raw pineapple leaf was first cut into small pieces with the length of 10 cm and then rolled used roll mill machine. After that, these small pieces were then immersed in 5% concentration of the NaOH. The 1% concentration of the HCL was used to neutralize the PLF. The functions of chemical treatments are to clean all the impurities, treat the fiber surface and also to stabilize the molecular orientation [2-4]. Vinod and Sudev [3] state that by undergoing the chemical treatments the mechanical properties of the material can be improved. After the formation process by using a hot compression mold, some mechanical testing was conducted that are tensile test (ASTM D 3039/D 3039M-00), shore hardness test, density measurement and microstructure analysis.

Table 2 Composition of PLF/PP composite

PLF (%)	PP (%)
70	30
60	40
50	50
40	60
30	70

3. RESULTS AND DISCUSSION

Figure 2 shows the graph of tensile stress versus composition of PLF/PP composites. The graph shows that the tensile stress, increased with the decrease of PLF contents. The reason for this distinct value is because at the composition of (PLF/PP) 30/70, a higher value of PP has resulted a high plasticity behavior due to the thermoplastic type of polymer. Meanwhile the

microstructure of each composite as shown in Table 3 shows that the voids percentage was reduced as PP content increased and it also shows a good adhesion between the PLF and PP. Hence, it has held the PLF firm and this affected their mechanical properties.

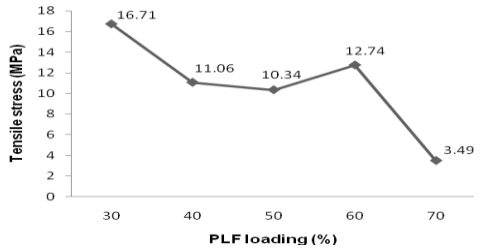

Figure 2 Tensile stress (MPa) versus PLF loading (%)

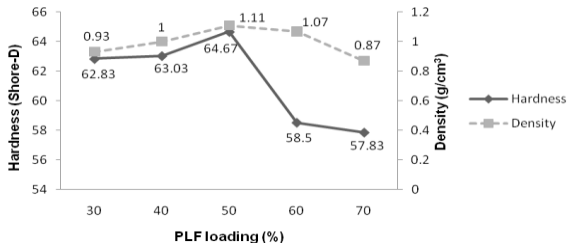

Figure 3 Hardness (Shore-D) and density (g/cm^3) versus PLF loading (%)

Table 3 Microstructure of PLF/PP composites

Ratio (%) PLF/PP	Microstructure view	Remark
70/30	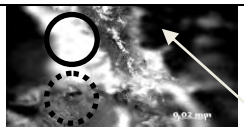	Void
60/40	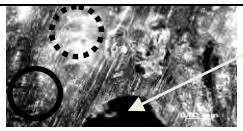	
50/50	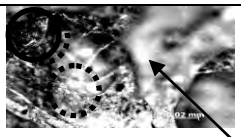	
40/60	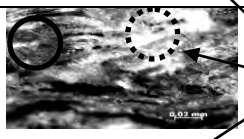	Good adhesion
30/70	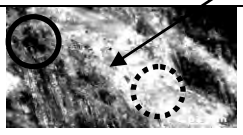	

PP PLF

Figure 3 shows the graph of hardness (Shore-D) and density (g/cm^3) versus composition of PLF in PLF/PP composites. The results show that the hardness and density has increased with the increasing of PLF until 50%PLF and after that both value has reduced as PLF content has been increased. Based on the mechanical properties test has been conducted, for tensile and density tests the best result is shown by 30%PLF, while for the hardness test for PLF loading 50% up to 30 % the values are almost same. Moreover, for PLF loading 70% up to 60%, all the properties is shown the lowest value is due to less wetted of PP with PLF.

4. CONCLUSIONS

The effects of pineapple leaf fiber loading on the properties of PLF/PP composite have been studied and determined. Based on the results of tensile stress, hardness and density, it can be concluded that the PLF/PP composite with the composition ratio of 30/70 has shown the best mechanical properties comparable to others composition ratios. However, for PLF/PP composites with PLF loading of 60% and 70% is not suitable for composite materials because it shows the lowers mechanical properties.

5. ACKNOWLEDGEMENT

The authors would like to thank the Malaysia Ministry of Higher Education, Malaysia Ministry of Science, Technology and Innovation for sponsoring this work under Grant PJP/2013/FKM (14A) /S01240 and Advanced Material Research Group (A-MAT), Faculty Mechanical Engineering, University Teknikal Malaysia Melaka (UTeM) for financially sponsoring during this research.

6. REFERENCES

[1] J.P. Dhal, and S.C. Mishra, "Processing and Properties of Natural Fiber-Reinforced Polymer Composite", *Journal of Materials*, pp.1–6. 2013.

[2] M.Z. Selamat, A.N.Kasim, S.A. Shamsudin, "Effect of bamboo fibre length on the mechanical properties of bamboo fiber/polypropylene composite," in 8th MUCET 2014.

[3] D. Chandramohan, and K. Marimuthu. "Tensile and Hardness Tests on Natural Fiber Reinforced Polymer Composite Material", Vol. 6, No. 1, 097 – 104.

[4] N.T. Phong, T. Fujii, B. Chuong, K. Okubo. "Study on How to Effectively Extract BFs from Raw Bamboo and Wastewater Treatment" Vol.1, No.1 pp.144-155, 2012.

[5] B. Vinod, and L.J. Sudev, "Effect of Fiber Orientation on the Flexural Properties of PLAF Reinforced Bisphenol composites", International Journal of Science and Engineering Applications. Vol. 2, ISSN-2319-7560, 2013.

[6] A.R. Mohamed, S.M. Sapuan, M. Shahjahan, and A. Khalina, "Characterization of pineapple leaf fibers from selected Malaysian cultivars", Vol.7 (1): 2 3 5 - 2 4 0. 2009.

[7] R. Shyamraj, P. Sivasubramanian, and P.B Dhanusha, "Investigationson Mechanical Properties of Pineapple Fiber Reinforced Polymer Composite Material", Vol. 4, 4-8, 2013.

Investigation of the stress conditions of U-bend 316L stainless steel after performing cold mechanical process

W.M.F.W Mohamad[1,2,*], M.Z. Selamat[1,2], B. Bunjali[3], H.M. Dom[1,2]

[1)] Faculty of Mechanical Engineering, Universiti Teknikal Malaysia Melaka,
Hang Tuah Jaya, 76100 Durian Tunggal, Melaka, Malaysia.
[2)] Centre for Advanced Research on Energy, Universiti Teknikal Malaysia Melaka,
Hang Tuah Jaya, 76100 Durian Tunggal, Melaka, Malaysia.
[3)] Department of Chemisty, Institut Teknologi Bandung,
Jl. Ganesha 10 Bandung, Jawa Barat-Indonesia.

[*]Corresponding e-mail: farid@utem.edu.my

Keywords: 316L Stainless Steel; cold mechanical process; stress conditions.

ABSTRACT – This study reports on the investigation of the stress conditions of the U-bend 316L stainless steel through the cold mechanical process, starting with cold rolling of 0 up to 50% reduction in thickness and then, bending. The stress conditions; such as applied and residual stresses of the U-bend steel were obtained experimentally from the bending stress-strain curves and resulted curvature. It was found that the applied and residual stress has a higher value in the steel with a 30% cold reduction, which was about 257 MPa and 240 MPa, respectively.

1. INTRODUCTION

Cold rolling and bending have been used as a common cold mechanical process of metallic materials which covers most of the engineering applications. Past researches have proved that the cold deformation processes produce such amount of stresses. They have developed a great solution for the prediction of stress conditions, either as individual or combination of an analytical, simulation and experimental [1-2]. For the experimental solution, there were numerous preparation methods of the bent shape, as recommended by the ASTM standard. It was involved in the preparation of the various bent sheet metal, such as U-bend, V-bend, C-ring and bent-beam. The U-bend shape was selected since the stress conditions were considered unknown [3]. Furthermore, this solution was also applied to measure the residual stress in the sheet metals which were initially straight shape by measuring the resulted curvature of the bent shape. Zhang *et. al.* [4] and Tan *et. al.* [5] have produced an analytical solution that the residual stress was a sum of the stress before unbending and elastic spring back stress.

Therefore, this study was emphasized on the determination of the stress conditions of the U-bend steel through an experimental solution. The applied and residual stress was estimated from the bending stress-strain curves of the U-bend steel with a different level of the cold reduction. In addition, the related bending behaviors of the U-bend steel were also highlighted in this research.

2. METHODOLOGY

Experiments were carried out on 316L stainless steel (SS) with chemical compositions (in wt.%) of 316L [Fe, 16.61% Cr, 10.44% Ni, 1.048% Mo, 2.03% Mn, 0.02% C, 0.0022% S, 0.03% P, 0.571% Si, 0.28% Cu and 0.0221% N] as provided by the manufacturer. The test specimen with an initial thickness of 2.0 mm were unidirectional rolled to 0, 10, 30 and 50% reduction in thickness (%RT). Three sets of the specimen were prepared for each particular cold reduction. Then, the specimens were CNC milled to a dimension of 80.0 x 20.0 mm, with a hole of 10.0 mm in diameter on both sides. The bending process was done according to ASTM G 30-97, using a two stage stressing. In the first stage, the specimen was stressed to a U-bend shape using the bending jig, which was attached to the tensile machine: model Instron 8802 (US) system of 250 kN capacity. The process was subjected to a 3-point bend test with a constant speed of 1.0 mm/min. The second stage of the bending process was performed by manually stressing the specimen, and the U-bend shape was finally obtained.

A simple analysis of the U-bend steel was done before and after unbending using an image mapping techniques as shown in Fig. 2(a). It was used to measure the resulted curvature, in terms of the longitudinal deflection, D, lateral deflection, W and bend angle, α. The metallography analysis of the specimens was done using microscopy techniques. The specimens were cut to a reduced scale, approximately 8.0 mm from its maximum bending region. A standard metallographies technique was applied during the sample preparation.

3. RESULTS AND DISCUSSION

The bending properties of the U-bend 316L SS were characterized according to their bending stress-strain curves. Fig. 1 shows the curves of the U-bend steel with different cold reduction. At the initial stage, all the U-bend steel show a similar pattern, where the applied stresses were gradually increased with a higher strain rate. A large bending load was needed to transform the straight to the semi U-bend shape. Within this portion, the steel was elastically deformed before it reaches the ultimate bending stress.

After exceed this limit, the stress was rapidly dropped until the steel was permanently deformed to the U-bend shape. This was probably due to the formation of the inner cracks in the center of the U-bend steel as shown in Fig. 2(b).

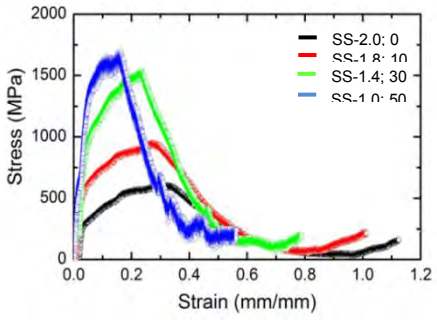

Fig. 1 Bending stress-strain curves.

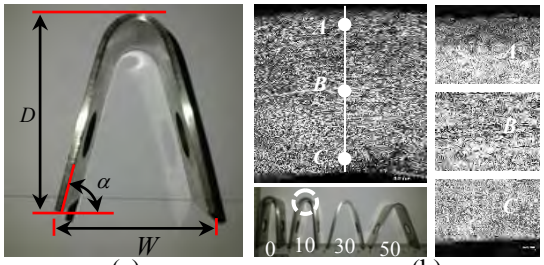

(a) (b)

Fig. 2 (a) Image mapping techniques, and (b) the formation of inner cracks.

Another bending behavior of the U-bend steel was related to the spring back phenomena. Table 1 illustrates the resulted curvature of the U-bend steel before and after unbending condition using an image mapping techniques. The increment of D and reduction of W after unbending, with reflected to the condition before unbending, was closed due to the spring back. It means that the specimen with a higher cold reduction produces a greater spring back and a higher residual stress.

Table 1 The measurement of the resulted curvature.

Sample ID	%RT	After unbending			Before unbending
		D_a (mm)	W_a (mm)	α_a (°)	W_b (mm)
SS-2.0	0	37.55	20.10	85.32	15.00
SS-1.8	10	37.40	24.10	80.01	14.75
SS-1.4	30	36.35	30.60	75.51	14.05
SS-1.0	50	33.70	40.10	65.22	13.90

Furthermore, the stress conditions of the U-bend steel were investigated according to the stress after and before unbending condition. It was obtained from their bending load-displacement and stress-strain curves. Fig. 3 shows the stress of each of the U-bend steel. The stress before unbending refers to an applied stress, σ_{ap} at the maximum deflection of the U-bend steels. Whereas, the maximum deflection refers to the final displacement in longitudinal direction before unbending, D_b with a bend angle, α_b of 90° into the U-bend shape. The D_b values of all specimens were about 37.70 mm. As expected, the U-bend steel without cold reduction (0%RT) shows a lower σ_{ap} of about 161 MPa. The value was increased to 209 and 257 MPa for the U-bend steel with 10 and 30 %RT, respectively. However, the σ_{ap} was decreased to 218 MPa for the U-bend steel after extensively cold reduction to 50 %RT.

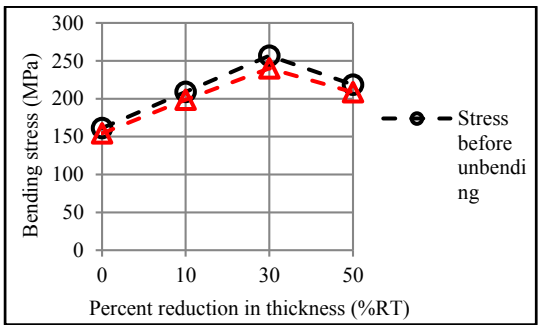

Fig. 3 The stress conditions of the U-bend steel.

The stress after unbending was closely referred to the residual stress, σ_{re}, as stated in the previous researchers [4,5]. From Fig. 3, the σ_{re} also shows a similar pattern with the σ_{ap} where the highest value was about 240 MPa for the U-bend steel with 30 %RT. In addition, the elastic spring back stress, $\Delta\sigma$ of all the U-bend steel have a negative value (where $\Delta\sigma = \sigma_{re} - \sigma_{ap}$). This was due to the nature of the spring back that it will be returned back to the previous bending path.

4. SUMMARY

The stress conditions of the U-bend 316 SS after performing cold mechanical process has been defined experimentally from the bending stress-strain curves and resulted curvature. It can be concluded that:

a. The processes were confirmly produced such amount of the residual stress. It has been preliminary predicted from the resulted curvature of the steel as a result of the spring back for each particular cold reduction.
b. The applied stress at the maximum deflection was higher than its residual stress. The highest value of the both stresses was obtained in the U-bend steel with 30 % cold reduction.

5. REFERENCES

[1] R. Schilling, "Sheet bending and determination of residual stress by means of FEM," *Engineering Structures*, vol. 26, pp. 1249–1259, 2004.
[2] M. Weiss, B. Rolfe, P.D. Hodgson, and C. Yang, "Effect of residual stress on the bending of aluminium," *Journal of Materials Processing Technology*, vol. 212, pp. 877–883, 2012.
[3] A.J. Sedricks, and B.C. Syrett, *Stress Corrosion Cracking Test Methods*, NACE: Houston; 1990.
[4] Z.T. Zhang, and S.J. Hu, "Stress and Residual Stress Distributions in Plane Strain Bending," *International Journal of Mechanical Sciences*, vol. 40, no. 6, pp. 533-543, 1998.
[5] Z. Tan, W.B. Li, and B. Persson, "On analysis and measurement of residual stresses in the bending of sheet metals," *International Journal of Mechanical Sciences*, vol. 36, no. 5, pp. 483–491, 1994.

Comparison of thermal conductivity for HHT-24 CNF-based nanofluid using deionized water and ethylene glycol as based fluid

N.S. Zaini[1,*], S.N. Syed Idrus[1], N. Abdullah[2], M.H.M. Husin[1], I.S. Mohamad[1]

[1)] Faculty of Mechanical Engineering, Universiti Teknikal Malaysia Melaka,
Hang Tuah Jaya, 76100 Durian Tunggal, Melaka, Malaysia.
[2)] Department of Chemistry, Centre for Foundation Studies, Universiti Pertahanan Nasional Malaysia,
Kem Sungai Besi, 57000, Kuala Lumpur, Malaysia

[*]Corresponding e-mail: nsalihazaini371@gmail.com

Keywords: Carbon nanofiber; nanofluid; thermal conductivity

ABSTRACT – Nanofluid are widely used in industrial applications due to their high thermal conductivity. In this experiments, thermal conductivity of various ratio carbon nanofiber based-nanofluid both in ethylene glycol and deionized water were investigated. The thermal conductivity of 1.0% CNF volume concentration at 40^0C for deionized water-based is 0.745 W/m.K while ethylene glycol-based is 0.349 W/m.K. It shows that deionized water-based recorded higher thermal conductivity compared to ethylene glycol-based. This is due to the effect of some parameter such as particle volume fraction, size and the temperature of thermal conductivity.

1. INTRODUCTION

Nanofluids are the mixture of nanoparticles, dispersing agent and based fluid in a solution. These fluids are stable colloidal suspensions of nanoparticles such as nanotube or nanofiber in base fluid. Choi and Eastman primarily studied nanofluids at Argonne National Library [1].

The potential of nanofluids as a new medium in enhancing heat transfer are closely related to their thermal conductivity. Choi et al. [2] proposed that thermal conductivity of nanofluid is higher compared to those currently used heat transfer fluids thus lead to the enhancement of heat transfer. However, the value of thermal conductivity for nanofluids might be differ according to the base solution use as the conductivity of the base solution itself play an important roles in determining the thermal conductivity result. Research from Ding et al. [3] conclude that the enhanced thermal behaviour of nanofluids could provide a basis for an enormous innovation for heat transfer intensifiction. This is a major importance to a number of industrial sectors including transportation, power generation, as well as heating, cooling, ventilation and air-conditioning. In this study, the thermal conductivity of water based and ethylene glycol based is compared.

2. METHODOLOGY

The nanoparticles used in this experiment are Pyrograf III Carbon Nanofiber High-Heat Treated (HHT-24). HHT-24 carbon nanofibers were produced by Pyrograf Products Inc. Nanofluids were prepared by mixing the carbon nanofiber and polyvinylpyrrolidone (PVP) in two different based-solutions. Those are deionized water and ethylene glycol solution. The samples were homogenized by using Digital Homogenizer LHG-15 for 3 minutes at 10000 rpm. The purposes of homogenization are to ensure the solid particles inside are uniformly dispersed. Next, the nanofluids sample undergoes ultrasonication cleaning process by being ultrasonicated using ultrasonic cleaner for about an hour at 25°C at the highest frequency. The ultrasonicator removes any contaminants in the nanofluid. The samples were then homogenized once again for five minutes at 2000 rpm. The thermal conductivity of the nanofluids was measured at three different temperatures (6°C, 25°C, 40°C) using KD-2 Pro Thermal Properties Analyser from Decagon Devices Inc. All samples were tested for thermal conductivity after being well homogenized to avoid any sedimentation which can affect the result.

3. RESULTS AND DISCUSSION

The thermal conductivity of nanofluid is tested and the data were shown at Figure 1. Table 1 show the percentage enhancement of ethylene glycol based nanofluids for three different temperatures (6^0C, 25^0C, and 40^0C) and the usage of 40% of PVP.

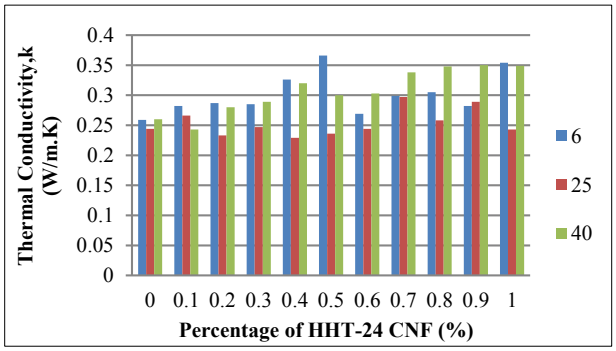

Figure 1 Thermal Conductivity for different temperature of ethylene glycol based nanofluid

The thermal conductivity of the nanofluid samples then compared with the thermal conductivity of the standard sample by calculating the enhancements of nanofluid through Equation 1:

$$\% \text{ of enhancement} = \frac{\text{T. C of samples} - \text{T. C of coolant/water}}{\text{T. C of coolant/water}} \text{ x } 100 \quad (1)$$

Table 1: Percentage of thermal conductivity enhancements for ethylene glycol based nanofluid

CNF %	Percentage of Enhancement (%) at temperature (°C)		
	6	25	40
0.1	8.88	9.02	-6.54
0.2	10.81	-4.51	7.69
0.3	10.04	1.22	11.15
0.4	25.87	-6.14	23.07
0.5	41.31	-3.28	15.38
0.6	3.86	0.41	15.21
0.7	15.44	22.22	28.52
0.8	17.76	6.17	32.32
0.9	8.88	18.93	33.08
1.0	36.68	0	32.70

The result of thermal conductivity and percentage enhancement of carbon nanofibers deionized water based nanofluids with the different percentage of PVP compared to ethylene glycol based nanofluids is show at Figure 2 and Table 2 respectively. The PVP used for the water-based nanofluid formulation is PVP with 10% weight of CNF.

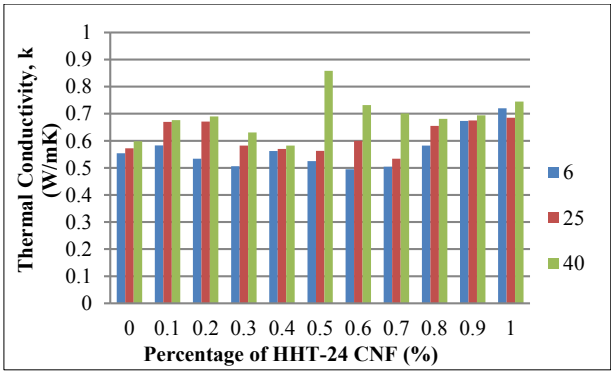

Figure 2 Thermal conductivity for different temperature of deionized water-based nanofluid

Then, the enhancement percentage is calculated according to the percentage of enhancement formula as stated in (1) for deionized water-based. Table 2 shows the tabulated data of percentage of thermal conductivity enhancement for deionized water-based nanofluid at different temperature.

At the tested concentrations, thermal conductivity increases with nanoparticle volume fraction, ϕ for both cases. From the result, it can be seen that deionized water recorded the higher thermal conductivity compared to ethylene glycol. However, in term of percentage enhancement, ethylene glycol recorded more percentage enhancement of thermal conductivity compared to deionized water. This is because; pure ethylene glycol has a specific heat capacity about one-half that of deionized water thus reducing the thermal conductivity of pure ethylene glycol. However, the mixture of ethylene glycol and water at rate 50/50 could increase the thermal conductivity [4].

Table 2: Percentage of thermal conductivity enhancements for deionized water-based nanofluid

CNF %	Percentage of Enhancement (%) at temperature (°C)		
	6	25	40
0.1	2.59	2.14	16.55
0.2	7.96	19.64	18.97
0.3	-1.11	19.82	8.79
0.4	4.07	3.93	0.34
0.5	-2.78	0.53	47.93
0.6	-8.33	-11.61	26.20
0.7	-6.67	-4.64	20.86
0.8	7.78	16.96	17.41
0.9	24.62	20.54	19.66
1.0	33.33	22.32	28.45

4. CONCLUSIONS

In general, adding solid nanoparticles increases thermal conductivity of nanofluid either for water based or ethylene glycol based nanofluids. Nanofluids with higher volume fraction rate of CNT possess high thermal conductivity compared to the pure base solution itself.

5. REFERENCES

[1] S. Choi. and J.A. Eastman, "Enhancing Thermal Conductivity of Fluids with Nanoparticles", in *International Mechanical Engineering Congress and Exhibition*, pp. 99-105,1995.

[2] W. Yu and H. Qie, "A Review on Nanofluids: Preparation, Stability, Mechanisms and Applications" *Journal of Nanomaterials,*vol. 2012, no. 1, pp. 1-17, 2012.

[3] Y.L. Ding, H.S. Chen, Y.R. He, A. Lapkin, and Y. Butenko, "Forced Convective Heat Transfer of Nanofluids" *Advance Power Technology*, 2007.

[4] L.S. Sundara, M.H. Farookyb, S.N. Saradab, M.K. Singha, "Experimental thermal conductivity of ethylene glycol and water mixture based low volume concentration of Al_2O_3 and CuO nanofluids," *International Communications in Heat and Mass Transfer,* vol. 41, pp 41-46, 2013.

The effect of nanocarbon characteristics on enhancing thermal properties of nanofluids

S. Zainal Abidin[1,*], I.S. Mohamad[1], N. Abdullah[2], A.Y. Bani Hashim[3]

[1)] Faculty of Mechanical Engineering, Universiti Teknikal Malaysia Melaka,
Hang Tuah Jaya, 76100 Durian Tunggal, Melaka, Malaysia.
[2)] Department of Chemistry, Centre for Foundation Studies, Universiti Pertahanan Nasional Malaysia,
Kem Sungai Besi, 57000, Kuala Lumpur.
[3)] Faculty of Manufacturing Engineering, Universiti Teknikal Malaysia Melaka,
Hang Tuah Jaya, 76100 Durian Tunggal, Melaka, Malaysia.

*Coresponding e-mail: Wanieyza_2792@yahoo.com

Keywords: Carbon nanotube; thermal properties; nanofluids

ABSTRACT – The different in nanocarbon structure may result in thermal conductivities performance. In this research, the understanding about the behavior and characteristic of different types of nanocarbon are investigated. The morphology and functionalized-group attachment on the nanocarbon surface were characterized using Scanning Electron Microscopy (SEM) and Fourier Transform Infra-Red (FTIR). The thermal conductivity testing were performed to select the best CNT which can possess a good thermal properties. The result shows that the CNT3 (HHT24) has the higher thermal conductivity enhancement.

1. INTRODUCTION

Nanofluids were formed by fine dispersion of nano-sized solid particles in a liquid. Even in dilute concentrations, typical colloids form aggregates that are dependent on the solution chemistry, surface charges, and thermal Brownian motion of the nanoparticles [1]. The external fields such as gravity and temperature can support or destroy the formation of aggregates. Thus, the tested nanofluids in most experimental shows that there is a competition between the growth of fractal-like structures, coalescence into large clumps, sedimentation, and fragmentation [2]. In general, the viscosity and thermal conductivity are sensitive to geometrical configuration and the connectivity [3] of the formed aggregated structure.

Carbon nanotubes with rolled-up graphene sheets have high thermal conductivity and has the ability to remain in stable suspension for a long period of time. The carbon nanotubes were discovered by Iijima in 1991 [4] and since that, carbon nanotubes have received much attention. The diameters and arrangement of the hexagon rings along the tube length determined the metal properties of the carbon nanotubes, metallic or semi-conductive. The consistent arrangement of the hexagon rings without any loose bonds make the carbon nanotube walls to become unreactive [5].

The intrinsic mechanical and transport properties of CNT make them an ultimate carbon fiber. By and large, CNT demonstrate an exceptional blend of stiffness, strength, and tenacity contrasted with other fiber materials which generally fail to offer one or a greater amount of these properties.

2. METHODOLOGY

The characterizations which being conducted for the selected nanocarbon such as Carbon Nanotube (Nanoamor-CNT), Multiwalled CNT and Carbon Nanofiber (Pyrograf-CNF). The objectives is to find the best nanocarbon, which can enhance and possess a good thermal properties based on the structural analysis. Thermal conductivity testing was conducted using KD2Pro Thermal properties Analyzer. The results were used to syncronized the performance of thermal conductivity with the surface characteristic of nanocarbons. Table 1 shows the properties of commercial carbon nanotubes used in this studies.

Table 1 Properties of the commercial CNT

Sample coding	Types	Outer Diameter (nm)	Specific Surface Area (m^2/g)
CNT1	Multiwalled-CNT	30-50	60
CNT2	Nanoamor - CNT	10-30	100
CNT3	Pyrograf - CNF	100	43

2.1 Scanning Electron Microscopy (SEM)

The Scanning Electron Microscopy (SEM) utilizes a focused beam of high energy electrons to create a mixed bag of signs on the surface of solid specimens. The signals that formed from the electron-sample correlations will produce the specimen or sample data that is the morphology (surface), composition of chemical, crystalline structure and also material content that make up the specimen observed under SEM. SEM was used to characterize the nanocarbons to generate high-resolution images with 10000x, 30000x, 60000x and 120000x magnification of shapes of objects and to observe the spatial variations in chemical compositions.

2.2 *Fourier Transform Infrared (FTIR)*

An infrared spectrum represents a fingerprint of a specimen with absorption peaks which correlate to the frequencies of vibrations between the obligations of the atom that making up the material. In order to make an identification and requires a frequency spectrum, as the measured interferogram signal cannot be interpreted, a means of decoding the individual frequencies is required. This can be solved only through the well-known mathematical method called the Fourier transform. This transformation will be performed and solved by the computer which then presents the user with desired spectral information for analysis.

2.3 Thermal Conductivity Testing

The thermal conductivity test of the nanofluid will be taken at three different temperatures which are at 6°C, 25°C and 40°C. To obtain such temperature of the nanofluid, those three samples will be immersed in the water bath so that the temperature of the samples will maintain at desired temperature.

3. RESULTS AND DISCUSSION

The morphology of three different types of carbon nanotubes is shown in Figure 1. The nanotubes morphology are randomly entangled and highly interconnected, probably due to the van der Waal's.

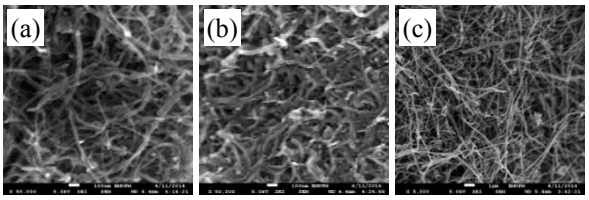

Figure 1 SEM images of a) CNT1, b) CNT2, c) CNT3

The surface areas contribute to the enhancement of physical and chemical properties of nanofluids. The properties that found to influence surface area were number of walls or diameter, impurities, and surface functionalization with hydroxyl and carboxyl groups. All images shown in Figure 1 illustrated agglomerate carbon nanotube and nanofibers, primarily with non-uniform tubular structure. The increase in diameter size will reduce the surface area. Higher surface areas are expected to provide a better media for thermal transport in nanofluid.

Figure 2 shows the FTIR spectra of the CNTs. On the horizontal axis is the infrared wavelengths expressed in term of a unit called wavenumber (cm^{-1}) which represent the number of waves fit into one centimeter. The peaks in the COOH spectrum represent the functional groups that are present in the molecule. The results reveal that the CNT1 (fMWNT) shows the higher COOH spectrum followed by CNT2 (Nanoamor), and CNT3 (HHT24). The higher in the peak spectrum will enable a good dispersion of CNT in nanofluids and improve the stability of nanofluids.

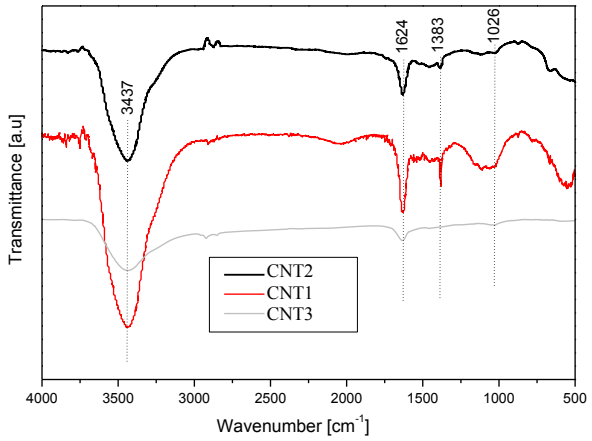

Figure 2 FTIR spectra of CNTs

Table 2 Thermal conductivity (W/mK) for CNT at various temperatures

CNT	Temperature (°C)		
	6	25	40
CNT1	0.55	0.50	0.50
CNT2	0.57	0.50	0.60
CNT3	0.58	0.60	0.60

Table 2 shows the thermal conductivity analysis for the all CNTs. CNT3 shows the higher thermal conductivity compared to others due to the decrement of diameter size in carbon nanofiber. The smallest diameter generates the best enhancement in thermal conductivity which contribute to the higher surface area.

4. CONCLUSIONS

In conclusion, the study of surface area of the selected CNT nanocarbon shows that the decrement in diameter size will attributed to the highest surface area and possesses a good thermal conductivity. The experimental studies shows that CNT3 (HHT24) generates the best enhancement in thermal conductivity. High surface area of the CNT3 (HHT24) offers a better media for thermal transport in nanofluids.

5. REFERENCES

[1] Weitz, D. A., Huang, J. S., Lin, M. Y., and Sung, J., "Dynamics of Diffusion-Limited Kinetic Aggregation," *Phys. Rev. Lett.*, vol. 53, pp. 1657–1660, 1985.

[2] Meakin, P., "Aggregation Kinetics," *Phys. Scr.*, vol. 46, pp. 295–331, 1992.

[3] J. Eapen, R. Rusconi, R. Piazza and S. Yip, "The Classical Nature of Thermal Conduction in Nanofluids", *Journal of Heat Transfer*, vol. 132, no. 10, pp. 1-14, 2010.

[4] Iijima.S. (2007). "Nano-carbon materials: Their Fundamentals and Various Applications including Nano-Biotechnology". University of Wien.

[5] Lin, T., Bajpai, V., Ji, T. and Dai, L., "Chemistry of Carbon Nanotubes*". Australian Journal of Chemistry*, vol. 56, no. 7, pp. 635-651, 2003.

Thermal properties and heat transfer study of dispersed fluid with functionalized Multi-Walled Carbon Nanotube (MWCNT) particles

F.N. Zahari[1,*], M.R.H. Noor Salim[1], I.S. Mohamad[1], N. Abdullah[2], S. Thiru[3]

[1)] Faculty of Mechanical Engineering, Universiti Teknikal Malaysia Melaka,
Hang Tuah Jaya, 76100 Durian Tunggal, Melaka, Malaysia.
[2)] Department of Chemistry, Centre for Foundation Studies, Universiti Pertahanan Nasional Malaysia,
Kem Sungai Besi, 57000, Kuala Lumpur, Malaysia.
[3)] Department of Mechanical Engineering, King Abdul Aziz University - North Campus
P.O. Box 80204, Jeddah 21589, Kingdom of Saudi Arabia.

[*]Corresponding e-mail: fatinbellanabila@gmail.com

Keywords: Thermal conductivity; MWCNT; specific heat capacity

ABSTRACT – Water, ethylene glycol and engine oil are commonly used in heat exchanger applications as coolant. However, these fluids possess low thermal conductivity. The advancement in nanotechnology has enabled nano-size particles to be included in a base fluid and this is known as nanofluids. The aim of this study is to investigate the most stable and homogeneous nanofluids with different weight percentage that produced excellent result in thermal properties and heat transfer characteristics. For this study, the usage of MWCNT as nanoparticles and deionized water as based fluids with surfactant were investigated for their stability and thermal properties. Different temperature and particle volume concentration were used in this study and this will affect the thermal conductivity, viscosity and specific heat as well as the heat transfer characteristics of nanofluids. As a result, the thermal conductivity and specific heat capacity of nanofluids were increased when the temperature and particle volume concentration increased. Besides that, the viscosity of nanofluids seem to decreased when temperature was increased but not for its particle concentration.

1. INTRODUCTION

Nanofluids are a new generation of thermal fluids which have particular features that affect their behavior. One of these features is response of nanofluids to temperature difference. Nanofluids have been found to possess enhanced thermophysical properties such as thermal conductivity, thermal diffusivity, viscosity and convective heat transfer coefficients as compared to those of base fluids like oil or water. Owing to their enhanced properties as thermal transfer fluids for instance, nanofluids can be used in engineering applications ranging from use in the automotive industry to the medical arena. Besides, it also being use in power plant cooling systems as well as computers. Focused on the nanofluids thermal properties, the temperature are greatly affected their thermal properties. It increasing the thermal conductivity for nanofluid when the temperature range increased [1,5]. The results suggested the application of nanofluids as coolant for devices with high energy density where the cooling fluid works at temperature higher than room temperature. Besides that, the viscosity of nanofluids also increased with increasing MWCNT concentration and decreasing temperature [2] meanwhile the specific heat of nanofluids decreases with an increase in concentration and an increase in temperature [3].

2. METHODOLOGY

2.1 Preparation of Nanofluids

To produce nanofluids, the MWCNT particles were used in this study and deionized water (DI) as well as polyvinylpyrrolidone (PVP) were used as base fluid and surfactant respectively. The nanofluids were prepared by dispersing MWCNT nanoparticles and PVP in a base fluid. They were mixed together by using a homogenizer at a rotational speed of 10000 rpm for about 5 minutes. Each of the samples will undergo 30 minutes of intensive ultrasonication to disperse the nanoparticles. This process was conducted by using the Elmasonic S30H Ultrasonicator (50-60 kHz frequency with 280W of output power). It generates high shear forces that break particle agglomerates into single dispersed particles.

2.2 Stability Test

Each samples need to undergo stability test. As for an investigation of the stability characteristics, the sedimentation of the nanofluid samples was observed for the duration of 100 hours by visual inspection and also by using laser shot technique. The stability of the nanofluid is generally determined by penetration of the laser beam emitted from the semiconductor laser diode which will travel through the nanofluid. If the laser light can travel through the nanofluid, the samples are considered as stable nanofluids. The stable nanofluid was then used for further experimentation. The stability of nanofluid was affected by the characteristics of suspended particle and base fluids such as the particle morphology, the chemical structure of the particles and base fluid [4,6].

2.3 Thermal Properties Test

To recognize the thermal properties of the nanofluid, several tests need to be conducted such as thermal conductivity, viscosity and specific heat. The tests were conducted at three different temperatures at 6 °C, 25 °C and 40 °C. In order to stabilize the samples temperature, the samples were placed inside the refrigerated water bath and this can minimize the effect of temperature variation.

For thermal conductivity test, the KD2Pro thermal analyzer (Decagon, USA) was used to measure the nanofluid thermal conductivity. It was set on automatic mode and left on the flat table to avoid any movement or table vibration during the measurement process. Any movement of the sample would create the convection.

For the viscosity test, the Brookfield rotational viscometer was used. Using multiple speed transmission and interchangeable spindles, a variety of viscosity ranges were measured. The viscosity of CNT-water nanofluids as a function of shear rate was measured. Besides that, nanofluids provide better fluid performance due to the higher shear rate at the wall which results in low viscosity there. Meanwhile, for specific heat test, it was conducted by employing the IKA C200 Bomb Calorimeter. The specific heat capacity determines the convective flow nature of the nanofluid and it necessarily depends on the volume fraction of the nanoparticles.

2.4 Heat Transfer Performance Test

Enhancement of heat transfer coefficient is much higher than the increase in the effective thermal conductivity [7]. They associated the possible reasons with the improved thermal conductivity, shear induced enhancement in flow, reduced boundary layer, particle re-arrangement and high aspect ratio of CNTs.

3. RESULTS AND DISCUSSION

Experiments were conducted to measure rheological properties of nanofluids in the particle volume concentration range of 0.2% - 1.0 % and the temperature range of 6 °C to 40 °C. Based on Table 1 and Table 3, the thermal conductivity of nanofluids increase when temperature and volume concentration increase same like specific heat. But for viscosity based on Table 2, it will decrease when temperature is high.

Table 1 Thermal conductivity for MWCNT nanofluids with different volume concentration and temperature

Volume concentration of nanofluids (wt %)	Thermal conductivity reading at different temperature (W/m.K)		
	6 °C	25 °C	40 °C
0.2	0.738	0.750	0.758
0.4	0.744	0.752	0.760
0.6	0.748	0.755	0.762
0.8	0.751	0.760	0.766
1.0	0.753	0.763	0.770

4. CONCLUSIONS

From the results it was found that the thermal conductivity was increased with an increase of particle concentration and temperature increment. The increase in thermal conductivity enhancement shows 23.5% for the volume concentration of 1.0%. Meanwhile, for the viscosity, it becomes much more dependent on the volume fraction of nanoparticles and base fluids also with the temperature. At low nanoparticle concentration, the viscosity of the base fluids are dominated and the viscosity increased when the temperature is decreased. This conditions vice versa when the concentration of nanoparticle and temperature is high. It was found that the specific heat of nanofluids decreased gradually with the increment in nanoparticle concentration however an increasing trend was found at elevated temperatures.

Table 2 Viscosity for MWCNT nanofluids with different volume concentration and temperature

Volume concentration of nanofluids (wt %)	Viscosity reading at different temperature (Pa.s)		
	6 °C	25 °C	40 °C
0.2	0.91	0.75	0.44
0.4	0.92	0.77	0.45
0.6	0.95	0.79	0.47
0.8	0.97	0.81	0.48
1.0	0.99	0.82	0.49

Table 3 Specific heat for MWCNT nanofluids with different volume concentration and temperature

Volume concentration of nanofluids (wt %)	Specific heat reading at different temperature (J/kg.K)		
	6 °C	25 °C	40 °C
0.2	0.398	0.410	0.427
0.4	0.390	0.405	0.420
0.6	0.385	0.402	0.416
0.8	0.381	0.400	0.414
1.0	0.378	0.399	0.410

5. REFERENCES

[1] L.S. Sundar and K.V. Sharma, "Thermal conductivity enhancement of nanoparticles in distilled water," *International Journal of Nanoparticles*, vol. 1, no. 1, pp. 66–75, 2008.

[2] Y. Ding, H. Alias, D. Wen & R.A. Williams, "Heat transfer of aqueous carbon nanotubes," *International Journal of Heat and Mass Transfer*, vol. 49, pp. 240, 2005.

[3] D.P. Kulkarni, R.S. Vajjha, D.K. Das and D. Oliva, "Application of aluminium oxide nanofluids in diesel electric generator as jacket water coolant," *Applied Thermal Engineering*, vol. 28, pp. 1774-1781, 2008.

[4] X.Q. Wang and A.S. Mujumdar, "Heat transfer characteristics of nanofluids: A review," *International Journal of Thermal Sciences*, vol. 46, no. 1, pp. 1-19, 2007.

[5] P.C. Mishra, S.K. Nayak and S. Mukherjee, "Thermal conductivity of nanofluids," *International Journal of Engineering Research and Technology*, vol. 2, no. 9, pp. 734-745, 2013.

[6] A. Ghadimi, R. Saidur and H.S.C. Metselaar, "A review of nanofluid stability properties and characterization in stationary conditions," *International Journal of Heat and Mass Transfer*, vol. 54, no. 17, pp. 4051-4068, 2011.

[7] S.K. Das, S.U.S. Choi, W. Yu and T. Pradeep, *Nanofluids Science and Technology*. New Jersey: John Wiley & Sons Inc.; 2007.

Effect of process variables on the tensile shear strength of spot welds in 6061-T6 aluminum alloy

S. Thiru[1,*], Siti Hajar Ahmad Razin[2], S. Hema[3], I.S. Mohamad[2]

[1)] Department of Mechanical Engineering, King Abdul Aziz University - North Campus
Jeddah 21589, Kingdom of Saudi Arabia.
[2)] Faculty of Mechanical Engineering, Universiti Teknikal Malaysia Melaka,
Hang Tuah Jaya, 76100 Durian Tunggal, Melaka, Malaysia.
[3)] School of Engineering, Linton University College, 71700, Mantin, Negeri Sembilan, Malaysia

[*]Corresponding e-mail: thiru@kau.edu.sa

Keywords: Resistance spot welds; weld strength; factorial design

ABSTRACT – The changes in mechanical and metallurgical behavior of spot welded region generally occur throughout the spot welding process and these changes are very significant for the safety and quality of the welded joints. Due to the influence of current flow, the squeezing time and the load applied on electrodes have a vital effect on the mechanical properties. This paper presents the effect of such parameters on the tensile shear strength of single lap spot welded 6061-T6 aluminium alloy. Two level four factor fractional factorial design was employed to develop mathematical models. It was found that change in weld thickness and current are the primary parameters that control the tensile shear behavior of the spot welds.

1. INTRODUCTION

Employing light materials such as aluminium and magnesium alloys as an alternative for steel is the need of the hour for the 'all-time' competitive automotive industry to survive, in terms of the growing energy and environmental regulations of the modern world. Aluminum alloy 6061-T6 is a widely used structural material for automobile, air craft and maritime industries since it is highly weldable and has favorable mechanical properties [1-3]. Since the resistance spot welding (RSW) is the most widely used process for the fabrication of automobile case parts due to its simplicity, low-cost, high production rate and automation accessibility [4], it is critical to understand the behavior of the welding process control parameters on the mechanical properties of the aluminum 6061-T6 alloy.

2. METHODOLOGY

2.1 Development of Design Matrix

After a series of trial runs, the experimental design matrix was developed in accordance with the design of experiments (DOE) methodology, by adopting a two level, four factor fractional factorial design ($2^{4-1}=8$) of eight runs. For a factorial design of experiment, it is crucial to select the "individually controllable" process control parameters which are generally selected either from the published literature or the trial runs. For the present study the electrode force (F), weld current (I), weld time (t) and work piece thickness (w) were selected as the four main parameters that influence the tensile shear strength, the response parameter to be evaluated. All the direct and indirect parameters involved in the RSW process were kept constant. The upper limit (highest level) and the lower limit (lowest level) of a factor were coded as (+1) and (-1) or simply (+) and (-) respectively according to the equation (1).

$$X_j = \frac{X_{jn} - X_{jo}}{J_j} \quad (1)$$

Where, X_j is the coded value of the factor; X_{jn} is the natural value of the factor; X_{jo} is the natural value of the basic level; J_j is the variation interval and j is the number of the factors. The selected process control parameters, their units, symbols and the limits are given in Table 1.

Table 1 Selected process control parameters and limits

Parameter	Unit	Symbol	Limits	
			High (+1)	Low (-1)
Force	kN	F	1.8	1.2
Current	kA	I	26.6	23.8
Weld Time	cycle	t	8	3
Thickness	mm	w	1	0.71

2.2 Experimentation

In the present work, a pedestal spot welder, Lecco -Italia NKLT(P) 28 was used. Prior to the experiments, all the critical process control parameters were calibrated.

Table 2 Design matrix for calculating the coefficients

S.	β_0	β_1	β_2	β_3	β_4	T_s'	T_s''	T_s'''
1	+	+	+	+	+	30.63	34.79	32.71
2	+	-	+	+	-	76.29	78.35	74.24
3	+	+	-	+	-	51.79	52.52	53.26
4	+	-	-	+	+	42.03	43.85	40.21
5	+	+	+	-	-	76.29	84.65	67.93
6	+	-	+	-	+	51.41	55.00	47.81
7	+	+	-	-	+	28.96	34.27	31.61
8	+	-	-	-	-	61.25	55.60	66.90

For welding current - digital multimeter; for electrode force- SP-231N Spotron hydraulic weld force gauge and for welding time – Casio digital stop watch were employed. The experiments were performed as per

the design matrix in a random way by using the table of random numbers to remove any systematic error of experiment to produce set of three welding current columns. Three replications of experimental data were collected for statistical modeling requirements and are tabulated along with the design matrix in Table 2.

2.3 Selection and Development of Mathematical Model

A linear model of the type $Q = f(F,I,t.w)$ was adopted for the study which can be written in the form of a polynomial by taking into account all the possible two factor interactions as:

$$T_s = \beta_0 + \beta_1 F + \beta_2 I + \beta_3 t + \beta_4 w + \beta_{13} tw + \beta_{14} Fw + \beta_{23} It + \beta_{24} Iw + \beta_{34} tw \quad (2)$$

Where T_s is the measured tensile shear strength, the response parameter, $\beta_0, \beta_1 .., \beta_4$ are the linear coefficients to be estimated which depend on the four process control parameters. The proposed model was developed by regression analysis, whose adequacy and the significance of its coefficients were tested by the analysis of variance (ANOVA) technique and Student's '*t*' test. The regression coefficients of the model were calculated using the method of least squares.

3. RESULTS AND DISCUSSION

3.1 Main and Interaction Effects

The proposed model for prediction of the tensile shear strength (T_s) of the aluminum 6061-T6 alloy after neglecting the statistically insignificant parameters is given by

$$T_s = 53.01 - 4.73F + 6.61I - 2.13t - 13.57w - 3.54Ft - 2.55Fw \quad (3)$$

From the mathematical model (3) it can be seen that all the four process variables considered for the study, the electrode force (*F*), weld current (*I*), weld time (*t*) and work piece thickness (*w*) control the tensile shear strength. The weld current has positive effect while the rest have inverse effect on T_s as shown in the surface plot in Figure 1.

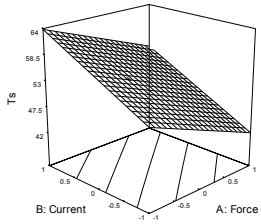

Figure 1: Surface plot on the effect of electrode force and current on tensile shear strength

It is well known that weld current is responsible for the heat input in arc welding [5]. An increase in weld current will increase the heat input resulting more melting and with pressure the atoms of the faying surfaces will be made closer enough to increase the joint strength. However the increase in welding force, time and dissimilar thickness at the same current level as per the model would decrease the tensile shear strength of the weld joint. Work piece thickness is proportional to the total resistance and need more current to perform melting and hence joining. Also an increase in electrode force will lead to indentation and splashing. The increase in weld time leads to overheating. Both of these reduce the joint strength. The model also showed that the welding force combining with the weld time (Figure 2) and change in workpiece thickness have significant interaction effects on the tensile shear strength as well. An increase in either of the electrode force, time and thickness will have an adverse effect on the strength of the joint.

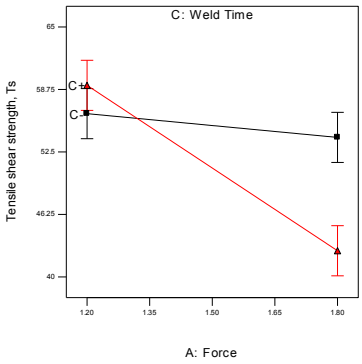

Figure 2 Interaction plot on the effect of electrode force and weld time on tensile shear strength

4. CONCLUSIONS

A mathematical model was developed to predict the effects of electrode force (*F*), weld current (*I*), weld time (*t*) and dissimilar work piece thickness (*w*) on tensile shear strength of aluminum 6061-T6 alloy spot welds. It was found that the weld current has direct relationship with the tensile shear strength while the rest have an inverse relationship. The welding force along with weld time and thickness has significant interactive influence causing an inverse effect on the tensile shear strength. The two level fractional factorial technique is found to be adequate and effective in predicting the main and interactions effect of the process control parameters on the tensile strength for resistance spot welds.

5. REFERENCES

[1] X. Sun, E.V. Stephens, M.A. Khaleel,"Effects of fusion zone size and failure mode on peak load and energy absorption of advanced high strength steel spot welds under lap shear loading conditions", *Engineering Failure Analysis*, vol. 15, pp. 356-367, 2008.

[2] Y. Zhou, P. Gorman, W. Tan, K.J.Ely,"Weldability of thin sheet metals during small-scale resistance spot welding using an alternating-current power supply", *Journal of Electronic Materials*, vol. 29, pp. 1090–1099, 2000.

[3] H.Zhang, J. Senkara, *Resistance welding: fundamentals and applications*, New York: Taylor & Francis CRC press; 2005.

[4] D. A. Ozyurek, "An effect of weld current and weld atmosphere on the resistance spot weldability of 304L austenitic stainless steel", *Materials and Design*, vol. 29, pp. 597–603, 2008.

[5] P. T. Houldcroft, *Welding process technology*, 3rd ed. London: Cambridge University Press; 2004.

Charpy impact response of oil palm empty fruit brunch fiber reinforced metal laminate system

Fadzila Hussain[1], D. Sivakumar[1,2,*], S. Kathiravan[1], Mohd Ahadlin Mohd Daud[1,2]

[1)] Faculty of Mechanical Engineering, UniversitiTeknikal Malaysia Melaka,
Hang Tuah Jaya, 76100 Durian Tunggal, Melaka, Malaysia.
[2)] Centre for Advanced Research on Energy, UniversitiTeknikal Malaysia Melaka,
Hang Tuah Jaya, 76100 Durian Tunggal, Melaka, Malaysia.

[*]Corresponding e-mail: sivakumard@utem.edu.my

Keywords: oil palm empty fruit brunch; fiber metal laminate; charpy impact

ABSTRACT – The low velocity impact response of novel oil palm empty fruit brunch fiber reinforced metal laminates system has been investigated. The specimens were tested using a pendulum impact tester according to ASTM E-23 in a flatwise direction. Impact resistances of the fiber metal laminates were benchmarked with monolithic aluminum. The main failure mechanism after impact had been investigated with detailed microscopic observation. Finally, it was found that energy absorption of aluminum is higher than fiber metal laminates.

1. INTRODUCTION

In order to improve the properties of existing composites, new research had led to the development of fiber metal laminate (FML). FML is a sandwich structure consisting of layers of fiber reinforced composite material and metal sheets. Farsani *et al*. [1] conducted a charpy impact experiment on basalt fiber reinforced epoxy composite (BFRE) and FML made of BFRE composite with aluminum and steel layers. ASTM D6110 standard was used for flatwise and edgewise specimens to investigate the Charpy impact response. It was found that the damage tolerance of FMLs is superior compared to the plain BFRE composite for both flatwise and edgewise impact loads. Steel layered FML has higher energy absorption levels compared to aluminum layers. Low velocity impact tests were undertaken by Carrillo and Cantwell [2] to highlight the impact energy absorption characteristics of thermoplastic matrix FML based on a self-reinforced polypropylene composite and a 2024-0 aluminum layer. They found that impacted plates exhibit a high level of energy absorption, with damages in the form of thinning in the aluminum plies and fractures in the composite layers. Gin Bo Chai and Periyasamy [3] stated that the response of FML to low velocity impacts is affected by many parameters, e.g: Type of metal, fiber, matrix, stacking sequence, metal volume fraction, impactor geometry, target shape, post-stretch percentage and others in their review. This huge interdependency results in the difficulty to attain the optimum FML. For laminated test pieces, tests may be performed both flatwise and edgewise, and for each of these, there exists the possibility of having the laminations put parallel or normal to the direction of blow [5]. The aim of this study is to investigate the Charpy impact response on a novel oil palm empty fruit brunch fiber reinforced composite with an Al 6061-O metal layer or in other words, oil palm composite fiber metal laminates (OPC FML). To obtain a better understanding of the behavioral impact of OPC FML, the monolithic aluminum was tested under charpy flatwise impact loads at room temperature and the results were compared with OPC FML. It means that the effect of different material properties and structures on behavioral impact is studied. All specimens are studied using microscopic observation in order to examine its' failure mechanisms.

2. METHODOLOGY

2.1 FML fabrication

The oil palm fiber reinforced polypropylene composite panel (OPC) with a thickness of 1.0mm was produced using 30wt%granulated empty fruit bunch palm fiber as reinforcement and 67wt%polypropylene (PP) as matrix with 3wt% Maleic anhydride grafted Polypropylene (MaPP) as its coupling agent. The composition was heated at 185°C for 8 minutes followed by fast cooling to room temperature in a picture frame mold. The FMLs were manufactured by stacking two 0.5 mm thick aluminum sheets 6061-O for the skin and one 1.0 mm thick oil palm fiber reinforced polypropylene composite as the laminate. The laminate was glued together using modified polypropylene film adhesive at the bi-layer surface of the material. The stack was heated to 155°C under a pressure of 1kg/cm² in a motorized hydraulic mold test press machine for 5 minutes before being left to cool slowly to room temperature. The dimensions of the OPC FML panel produced were 200 x 200x2 mm.

2.2 Impact test on FML specimen

Generally the charpy test piece is supported by a horizontal beam and is broken by a single swing of a pendulum. In this work, impact specimens with dimensions of 55x10x2mm were cut from the OPC FML panels using a water jet cutting machine. Low velocity impact tests were carried out using a pendulum impact tester (Instron CEAST 9050) with a hammer capacity of 50J according to ASTM E-23. Figure 1 shows the schematic diagram of flatwise charpy impact

test. Three samples were tested for each material, and the average absorbed energy was recorded.

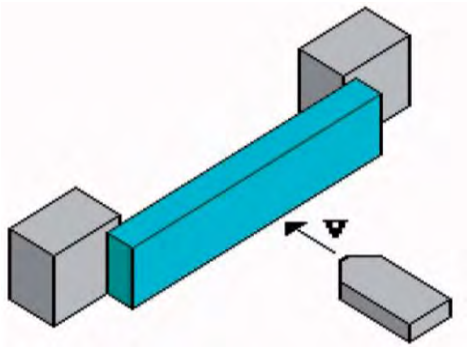

Figure 1 Schematic diagram of flatwise impact

3. RESULTS AND DISCUSSION

Figure 2 shows the average energy absorption for OPCFML and aluminum impacted in a flatwise direction at room temperature. In this experiment, aluminum is generally able to absorb higher energies compared to OPC FML material. The low energy absorption of FML can be contributed to weak bonding between the aluminum and composite laminates.

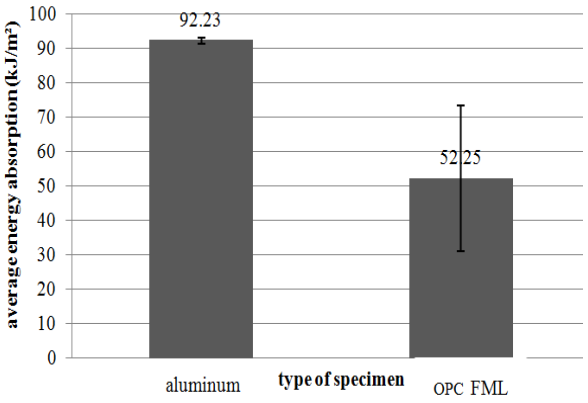

Figure 2 Energy absorption for each material

Figures 3 and 4 show the specimens after impact for both materials. The main failure mechanisms are different. Figure 3 shows the main failure mechanism on the aluminum material was damaged at the region of the line of impact.

Figure 3 Failure mechanism of aluminum

As can be seen in figure 4, plastic deformation of the aluminum layer and delamination are observed at the location of impact and are is detected as the failure mechanism. No aluminum tearing was observed. Due to the high rate strain at the impact location, the sequence of the failure mechanisms is difficult to recognize, but the initial failure is due to delamination, then fiber breakage and metal failure [1].

Figure 4 Failure mechanism of OPC FML

4. CONCLUSIONS

A new type of FML based oil palm empty fruit brunch fiber, OPC FML is studied using the Charpy impact for the first time. Aluminum and OPC FML specimens were studied for flatwise impact behavior. By comparing and studying the achieved experimental results, we can conclude that the impact energy of aluminum has more strength compared to OPC FML. Many parameters can influence the energy absorption for FML such as the type of metal, fiber, matrix, stacking sequence, bonding and others.

5. ACKNOWLEDGEMENTS

This research is supported under the Exploratory Grant Scheme provided by the Ministry of Education Malaysia.
(No. ERGS/2013/FKM/TK01/UTEM/02/07/E00018)

6. REFERENCES

[1] R. E. Farsani and V. Daghigh, “Charpy impact response of basalt fiber reinforced epoxy and basalt fiber metal laminate composites: experimental study,” vol. 23, no. (6), pp. pp.729–744, 2014.

[2] J. G. Carrillo and W. J. Cantwell, “Mechanical properties of a novel fiber–metal laminate based on a polypropylene composite,” *Mech. Mater.*, vol. 41, no. 7, pp. 828–838, Jul. 2009.

[3] G. B. Chai and P. Manikandan, “Low velocity impact response of fibre-metal laminates – A review,” *Compos. Struct.*, vol. 107, pp. 363–381, Jan. 2014.

[4] G. Reyes and H. Kang, “Mechanical behavior of lightweight thermoplastic fiber–metal laminates,” *J. Mater. Process. Technol.*, vol. 186, no. 1–3, pp. 284–290, May 2007.

[5] Roger Brown,*Handbook of polymer testing: physical method* , USA ; Marcel Dekker ;1999

Thermal performance of carbon-based microencapsulated phase change materials

A.Z.I. Abdullah[1], M.F.B. Abdollah[1,2,*], B.T. Tee[1,2], H. Amiruddin[1,2], A.K. Mat Yamin[1,2], N. Tamaldin[1,2]

[1)] Faculty of Mechanical Engineering, Universiti Teknikal Malaysia Melaka,
Hang Tuah Jaya, 76100 Durian Tunggal, Melaka, Malaysia.
[2)] Centre for Advanced Research on Energy, Universiti Teknikal Malaysia Melaka,
Hang Tuah Jaya, 76100 Durian Tunggal, Melaka, Malaysia.

[*]Corresponding e-mail: mohdfadzli@utem.edu.my

Keywords: Phase change materials; carbon-based materials; thermal performance

ABSTRACT – The aim of this study is to investigate the effect of carbon-based materials for the thermal performance of microencapsulated phase change material (μPCM). The sample was prepared separately by mixing 5 wt.% of Multiwall Carbon Nanotube (MWCNT) and 5 wt.% Expanded Graphite (EG) with μPCM using a powder metallurgy technique. The mixed powder was then compacted into a disc with a diameter of 45 mm and thickness of 5 mm using a hot compaction technique. The thermal performance was tested according to the ASTM standard. It was found that the addition of MWCNT into μPCM can absorb heat effectively as compared to pure μPCM and μPCM/EG composite.

1. INTRODUCTION

Phase change material (PCM) is suitable to be applied as energy storage, thermal protection and passive cooling system [1]. This is because of its desirable characteristic such as high latent heat of fusion, low vapor pressure during melting, no super cooling and chemically inert and stable [2-3]. In principle, the heat generated by any system could be absorbed by the PCM by attaching it on the system. PCM acts as heat sink for the system to eliminate the heat produced. However, the PCM could melt when the temperature of the system exceeds the melting point and the high latent heat of PCM. The melting PCM causes complexity and limits the full use of its function. In order to solve the limitation, micro-encapsulated technique was employed to PCM to solve the problem. Microencapsulated phase change material (μPCM) products are very small bi-component particles consisting of a core material, the PCM and an outer shell or capsule wall that hold the melted PCM from leaking. Therefore, whether the PCM is in the liquid or solid state, the capsule itself will remain as a solid particle.

The μPCM has disadvantage of low thermal conductivity to meet required heat exchange rates. Many techniques were proposed to improve thermal conductivity of PCM such as inserting fin, incorporating carbon based materials and adding metallic and nonmetallic materials [4]. Most researchers use core PCM, typically Paraffin wax instead of μPCM, therefore the matrix lead to melt compare to μPCM.

Based on the above review, there are a limited number of studies [1-4] that investigate the effect of carbon-based materials on the thermal performance of μPCM. This study aims to investigate further the thermal performance between μPCM/EG and μPCM//MWCNT composites.

2. METHODOLOGY

The μPCM type of PX52 was supplied by Rubitherm Technologies, while for MWCNT and EG was supplied by Microtek Laboratories. Table 1 shows the thermal properties of the materials.

Table 1 Thermal properties of the materials

[a]Properties	μPCM	MWCNT	EG
Melting temperature, ^{o}C	52	3625	3000
Thermal conductivity, W/m.k	0.1	3500	200
Latent heat capacity, kJ/kg	100	-	-
Density, g/cm^3	0.65	0.03	2.2

[a]From manufacturer

The samples were prepared separately by mixing 5 wt.% of MWCNT and 5 wt.% EG with μPCM using a ball mixer. The mixed powder was then compacted into a disc with a diameter of 45 mm and thickness of 5 mm using a hot hydraulic press. The samples are show in Figure 1.

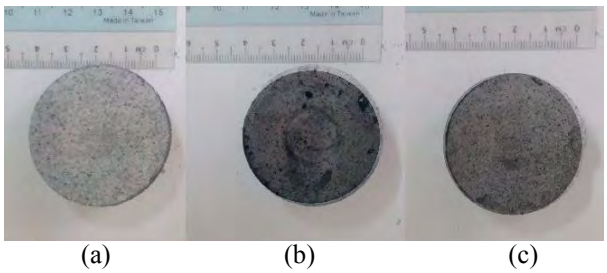

(a) (b) (c)

Figure 1 Photo of samples of (a) μPCM, (b) μPCM/EG composite, and (c) μPCM/MWCNT composite.

The thermal performance of the prepared sample was tested according the modified method in correlation to the ASTM C518–10 [6]. The measurement stack of the apparatus is shown in Figure 2. The sample is placed between the hot and cold copper plates. The hot plate above the electric heater assures unidirectional heat flow from the heater up through the sample. The cold plate above the sample provides uniform temperature distribution on its surface. Unidirectional heat flow is achieved by adjusting the electric power supply to such a level that temperature of the heater is equal to the hot plate temperature. The sample was covered by aluminum. The aluminum casing was heated at 12V of nominal voltage and 5 Watt of power. All tests were performed at room temperature. The temperature of aluminum casing was recorded by using an infrared thermometer for each minute. The result was obtained in the form of the temperature profile of aluminum casing over time.

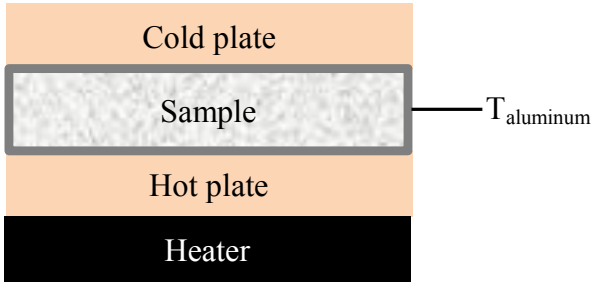

Figure 2 Measurement stack in plate apparatus.

3. RESULTS AND DISCUSSION

Figure 3 shows the temperature profiles of aluminum with and without µPCM composites. It was clearly shown that the temperature of aluminum increases over time. However, the magnitude of temperature significantly decreases when the µPCM is present. Besides, the combination of µPCM and MWCNT effectively reduce the temperature of aluminum casing to 91% over the time. This shows that the composite absorbs some amount of heat from the aluminum casing, and hence decrease the temperature. The present of MWCNT into µPCM can absorb more heat from the aluminum casing as compared to the pure µPCM and µPCM/EG composite. This is due to the fact that the MWCNT has higher thermal conductivity and larger surface area compared to EG. M. Lajvaerdi et al. [5] reported that the thermal conductivity of paraffin increases to 31% with addition of 2 wt.% of MWCNT.

4. CONCLUSIONS

In conclusion, the thermal performance of µPCM can be improved by employing carbon-based materials as an additive. However, the µPCM/MWCNT composites show a great improvement in terms of heat absorption due to the fact that the MWCNT has higher thermal conductivity and larger surface area compared to EG.

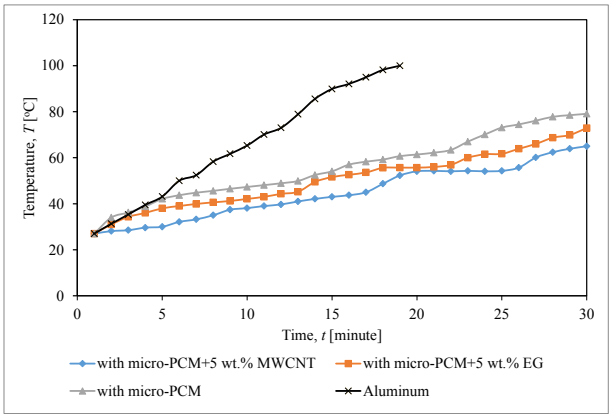

Figure 3 Temperature profiles of aluminum casing over time with and without µPCM composites.

5. ACKNOWLEGEMENT

The authors gratefully acknowledge contributions from the members of the Green Tribology and Engine Performance (G-TriboE) research group. This research was supported by the grant from the Ministry of Education Malaysia (Grant No.: RAGS/2012/FKM/TK01/1 B00001).

6. REFERENCES

[1] S. Alhallaj, R. Kizilel, A. Lateef, R. Sabbah, M. Farid, J.R. Selman, "Novel PCM thermal management make li-ion batteries a viable option for high power and high temperature application," in *The 22nd International Battery Seminar & Exhibit*, 2005.

[2] B. Zalba, J.M. Marin, L.F. Cabeza, H. Mehling. "Review on thermal energy storage with phase change: materials, heat transfer analysis and applications," *Appl. Therm. Eng,* vol. 23, no. 3, pp. 251–283, 2003.

[3] S.D. Sharma, K. Sagara, "Latent heat storage materials and systems: a review," *International Journal of Green Energy*, vol. 2, no. 1, pp. 1–56, 2005.

[4] T.P. Teng, C.C. Yu. "The effect of heating rate for phase change materials containing MWCNTs," *International Journal of Chemical Engineering and Applications*, vol. 3, no.5, pp. 340-342, 2012.

[5] M. Lajvardi, K. Lafdi, O. Mesalhy, "Carbon Nanotube in Passive Cooling," in *The 4th International Conference Nanostructure*, 2002.

[6] ASTM C518 – 10: Standard Test Method for Steady-State Thermal Transmission Properties by Means of the Heat Flow Meter Apparatus.

Fabrication and testing of energy regenerative suspension

M.A. Abdullah[1,2,*], J. F. Jamil[1], N.S. Muhammad[1]

[1)] Faculty of Mechanical Engineering, Universiti Teknikal Malaysia Melaka,
Hang Tuah Jaya, 76100 Durian Tunggal, Melaka, Malaysia.
[2)] Centre for Advanced Research on Energy, Universiti Teknikal Malaysia Melaka,
Hang Tuah Jaya, 76100 Durian Tunggal, Melaka, Malaysia.

*Corresponding e-mail: mohdazman@utem.edu.my

Keywords: Regenerative suspension; energy harvesting; energy efficient vehicle.

ABSTRACT - The research and development of the energy alternative for automotive industry is important as the world is demanding on the energy efficient vehicle (EEV). The use of hybrid vehicle and electric vehicle is one of the steps to the EEV vehicle which using alternative way other than using fuels to propel the vehicle. This research emphasizes the development of energy regenerative suspension system (EReSS) as the energy harvesting system for wasted energy on the vertical vibration in the suspension system of a vehicle. The EReSS is fabricated and tested on the laboratory experimentation.

1. INTRODUCTION

The energy loss on the suspension system of a vehicle is neglect on past research. The loss that is neglect is the energy dissipated in the suspension vertical vibration. The function of the suspension is to support the body, road disturbance and give response to the wheel to hold the road surface. The energy efficient vehicle (EEV) is popular this time and several researches have been done for better EEV vehicle in the future. Electromagnetic regenerative suspension transforms the vertical vibration to electric energy that can be stored and reuse [1]. The vehicle dissipation of the suspension system is different at different road surface, vehicle velocity and stiffness of damper. It indicates that the velocity and the tire pressure is directly proportional and affects the power dissipation. Other research states that the energy dissipation is taking the rider comforts and road handling into account [2]. Schematic analysis of the road surface, dynamics, ride and power at the same time is currently not available [3]. The usage of energy regenerative suspension reduces the electrical demand on the vehicle alternator at the same time reduces the engine work load. The system of regenerative will improve the fuel efficiency of the vehicle by designing the appropriate system to harvest the energy from the vehicle vibration.

2. METHODOLOGY

The design of the energy regenerative suspension (EReSS) is drawn in the computer-aided-drafting (CAD) software. This is to ensure the dimension of the fabrication product parts fit to each other. The drawing is illustrates in Figure 1.

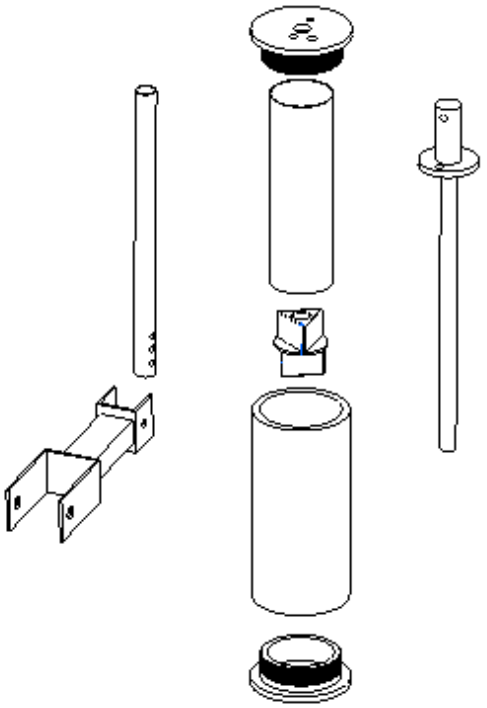

Figure 1 CAD drawing of EReSS

The fabrication process is done part by part. The material use for the EReSS is different for each of the part. The EReSS system will be tested on a test rig on the laboratory. On the test rig, the EReSS is operated such that the system is on the vehicle suspension system by moving it upwards and downwards. The different of the testing on the test rig is that the frequency can be set and constant whereas if the test is done on the car suspension, the frequency cannot be set because of the road irregularity.

3. RESULTS AND DISCUSSION

The EReSS is fabricated by referring the CAD data and the product is shown in Figure 2. The design of the EReSS is retrofit which is not disturbing the original suspension system of the vehicle. This EReSS can function automatically by following the suspension movement. The EReSS is then tested in laboratory to record the voltage produces by the system. The experiment is done on a test rig in the laboratory and the data of the experiment is shown in Table 1. The

frequency of the experiment is different which is set from 10Hz to 50Hz. The coil diameter used for the testing is 0.29mm and standard magnet magnetic flux density of 0.2T. The number of loop that is used in the system is different to record the different value of voltage produces by each set of coil loop. From the result of experiment, the number of loop used in the system affected the voltage produces by the EReSS. The greater the number of loop, the greater the voltage produces by the system. The highest voltage reading is occurs at 40Hz frequency with the voltage value of 3.03V. The use of EReSS reduces the load for the engine as it reduces the use of the alternator. Thus, the fuel efficiency of the vehicle increases. Other than that, the stored energy by the EReSS can be use for the electrical system of the vehicle and reduce the usage of the battery.

Figure 2: Fabricated EReSS system.

Table 1: Voltage reading of EReSS experiment.

	Voltage (V)		
Loop (N)/ Frequency (Hz)	400	250	100
10	0.82	0.43	0.27
20	2.06	1.98	1.25
30	1.64	2.01	1.56
40	3.03	2.24	1.98
50	1.40	1.15	0.73

4. CONCLUSIONS

The EReSS system can harvest wasted energy and convert the vibration energy to voltage charge. This system can be use in EEV vehicle that will increase the fuel efficiency of vehicle and reduces the usage of alternator. Besides, this system is an alternative source of energy that can be reuse and stored from the harvested wasted energy on the vehicle suspension system. The EReSS is an important system that is suitable to be use on hybrid or electric car in the future. This system has potential to fulfill the world demand on reducing the fuel consumption of vehicle in automotive industry.

5. ACKNOWLEDGEMENT

The authors gratefully acknowledged the Advanced Vehicle Technology (AcTiVe) research group of Centre for Advanced Research on Energy (CARe), the financial support from Universiti Teknikal Malaysia Melaka and The ministry of Education, Malaysia under Short Term Research Grant, Grant no. PJP/2014/FKM(10A)/S01330 and Fundamental Research Grant Scheme (FRGS), grant no.: FRGS/2013/FKM/TK06/02/2/F00165

6. REFERENCES

[1] M.A Abdullah, N. Tamaldin, M.A. Mohamad, R.S.Rosdi and M.N.I. Ramlan, “Energy Harvesting andRegeneration from the Vibration of Suspension System ”, Applied Mechanics and Materials, TransTech Publications, Vols. 699, pp 800-805, 2015, *doi:10.4028/www.scientific.net/AMM.699.800.*

[2] S. Z. Pei, “Design of electromagnetic shock absorbers for energy harvesting from vehicle suspensions”, Masters of Science in Mechanical Engineering thesis. Stony Brook University, New York, United States of America, 2010.

[3] Z. Li, L. Zuo, G. Luhrs, L. Lin and Y. Qin, “Electromagnetic energy-harvesting shock absorbers:design, modeling and road tests”, IEEE Transactions on Vehicular Technology, vol.62, no. 3, 2013.

[4] N. H. Amar, R. Ramli, H. M. Isa, W. N. L. Mahadi and M. A. Z. Abidin, “A review of energy regeneration capabilities in controlablesuspension for passengers' car”. Energy Education Science and Technology Part A: Energy Science and Research 2012, vol. 30(1) : 148-158.

[5] O. D. Raz, “Design and performance of electric shock absorber”. Master of Science in Electrical Engineering thesis. Lousiana State University and Agricultural and Mechanical college, United States of America, 2003.

[6] Z. Li, L. Zuo, J. Kuang and G. Luhrs, “Energy-Harvesting shock absorber with a mechanical motion rectifier”. Smart Materials and Structures. 2013.

[7] B. Ebrahimi, “Development of hybrid electromagnetic dampers for vehicle suspension system”. Doctor of Philosophy in Mechanical Engineering thesis, University of Waterloo, Canada, 2009.

Experimental validation of single cylinder diesel engine using engine simulation tools

M.H. Ahmad[1], N. Tamaldin[1,2,*], A.K.M. Yamin[1,2], S.C. Lee[1]

[1)] Faculty of Mechanical Engineering, Universiti Teknikal Malaysia Melaka,
Hang Tuah Jaya, 76100 Durian Tunggal, Melaka, Malaysia.
[2)] Centre for Advanced Research on Energy, Universiti Teknikal Malaysia Melaka,
Hang Tuah Jaya, 76100 Durian Tunggal, Melaka, Malaysia.

[*]Corresponding e-mail: noreffendy@utem.edu.my

Keywords: Biodiesel; Lotus Engine Simulation (LES); palm oil

ABSTRACT - This paper show the experiment validation of single cylinder diesel engine deals with performance used biodiesel as a fuel. The LES was used to validate the experiment. The biodiesel used in the experiment was the B5 biodiesel which was 5% palm biodiesel and 95% diesel fuel. The engine speed was varied from 1500 to 3500 rpm The data from the experiment was stimulate in the LES for validate with the experiment data. The density and calorific value of the B5 biodiesel fuel is tuned in the simulation. The performances (power and torque) were compared with the simulation result. The results showed that the data from experiment and simulation have minor percentage error but the pattern of the graph of torque and power were same.

1. INTRODUCTION

Biodiesel is the one of the alternative fuel that had been used for the heavy duty transportation and also passenger vehicle that used diesel engine [1]. The main purpose in producing the biodiesel is to reducing the emission that produce from the diesel engine [4].

Biodiesel fuel is the mixture of blended of the substances with the petroleum diesel as a previous study [3]. Qui et al. [5] and Nagi et al. [3] found that the substances can be from vegetable, palm and others. The palm oil biodiesel is the liquid palm oil and its blend with petroleum diese [3]. The palm biodiesel is classified based on the ratio of the palm oil. Foon et al. [2] stated that the B5 biodiesel means the percentage of the palm oil is 5% and other 95% is the petroleum diesel. Khalid et al. [6] stated the performance of the biodiesel is based on the density, viscosity, octane number, flash point, calorific value, acid value, and flash point. Two main standard in producing the biodiesel which are European Standard for Biodiesel (EN 14214) and the American Standard Specifications for Biodiesel Fuel (B100) Blend Stock for Distillate Fuels (ASTM 6751) [2].

In this study, the biodiesel B5 was tested in a 4-stroke single cylinder diesel engine. The performance (torque and power) was evaluated and validate the data using the LES. Lotus Engine software is a simulation program that can predict the performance of the engine system [8].

2. METHODOLOGY

The purpose of this study is experimental validation, which involved the experimental and simulation. The main result obtained were the engine performance (torque and power) for B5 biodiesel fuel.

2.1 Experimental Procedures

The experiment used 4 stroke single cylinder vertical diesel engines coupled with the dynomite engine dynamometer as shown in Figure 1.

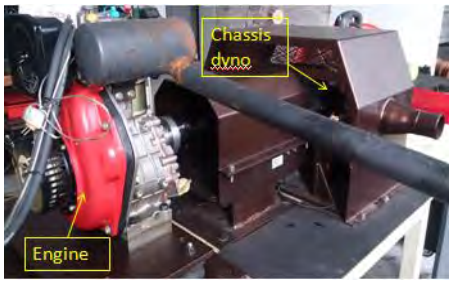

Figure 1 Single cylinder engine dynamometer

The engine specification is shown in table 1. The experiment run with B5 biodiesel under engine speed of 1500 to 3500 rpm. The result obtained was shown in term of the engine performance (power and torque) respectively.

Table 1 Specification of the engine [7]

Engine type	**Single cylinder vertical 4stroke, air cooled, direct injection**
Bore(mm)	70
Stroke(mm)	55
Compression ratio	19:1
Max Output(hp)	4.7
Max Fuel Capacity(l)	12.5

2.2 Simulation Procedure

The simulation used engine simulation tool to predict the engine behavior. The model of the engine was modeled in the simulation according the manufacturer engine specification. The properties of the B5 biodiesel was supplied to the simulation based on the density and calorific value shown in table 2. The

data from simulation was compared to the experiment for validation

Table 2 Properties of B5 biodiesel [2]

Density	Calorific value
0.8459 kg/l	44 MJ/kg

3. RESULTS AND DISCUSSION

The results for this experimental is shown in term of engine performance represented by torque and power against engine speed (rpm). Figure 2 shows torque (Nm) versus engine speed (rpm).

Figure 2 Engine torque (Nm) against speed

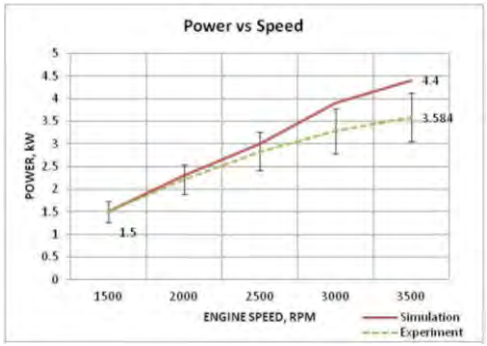

Figure 3 Power (kW) against engine speed

The engine speed was varied from 1500 rpm to 3500 rpm. The simulation data give the minimum value of torque from 9.7 Nm and the maximum value of 12.5 Nm at 3000 rpm. However, when compared to the experimental, the result shows that the minimum value of torque was 9.4 Nm and the maximum value was 10.8 Nm at 3000 rpm. All of the torque values from simulation fall within 15% error from the experimental values.

Figure 3 show the performance (power, kW) against the engine speed. The simulation data give the minimum value of power from 1.5 kW and the maximum value of 4.4 kW. However, when compared to the experimental, the result shows that the minimum value of power was 1.5 kW and the maximum value was 3.6 kW. For result in Figure 3, most of the lower end readings fall within 15% error bar from experimental values while only higher ends data at engine speed above 3000 rpm deviate more than 15%.
Comparing the experiment data against simulation showed that the different between them only in the range of 10.3% for torque and 11.8% for power. This range is acceptable due to the fact that most of the readings ranges within 15% error bar as shown in both Figure 2 and 3.The behavior of these result show similar trends and agreed to each other. .

The different value between the experiment and simulation can be caused by several potential hypothesis like the engine condition and the surrounding for the experiment. The engine have been utilizing it for various study and make the engine loss it efficiency.

4. CONCLUSIONS

This investigation provides an overview of engine behavior and correlation between experimental data and simulation for single cylinder diesel engine performance running with B5 palm oil based biodiesel. Therefore, the result would be useful for predicting the engine performance in term of torque (Nm) and power (kW) with the B5 palm oil biodiesel.

5. ACKNOWLEDGEMENT

The authors would like to acknowledge G-TriboE research group, CARe, UTeM for providing the technical support and facilities to perform this study. The author would like to also acknowledge UTeM and MTUN under research grant MTUN/2012/UTHM-FKM/1/M00001 and MTUN/2012/UMP-FKM/1/M00005 for granting the financial support in this study.

5. REFERENCES

[1] J. I. R. Lalvani, K. Kirubhakaran, M. Parthasarathy, R. Sabarish, K. Annamalai. Performance characteristics and Emission Analysis of a Single Cylinder Diesel Engine Operated on Blends of Diesel and Waste Cooking Oil. IEEE(2013).pp 781-785.

[2] C. S. Foon, C. Y. May, Y. C. Liang, M. A. Ngan, Y. Basiron. Palm Biodiesel: Gearing Towards Malaysian Biodiesel Standards. Malaysia Palm Oil board. pp 28-34.

[3] J. Nagi, S. K. Ahmad, F. Nagi. Palm Biodiesel and Alternative Green Renewable Energy for the Energy Demands of the Future. ICCBT (2008). PP 79-94.

[4] R.Wang, M.A.Hanna, W.W.Zhou, P.S. Bhadury, Q.Chen, B.A.Song. Production and selected fuel properties of biodiesel from promising non-edible oils: Euphorbia lathyris L., Sapium sebiferum L. and Jatropha curcas L. Bioresource Technology ,Vol.102,(2011), pp 1194-1199.

[5] F.Qiu, Y.Li, D.Yang, X.Li, P.Sun. Biodiesel production from mixed soybean oil and rapeseed oil. Applied Energy , Vol.88,(2011),pp 2050-2055.

[6] A. Khalid, S.A.Osman, M.N.M.Jaat, N.Mustaffa, S.M.Basharie, B.Mansoor. Performance and Emission Characteristic of Diesel Engine Fuelled by Biodiesel Derived from Palm Oil. Applied Mechanics and Materials, Vol. 315 (2013).pp 517-522.

[7] Yanmar Service Manual Industrial Diesel Engine. Retrieved from http://www.pramacparts.com/MANUAL.pdf.

Formula varsity race car - Roll dynamic analysis

M.A. Abdullah[1,2,*], J.F. Jamil[1], N. Ismail[1], M.Z. Mohammad Nasir[1,2], M.Z. Hassan[1,2]

[1)] Faculty of Mechanical Engineering, Universiti Teknikal Malaysia Melaka,
Hang Tuah Jaya, 76100 Durian Tunggal, Melaka, Malaysia.
[2)] Centre for Advanced Research on Energy, Universiti Teknikal Malaysia Melaka,
Hang Tuah Jaya, 76100 Durian Tunggal, Melaka, Malaysia.

*Corresponding e-mail: mohdazman@utem.edu.my

Keywords: Pneumatic gear shifter; wireless gear shifter; gear shifter mechanism; gear lever

ABSTRACT - This paper presents the roll dynamic analysis of a Formula Varsity (FV) race car. The analysis is performed to study the stability and the dynamics of the race car including roll moment. The data for the dynamic analysis is recorded using Lego Mindstorms gyro sensor and analyzed using Matlab/SIMULINK software. Side drop test and cornering experiment at low speed are performed. The data recorded is analyzed. Based on the results, the dynamic performance of the race car can be demonstrated. The responses from cornering experiments can be used to identify the parameters of stiffness and damping of the car. The parameters of the car can be tuned to produce better dynamic performance for racing.

1. INTRODUCTION

The dynamic performance of vehicles is important to control the stability and the drivability of the vehicle [1]. One of the engineers made research about dynamic automotive which observing a car that driven in a sharp corner if the centrifugal force in the hands of drivers will lead to crash [2]. Driving method is the main problem in that time. The performance of a vehicle can be observed during acceleration, braking and cornering. The sharp cornering is important to determine the stability and the ability of the vehicle to balance. The balance is depending on the vehicle dynamics and the driver behaviors [3]. Operation of the vehicle depends on the road and type of driving. Current research of vehicle dynamic performance uses computational approach [4]. This research method is acceptable for the theoretical validation. The vehicle and road conditions are modeled and the simulation performed using engineering software on computer. Some of the road conditions are neglected to reduce the time of simulation of the vehicle. Universiti Teknikal Malaysia Melaka (UTeM) has already finished the construction of the Formula Varsity Race Car that is designed and completed by the UTeM Racing Team (URT) [5]. Finite Element Analysis (FEA) of the car is already completed.

In this research, the roll dynamic analysis of the race car is performed experimentally to get the data. The main issues of the race car are controlling the movement direction and controlling the stability if there is problem occurs on the road such as hole and the cornering.

2. METHODOLOGY

The FV Race Car is shown in Figure 1. This car is used to for the roll dynamic analysis. The car is equipped with sensor at the center of gravity (COG). Two experiments are performed; side drop test (Figure 2) and cornering test at 20 km/h (Figure 3). The roll data will be analyzed using Matlab/SIMULINK software. The sensor used on the car is LEGO NXT Mindstorms gyro. The data will be taken using the sensor and will be transfer to the computer to. Figure 4 shows the sensor used for the data acquisition (DAQ).

Figure 1 URT FV race car

Figure 2 Side drop test

Figure 3 Cornering test

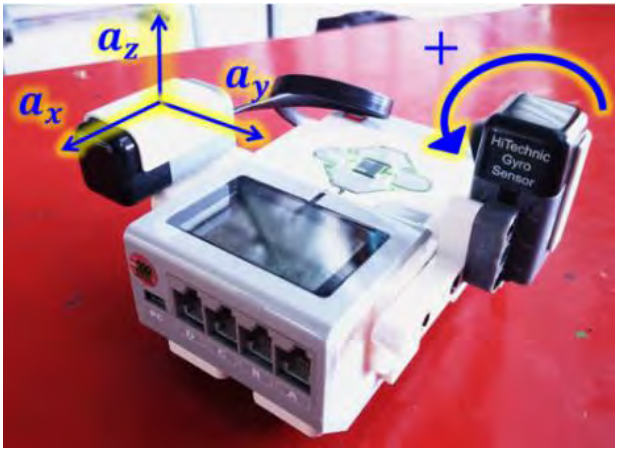

Figure 4 Lego Mindstorm EV3 DAQ

3. RESULTS AND DISCUSSION

Figure 5 and 6 show the roll moment of the car during side drop test and cornering test at 20 km/h. During side drop test, the roll moment is fluctuating obviously. The roll moment is also significantly recorded during cornering. This is due to motion rotating the vehicle to the right and left about horizontal axis.

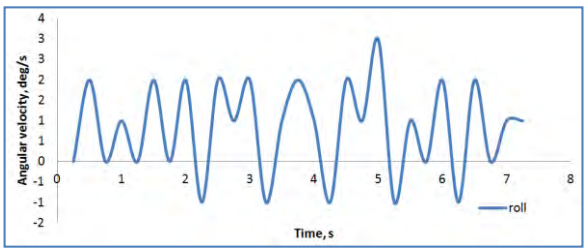

Figure 5: Roll moment for side drop test.

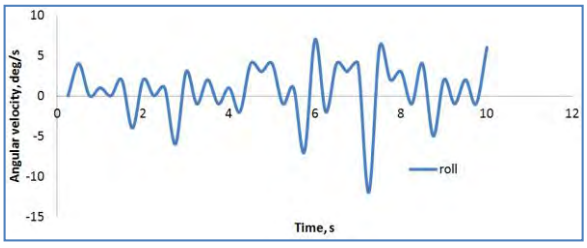

Figure 6: Roll moment for cornering test

4. CONCLUSIONS

The simple vehicle dynamics experiments of the URT FV race car are performed. The data is analyzed and studied. The data is important to predict the race car performance during racing. Few changes on the stiffness of suspension and tire are also can be carried out to tune the dynamics behaviors of the race car. URT FV race car is one of the best achievements by the Universiti Teknikal Malaysia Melaka. The aerodynamic condition and the design of the car is one of the glories for the car. The roll and accelerations are important for the vehicle because they affect the peak levels and the safety of the vehicle itself.

5. ACKNOWLEDGEMENT

The authors gratefully acknowledged the Advanced Vehicle Technology (AcTiVe) research group of Centre for Advanced Research on Energy (CARe), the financial support from Universiti Teknikal Malaysia Melaka and The ministry of Education, Malaysia under Short Term Research Grant, Grant no. PJP/2014/FKM(10A)/S01330 and Fundamental Research Grant Scheme (FRGS), grant no.: FRGS/2013/FKM/TK06/02/2/F00165

6. REFERENCES

[1] M.A. Abdullah, F.R. Ramli and C.S. Lim, "Railway Dynamics Analysis Using Lego Mindstorms", Applied Mechanics and Materials, Trans Tech Publications, Vols. 465-466, pp 13-17, 2014, doi:10.4028/www.scientific.net/AMM.465-466.13.

[2] A.K. Simons, "Mechanical Response of Human Body to Wheeled Vehicle Vibration, Paper presented at 40th Annual Conference of Human Engineers, N.Y.U., Sept. 1956.

[3] T.D. Gillespie, "Fundamental of Vehicle Dynamics", Society of Automotif Engineering, Inc., 400 Commonwealth Drive Warrendale. PA 15096-0001, 1992.

[4] R. Grzebieta, M. Bambach, A. McIntosh, K. Digges, S. Job, D. Friedman, K. Simmons, E.C. Chirwa, R. Zou, and F.A. Pintar, "The dynamic rollover protection (DROP) research program", Proc. 8th International Crashworthiness Conference, Milan, Italy, 2012.

[5] M.A. Abdullah, M.R. Mansor, Musthafah M.T., S.I. Abdul Kudus, M.Z. Hassan and M.N. Ngadiman, "Design, Analysis and Fabrication of Chassis Frame for UTeM Formula VarsityTM Race Car". International Journal of Mining, Metallurgy & Mechanical Engineering (IJMMME) Volume 1, Issue 1, 75-77 (2013) ISSN 2320–4060, 2013.

Driving assistance system – Automatic parking maneuver using Lego Mindstorms

M.A. Abdullah[1,2,*], M.A. Romeli[1], F.R. Ramli[1,2], M.K. Mohamed Nor[1]

[1)] Faculty of Mechanical Engineering, Universiti Teknikal Malaysia Melaka,
Hang Tuah Jaya, 76100 Durian Tunggal, Melaka, Malaysia.
[2)] Centre for Advanced Research on Energy, Universiti Teknikal Malaysia Melaka,
Hang Tuah Jaya, 76100 Durian Tunggal, Melaka, Malaysia.

*Corresponding e-mail: mohdazman@utem.edu.my

Keywords: Vehicle autonomous; driver assistance; automatic parking; Lego Mindstorms.

ABSTRACT - In this paper a conceptual driving assistance system for automatic parking is developed and tested using Lego Mindstorms. A scaled model car is assembled using Lego Mindstorms parts. Using basic yes-no sequences in the parking maneuver flow, the car is programmed to measure a parking space and park automatically (side parking). Based on the successful performance of the parking, the conceptual automatic parking is possible to be improved for actual car.

1. INTRODUCTION

Automatic Parking System (APS) had been developed which has a good maneuver performance for vehicle [1]. The system is equipped with sensors information fusion, position estimation, path planning and tracking algorithm. In order to demonstrate the vehicle verification, the electric power steering system is controlled for tracking the path that had been planned. The parking space is measured up by using ultrasonic sensor. Drivers are able to use a user interactive interface in order to choose and select the parking space if it fits enough for parking the vehicle. After that, the steering movements would take place on the basis of pure pursuit tracking algorithm and also inertial navigation method [2]. Based from a simulation and experiment result, it shows that the system produce good performance through the verification of automatic parking system under parallel parking and reverse parking. Furthermore, the parking space only requires 1.5 times longer than vehicle length. Thus, parking maneuver is more efficient and safer through the utilization of advanced safety technique for automatic parking. An experiment of the system had been conducted using the Mitsubishi Savrin [3]. Sensors are mounted to the vehicle and measure the state of experimental vehicle. The heading angle of vehicle is measured by using Gyro while acquisition of wheel rotation and calculation of distance traveled is being measured by incremental wheel pulse transducer (WPT). On top of that, the vehicle is able to estimate the vehicle positions through the inertial navigation method based on instruments above. Furthermore, there is also other equipment which also built in the system such as ultrasonic sensor and touch panel. The ultrasonic sensor is used to configure environment and are based on time-of-flight (TOF) method, while the touch panel sensor enable the user to interact with the system. The RTK-GPS provides real-time X and Y coordinates and of vehicle's position and also high accuracy of data calculated from sensor data and microprocessor.

In this research, a simple scaled model car is assembled using Lego Mindstorms. A basic parking maneuver program is developed and tested experimentally.

2. METHODOLOGY

The car is assembled using Lego Mindstorms parts with ultrasonic sensor to measure distance. Figure 1 and 2 show the basic dimensions of the car. Lego Education NXT software is used for the parking maneuver programming. Figure 3 shows the parking flow sequences. The parking area is set with buffer for the car to move to fit into the parking spot (Figure 4).

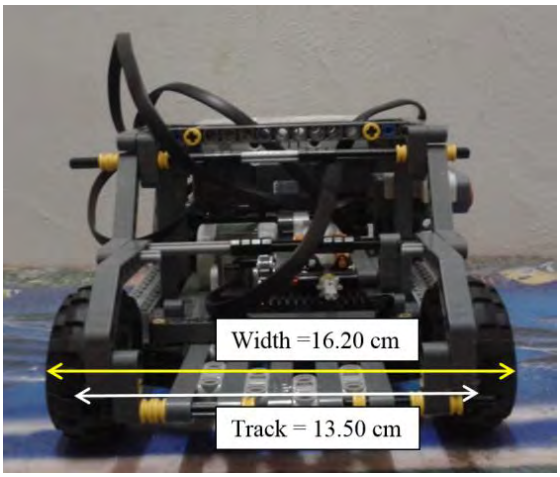

Figure 1: Track and width.

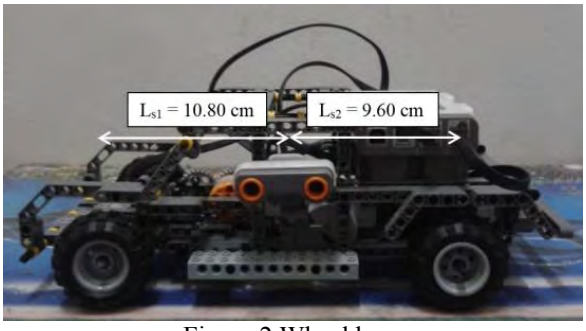

Figure 2 Wheel base

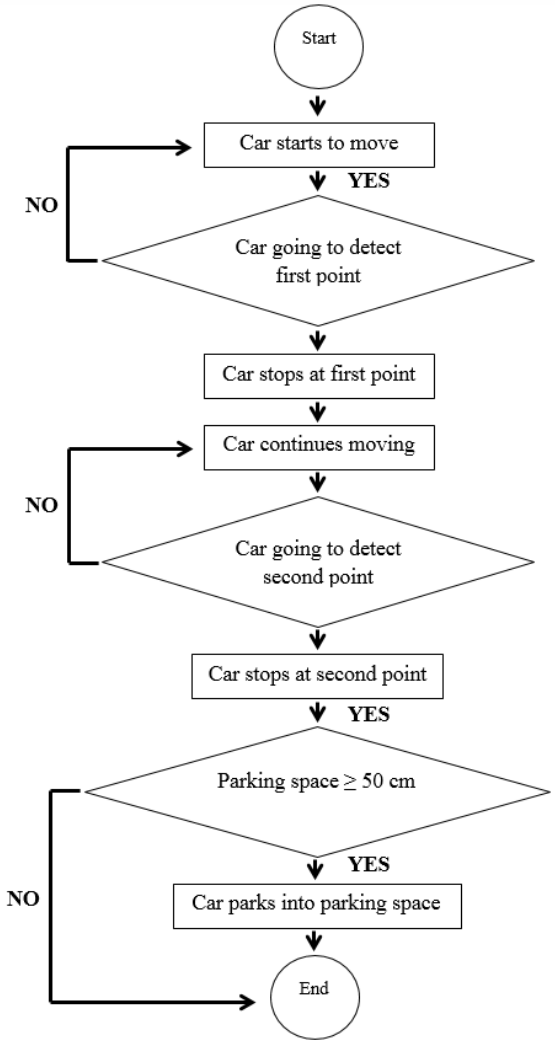

Figure 3 Automatic parking flow

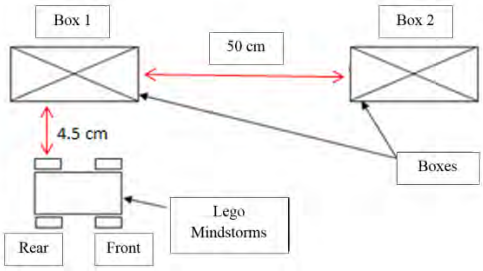

Figure 4 Parking spot

3. RESULTS AND DISCUSSION

Figure 5 shows the actual footage of the car automatically successfully park by itself fitting into the parking spot. The car used only one ultrasonic sensor to measure the parking spot length. Once the length is measured enough (more than minimum required length), the car proceeded with parking maneuver.

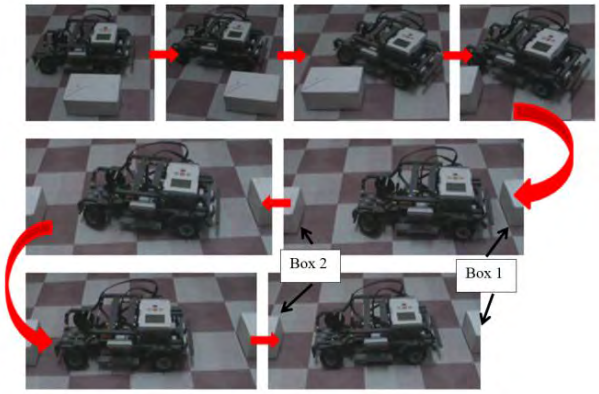

Figure 5: Parking result

4. CONCLUSIONS

A conceptual automatic parking system has been developed and successfully tested. The system used basic yes-no sequences to measure the parking spot and using ultrasonic sensor and moved the car using available motors (front steering and rear-drive). The performance of the car is observed based on the avoidance from hitting the boxes and fit perfectly into the parking spot. The car is considered as non-holonomic type of automatic moving machine. With some improvement using available parts, the system can be applied on actual passenger vehicle to assist driver who has difficulty in doing parallel parking maneuver.

5. ACKNOWLEDGEMENT

The authors gratefully acknowledged the Advanced Vehicle Technology (AcTiVe) research group of Centre for Advanced Research on Energy (CARe), the financial support from Universiti Teknikal Malaysia Melaka and The ministry of Education, Malaysia under Short Term Research Grant, Grant no. PJP/2014/FKM(10A)/S01330 and Fundamental Research Grant Scheme (FRGS), grant no.: FRGS/2013/FKM/TK06/02/2/F00165.

6. REFERENCES

[1] T.S. Hsu, J.F Liu, P.N. Yu, W.S. Lee, and J.S. Hsu, "Development of an automatic parking system for vehicle", Vehicle Power and Propulsion Conference. China, 2008. pp. 1-6.

[2] Laugier, C., Fraichard, Th., Garnier, Ph., Paromtchik, I.E., and Scheuer, A., "Sensor-based control architecture for a car-like vehicle", Autonomous Robots, 6, 2, pp. 165–185, 1999.

[3] I.E. Paromtchik and C. Laugier, "Autonomous parallel parking of nonholonomic vehicle", Intelligent Vehicle Symposium, 1996, pp. 13–18.

Autonomous vehicle convoy using Lego Mindstorms

M.A. Abdullah[1,2,*], M.A. Azan[1], F.R. Ramli[1,2], M.K. Mohamed Nor[1]

[1)] Faculty of Mechanical Engineering, Universiti Teknikal Malaysia Melaka,
Hang Tuah Jaya, 76100 Durian Tunggal, Melaka, Malaysia.
[2)] Centre for Advanced Research on Energy, Universiti Teknikal Malaysia Melaka,
Hang Tuah Jaya, 76100 Durian Tunggal, Melaka, Malaysia.

*Corresponding e-mail: mohdazman@utem.edu.my

Keywords: Vehicle autonomous; vehicle convoy; vehicle platoon; autonomous convoy; Lego Mindstorms.

ABSTRACT - Autonomous vehicle convoy is a future driving and technology system that have been researched and developed for decades to solve problems in our transportation system nowadays. The increasing of road traffic has contributed to traffic congestion and more severely causes accidents. The aims of this study are to develop convoy algorithm and demonstrate autonomous vehicle convoy system using the LEGO Mindstorms Education EV3 by performing convoy experiment using small scaled car. The convoy or platooning need to satisfy the range of constraints by keeping the control parameters. It consists of one leader and two followers which have to maintain speed and safe distance while moving at designated route.

1. INTRODUCTION

The development in vehicle platooning has been a research for many years and decades to get improvement and effective way of convoy system such as the communication between the vehicles, the safety distance, the control velocity and other control parameters to ensure the safety and passenger comfort. Many researches have been made to study the implementation of convoy driving in reducing the congested road or motorway, smooth the traffic flow and more [1]. Nowadays, autonomous vehicle convoy or platooning is also a driving system that has been researched and studied recently. A research from [2] about adaptive control of an automatic convoy of vehicle described that autonomous vehicle convoy is a group of automated vehicles move together like a virtual train that their movement been controlled automatically but supposedly the first or the lead vehicle plays an important role that professionally trained driver to drive and guide the convoy manually. The main problem in the convoy driving that have been focused from previous research on car following is to maintain the safe distance constantly [3]. The methods to counter the problem have been discussed that by using the guidance-based motion planning algorithm for time optimal autonomous rendezvous with moving vehicle convoys. In this research, 3 simple and identical scaled model cars are assembled using Lego Mindstorms. Using available sensors such as ultrasonic and colour sensor, the convoy mechanism is programmed in Lego Mindstorms Education EV3 software.

2. METHODOLOGY

The cars are assembled using Lego Mindstorms parts equipped with colour sensor (for leader) to follow certain route and ultrasonic sensor (for followers) to measure and maintain safe distance. Figure 1 shows the experiment setup for autonomous vehicle convoy.

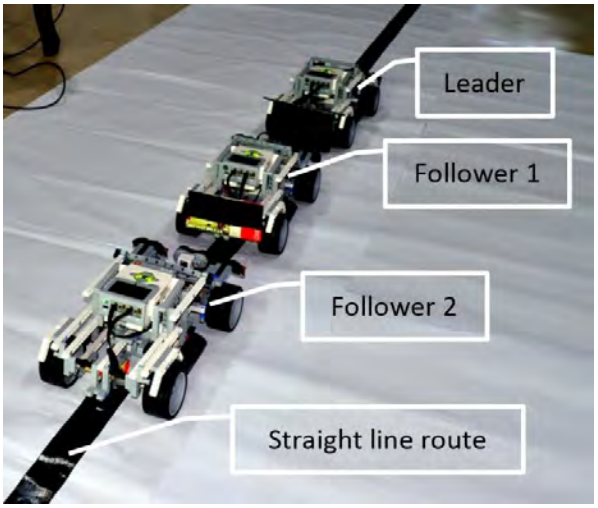

Figure 1 Autonomous convoy experimental setup

The experiment has two manipulated variables which are the speed rotation of the drive motor and the vehicle distance travel. The power speed rotation of the drive motor is setup at 40 %, 50 % and 60 %, where the vehicle distance travel setup for 100 and 200 centimeters. The responding variables need to be record are the time travel and the distance gap between the vehicles. The constant variables is the initial distance between the vehicles, 14.9 centimeters that been defined as the safe distance in this project. The safe following distance is actually greater than a car length and varies depending on speed travelling, road condition and type of vehicle. In this project, 15 centimeters length has been assume as the safe following distance because the scaled model car is made of from LEGO or bricks components that very light and low mass inertia. The algorithm for the autonomous vehicle convoy is shown by Figure 2.

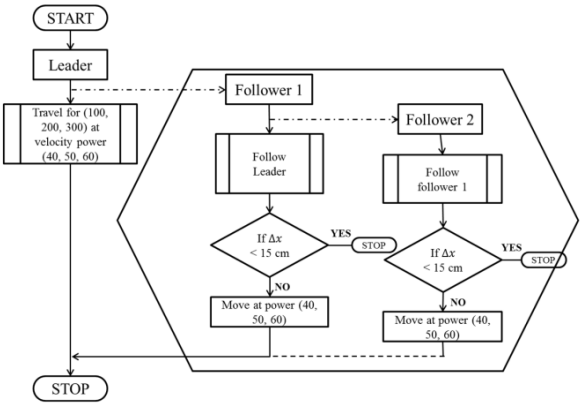

Figure 2: Algorithm flow

3. RESULTS AND DISCUSSION

Figure 3 and 4 present the gap distance against velocity power for distance travel 100 and 200 cm respectively. From the graphs, at 40 velocity powers, the gap distance between Leader and Follower 1 decrease by 1.9 cm, and decrease 3.1 cm between Follower 1 and Follower 2. At 50 velocity power, the gap distance between Leader and Follower 1 decrease by 3.5 cm, and decrease 3.18 cm between Follower 1 and Follower 2. At 60 velocity power, the gap distance between Leader and Follower 1 decrease by 4.6 cm, and same goes between Follower 1 and Follower 2. Thus, it shows that the higher velocity power (speed) travel, the shorter distance gap between the vehicles. The higher speed produces large momentum, thus taking more time to brake or stopping the vehicles.

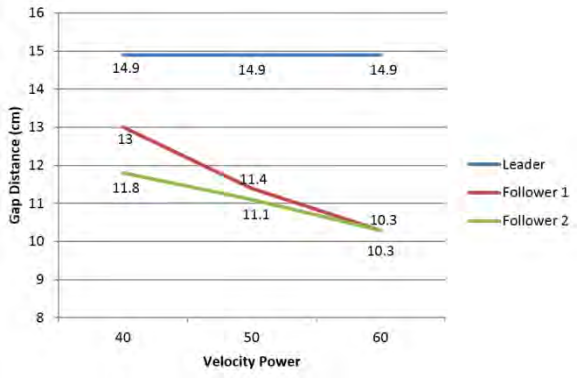

Figure 3 Gap distance for 100 cm test

For 200 cm test, at 50 velocity power, the gap distance between Leader and Follower 1 decrease by 3.1 cm, and decrease 3.5 cm between Follower 1 and Follower 2. The higher gap 11.8 cm for Follower 1 compared to 11.8 cm for Follower 2 is perhaps due to late response of Follower 2.

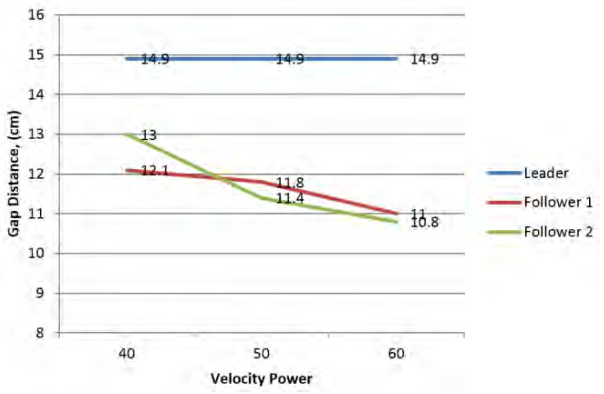

Figure 4: Gap distance for 200 cm test

4. CONCLUSIONS

In this research, an autonomous convoy system has been implemented and successfully tested using Lego Mindstorms scaled model cars. The followers have followed the leader and maintain safe distance between them. Using available parts, the system can be implemented on actual passenger vehicles for autonomous convoy driving and giving comfort for drivers to follow vehicles in convoy.

5. ACKNOWLEDGEMENT

The authors gratefully acknowledged the Advanced Vehicle Technology (AcTiVe) research group of Centre for Advanced Research on Energy (CARe), the financial support from Universiti Teknikal Malaysia Melaka and The ministry of Education, Malaysia under Short Term Research Grant, Grant no. PJP/2014/FKM(10A)/S01330 and Fundamental Research Grant Scheme (FRGS), grant no.: FRGS/2013/FKM/TK06/02/2/F00165

6. REFERENCES

[1] D. Martinec and Z. Hurak, "Vehicular platooning experiments with LEGO MINDSTORMS NXT", Denver, USA, s.n., 2011, pp. 6.

[2] R. Kovacs, K. Lorincz, and J.K. Tar, "Adaptive control of an autonomatic convoy of vehicles", Budapest, Hungary, s.n., 2007, pp. 6.

[3] F. Kunwar, and B. Benhabib, "Motion planning for autonomous rendezvous with vehicle convoys", Toronto, Canada, s.n., 2006, pp. 6.

The effect of different thickness material stacking for four layer spot welding

Mohd Harris Fadhilah[1,2,*], Nur Fatihah Madi[1],

[1)] Faculty of Engineering Technology, Universiti Teknikal Malaysia Melaka, Hang Tuah Jaya, 76100 Durian Tunggal, Melaka, Malaysia.
[2)] Green Materials Research Group, Universiti Teknikal Malaysia, Melaka, Hang Tuah Jaya, 76100 Durian Tunggal, Melaka Malaysia

[*]Corresponding e-mail: mohdharris@utem.edu.my

Keywords: Spot welding; material stacking; metal sheet

ABSTRACT – Spot welding is a common metal joining process in automotive industries. At actual production line, resistance spot welding of four layer metal sheet generally is more challenging than spot welding of three layers metal sheet, especially for welding gun optimization plan. This report intended to research the mechanical properties of four layer welded sheets of different thickness. In this research, the strength on the tensile shear-test of lap joint in spot welding of 2.80mm, 3.50mm and 4.4mm thickness of four layer welded sheet were investigated. All the results were then compared with three layer of welded sheet with thickness 2.80mm which was set as the benchmark.

1. INTRODUCTION

Resistance spot welding (RSW) process is one of the oldest in the electrical welding processes that are mostly used in the modern manufacturing technology such as bridges, shipbuilding, home appliance and more. The automotive industry has introduced the four-layer weld configuration, which represent new challenges compared to normal two-sheet and three-sheet lap welds. Nielsan et al.[1] stated that the process is more complicated by introducing various combinations of different material and different thickness. The development of new, four-sheet weld for use in the automotive industry represents new challenges to the industry, especially to ensure welding fusion for each 4-layer-sheet spot weld. The strength of resistant spot welded joints is important for improving auto body rigidity, which is one of the key factors in crash test activity.

Therefore, the objective of this project is to study the strength of four layer welded sheets from different thickness material combinations and to compare the strength of four layer welded sheets with three layer welded sheets.

2. METHODOLOGY

2.1 Sample Preparation

The sample was fabricated into lap joint. Each sheet was labeled according to Fig 1 since the plate assembly consists of four sheets for each specimen. The material composition is shown in Table 1.

I. a = JIS G3141 SPCC-1B
II. b = JIS G3141 SPCC-SD
III. c = JIS G3141 SPCC-SD
IV. d = JIS G3141 SPCC-SB

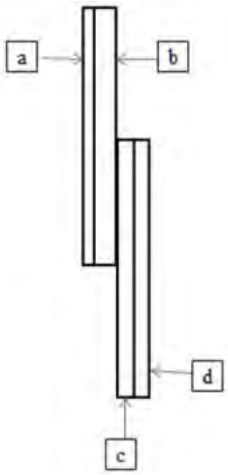

Figure 1 Welding Sample with Label

Table 1 Composition of the JIS G3141 SPCC metal sheet

Material	Element				
JIS G3141 SPCC	C 0.04%	Si 0.02%	Mn 0.16%	P 0.001%	S 0.004%

The material was cut according to drawing dimension. For all models, the sample length and width were held constant. All plates had the same dimension which were 100mm x 25mm. The thickness of each plate was different which were 0.5mm for the lowest thickness and 1.2mm for the highest thickness.

2.2 Welding Process

The RSW technique was ready to run after the sample preparation of sheet metal completed. For this project, the experiment was conducted on Inverter AS-25 weld gun. The specimens were the combination of different thickness of sheets metal which is from 0.5mm to 1.2mm. The current that applied for the welding was 9.0 kA and the electrode force is 2.5 kN. The parameter of spot weld machine was kept constant for all specimens.

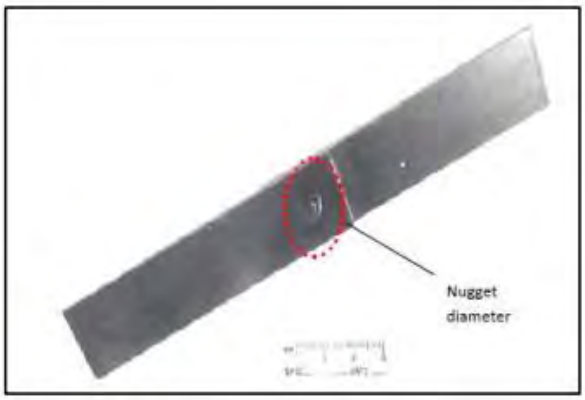

Figure 2 Specimen of Sheet Metal which is Lap Joints after RSW

2.3 Tensile Test

This method was suitable and simple to test the strength of the welded joint of sheet metal in terms of the tensile strength of the joint before fail or tear apart. Tensile-shear test was used to determine the maximum lap-shear force that can be achieved after the overlapping sheet metal joint together using RSW. A total twenty specimens underwent the tensile-shear test to obtain the maximum load before break due to shear force applied to weld area. The result is discussed in the next section.

3. RESULTS AND DISCUSSION

Table 2 shows the thickness of the specimen influences the maximum load, ultimate tensile stress and modulus young. Referring to Table 2, the tensile shear strength increased significantly with the increase of sheet thickness. Based on Table 2, it is showed that sheet 3.50mm-thickness value data requires further investigation. Based on the previous study, the ultimate value tensile stress will increase when the thickness of the welded sheet increases because the higher thickness will reach the breaking point much slower [2]. From the observation, it was predicted that this happened due to insufficient growth of weld nugget at the specimen. Insufficient growth of nugget may occur from insufficient current supply and also because insufficient weld time.

Table 2 Tensile test data for different thickness and layer

Total Layer	Thickness [mm]	Max Load [N]	Ultimate tensile Stress [MPa]	Modulus (Automatic Young's) [MPa]
3	2.80	7641.98	109.17	15584.31
4	2.80	7414.09	105.92	17703.26
4	3.50	8436.01	96.41	11148.32
4	4.40	11904.55	108.22	13876.35

4. CONCLUSIONS

Based on the project, the strength of four welded sheet can be said have higher tensile strength compared to the three layers. However, due to the result of sample 3.5mm thickness and 4 layer welded sheet, this research requires further investigation.

The mechanism of the strength of welded sheet with same layer but different thickness has been tested by using tensile shear test method. The weld strength of 4.4mm-sheet thickness measure by tensile shear test were found to be relatively high compared to the 2.80mm-sheet thickness and 3.50mm-sheet thickness. The study discovered that the maximum peak load for 3.50mm-sheet thickness is higher compared to 2.80mm-sheet thickness which means 3.50mm-sheet thickness was better than 2.80mm-sheet thickness. Even though, the less thickness of spot welded sheet would reduce the car weight and reduce petrol consumption it would also reduce the rigidity of the car. Lower strength of spot weld can lead into total destruction of manufacturing parts of car bodies. Therefore, the failure characteristics and performance of the spot welds significantly affect the durability and safety design of the vehicles [3].

5. REFERENCES

[1] Nielsan, C.V., Friis, K.S., Zhang, W, and N Bay, "Three-Sheet Spot Welding of Advanced High-Strengh Steels," *Welding* , vol.90, Journal, pp.32-40, 2011.

[2] Pouranvari, M. et al., 2011. " Influence of Fusion Zone Size and Failure Mode on Mechanical Performance of Dissimilar Resistance Spot Welds of AISI low carbon steel and DP600 advanced hi strength steel," *Materials & Design*, vol.32(3), pp. 1390-1398,2011.

[3] Ambroziak, A. & Korzeniowski, M., "Using Resistance Spot Welding for Joining Aluminium Elements in Automotive Industry," *Archives of Civil and Mechanical Engineering*, vol.10(1), pp.5-13, 2010

Pneumatic gear shifter analysis

M.A. Abdullah[1,2,*], M.A. Mohd Ahyak[1], M.A.I. Abd Hamid[1], F.R. Ramli[1,2], S.A. Shamsudin[1,2]

[1)] Faculty of Mechanical Engineering, Universiti Teknikal Malaysia Melaka,
Hang Tuah Jaya, 76100 Durian Tunggal, Melaka, Malaysia.
[2)] Centre for Advanced Research on Energy, Universiti Teknikal Malaysia Melaka,
Hang Tuah Jaya, 76100 Durian Tunggal, Melaka, Malaysia.

*Corresponding e-mail: mohdazman@utem.edu.my

Keywords: Pneumatic gear shifter; wireless gear shifter; gear shifter mechanism; gear lever.

ABSTRACT - Conventional design of transmission gear shifter is basically consists of mechanical linkage of gear lever attached on the side of motorcycle engine with pivot directly connected to the gear shifting mechanism. Shifting up and down of gear positions are performed by moving foot or toe upward and downward on the lever respectively. For disable rider (rider requires special need), shifting gear for manual transmission type of motorcycle with or without clutch system is difficult. In this research, a pneumatic gear shifter is designed and tested. It consists of pneumatic circuit with actuator, tanks and air compressor. The movement of gear lever is performed by the pneumatic actuator. Pneumatic tanks are installed to achieve optimum pressure. It also controlled by wireless system for convenient purpose and buttons installed at the handle. Simple experiment is performed to measure the force for each gear position.

1. INTRODUCTION

The transmission of a light vehicle is determined by the number of force applied to the gearshift. Most motorcycle gearshift assemblies in recent years have been fabricated with a foot pedal that is shifted upwardly and downwardly by the bottom and top surfaces of the toe or foot. In transmission system, conventionally, it has a mechanical linkage that connects the gear lever to the gear switching mechanism. The mechanism for gear changing of the transmission still remains the same that is the reliance towards the gear lever situated on the left leg of the rider [1]. The transmission system size, weight and type are varied from one manufacturer to another. Nevertheless, its basic principle on how the system works remain constant although it is produced by different manufacturers. For the simplest form of this system, it will only contain a centrifugal clutch attached to the crankshaft and then redirected to the sprocket via chain. As the engine speed increases, the clutch activates and propels the rear wheel [2][3]. A solenoid gear shifter or an electric solenoid shifter is an invention that is equipped onto motorcycle or car for the gear changing process [4]. Solenoid gear shifting mechanism uses magnet to move upwardly and downwardly [5]. This movement depends on the magnetic field that is produce by the magnet when power is supply through it.

In this research, a gear shifter test rig is designed and used to analyze the forces required for shifting up and down in pneumatic gear shifter demo set.

2. METHODOLOGY

A gear shifter jig is developed to measure the forces required to shift the gear. Since the jig will be used for the testing of a pneumatic actuator; it will be made from plywood with thickness of 15 mm. Figure 1 shows the design of the test rig. Figure 2 shows the pneumatic gear shifter demo set. The forces are measured and recorded for analysis.

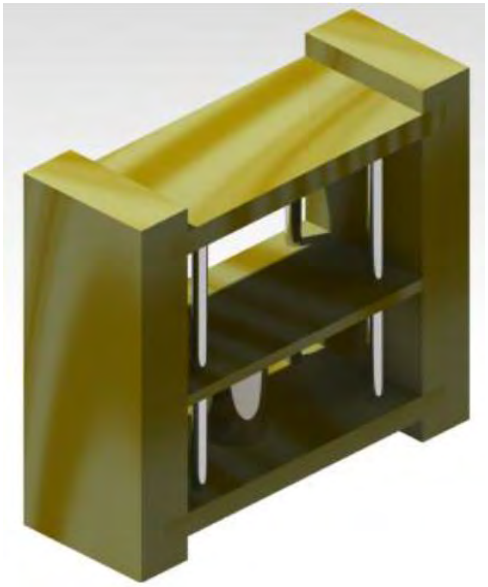

Figure 1 Gear shifter test rig design

3. RESULT AND DISCUSSION

Figure 3 to 6 show force (in kg) graph for the data of the 1st to 4th gear shifting (blue, ♦ = shift up from current gear, red, ■ = shift down from current gear). The average value of mass needed for engaging and disengaging is around 6 kg and 4 kg respectively. The amount of force required to be exerted by the riders depend on the speed of his leg; experiment result as tabulated in Table 1 shows the trend of force required for shifting on a light vehicle which is Honda Wave 110. The engagement and disengagement of gear *n* mean shifting from gear *n*-1 to gear *n* or from gear *n*+1 to gear *n*. From the table, it can be seen that based on all 20

data taken for each gear shifting, the amount of force required remain in the range of 45 N to 55 N.

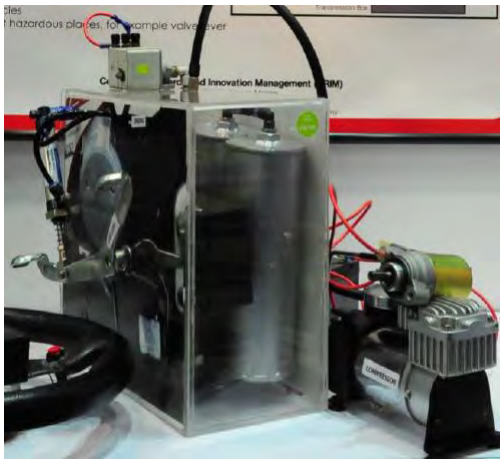

Figure 2 Pneumatic gear shifter

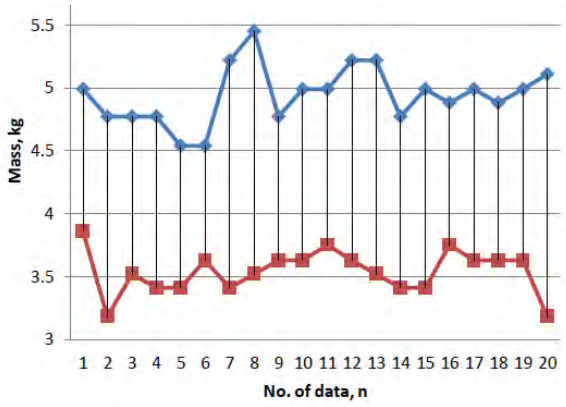

Figure 3 1st gear forces

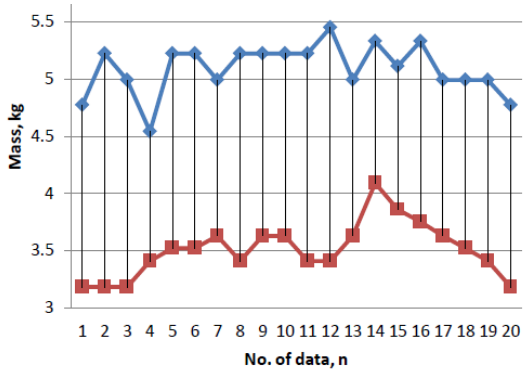

Figure 4 2nd gear forces

4. CONCLUSIONS

The analysis of wireless pneumatic gear changer has been performed. The test rig has proven experimentally produced suitable amount of force and pressure to engage and disengage gears using pneumatic actuator on the gear lever. The pneumatic gear shifter prototype is available for future improvement and installation on actual motorcycle.

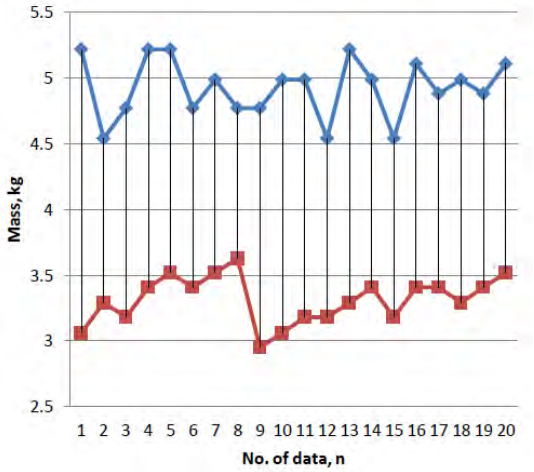

Figure 5 3rd gear forces

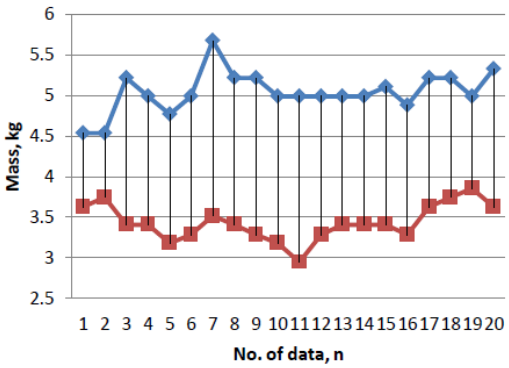

Figure 6 4th gear forces

5. ACKNOWLEDGEMENT

The authors gratefully acknowledged the Advanced Vehicle Technology (AcTiVe) research group of Centre for Advanced Research on Energy (CARe), the financial support from Universiti Teknikal Malaysia Melaka and The ministry of Education, Malaysia under Short Term Research Grant, Grant no. PJP/2014/FKM(10A)/S01330 and Fundamental Research Grant Scheme (FRGS), grant no.: FRGS/2013/FKM/TK06/02/2/F00165

6. REFERENCES

[1] C.A. Yunus, M.A. Boles and Y. He, "Thermodynamics An Engineering Approach", Mc-Graw Hill Companies, 2009.

[2] J.C. Haartsen, "The Bluetooth Radio System", Ericsson Radio System B.V., 2000.

[3] M. Molly and M.B. Pautot, "The GSM System for Mobile Communications", 1992.

[4] G.H. Lee, "A Study on the Speed Control of a Closed-Loop Hydrostatic Transmission", Seoul University, 1995.

[5] G.A. Thomas, "Electronically Controlled Gear Shift Mechanism Particularly Suited for Racing Cars", United States Patent, 1996.

Taguchi modeling of process parameters in VDG-MOSFET device for higher I_{ON}/I_{OFF} ratio

K.E. Kaharudin[1,2,*], A.H. Hamidon[1,2], F. Salehuddin[1,2]

[1)] Faculty of Electronics and Computer Engineering, Universiti Teknikal Malaysia Melaka, Hang Tuah Jaya, 76100 Durian Tunggal, Melaka, Malaysia.
[2)] Centre for Telecommunication Research and Innovation, Universiti Teknikal Malaysia Melaka, Hang Tuah Jaya, 76100 Durian Tunggal, Melaka, Malaysia.

[*]Corresponding e-mail: khairilezwan@yahoo.com.my

Keywords: ANOVA, ATHENA, ATLAS, Taguchi

ABSTRACT – The miniaturization in the size of planar MOSFET device seems to be limited when it reaches to 22nm technology node. The most common approach to overcome this problem is to replace silicon dioxide (SiO_2) and polysilicon with high-k dielectric material and metal gate respectively. However, in this paper, the vertical double gate architecture of MOSFET device with ultrathin pillar was introduced by keeping both silicon dioxide (SiO_2) and polysilicon as the main materials. The proposed MOSFET architecture was known as Ultrathin Pillar Vertical Double Gate (VDG) MOSFET device and it was integrated with polysilicon-on-insulator (POI) technology for a superior electrical performance. The virtual device's fabrication and characterization were done by using ATHENA and ATLAS modules of SILVACO Internationals. The process parameters of the device were then optimized by utilizing L_{27} orthogonal array of Taguchi method in order to obtain the highest value of drive current (I_{ON}) and the lowest value of leakage current (I_{OFF}). The highest value of I_{ON}/I_{OFF} ratio was observed to be 2.154×10^{12}. Whereas the nominal threshold voltage (V_{TH}), drive current (I_{ON}), leakage current (I_{OFF}) and sub-threshold swing (SS) were observed to be 0.437 V (±12.7% of 0.447 V), 701.9 µA/µm, 9.374×10^{16} A/µm and 63.66 mV/dec respectively. These results are well within the prediction value of International Technology Roadmap Semiconductor (ITRS) 2013 for low power (LP) multi-gate (MG) technology requirement in year 2020.

1. INTRODUCTION

Producing planar MOSFET devices with a very short channel length seems to be very challenging and complicated especially for below 22nm technology node. The reduction of MOSFET's size is always related to the deterioration of the device's characteristics. The most critical device's characteristics that are important to be preserved are known as drive current (I_{ON}) and leakage current (I_{OFF}). An attempt to reduce the physical gate (Lg) of conventional MOSFET device has result in a very close proximity between drain region and the source region thereby introducing various short channel effect (SCE) problems. These SCEs lead to the increase of leakage current (I_{OFF}) which will deteriorate the device's performance. A lot of researches have been done to circumvent these SCE problems. One of them is to integrate the combination of high permittivity (high-k) dielectric material and metal gate into the MOSFET's structure. However, in this current research, traditional silicon dioxide (SiO_2) and polysilicon material are still being used by introducing ultrathin pillar polysilicon-on-insulator (POI) Vertical Double Gate (VDG) design architecture.

This paper emphasizes on utilizing L_{27} orthogonal array of Taguchi method that consists of thirteen process parameters which are substrate implant dose, V_{TH} implant dose, V_{TH} implant energy, halo implant energy, halo implant tilt, source/drain (S/D) implant dose, compensation implant dose and etc. The gate oxide temperature and polysilicon oxidation temperature are selected as noise factors in order to get the optimum results. The main objective of the current work is to maximize the drive current (I_{ON}) value and to minimize the leakage current (I_{OFF}) value. Besides that, the threshold voltage (V_{TH}) value must be ensured to be within ±12.7% of low power (LP) multi-gate (MG) requirement in ITRS 2013 prediction (0.447V) for year 2020.

2. MATERIALS AND METHODS

2.1 Virtual Fabrication Process

The virtual fabrication process of VDG-MOSFET device was simulated by using ATHENA and ATLAS modules of SILVACO International. ATHENA module was used for process simulation of MOSFET's device. Meanwhile, ATLAS module was used for device simulation and electrical characterization.

Compensation implantation was utilized later by implanting phosphor dosage of 2.51×10^{12} atom/cm^3 with energy level of 63 Kev and tilt angle of 7°. This step is taken in order to reduce parasitic effects that could increase the leakage current (I_{OFF}). Next, silicide (CoSi) was formed on the source and drain region by sputtering cobalt on silicon surface. This transistor was then connected with aluminum metal. The aluminum layer was deposited on the top of the Intel-Metal Dielectric (IMD) and unwanted aluminum was etched to develop the contacts [1]. The procedure was completed after the metallization and etching were performed for the electrode formation, and the bonding pads were opened. The final structure of VDG-MOSFET device

was completed by mirroring the right-hand side structure. The completed structure of VDG-MOSFET device is illustrated as in Figure 1.

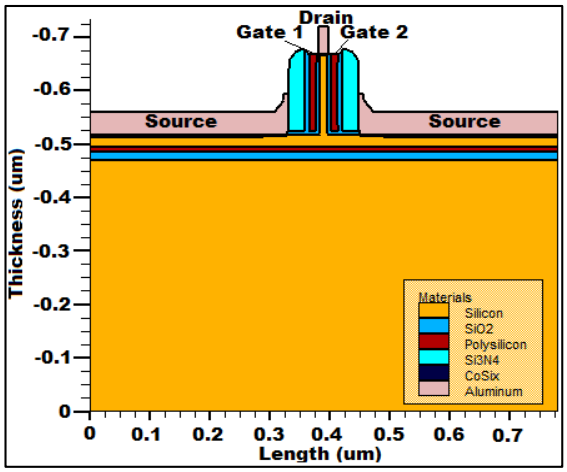

Figure 1 Structure of VDG-MOSFET device

Table 1 L_{27} Orthogonal Array Taguchi Method

Exp No.	Process Parameter Level												
	A	B	C	D	E	F	G	H	J	K	L	M	N
1	1	1	1	1	1	1	1	1	1	1	1	1	1
2	1	1	1	1	2	2	2	2	2	2	2	2	2
3	1	1	1	1	3	3	3	3	3	3	3	3	3
4	1	2	2	2	1	1	1	2	2	2	3	3	3
5	1	2	2	2	2	2	2	3	3	3	1	1	1
6	1	2	2	2	3	3	3	1	1	1	2	2	2
7	1	3	3	3	1	1	1	3	3	3	2	2	2
8	1	3	3	3	2	2	2	1	1	1	3	3	3
9	1	3	3	3	3	3	3	2	2	2	1	1	1
10	2	1	2	3	1	2	3	1	2	3	1	2	3
11	2	1	2	3	2	3	1	2	3	1	2	3	1
12	2	1	2	3	3	1	2	3	1	2	3	1	2
13	2	2	3	1	1	2	3	2	3	1	3	1	2
14	2	2	3	1	2	3	1	3	1	2	1	2	3
15	2	2	3	1	3	1	2	1	2	3	2	3	1
16	2	3	1	2	1	2	3	3	1	2	2	3	1
17	2	3	1	2	2	3	1	1	2	3	3	1	2
18	2	3	1	2	3	1	2	2	3	1	1	2	3
19	3	1	3	2	1	3	2	1	3	2	1	3	2
20	3	1	3	2	2	1	3	2	1	3	2	1	3
21	3	1	3	2	3	2	1	3	2	1	3	2	1
22	3	2	1	3	1	3	2	2	1	3	3	2	1
23	3	2	1	3	2	1	3	3	2	1	1	3	2
24	3	2	1	3	3	2	1	1	3	2	2	1	3
25	3	3	2	1	1	3	2	3	2	1	2	1	3
26	3	3	2	1	2	1	3	1	3	2	3	2	1
27	3	3	2	1	3	2	1	2	1	3	1	3	2

2.2 Taguchi L_{27} Orthogonal Array Method

In the current research, Taguchi L_{27} orthogonal array is developed in order to investigate the impact of thirteen process parameters on I_{ON}/I_{OFF} ratio. The design of experiment (DoE) consists of 27 experiment rows with different combination level of process parameters is constructed as shown in Table I.

3. RESULTS AND DISCUSSION

From Figure 2, it was observed that factor A1, B1, C2, D3, E1, F1, G3, H2, J3, K1, L3, M1 and N1 have been selected as the optimum value for drive current (I_{ON}) due to their highest SNR. Meanwhile, Figure 3 indicates that factor A2, B2, C1, D1, E3, F1, G1, H3, J2, K1, L1, M3 and N3 were the most optimum value for leakage current (I_{OFF}).

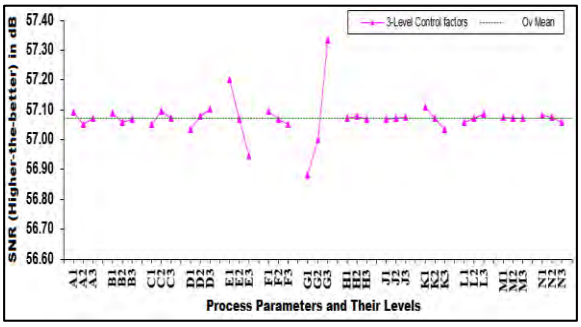

Figure 2 Factor effect plot for SNR (Higher-the-better) for Drive Current (I_{ON})

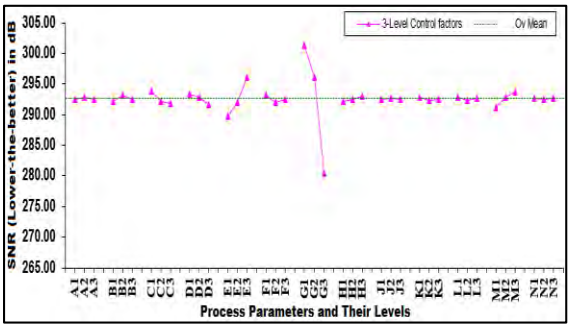

Figure 3 Factor effect plot for SNR (Lower-the-better) for Leakage Current (I_{OFF})

4. REFERENCES

[1] K.E. Kaharudin, A.H. Hamidon, F. Salehuddin, "Impact of Height of Silicon Pillar on Vertical DG-MOSFET Device," *International Journal of Computer, Information*, Systems and Control Engineering, Vol. 8, No. 4, pp. 576-580, 2014.

[2] M. Masahara et al., "Ultrathin Channel Vertical DG MOSFET Fabricated by Using Ion-Bombardment-Retarded Etching", *IEEE Transactions on Electron Devices*, Vol. 51, pp. 2078-2085, 2004.

[3] J. E. Suseno and R. Ismail, "Design of Double Gate Vertical MOSFET using Silicon on Insulator (SOI) Technology*", International Journal of Nano Devices, Sensors and Systems*, Vol. 1, pp. 34-38, 2012.

Inline pin fin heat sink model and thermal performance analysis for central processing unit

Khalil Azha Mohd Annuar[1,*], Fatimah Sham Ismail[2], Mohamad Haniff Harun[1], Mohamad Firdaus Mohd Ab Halim[1]

[1)] Faculty of Technology Engineering, Universiti Teknikal Malaysia Melaka,
Hang Tuah Jaya, 76100 Durian Tunggal, Melaka, Malaysia.
[2)] Centre of Artificial Intelligence and Robotics, Faculty of Electrical Engineering,
Universiti Teknologi Malaysia, 81310 Skudai, Johor, Malaysia.

[*]Corresponding e-mail: khalilazha@utem.edu.my

Keywords: Heat sink; thermal; heat transfer

ABSTRACT – The thermal management issue is common in electronic products such as computers, projectors and others. The trend shows that by increasing the power density, indirectly it will increase the temperature and power dissipation in CPU processor. This is a major challenge to the product designer of electronics cooling system to find an alternative technique to solve the problem. Therefore, in order to control and minimize the heat produced by the CPU's processor, the conventional external heat sink is added to the overall thermal management mechanism. In this paper, 3D simulation inline pin fin heat sink is designed using COMSOL Multiphysics software. The outcome of this study hopefully can shed some light on how to optimize inline pin fin arrangement heat sink design.

1. INTRODUCTION

Nowadays, the demand of using high performance, functionality and small size electronic appliances such as computers and laptops are very popular. The advancement of microelectronic technology in producing high speed and small size system leads to an increase of heat generation per volume from each electronic components, hence could reduce the performance of the electronic component, effects its lifetime or even crashing the entire operation of the system if it does not managed correctly. This is a big obstacle to the product designers to tackle the problem by finding an alternative technique.

There are many cooling techniques and system designs is applied to remove the heat from the electronic devices. For example, in desktop computer, heat sink is used to dissipate heat from the CPU due to economical reason and practical. Heat sink is a device that allows the transfer of heat away from the heat source such as CPU processor, random access memory (RAM) and et cetera.

There are many heat sink design in the market such as plate fin and pin fin. Therefore, heat sink with high heat transfer rate is needed. The selection of suitable heat sink geometry is required not only to be able to fit inside a limited space in the motherboard, it also has to be lightweight, economical and the most important aspect is excellent characteristics of the heat dissipation.

According to Kim et al. [1], pin fin heat sink model with low power dissipation from the heat source provides small thermal resistance. Hence the pin fin heat sink should give better thermal management performance compare to the plate fin heat sin model [1-3].

In this paper, 3D simulation pin fin aluminum heat sink model with various inline arrangement is design by using COMSOL Multiphysics software. The model which is applied on the CPU Intel® Atom™ Processor N450 by mounting it on top of the CPU processor chip. More than 30 models were simulated and important data such as the maximum temperature generation from the temperature profile is gathered. A few assumptions to minimize the complexity of modelling such as air box channel dimension, velocity of air inlet from the blower fan, heat sink design such as base, pin dimension and total number of pin, power dissipated from the chip and chip dimension.

2. METHODOLOGY

Heat is defined as energy of the temperature value. In thermodynamics, heat transfer is a process of thermal energy movement from hot area to cold area. There are three fundamental mechanisms in heat transfer which are conduction, convection and radiation. The 3D heat conduction equation is described as equation (1) below.

$$\rho C_p \frac{\partial T}{\partial t} - \nabla.(k\nabla T) = Q \quad (1)$$

Where ρ is density (kg/m^3), C_p is the heat capacity (J/Kg^{o}C), k is thermal coefficient of the material (W/mK) and Q is volume heat source (W/m^3). Then heat convection equation as equation (2).

$$n \cdot (k\nabla T) = q + h(T_{amb} - T) \quad (2)$$

Where n is the normal vector of the heat flux, $h(T_{amb}-T)$ as known Newton law of cooling, which is use to specifies the heat flux cause by forced (airflow) or natural convection process, and T_{amb} is ambient temperature.

The overview of modelling development is shown in Figure 1 which comprises of four stages. The operating condition and model parameter values for heat sink model are listed in Table 1.

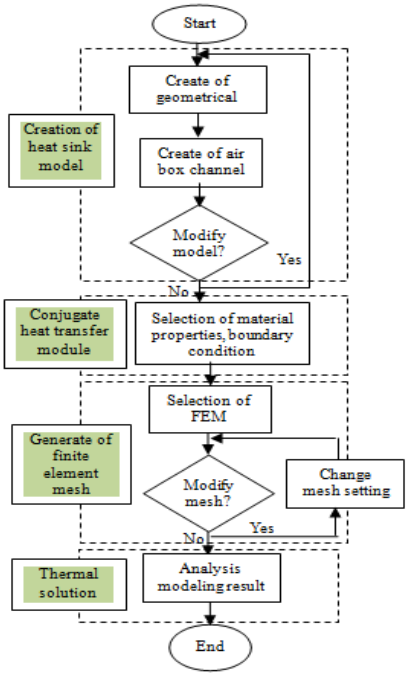

Figure 1 Heat sink modeling algorithm

Table 1 Inline pin fin heat sink model parameter

Parameter		Values
Air box Channel	Length	6 cm
	Width	5 cm
	Height	2 cm
CPU	Length	2.2 cm
	Height	0.1 cm
	Power dissipated	5.5 W
Pin fin	Height	1.7 cm
	Diameter	0.2 cm
	Number of pin	36
Heat sink base	Base thickness	0.2 cm
	Diameter	4 cm
Air flow inlet	Inlet velocity	10 cm/s
	Inlet temperature	20 °C
Material		Aluminium

3. SIMULATION RESULTS AND DISCUSSION

In this paper, the simulation was done using COMSOL Multiphysics software under Conjugate Heat Transfer module on a computer equipped with 12GB RAM and Intel i3-2120 3.30 GHz processor.

Figure 2 shows three 3D inline arrangement of pin fin heat sink thermal performance simulation results out of 30 models. The different is position between pin fins located on the base of heat sink. The analysis shows that different inline arrangement of pin fin mounted on the base heat sink gave different thermal management performance even though the cross sectional area of each model is constant. From the three types of arrangement, Figure 2(a) is designed based on 6 X 6 (x and y axis) selection design, which give optimum temperature of only 90.78ºC lower than the remaining arrangement. These results show that a good heat thermal performances can be optimized by selecting the correct geometry of the pin fin.

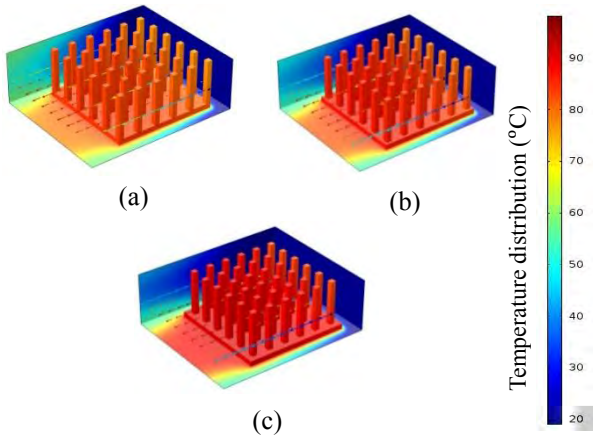

Figure 2 3D inline pin fin heat sink models with different alignment. (a) Model A (max temp: 90.78ºC); (b) Model B (max temp: 93.2ºC); (c) Model C (max temp: 97.26ºC)

4. CONCLUSIONS

This paper has presented thermal performance of various inline arrangement of pin fin heat sink model for CPU Intel® Atom™ Processor N450. The simulation result showed that different inline arrangement of pin fin would give variable heat thermal performance. Therefore the selection of the suitable inline arrangement of pin fin is crucial during the product design stage. Apart from this method, a population based evolutionary algorithm optimization can be applied in order to find the optimal inline arrangement of pin fin. For future work, the focus will extend to other parameter of the heat sink, for example heat sink material, shape and position of air inlet.

5. ACKNOWLEDGEMENT

The authors appreciate the support granted by Universiti Teknikal Malaysia Melaka (UTeM) in pursuing this research.

6. REFERENCES

[1] D.K. Kim, J.K. Bae and S.J. Kim, “Comparison of thermal performances of plate-fin and pin-fin heat sinks subject to an impinging flow” in *Thermal and Thermomechanical Phenomena in Electronic System,* 2008, pp. 360-366.

[2] C.T. Chen and S.H. Jan “Dynamic simulation, optimal design and control of pin fin heat sink processes” in *Journal of the Taiwan Institute of Chemical Engineers 43,* vol. 43**,** pp. 77-88, 2012.

[3] N.V.S. Shankar, R. Desala, V. Babu, P.V. Krishna and M.M. Rao, “Flow simulation to study the effect of flow type on the performance of multi – material plate fin heat sinks” in *International Journal Of Engineering Science & Advanced Technology,* vol. 2**,** pp. 233-240, 2012.

Stress level on sustainable vibration isolator using numerical method

M.A. Salim[1, 2,*], S.N. Jamaluddin[1, 2], A. Putra[1, 2], M.A. Abdullah[1, 2]

[1)] Faculty of Mechanical Engineering, Universiti Teknikal Malaysia Melaka,
Hang Tuah Jaya, 76100 Durian Tunggal, Melaka, Malaysia.
[2)] Centre for Advanced Research on Energy, Universiti Teknikal Malaysia Melaka,
Hang Tuah Jaya, 76100 Durian Tunggal, Melaka, Malaysia.

[*]Corresponding e-mail: azli@utem.edu.my

Keywords: Vibration isolator; finite element analysis, rubber bearing

ABSTRACT – This paper represents the stress distributions study on sustainable vibration isolator using numerical method. Rubber materials were used and modeled because it is a hyperelastic material and it also accepted as an isotropic and incrompressible behavior. Mooney-Rivlin model were used to investigate the stress and strain indicator. Numerical analysis were chosen as a tools to model the sustainable vibration isolator due to stress distributions. According to the analysis, by increase the number of metal plate, it was found that the deformation is reduced, however the stress distributions become higher.

1. INTRODUCTION

Seismic isolation is a technique that has been widely used around the globe to protect building structures, bridges, liquid storage tanks, oil lines and nuclear reactor plants from the detrimental effects of earthquake ground shaking. Construction of buildings with seismic isolation has increased at an almost exponential rate since the 1980s in Japan and China [1]. An isolator is used to decouple the ground vibration from reaching the structure. This is significant to prevent injury to the occupants and damage to the content.

Essentially, all isolation systems can be separated into two primary classes. They are frictional type sliding isolator and laminated rubber bearing isolators with and without lead-core. Friction base isolation decouples a structure from the soil by introducing flexibility and energy absorption system between the construction and its creation. A laminated rubber bearing consists of rubber layers bonded and alternated by rigid steel shims. It has high hardness and strength-to-weight proportions, long fatigue life and immunity to electrochemical corrosion. Many of seismic isolated structures now use laminated rubber bearing as the seismic isolation device.

There are two basic concepts of vibration isolating motions which are horizontal and vertical isolation systems. The basic concept of horizontal motions is described by a simple pendulum that swing from right to left while vertical motions is described as mass-spring vertical isolator that move upward and down endlessly. The horizontal isolation system usually used for constructions that has high seismic movement, such as earthquake while the vertical system, for a structure that located near vertical vibration sources such as railway stations.

Recent growth and research widely focuses on the isolation of vibration causes by the earthquake which is mainly horizontal vibration and of vertical isolation system for buildings and structure should be taken into consideration to control the vertical vibration problem.

Carrying out of laminated bearing is only meant to work well for earthquake protection which is mainly for low frequency and horizontal oscillation. Investigation on the bearing for horizontal vibration, especially during high frequency region is therefore of interest.

This study was conducted to understand the behavior of the sustainable vibration isolator due to axial vibration at high frequency using numerical analysis.

2. MATERIALS AND NUMERICAL ANALYSIS

Rubber materials were modeled by a hyperelastic material and accepted to be isotropic and incompressible. From the tensile test done along the rubber material, namely unfilled rubber, the stress and strain reading indicate close behavior with Mooney-Rivlin constitutive model. The constitutive model is expressed as

$$W(I_1, I_2, I_3) = \sum_{i,j,k}^{\infty} (C_{ijk}(I_1 - 3)^i (I_2 - 3)^j (I_3 - 3)^k) \qquad (1)$$

Where W is the strain energy potential and I_1, I_2, I_3 are the first three invariant of the Green deformation tensor [2]. Since the rubber used is almost incompressible, I_3 = 1, the expression can be reduced to

$$W(I_1, I_2) = \sum_{i,j}^{\infty} (C_{ij}(I_1 - 3)^i (I_2 - 3)^j) \qquad (2)$$

The material parameter of the rubber stuck in in the Ansys Workbench data properties can be stated in terms of initial shear modulus G and initial bulk modulus K where $G = 2(C10+C01)$ and $D1 = 2/K$. This type of rubber can withstand up to 600% of strain before it fails.

The steel was modelled with linear elastic properties only (E=2×10^{11} Pa, v = 0.3) because the loads should not be large enough to cause inelastic deformations. The properties of materials used in the numerical analysis are shown in Table 1.

The finite element modelling of the sustainable vibration isolator was carried out using the ABAQUS finite element analysis (FEA) software. The static analysis can be measured the total deformation, total stress and total strain. The vibration characteristics of the isolator were defined in terms of the transmissibility frequency response function which is the ratio of the displacement response of the output end plate to the input displacement excitation applied to the input end plate for future analysis.

Table 1. Material properties

Material parameter	Rubber	Steel structural
Density [kg/m^3]	920	7850
Material Model	Hyperelastic	Linear Elastic
Young Modulus [Pa]	1.5×10^6	2×10^{11}
Poisson Ratio	0.49	0.3
Yield Strength [MPa]	250	31.026
Material Constant C_{10} [Pa]	1.5×10^5	-
Material Constant C_{01} [Pa]	0.9×10^5	-
Incompressibility Parameter D_1	8×10^{-8}	-

For purposes of analysis, it is assumed that the springs and dampers are separate elements. The metal plates were modelled using fully integrated axisymmetric solid elements of type CAX8 in the ABAQUS element library, whereas axisymmetric solid element CAX8H was used to model the rubber portion of the isolator. The elements CAX8H are hybrid, fully integrated axisymmetric solid elements which are formulated for incompressible or nearly incompressible material behavior.

The cylindrical shape sustainable vibration isolator were designed with same total distance and width. Only the number of metal plates were differ in each isolator which made the rubber pad thickness also varies in each model. The dimensions of each isolator model are given in Table 2.

Table 2. Dimensions of each isolator

Model	Type of isolator	Metal plate thickness	Total rubber thickness	Diameter	Single rubber layer thickness
1	Solid	3	140	225	140.00
2	1 Metal	3	140	225	68.50
3	2 Metal	3	140	225	44.67
4	3 Metal	3	140	225	32.75
5	4 Metal	3	140	225	25.60
6	5 Metal	3	140	225	20.83
7	6 Metal	3	140	225	17.43

3. RESULTS AND DISCUSSION

Static analysis was done for all the model isolator on the total deformation, total elastic stress and total elastic strain behavior. Table 3 depicts the result for each model, including the safety factor for each fabric. It is observed that the reduction in total length of the isolator after applied with force is progressively decreased by increasing amount of interlayer metal plate. Increasing number of metal plate has increased the stiffness of the isolator. Highest total deformation can be seen in model 1 which was 8.5465 and improves at about 77% as the spring added with six plates. Based on the maximum total deformation in Table 3, model 7 had the lowest total deformation, which was 1.8901 mm and made it the most stable model. The bulging effect was cut when the vertical stiffness increased, thus the spring has become more stable.

From the maximum total stress distribution result, stress distribution was discovered to be centralized in the steel layers. Rubber is an easily deformed material, thus in this composition of rubber and metal, steel plate is the layers that carry the stress occurred. The largest maximum stress occurred on model 5, isolator with 4 metal plates while the lowest was model 1, solid rubber isolator. Model 5 and model 1 had maximum equivalent stress of 40.819 MPa and 0.22651 MPa each. Multiple plate isolators have higher stress distribution because the vertical stiffness has increase. The force imposed on the top surface of spring were spread and passed through the steel layers and the closest steel to the input force experienced greatest stress. First steel layer absorbs most of the stress exerted and the balance, stress gone through the next layer and then along. When only single layer steel existed in a spring, the force will be concentrated on it. Yet with more interlayer steel added, the power had been shared within existing steel layers. Even though the stress distribution had increased for multiple plate isolator, the safety factor for metal plate were still high which show that it was safe to be used.

Table 3: Results of static analysis

Model	Max. Total Deform (mm)	Max. Eq. Stress -Von Misses, (MPa)	Max. Eq. Elastic Strain -Von Misses, (MPa)	Angle of Buckling Deform (°)	Min. Safety Factor for Metal Plate	Min. Safety Factor for Rubber Layer
1	8.5465	0.22651	0.147860	14.5	-	34.4356e 6
2	5.5531	12.916	0.124930	14.0	19.36	41.13
3	4.0105	32.108	0.096122	13.0	7.786	53.73
4	3.0944	40.114	0.081612	11.2	6.232	63.41
5	2.5161	40.819	0.079524	10.8	6.125	65.07
6	2.0837	35.662	0.081506	9.9	7.0102	63.43
7	1.8901	33.465	0.071662	9.7	7.4705	72.58

4. SUMMARY

Static analysis of a sustainable vibration isolator has been modelled using the finite element method. It was found that the deformation of the rubber due to load can be reduced by embedding layers of metal plates. However, this generates higher stress distributions compared to pure solid rubber and the stress concentrates mainly on steel plate layers.

5. REFERENCES

[1] Warn, G.P. and Ryan, K.L., "A Review of Seismic Isolation for Buildings: Historical Development and Research Needs," Buildings, vol. 2, no. 4, pp.300–325, 2012.

[2] Saintier, N., Cailletaud, G. and Piques, R., "Crack initiation and propagation under multiaxial fatigue in a natural rubber," International Journal of Fatigue, vol. 28, pp.61–72, 2006.

The effect of diffuser angle on modified generic side view mirror

Nur Rashid bin Mat Nuri[1,*], Abdul Rahman bin Mohd Nasir[1], Mohd Suffian bin Ab Razak[1]

[1)] Faculty of Engineering Technology, Universiti Teknikal Malaysia Melaka,
Hang Tuah Jaya, 76100 Durian Tunggal, Melaka, Malaysia.

[*]Corresponding e-mail: nrashid@utem.edu.my

Keywords: Modified generic side view mirror; diffuser angle; pressure distribution

ABSTRACT – In this paper, an aerodynamics effect of modified generic side view mirror with different diffuser angle, fix foot height and constant foot width are discussed. The numerical simulation is done by using Hyperworks software. The results obtained are discussed in term of drag coefficient, turbulence separated region and pressure distribution around the side mirror and at side mirror surface. With all these results, the effect of different diffuser angle on modified generic side view mirror has been understood.

1. INTRODUCTION

Side view mirror primary function is to provide a clear vision outside the vehicle during driving, so that the driver does not need to divert his/her attention from vehicle's direction of motion. Side view mirror aerodynamics analysis is common in automotive vehicle development. Although the effect of drag is considerably small compared to the total vehicle drag, it is critical in terms of noise induced by the side view mirror and also in case where water entrains around the door glass during raining. At high speed (e.g. > 100 km/h), atmospheric air flow in reality is turbulent; during car moving, it cause the car body to withstand the impact of air and when it couples by external shape such as the side mirror, the flow becomes chaotic which lead to intermittent wind noise. Furthermore, during raining the effect of side mirror is imminent that it cause the water droplet to stale around the door glass. This is due to vortex generated behind the side view mirror as well as low pressure induced around the area [1].

2. METHODOLOGY

To understand the basic fundamental of aerodynamics phenomenon on side mirror, it is well known that one has to start with a simple model in order to reduce the complexity of the model. A simple geometry known as generic side mirror geometry is quarter of a sphere mounted on a half-cylinder with its dimension as shown in Figure 1.

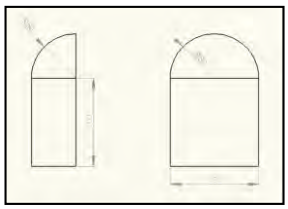

Figure 1 Generic Side Mirror Geometry.

Three parameters which are the most important to noise generation from a side view mirror are foot height, foot width and diffuser angle [2]. On this simulation, all above factors are considered with fix foot height and foot width with different diffuser angles.

The entire model has been designed based on defined parameters using CATIA software as shown in Table 1.

Table 1: Designed model

Name of model	Foot height (mm)	Foot width (mm)	Diffuser angle (°)
40-30-00	40	30	0
40-30-05	40	30	5
40-30-10	40	30	10
40-30-15	40	30	15

Then, it will be analyzed using Hyperworks Virtual Wind Tunnel software. The parameters used as shown in Figure 2.

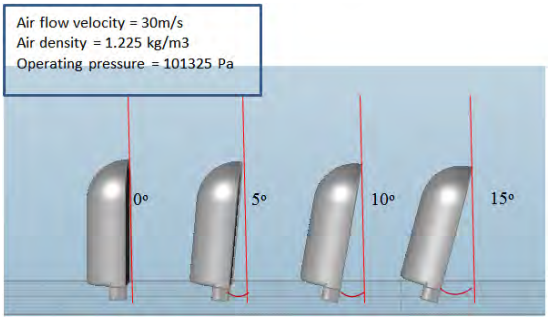

Figure 2: Diffuser angle parameter

3. RESULTS AND DISCUSSION

The results were divided into 3 sections:

(i) Drag coefficient (Cd)

Figure 3 shows the drag coefficient between these four models. Clearly, the 40-30-00 model has the highest drag coefficient compared to others.

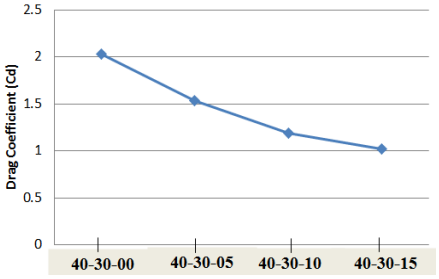

Figure 3 Drag coefficient (Cd) of four models

(ii) Streamlines

Figure 4 shows the comparison of turbulence separated region in term of streamlines between these four models at the top view. By looking at 40-30-00 streamlines pattern, big area of turbulence separated region was created behind the side view mirror. When the diffuser angle has increases, the separated region will become smaller. Therefore, 40-30-15 proved that 15° angle was the good angle where it shown that it only created the smallest turbulence separated region area than the other models.

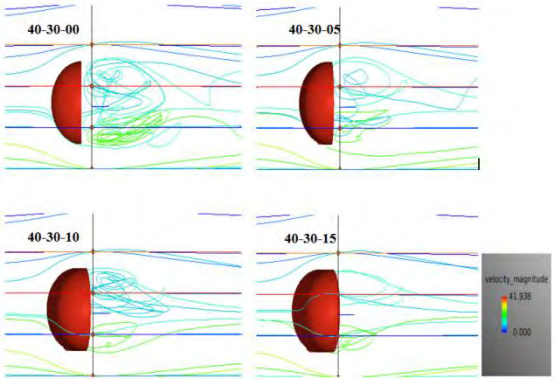

Figure 4 The turbulence separated region in term of streamlines around the side mirror at the top view.

The other view which was the side view of the turbulence separated region in term of streamlines can be seen at Figure 5. The 40-30-00 has complex and large turbulence separated region flow behind the side mirror. As diffuser angle become larger, the turbulence separated region become smaller and less complex. The more turbulence separated region appeared, the more drag generated.

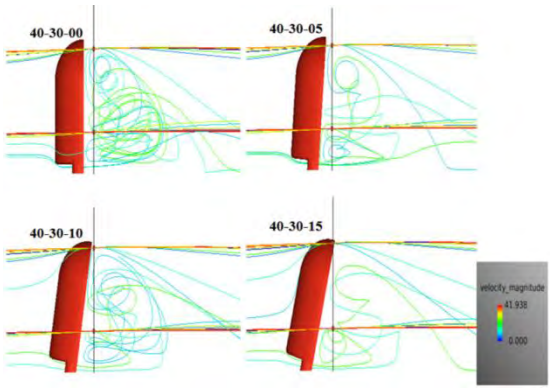

Figure 5 The turbulence separated region in term of streamlines at side view of the side mirror.

(iii) Pressure Distribution

Figure 6 shows the contour of pressure distribution at the mirror. It shows that the high pressure distribution area was at approximately center of the side mirror and the region become bigger when the diffuser angle increases.

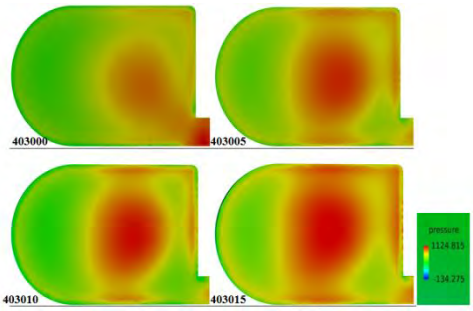

Figure 6: The pressure distribution at the mirror.

Next, the pressure distribution on the housing of the side mirror can be seen in Figure 7. It shows that the high and low pressure area were distributed uniformly even when diffuser angle become larger.

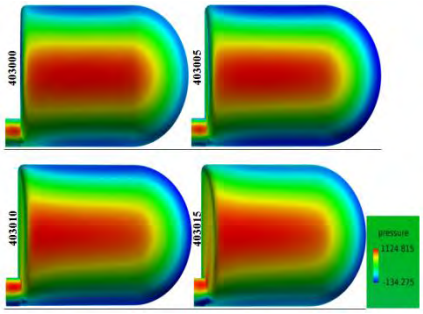

Figure 7 The pressure distribution on the housing of side mirror.

4. CONCLUSIONS

After comparing results obtained by simulations using different diffuser angle, fix foot height and constant foot width, it can be summarized that 40-30-15 model which has 15 ° diffuser angle, 40 mm of foot height and 30 mm of foot width was better model compared with other models in term of small turbulence separated area and low drag coefficient. Moreover, this model has larger high pressure distribution at the mirror.

5. ACKNOWLEDGEMENT

The author would like to acknowledge the Ministry of Science Technology and Innovation and Universiti Teknikal Malaysia Melaka for the support and funding throughout this studies.

6. REFERENCES

[1] M. Olsson, *Designing and Optimizing Side View Mirrors*, Chalmers University of Technology; 2011.

[2] Thorsten Grahs and Carsten Othmer, "Evaluation of aerodynamic noise generation: Parameter study of a generic side mirror evaluating the aeroacoustic source strength," in *European Conference on Computational Fluid Dynamics*, Netherland, 2006.

Design from nature: Development of a database to support product development

S.F. Wong[1], S. Maidin[1,*]

[1)] Faculty of Manufacturing Engineering, Universiti Teknikal Malaysia Melaka, Hang Tuah Jaya, 76100 Durian Tunggal, Melaka, Malaysia.

[*]Corresponding e-mail: shajahan@utem.com.my

Keywords: Bio-inspired design; database; top-down approach

ABSTRACT – Although biomimetic is a good source of ideas for design, however it is not widely used. This is due to lack of systematic process for engineers to find biological analogies related to the design problem and to transfer knowledge of biological design to engineering problem. Besides, the biological design feature information is scattered. In order to ensure there is a design aid tool to solve human challenges in terms of solving complex design problem and challenges, this research proposed a database with biomimetic design feature information. Questionnaire survey was carried out with 35 final year Department of Design students to test the functionality, usability and their satisfaction of the database. It was found that the database assist them by providing various visual design features that could be adopted from nature to solve design problem and improve creativity in product design.

1. INTRODUCTION

Biomimicry or Biomimetic is the study of structure and function in biological systems as models for the design, engineering of materials and machines in order to solve complex human problems. Biomimetic come from the Greek words bios meaning life and mimesis meaning imitation [1]. Sometimes a closely related term bionics which means combined from biology and technics is also used. Besides that, there are alternative terms to 'bionic' or 'biomimetic', these are 'biologically inspired' or 'bio-inspired'. Biologically inspired design is to implement the functions, mechanisms and principles which is inspired by nature. In recent years, many engineering design has been inspired by nature. Nature's design can generate a new idea and can solve engineering design problems. On the other hand, biomimetic can create opportunities to generate new materials, processes and devices. The increased need for biologically inspired design is caused by two factor, these are the need for sustainable development and the perception that nature's design can create opportunities for innovation [2].

2. METHODOLOGY

2.1 Biomimetic Database

The biomimetic examples are collected then were arranged into classified categories for every function of the organisms. Biological systems are assembled, categorized and arranged systematically before uploading into a database. The database was developed to be user friendly design interfaces. The Tables, Forms, Queries and Reports are created then the relationship between them was made by using macro tool. There are 13 functions incorporated to the database. These are adhesion, anti-reflective, energy, force, hydrophobicity, hydrophilicity, mechanical strength, self-cleaning, structural coloration, thermal insulation, lightweight, self-repair and robotics [3]. The biomimetic design features information are searched, collected and arranged by functions.

3. RESULTS

Figure 1 to Figure 6 shows the main form and the end form respectively.

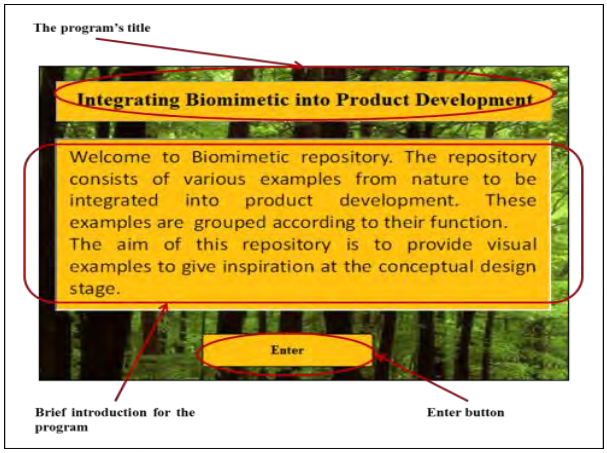

Figure 1 Main form (Before running)

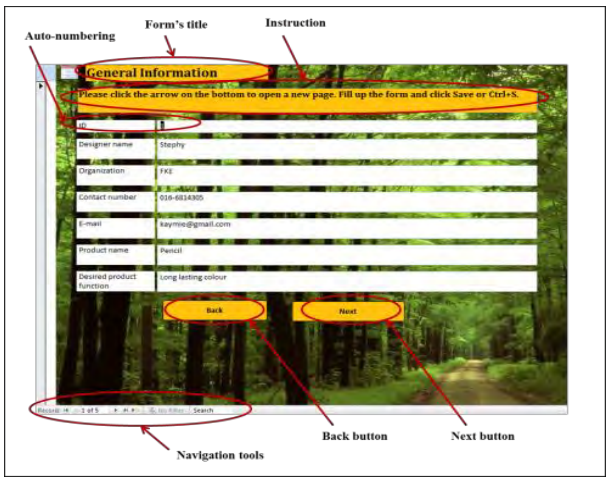

Figure 2 General information form (After running)

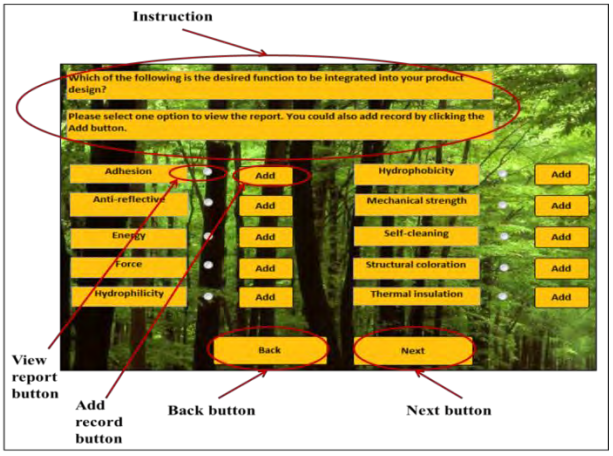

Figure 3 Report for Adhesion

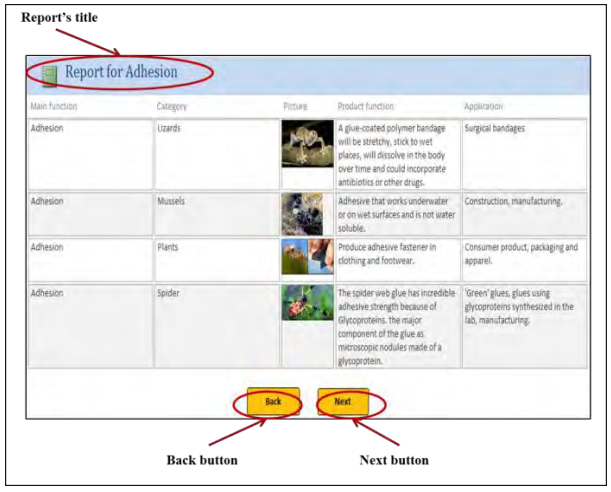

Figure 4 Select function form (Before running)

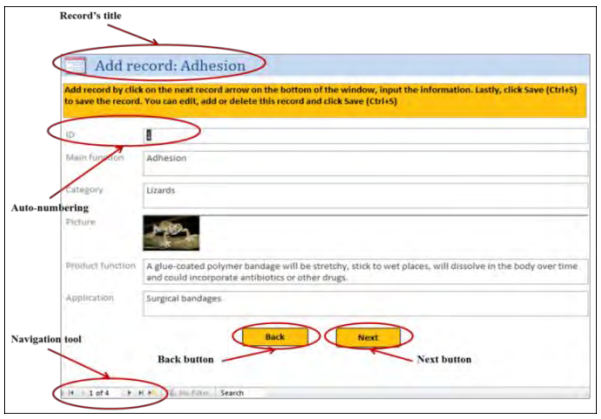

Figure 5 Add record form for Adhesion

Figure 6 The End form

4. SUMMARY

The information of biomimetic design features was uploaded into the MS Access to ease the management of data. The scattered information was arranged by function. Result from the questionnaire survey received from 35 final year students shows they were satisfied with the database in terms of user interface design, ease of use and layout design. On the other hand, there was one respondents suggested to create more creative design interface, more information about mechanical, physical and chemical properties and more examples of biomimetic design features. However, in conclusion, the database was useful as an initial tool to provide visual information of biomimetic design features to aid design.

5. REFERENCES

[1] T. Speck, O. Speck, N. Beheshti and A. C. Mcintosh, "Process sequences in biomimetic research". *Design and Nature IV*, 3-11, 2008.

[2] M. Helms, S. S. Vattama and A. K. Goel, "Biologically inspired design: process and products" *Design Studies*, *30*(5), 606-622, 2009.

[3] Bhushan, B. "Biomimetics: lessons from nature–an overview". *Philosophical Transactions of the Royal Society A: Mathematical, Physical and Engineering Sciences*, *367*(1893), 1445-1486, 2009

Study of electrical characteristic for 50nm and 10nm SOI body thickness in MOSFET device

M.N.I.A. Aziz[1,*], F. Salehuddin[1], A.S.M. Zain[1], K.E. Kaharuddin[1,2]

[1)] Faculty of Electronics and Computer Engineering, Universiti Teknikal Malaysia Melaka, Hang Tuah Jaya, 76100 Durian Tunggal, Melaka, Malaysia.
[2)] Centre for Telecommunication Research and Innovation, Universiti Teknikal Malaysia Melaka, Hang Tuah Jaya, 76100 Durian Tunggal, Melaka, Malaysia.

[*]Corresponding e-mail: naazirullifwatt@hotmail.com

Keywords: MOSFET, Silvaco, SOI

ABSTRACT – Silicon on insulator (SOI) technology is an effective approach of mitigating the short channel effect (SCE) problems. The SOI is believed to be capable of suppressing the SCEs, thereby improves the overall electrical characteristics of Metal Oxide Semiconductor Field Effect Transistor (MOSFET) device. SCE in SOI MOSFET are heavily influenced by thin film thickness, thin-film doping density, buried oxide thickness and etc. This paper will analyze the effect of buried oxide layer thickness (BOX) towards SOI MOSFET device. The 50nm and 10nm thickness of buried oxide in SOI MOSFET was developed by using SILVACO TCAD tools. From the observation made, the electrical characteristic of 50nm BOX thickness is slightly better than 10nm. It is observed that the value drive current (I_{ON}) of 10nm BOX thickness SOI MOSFET was only 6.9% lower than 50nm. However, the electrical characteristics of 10nm BOX thickness SOI MOSFET are still in the range of ITRS 2013 prediction.

1. INTRODUCTION

Silicon-on-insulator (SOI) MOSFET development was improves a lot lately with a lot of researcher try to improve this technology with a new approach. Silicon-on-insulator or known as SOI now not limited to single gate but now it will be implanted in double gate and maybe triple gate later. The history of SOI MOSFET can be trace back from 80 year ago when J.E Lilienfield introduced first field effect concept called method and apparatus for controlling electric current. He state on his concept, there are three terminal device where the source to drain current is controlled by a field effect from the gate and is dielectrically insulated from the rest of the device. The active part of the device was built on a thin semiconductor film which is deposited on an insulator, believe or not this first proposed FET concept was indeed an introduction of SOI MOSFET, But due to lack of equipment and technologies, this concept been long forgotten until the development of SIMOX or known as implanted oxygen technology in 1966. The main route for this silicon on insulator technology is using silicon dioxide (SiO2) as main material.

Short channel effect (SCE) was the main problem for MOSFET when it comes to scaling down to become Ultra-thin Body (UT). SCE happen, when the barrier of electron injection accidently been reduce due to the effective channel length (L_{eff}) becoming too short. This SCE can lead to several problems to MOSFET model such as a shift of Threshold voltage when channel length been decrease, lack of pinch off. Furthermore, SCE shows that it reduced the controllability of gate voltage and drain current thus increasing drain-off current and degradation of subthrehold slope. Thus SOI MOSFET been introduce to reduced short channel effect (SCE) influenced, although this SOI MOSFET still having short channel effect (SCE) but it still btter then conventional bulk MOSFET. Most of SCE from SOI MOSFET was influenced from thin film thickness, thin-film doping density, substrate biasing and buried oxide thickness. This research is about the effect of electrical characteristic of SOI MOSFET when the buried oxide thickness been varied

2. METHODOLOGY

Initially, P-type silicon with <100> orientation was developed. Then, the Buried Oxide Layer (BOX) formation was created. After that, 200Å oxide layer was grown on top of silicon bulk. This oxide layer had been used as mask during P-well implantation process. After doping process completed, the oxide layer been etched and it was followed by annealing process. This annealing process been done to strengthen the structure. After that process, shallow trench isolation (STI) has been conducted to isolated neighbour transistor. A 130Å stress buffer been applied on the wafers with 25 min diffusion processes. LPCVD process or known as Low-Pressure Chemical Vapour Deposition been used to deposited a 1350Å nitride layer. The purpose of this nitride was to act as mask when silicon was etched to expose the STI area. Photo resistor layer then deposited on the wafer layer and unwanted part will be etched using the Reactive Ion Etching (RIE) process. Purpose for Oxide layer been grown on the trench sides is to eliminate impurity from entering the silicon substrate.

After that, to eliminate extra oxide on the wafer, the chemical Mechanical polishing (CMP) was applied and final process the STI was annealed for 15 minute at 900°C temperature. A sacrificial oxide layer was then grown and etched to eliminate any defect that occur on the surface, before Boron Difluoride (BF2) threshold-adjustment been done in the channel region the gate

oxide must be grown first. The polysilicon gate was then deposited and followed by halo implantation. Indium was doped to get a better performance for every MOSFET. Depositing sidewall spacer then been conducted and been used as mask for source/drain implantation. Arsenic was implanted with certain value of concentration to get smooth current flow in NMOS device, after that silicice layer been produced and then be annealing at the top of polysilicon.

After all the process, the next stage is to deposited Boron Phospor Silicate Glass (BPPG) layer. This layer will acted as Premetal dielectric (PMD) that will be the first layer deposited in the wafer surface when transistor produced. This transistor then will be connected with aluminum metal, after that second aluminum layer was deposited on top of the intel-Metal Dielectric (IMD) and unwanted aluminum was etched to create the contacts. The step was ended when etching and metallization was performed for electrode formation and bonding pad was opened.

3. RESULTS AND DISCUSSION

Figure 1 shows the overlay graph Gate Voltage (V_G) versus Drain Current (I_D). It shown clearly that the value of I_{ON} for 50nm and 10nm SOI MOSFET is 707.48µA/µm and 658.29µA/µm respectively. For I_{OFF} value, the different between 50nm and 10nm are also not having any major different and both are still in value of ITRS 2013. Based on the analysis, it can be seen that both of them have a good transition between off and on states.

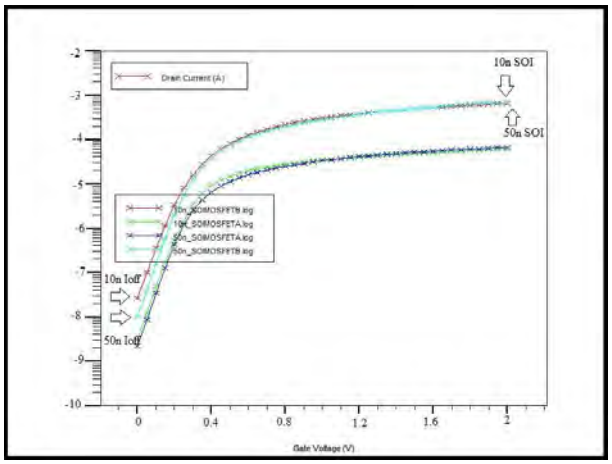

Figure 1 Overlay of 10nm and 50nm I_{ON} and I_{OFF} value.

Table 1 shows specifically the value of 4 electrical value that been measured for both 10nm and 50nm SOI MOSFET device.

Table 1 Electrical Characteristic of 50nm and 10nm SOI MOSFET

Electrical characteristic	50nm	10nm
I_{ON} (µA/µm)	707.48	658.289
I_{OFF} (pA/µm)	10.64	25.86
S_S (mV/dec)	82.96	85.59
V_{TH} (V)	0.2887	0.2896

4. CONCLUSIONS

This paper focus on study of electrical characteristic of SOI MOSFET when thickness of Buried Oxide layer been modified and then those value been compared to ITRS 2011 value either it still on range of ITRS value or not. The analysis of result shows that the value of 50nm and 10nm SOI MOSFET. It shown that the value of I_{ON} for 10nm SOI MOSFET device is 6.9% slightly lower than 50nm. However this value is still applicable in ITRS 2013.

5. REFERENCES

[1] Anurag Chaudhry and M. Jagadesh Kumar, "Controlling Short-channel Effects in Deep Submicron SOI MOSFETs for Improved Reliability: A Review", *IEEE Trans. on Device and Materials Reliability,* Vol.4, pp.99-109, March 2004.

[2] D. Flandre, J. Colinge, J. Chen, D. Ceuster, J. Eggermont, L. Ferreira, B. Gentinne, P. Jespers, A. Viviani, R. Gillon, J. Raskin, A. Vander Vorst, D. Vanhoenacker-Janvier and F. Silveira, *Analog Integrated Circuits and Signal Processing*, vol. 21, no. 3, pp. 213-228, 1999.

[3] K. Kaharudin, A. Hamidon and F. Salehuddin, 'Design and Optimization Approaches in Double Gate Device Architecture', *International Journal of Engineering and Technology (IJET)*, vol. 6, no. 5, pp. 2070-2079, 2014.

[4] J. Colinge, 'Multiple-gate SOI MOSFETs', *Solid-State Electronics*, vol. 48, no. 6, pp. 897-905, 2004.

Redesign of automotive brake pedal based on castability analysis

M.N.Sudin[1,2] , F.R.Ramli[1,2] S.A. Shamsuddin[1,2], M.M.Tahir[1,2] , M.M.Mustafa[1] and M.A. Affan[1]

[1)] Faculty of Mechanical Engineering, Universiti Teknikal Malaysia Melaka,
Hang Tuah Jaya, 76100 Durian Tunggal, Melaka, Malaysia.
[2)] Centre for Advanced Research on Energy, Universiti Teknikal Malaysia Melaka,
Hang Tuah Jaya, 76100 Durian Tunggal, Melaka, Malaysia.

[*]Corresponding e-mail: nizamsudin@utem.edu.my

Keywords: Automotive brake pedal; castability; design review

ABSTRACT – Change of automotive component material for any particular purposed (i.e. weight reduction, cost reduction) may affect the manufacturing process which will influence the final geometry of product. For this reason, an original automotive brake pedal that was initially made of steel was substituted with aluminum alloy and aim to be manufactured by casting process. In this research, the design review and modification on the brake pedal was carried out based on the casting rules. Initial castability evaluation on the original and modified brake pedal design was carried out using Ansys FLUENT simulation software. The results of the study show that changes on the design features of an original brake pedal were necessary as to improve its castability.

1. INTRODUCTION

Brake pedal is an important automotive component to stop or reduce the speed of a motor vehicle. At present, many cars have brake pedal that is made of steel. A brake pedal may consist of three major components namely brake pedal, rubber foot and switch pad contact [1]. Each brake pedal component has to undergo a series of sheet forming processes before assembled together by welding process. Changing the material of a brake pedal to a lighter material such as aluminum may affect the final geometries and the manufacturing process. Thus, automotive design engineers have to modify the original design of a brake pedal as to fulfill the new manufacturing process requirement.

In aluminum alloy brake pedal production, casting has an advantage of producing in single process and suitable to substitute the original manufacturing processes (combination of press forming and welding process) [2]. However, castability of brake pedal should be investigate and analyze early in design in order to form the component without formation of effects such as cracks, segregations, pores or misruns [3]. According to Ravi [4] there are three major approaches for castability analysis: process simulation, parametric cost estimation and features-based castability checks. Geometric features such as undercuts, holes, sharp corners and hot spots were recognized from a solid model of the casting and analyzed by a number of dimensionless criteria functions. These criteria were developed through a detailed study of design heuristics used by practicing engineers and were written as functions of geometric attributes of component and tool features.

This paper intends to improve the original brake pedal design based on castability. An original brake pedal design was evaluated and the geometries that were critical modified and redesign to a new brake pedal design. The comparison between these two designs was carried out to prove that the modified brake pedal design is better in terms of castability.

2. METHODOLOGY

The research was carried out in three stages of process as following:

Stage 1: Brake pedal design review
Stage 2: Modification of brake pedal
Stage 3: Castability analysis

The original brake pedal design was reviewed based on the casting rules. This is where the steel design of brake pedal shows a potential problem at the joining region between pedal pad and brake pedal arm due to sharp corner. The critical area was found at the bottom of this joint. The other locations that have critical area are the sharp corner and edges in the middle of the brake pedal arm.

At the joint between brake pad and brake pedal assembly the ribs were added according to castability rules such in Figure 1. The added dimension of ribs was 20.2 mm on both sides which is approximately 80% from the total length of the joint. The ribs were also added in the front and behind of the joint with the dimension of 7.5 mm. According to the castability rules, the fillet was required to avoid stress concentration. On the other location of brake pedal arm the fillets were added with the dimension ranging from 1-3.75 mm depending on the part thickness.

Afterwards, the castability analysis of brake pedal designs was performed by using Ansys FLUENT simulation software. Pressure distribution and temperature changes were used to differentiate the castability of these two designs. The modified area of pedal pad was chosen as the point for comparison between the original and modified brake pedal design.

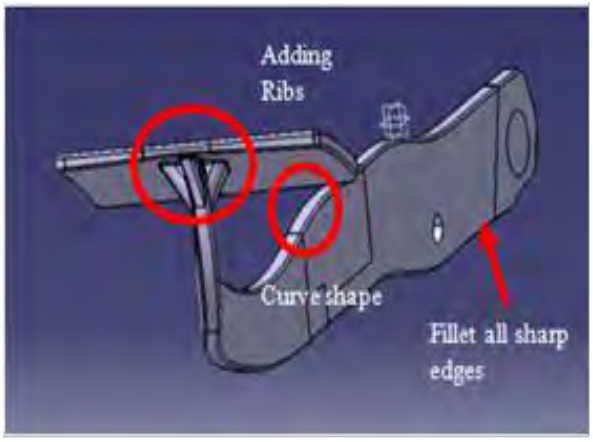

Figure 1 Modification Design

3. RESULTS AND DISCUSSION

The result of the comparison between new modification brake pedal and the old brake pedal design are summarized in Table 1.

Table 1 Brake Pedal Comparison Based on Castability

Castability Characteristics	Old Design	New Design
Max Pressure (kPa)	187	151
Temperature (K)	827	855
Air Entrapment	Yes	No

Comparing the old designed brake pedal and the new designed brake pedal, the maximum pressure value was less than the original brake pedal after the addition of the ribs at the joining sections. High pressure at the surface of the casting may lead to hot tearing which caused by the non-uniform cooling rate of the material that lead to quicker solidification. Uneven cooling rate may also cause a misrun when the temperature of the material drops. This happened when the temperature decreased and solidified earlier before filled up sufficiently into the cavity. The porosity may occur due to shrinkage of the solidified aluminum. Hot tear, misrun and porosity may occur at the joining location of the sharp angles at the corners.

The effect of high pressure may lead to the porosity due to entrapment of air that happened at the pedal pad surface where the concentration stresses are high. This may happened due to the incorrect shape dimension of the joint from thin to thick area and formed a separation direction of metal flow that was inadequate. The separation of metal flow may cause cold shut due to the evolution of the gas that had happened. The gas evolved or expanded when it accumulated at the region area of porosity.

The temperature of molten metal is important as it represents the fluidity of material. High temperature of molten metal may cause causalities of the material to flow smoothly before it solidified. Low temperature of the casting may lead to solidification of the material become quicker. This will influenced the flow distribution that could not reached the location to fill the mold sufficiently due to quick solidification of the material and may lead to defection such as porosity due to shrinkage of the material. Shrinkage happened due to the material thermal expansion at the time molten metal when it began to solidify. Significantly the temperature of the original brake pedal showed that the molten metal was not reachable enough by the end location of the casting

Unlike the new brake pedal, the temperature of the molten metal was as even as the liquids condition. This showed that the temperature maintained at the melting point condition. When the temperature was high, the flow of the molten metal increase in time, and the molten metal was able to fill sufficiently into the mold cavity before solidification. This potentially happened when the molten metal started to solidify before filling up the cavity. For the new designed, the potential of the defect was probably less due to the temperature of the molten metal was maintained and helped the flow of the material to fill up sufficiently in the mold cavity.

4. CONCLUSIONS

Based on the result, the ribs and fillet of the design influenced the castability of brake pedal design. The pressure and temperature elements affected the castability of the brake pedals where they influenced the fluidity and the flow of the material. New design of brake pedal proved that the casting defect can be reduced and it will be easier to cast based on the simulation result obtained.

5. ACKNOWLEDGEMENT

The authors would like to thank Universiti Teknikal Malaysia Melaka (UTeM) for the financial support under short term grant with reference number (PJP/2012/FKM (46C)/S01051).

6. REFERENCES

[1] N. A. Hamid, “Component Design and material properties, The design of light weight of an automotive brake pedal” pp.14-22, 2007.

[2] S. Kalpakjian and S.R.Schmidt, “Fundamental of metal casting process” , Manufacturing, Engineering and Technology, Vol 6, pp261-316.

[3] M. D. Sabatino and L.Arnberg “Castability of aluminum alloys” *Transactions of the Indian Insitute of Metals*, Vol 62, Issue 4-5, pp321-325, 1999.

[4] B Ravi, “Casting method optimization driven by simulation”, *Mineral and Metal Review*, vol 34, pp33-34, 2008.

Energy audit for lighting in an academic building – Case study in UTeM

Younus Fahad Breesam[1], B.T. Tee[1,2*], Z.M. Zulfattah[1,2]

[1)] Faculty of Mechanical Engineering, Universiti Teknikal Malaysia Melaka,
Hang Tuah Jaya, 76100 Durian Tunggal, Melaka, Malaysia.
[2)] Centre for Advanced Research on Energy, Universiti Teknikal Malaysia Melaka,
Hang Tuah Jaya, 76100 Durian Tunggal, Melaka, Malaysia.

[*]Corresponding e-mail: tee@utem.edu.my

Keywords: FKM building; lighting; illumination

ABSTRACT - Lighting is essential for both domestic and industry usage. In Malaysia, it was estimated lighting used approximately 20% of the total energy total consumption of buildings and has potential for energy saving opportunities and achieves energy efficiency apart from good operational practices.an Energy audit is a tool used to assess and identify lighting energy consumption in the specified building or area. In this project, the energy audit focuses on the lighting systems in a FKM academic building at Technology Campus. By understanding the current lighting system condition and energy data analysis, It can help in evaluating the current performance of the lighting system. Energy reprofit is proposed to accommodate the occupant usial confort and performance. Mostly the lighting levels in every audited zone exceed Malaysian Standard MS 1525:2014.

1. INTRODUCTION

Electrical energy is very important in human life, but much of it content is wasted by inefficiencies in the energy conservation and distribution processes. Building's energy used accounted for the largest share of the final energy use by the commercial and residential sector. Air conditioners are shown to be the major energy users (57%) in office buildings, followed by lighting (19%), lifts and pumps (18%) and other equipment (6%) [1].

The global contribution from buildings towards energy consumption, both residential and commercial, have steadily increased, reaching figures between 20% and 40% in developed countries. Growth in population, increasing demand for building services and comfort levels, together with the rise in time spent inside buildings, assures the upward trend in energy demand will continue in the future. For this reason, energy efficiency in buildings is today a prime objective for energy policy at regional, national and international levels [2].

Stable illumination is a vital part in an interior environment. It is impossible to create a pleasing environment without proper lighting. Illumination is essential to identify and define an interior. Light helps to define an interior in terms of spatial size, depth, ambience and appearance. An energy audit is an evaluation of energy consumption in a domestic, commercial, or any other premises. It is generally used to determine where energy can be saved, conserved or used more efficiently [3].

2. BACKGROUND

Chia et al.[4] showed analysing some cases of the structure of electric consumption and electric facilities of the official buildings. The lighting load is the second biggest load of the studied building and is substantially saved if the efficiency of luminaries selection is used with the supplementary artificial lighting. Most existing lighting systems were designed without considering energy efficiency. Finally, this action saves replacing element cost and maintenance fee and the power factor of electronic ballasts is more than 95%, thus, it can reduce the current and improve user's safety. This action also can enhance circuit stability and reduce power line loss.

Ravi et al.[5] Studied on the efficient illumination design and occupancy of the main building of Asia Pacific, University of Technology and Innovation (APUTI).

It resulted in a total power saving of 16.59kW per day and 11 hours taken as the normal operating hours (7:30am to 6.30pm) for which an energy saving of 182.9 kWh has been achieved. Average annual energy saving of 50,000kWh has been achieved excluding weekends and public holidays (around 255 days), which contributes to 2.28% of the total energy consumption. The authors concluded that a total of 67520kWh is saved by the above two methods which contributes to 3.08% of the total energy consumption.

3. METHODOLOGY

In this work, the building is divided into many areas like, lobby room, corridors, meeting room, office room, lecturer room, and library. The normal operating hours for FKM's academic building ground floor and first floor start from 8.00 am until 5.00 pm depending on the classes' timetable and mainly used during weekdays.

A proper observation in the academic building is based on visual verifications such as the lighting system arrangement, occupant behavior on lighting usage and type of lighting lamp used for each zone area.

Once the data successfully gathered, digital lux meter used to conduct lighting measurement in each zone area by placing it in the specific zone at about 0.8 meters above the ground level. The lighting system

energy data analysis can be done upon the types of lamps for each zone is specified. The analysis involves the electricity usage of FKM's academic building, comparison a certain period of time and the approximate total of the average cost of the academic building's. Power density can be calculated as using the equation (1).

$$Power\ Density\ (W/m^2) = Lamp\ Capacity\ (W) / Area\ (m^2) \quad (1)$$

For each zone, the data can be used to calculate the amount energy consumed during observation period from 8.00 am to 5.00 pm. The data collected from all floors building to calculate the amount of energy consumed by the lighting and the operating cost unit can be calculated as in equations (2) and (3) respectively:-

$$\text{Energy usage} = \text{Power (Watt)} \times \text{Total Operating Hours (Hour)} \quad (2)$$

$$\text{Cost} = \text{Energy usage (kWh)} \times \text{Electricity tariff (cent per kWh)} \quad (3)$$

The Building Energy Index (BEI) is the most commonly used for comparing energy in buildings as shown in equation (4):-

$$\text{FKM Building Energy Index} = \text{Total Energy usage for 2013 Nov. to 2014Oct} \ / \ \text{Total FKM Gross Floor Area} \quad (4)$$

4. RESULTS AND DISCUSSION

The energy consumption was calculated based on the wattage capacity and its operation during office hours period. The wattage capacity from each zone for both floors was accumulated and the data used to obtain the energy consumption estimation. Table 1 shows the estimated energy consumption for all floors and total electricity cost.

Table 1 Energy consumption estimation for all floors.

Floor	kWh per month before retrofit
Ground	2177.28
First	1703.52
Second	4163.52
Third	4464.80
Fourth	2598.72
Fifth	4483.44
Sixth	4440.48
Total	24131.76
Cost (MYR)/month	8928.7512

The energy saving calculation involved the difference before and after retrofit plan. Table 2 shows the proposed retrofit plan to implement on the all floors.

Table 2 Comparison before and after retrofit proposal.

Before retrofit	After retrofit	Floors Involved
Currently using 36 W fluorescent lamps (TL-D 36W)	Change to 28W High Efficiency fluorescent lamps (TL5)	All Floors
Operating hours- 9 hours	Change to 8 hours (1 hours –switching off during break time)	All Floors
Maintain 18 W Recessed mounted channel fluorescent fitting (TL-D 18 W)	Maintain 18 W Recessed mounted channel fluorescent fitting (TL-D 18 W)	All Floors

The new energy consumption after retrofit plan has been calculated and lighting electricity cost per month are listed as in Table 3.

Table 3 Energy Consumption Estimation for each floor after retrofit plan.

Floor	kWh per month before retrofit	kWh per month after retrofit
Ground	2177.28	1753.9
First	1703.52	1361.2
Second	4163.52	3337.9
Third	4464.80	3388.8
Fourth	2598.72	2191.7
Fifth	4483.44	3642.5
Sixth	4440.48	3664.8
Total	24131.76	19,940.80
Cost (RM)/month	8928.7512	7378.096

5. CONCLUSIONS

The highest electricity usage was recorded in April 2014 and energy consumption of 668.707 kW hand lower electricity usage was recorded in November 2013 525.776 kWh. The energy consumption fluctuates throughout the year except from November 2013 to October 2014 almost constant recorded energy consumption range between 525.776 kWh and 668 kWh. From preliminary analysis, FKM academic building fifth floor consumed the largest a mount of energy is about 4483.44kWh per month. Quantitatively, the electricity usage consumed about 24131.76 kWh per month and costing MR 8928.75 per month. The feasibility measures to save energy and money can be applied in the FKM academic building. By implementing the proposed retrofit by replacing the current lamps to 28W High Efficiency fluorescent lamps (TL5), it can save energy and reduce electricity bills. From the calculation, it can save almost 4190.96kWh per month, which accounted about MR 1550.65 per month. Annually, it can save abuot MR 18607.77 equivalent to approximately 1.5 years of the simple payback period and 75.6% simple rate of return.

6. ACKNOWLEDGEMENT

The authors would like to thank Universiti Teknikal Malaysia Melaka for the financial support through short term research grand award (PJP/2012/FKM(6A)/S01077).

7. REFERENCES

[1] R. Saidur and H. Masjuki, "Energy and Associated Emission Analysis in Office Buildings, *International Journal of Mechanical and Materials Engineering*. 2008, " vol. 3, no. 1, pp. 90–96.

[2] L. Pérez, J. Ortiz, and C. Pout, "A review on buildings energy consumption information" *Energy and Buildings.*, 2008, vol. 40, no. 3, pp. 394–398.

[3] K. Shailesh, S. Tanuja, M. Kumar, and R. Krishna, "Energy consumption optimisation in classrooms using lighting energy audit," *Natl. Conf. Challenges Res. Technol. Coming Decad. (CRT 2013)*, pp. 1-5, Sept 27-28, 2013.

Energy analysis on ACMV system for an academic building – Case study in UTeM

Ahmad Zubair Yahaya[1], B.T. Tee[1.2.*],Yusmady Mohamed Arifin[1,2]

[1)] Faculty of Mechanical Engineering, Universiti Teknikal Malaysia Melaka,
Hang Tuah Jaya, 76100 Durian Tunggal, Melaka, Malaysia.
[2)] Centre for Advanced Research on Energy, Universiti Teknikal Malaysia Melaka,
Hang Tuah Jaya, 76100 Durian Tunggal, Melaka, Malaysia.

[*]Corresponding e-mail: tee@utem.edu.my

Keywords: ACMV; energy audit; building

ABSTRACT - Air-conditioning mechanical & ventilation system (ACMV) is one of the main contributors to the total building energy consumption. Thus, building energy audit is conducted in order to measure and analyse energy consumption patterns, monitoring of how the energy used, how the system element interrelate and record actual energy consumption. The study has been conducted at FKM's Building in UTeM's Technology Campus. Based on the collected data and information, the total of the building cooling load is being estimated. In addition, the Building Energy Index is also being determined. Finally, economic analysis is included with potential alternative measures to achieve optimum building energy usage.

1. INTRODUCTION

Air-conditioning & mechanical ventilation system (ACMV) is the main source of energy consumption for a non-residential building [1]. Any saving made on the energy consumption of this system will give significant impact on the building energy cost. Critical evaluation and advanced study is required in order to provide measures in achieving optimal building energy efficiency.

Globally, buildings consume about 40% of the total energy consumption and most of the energy is used for the purpose of heating, ventilation and air conditioning (HVAC) systems which are supported by Abdeen [2]. Yau has found in buildings, more than 50 % of the energy is consumed by the HVAC systems, especially in hot regions [3].The project is aimed to evaluate whether current energy usage is used efficiently or is being wasted, identify areas with potential for energy saving. This undertaking also aimed to look over the energy optimization stage in the building with compliance to a recommended comfort level.

2. METHODOLOGY

The energy audit process was started with the physical parameter measurement of the building, evaluation of historical electricity data and descriptive information about the building plant layout for each floor. The air velocity meter was used as shown in Figure 1 to conduct the physical parameters measurement. Before performing a physical data measurement, the following procedures are implemented:

(a) A selected rooms are cleaned and all the measurements were finished without the presence of occupants.
(b) All of the selected rooms are left to stabilize about one hour before conducting a measurement.
(c) The air velocity meter needs to be stabilized about 5 minutes before taking the real measurement.

Figure 1 Air velocity meter

The procedures mentioned above are based on the study by Lim et al [4]. The physical parameter measurement was conducted in the middle of the room. The objective of stabilizing as mentioned is to increase the accuracy of measurement data and also to make sure that the air-conditioning system in rooms selected are suitable for airflow measurement. The time and height while taking measurement by using an air velocity meter is following the standards as described in ASHRAE Standard 55-2014 [5]. The height of the air velocity meter probe is set at a height of 1.1 meters from a floor. Every one minute, air velocity meter measured and recorded the value.

3. RESULTS AND DISCUSSION

The results of physical parameter measurement are then compared with recommended indoor design conditions as outlined by Malaysian Standard MS1525:2014 [1]. The purpose is to evaluate the performance of the current ACMV system, whether it is still operating under comfort condition or not. The recommended indoor design condition of an air-conditioned space is 24^{o}C – 26^{o}C, 50 % - 70 % and 0.15 m/s – 0.50 m/s for design dry bulb temperature, design relative humidity and air movement respectively.

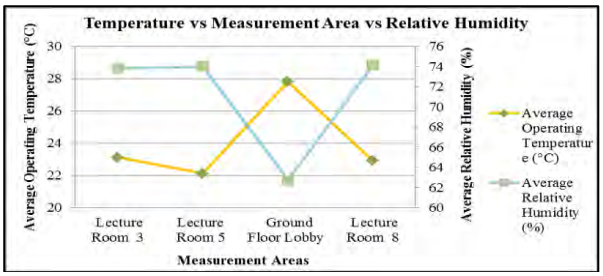

Figure 2 Temperature vs Measurement Area vs Relative Humidity at Ground Floor

Based on the result in Figure 2, the operating condition of Lecture Room 5 and Lecture Room 8 were operated below than the recommended range of design dry bulb temperature, meanwhile for the relative humidity, all the measured areas at ground floor are significantly over than the recommended value except in the Ground Floor Lobby. However, the temperature of the Ground Floor Lobby area is significantly higher than recommended standard. This is because of the Ground Floor Lobby is an open area with automatic gate that frequently close and open. This situation actually allows more heat to enter the lobby area.

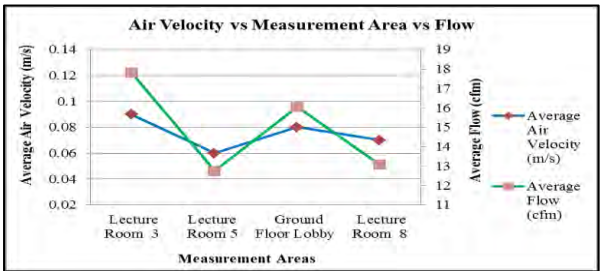

Figure 3 Air Velocity vs Measurement Area vs Flow at Ground Floor

In terms of air velocity, the measurement result for the ground floor are below than recommended standard (as shown in Figure 3). After an inspection was done on the ACMV system, it was identified that most of the the diffusers at the ground floor are not working in good condition and this is probably due to duct system leakage, dirty air filters and clogged from air particles.

Cooling load is the rate at which energy needs to evacuate from space. Based on the obtained information and measurement data, the total building cooling load can be estimated. According to Table 1, the ground floor gave the highest cooling load amount at 200.8794 kW. This is because the ground floor has more occupants compared to other floor and high exposure to the heat from the main entrance of the building. Meanwhile, the fifth floor of the building the lowest amount of cooling load 125.9162 kW.

Based on the annual electricity usage calculation, the Building Energy Index is being determined and the value of the Building Energy Index for whole of the building is 757.715 kWh/m²/year and for each level is 108.245 kWh/m²/year. Meanwhile, the value of the Building Energy Index based on the cooling load is 736.6 kWh/m²/year. Pusat Tenaga Malaysia has suggested the typical buildings in Malaysia have the BEI in the range of 200 to 300 kWh/m^2/year [6]. Both of the results shows that the consumption is higher than the recommended range for typical building.

Retrofit Analysis has been conducted in this study and two types of retrofit installations have been suggested which are variable frequency drive and 7-day programmable thermostat. The saving is estimated to be at 4% for installing variable frequency drive (VFD) and 2% for programmable thermostat which required RM 2204.56 and RM 1653.42 per month respectively. Based on the monthly cost saving at RM 3306.84 per month, the total of implementation cost will be recovered within 25 months.

Table 1 Cooling Load Summary for the Case Study Building

Level	Load (kW)	Load/Unit (TR)
Ground Floor	200.8794	57.11994
First Floor	162.1099	46.10635
Second Floor	157.1845	44.70552
Third Floor	130.2492	37.04471
Fourth Floor	161.6559	45.97723
Fifth Floor	125.9162	35.81228
Sixth Floor	126.6942	36.02489
Total	1064.689246	302.7909

4. CONCLUSIONS

According to the physical parameter measurement, most of the floors of the building do not achieve the acceptable air velocity recommended by Malaysian Standard. This is due to lack of maintenance of ACMV system and having equipment in ACMV system not functioning well. Overall, most of the temperatures at each level are below than the recommended comfort condition. Based on the calculation, an ACMV system was contributed about 49.4% of the total monthly energy usage.

5. REFERENCES

[1] Malaysian Standard 1525, *Code of practice on energy efficiency and use of renewable energy for non-residential buildings*; 2014.

[2] M. O. Abdeen, "Energy environment and sustainable development," Renewable and Sustainable Energy Reviews, vol. 12, pp. 2265–2300, 2008.

[3] Y. H. Yau, "The use of a double heat pipe heat exchanger system for reducing energy consumption of treating ventilation air in an operating theatre-A full year energy consumption model simulation," Energy and Buildings, vol. 40, pp. 917-925, 2008.

[4] J. S. C., Lim, A. Husain, B. T. Tee, " Simulation of Airflow in Lecture Rooms," Energy and Buildings, 2005.

[5] Ashrae Standard, *Handbook of thermal environmental conditions for human occupancy*, Atlanta:ASHRAE; 2004.

[6] H. Z. Xin, "The role of building active energy conserving strategies of the malaysia energy commission diamond building," Sustain, 2012.

Preliminary study on tribological properties of banana peel broth as additive in paraffin oil

M.M.B. Mustafa[1], N.A.B. Masripan[1,2*], M.F.B. Abdollah[1,2], J. Basiron[1]

[1)] Faculty of Mechanical Engineering, Universiti Teknikal Malaysia Melaka, Hang Tuah Jaya, 76100 Durian Tunggal, Melaka, Malaysia.
[2)] Centre for Advanced Research on Energy, Universiti Teknikal Malaysia Melaka, Hang Tuah Jaya, 76100 Durian Tunggal, Melaka, Malaysia.

[*]Corresponding e-mail: norazmmi@utem.edu.my

Keywords: Banana peel broth; paraffin oil; coefficient of friction; wear

ABSTRACT - Natural material as the additive in the engine oil promotes a sustainable material development through the utilization of renewable resources. This paper presents the preliminary study on the friction and wear of banana peel broth as the natural additive to the Paraffin oil conducted using four-ball tester at different load, temperature and speed. The mixture is prepared by dispersion method using the ultrasonic homogenizer. Inverted microscope is used to measure the wear scar diameter. It is found that the coefficient of friction and wear scar diameter reduced significantly at high load, temperature and speed.

1. INTRODUCTION

It is common to refer the banana skin as a slipping tool and yet sometimes would cause accidental slip. The banana skin has the ability to be used as a lubricant where it could help reduce the coefficient of friction (COF).

K. Mabuchi et al. [1] carried out studies on COF under banana skin on floor material. The COF was measured using six degrees of freedom force transducer under a flat panel of linoleum. A shoe sole pushed and rubbed by a foot motion on the panel with banana skin located in between to measure the frictional and vertical force simultaneously. COF resulted from the test is much lower compared to the value of common materials and similar to the well lubricated surface.

Lubrication has become an important part of improving the engine performance where it has simultaneously improved the fuel economy while reducing emissions. Research has been carried out with the aim to enable engine components to last longer by cutting down the COF, which saves energy, improves efficiency, and generally results in quieter operation.

Low oxidation stability is one of the major factors hampering industry acceptance of vegetable oil-based lubricants [2]. There is still a lack of tribological studies which incorporated natural material such as banana skin. Therefore, it is very important to investigate the potential of using the banana skin as lubricant in term of friction and wear to make sure it can be adapted by the industry.

2. METHODOLOGY

Tribological characteristics of paraffin oil with 20% banana peel broth were evaluated using a four-ball tester (TR 30L) at different speed, temperature and load as explained in Table 1.

Table 1 Parameters for tribological testing

Parameters	Value
Speed (rpm)	500, 1000
Load (N)	60, 250, 500
Temperature (°C)	27, 80, 100

The paraffin oil with 20 % of banana peel broth samples were prepared by dispersing the determined weight of blended banana peel broth in the paraffin oil using the ultrasonic homogenizer. The viscosity index of the mixture was then measured using a Brookfield Viscometer.

The lubricant used for the experiment is paraffin oil as based oil and paraffin oil with 20% of banana peel broth as to investigate the effectiveness of natural material as the lubricant in term of friction and wear.

In four-ball tester, three 12.7 mm diameter carbon-chrome steel ball were clamped together and covered with lubricant for evaluation. Fourth steel ball which referred to as top ball was held in collet and assembled at the spindle and rotate using an AC motor. Table 2 shows the mechanical properties of the ball bearing.

Data gathered by the TR 30 L four-ball tester was recorded using a data acquisition system is in form of frictional torque, T (N/m). This frictional torque was converted into form of kg/mm. The frictional torque in the unit of kg/mm was then used in determining the COF, μ using Equation (1).

Table 2 Mechanical properties of material

Properties	Ball bearing (Carbon-chromium steel)
Hardness (*H*),HRC	62
Density (ρ), g/cm^3	7.81
Surface roughness (R_a), μm	0.022

$$\mu = \frac{T\sqrt{6}}{3Wr} \quad (1)$$

Where, W is the applied load in kg and r is the distance from the center of the contact surfaces on the lower balls to the axis of rotation, which is 3.67mm. In order to obtain the wear volume losses L, the wear scar diameters, d was first measured using Axiovert 200-M inverted microscopes. The Equation (2) is used to determine the wear volume losses, V of the ball bearing with radius R.

$$V = \frac{\pi(d)^4}{64(R)} \quad (2)$$

3. RESULTS AND DISCUSSION

3.1 *Viscosity index*

From Table 3, it is clearly shown that the dispersion of banana peel broth increased the viscosity of the paraffin oil.

Table 3 Viscosity of the paraffin oil + 20 % of banana peel broth

Temperature (°C)	**40**	**100**
Kinematic Viscosity, cSt (mm²/s) of paraffin oil + 20 % banana peel broth	38.4	32.3
Kinematic Viscosity, cSt (mm²/s) of paraffin oil		17.5
Viscosity Index (VI) paraffin + 20 % banana peel broth	697.0	
Viscosity Index (VI) paraffin oil	102.0	

3.2 *Effect of Load and Temperature to Coefficient of Friction*

As refer to Figure 1, it is clearly shown that dispersion of banana peel broth in the paraffin oil is apparently reducing the COF at high temperature and speed. For all normal load tested, the COF reduced for 1000 rpm speed. It is evidence that the temperature gives a significant effect on the reduction of COF as refer to Figure 2. This suggests that banana peel broth is effectively protecting the frictional surface by reducing the contact surface and creating a separation boundary at high temperature, load and speed.

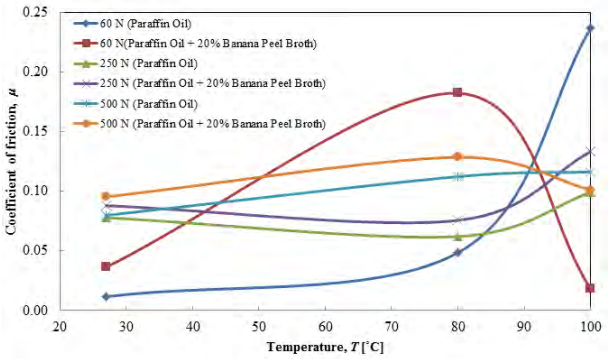

Figure 1 COF vs. temperature at 1000 rpm

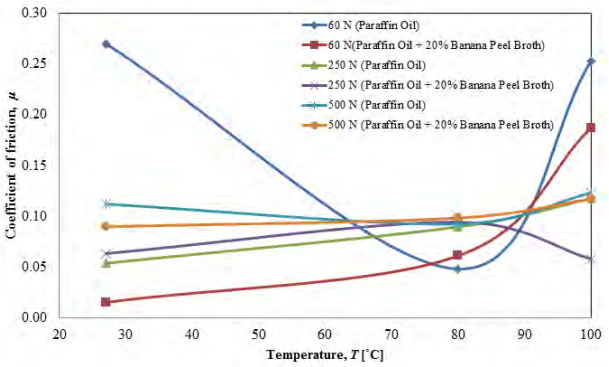

Figure 2 COF vs. temperature at 500 rpm.

3.3 *Effect of load to wear volume*

Wear volume losses for the test speed of 500 and 1000 rpm was reduced at each normal load tested as refer to Figure 3. This suggests that banana peel broth effectively played the role of ball bearings by changing the sliding friction to rolling friction between the friction pair which result in reducing the contact area between the frictional surfaces. Furthermore, a smoother worn surface obtained due to the polishing effect of lubrication containing banana peel broth [3]. This is in accordance with a significant reduction of wear volume losses.

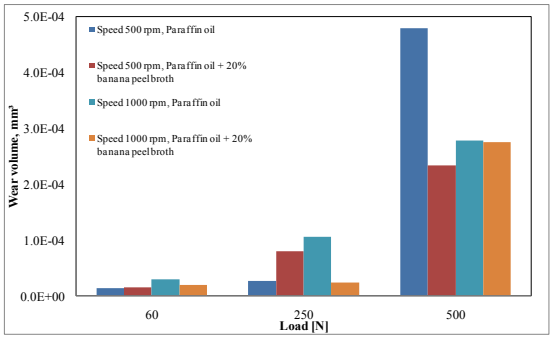

Figure 3 Wear volume plots against applied normal load for temperature of 100° C

4. CONCLUSIONS

Dispersion of banana peel broth in the paraffin oil has significantly reduced the COF and wear volume losses at high temperature of 100° C.

5. REFERENCES

[1] K. Mabuchi, K. Tanaka, D. Uchijima, and R. Sakai, "Frictional coefficient under banana skin," *Tribology Online*, vol. 7, no. 3, pp. 147-151, 2011.

[2] N.J. Fox, and G.W. Stachowiak, "Vegetable oil-based lubricants-A review of oxidation," *Tribology International*, vol. 40, pp. 1035-1046, 2007.

[3] M.I.H.C. Abdullah, M.F.B. Abdollah, H. Amiruddin, N. Tamaldin, and N.R.M. Nuri, "Optimization of tribological performance of hBN/AL_2O_3 nanoparticles as engine oil additives," *Proceedia Engineering*, vol. 68, pp. 313-319, 2013.

Investigation on oxidation of jatropha oil

A.M.H.S. Lubis[1,*], B. Ariwahjoedi[2], M.B. Sudin[3]

[1)] Faculty of Mechanical Engineering, Universiti Teknikal Malaysia Melaka,
Hang Tuah Jaya, 76100 Durian Tunggal, Melaka, Malaysia.
[2)] Department of Fundamental and Applied Science, Universiti Teknologi PETRONAS,
Bandar Seri Iskandar, 31750, Tronoh, Perak, Malaysia.
[3)] Department of Engineering, School of Engineering Science and Technology, Nilai University
No. 1, Persiaran Kolej, 71800, Nilai, Negeri Sembilan, Malaysia

[*]Corresponding e-mail: munir@utem.edu.my

Keywords: Jatropha, lubricant, oxidation

ABSTRACT – Oxidation is an undesired process in lubrication application. The application of jatropha oil as alternative lubricant base stock has emerged recently. However, the low resistance to oxidation of most natural plant seed oil has limited its application as lubricant. In this work, the oxidation of jatropha oil has been studied. The oil was oxidized by air bubbling method at 95±3°C for 72 hours in the presence of copper. The viscosity and functional group changes due to oxidation were studied before and after oxidation test. Jatropha oil was found oxidized by autoxidation mechanism to produce hydroperoxide, aldehyde and ketone which capable to increase viscosity of the oil.

1. INTRODUCTION

Natural plants seed oils have been used to lubricate parts in motion long time ago before the industrial revolution era. Today, due to environmental issues, the application of these kind oils has emerged again. Not only because it environmentally friendly but also the availability and renewability of these kind of oils.

Jatropha oil (JO) is currently considered as main source for diesel oil substitute [1]. However, jatropha oil it was also found that JO possess good lubrication properties which make it possible to consider as alternative source of lubricant [2]. It has good wear preventive characteristics either used in native oil or as additives in mineral base commercial lubricant oil.

Although application of jatropha oil as alternative lubricant has its own advantage, it also has several disadvantages that will limit its function in lubricating parts. One of the disadvantages is the resistances to oxidation. Resistance to oxidation is very important for a lubricant since it is determine the service life of the lubricant. This process is capable to initiate tribo-chemical degrading process due to the heat generated friction.

It is known that the fatty acid alkyl chain contained in most plant seed oil is susceptible to oxidation both at double bonds and adjacent allylic carbons [3]. Jatropha oil is found to has about of 29-44.2% of linoleic acid (C18:2) [4]. Thus, presence of this double carbon fatty acid is believed will influence its oxidative resistance when used as lubricant due to heat generated friction. In this study, the oxidation of jatropha oil was investigated

2. METHODOLOGY

2.1 Material

Crude jatropha oil (CJO) is used as main lubricant in this research. The oil was obtained from local market, used as sample without any treatment.

2.2 Oxidation Test

The oxidation test was carried out by air bubbling method. Jatropha oil (100 mL) was heated up to 95±3°C in a flask for 72 hours and 10±0.5 L/h air was flown into the oil. A copper strip was used a catalyst and drawn into the oil. Temperature of the oil samples and the rate of air flow were checked periodically to maintain them to be constant. Oxidative behavior of the oil samples was determined from the changes of viscosity after the test.

2.3 Viscosity

Viscosity of oil samples were measured at 40°C using capillary viscometer according to ASTM D-445-04 standard method (Test Method for Kinematic Viscosity of Transparent and Opaque Liquids (and the Calculation of Dynamic Viscosity).

2.4 Functional Group Analysis

Fourier transform infrared spectroscopy (FTIR) analysis was applied to examine functional groups of the oil sample before and after oxidized. A Shimadzu FTIR-8400S analyzer within scanning range of 600 – 4000 cm^{-1} was employed. This method has found as a very useful method to study oxidation of lubricant [5].

3. RESULTS AND DISCUSSION

In the frictional system, the frictional heat generated during process of friction could accelerate the oxidation. The oxidation process will result in the increase on oil viscosity, reduction of the oil polarity, formation of sludge and varnish, corrosion of the metal surfaces, *etc* [6]. These effects of oxidation will significantly reduce friction and wear prevention properties of the oil. Figure 1 shows the viscosity changes due to prolong heating on the jatropha oil. It can be seen that the oxidation process has increased the

CJO viscosity up to 68.2 % from the initial value (32.9 cSt) after heated for 72 hours.

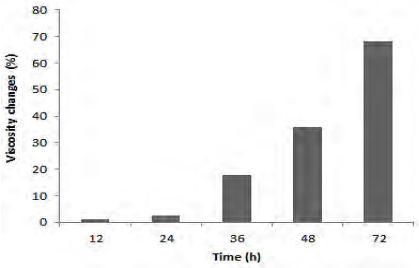

Figure 1 Effect of oxidation to jatropha oil viscosity

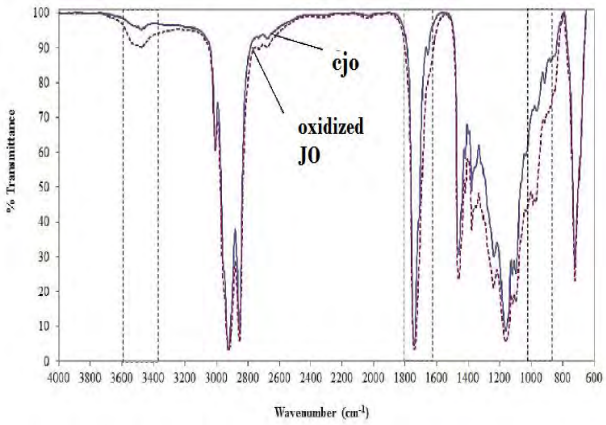

Figure 2 FTIR spectra of crude and oxidized jatropha oil

Figure 2 shows the FTIR spectra of jatropha oil oxidized by prolong heating. Most f the peaks were similar before and after the heating at except three regions. The unsaturated (double carbon) bonds contained in most vegetable oil are known prone to oxidation [6]. The oxidation of unsaturated fatty acids contained in the oil taken place by auto-catalytic (autoxidation) process which once started, the reaction is self-propagating and self-accelerating although also can be accelerated by presence of catalysts such as metal, heat and light [3]

The autoxidation of fatty acid is typically consisting of initiation, propagation, and termination process [7]. In initiation process, a-methylenic H atom is abstracted from the unsaturated molecule to form an alkyl radical which generates free radicals (RH → R• + H•). Since the free radical is highly reactive, it can react with atmospheric oxygen, thus a simple reaction resulting from the radical nature of the oxygen molecule produces a peroxy radical (R• + O_2 → ROO•). Disappearance of peaks at 1658 and 1710 cm-1 band, which typically show C=C bond vibration, is believed associated with oxidation attack to the double bond (-HC=CH-) at the unsaturated site. In the propagation reactions, the peroxy radical reacts with another unsaturated molecule (RH) to form a hydroperoxide (ROOH) and a new unstable methyl radical (R•). A spectra change was observed at the range of 3700 – 3500 cm^{-1} band which is typically associates with hydroxyl functional group. This indicates the formation of hydroperoxide in the oxidized jatropha oil (ROOH). These hydroperoxide produced are unstable and may degrade to radicals that accelerate propagation of the reactions (ROOH → RO• + •OH). As a new free radical is generated, more oxygen is incorporated into the system and the newly propagated radical then reacted with oxygen again to produce another peroxy radical (RO• + RH + O_2 → ROH + ROO• and OH• + RH + O_2 → ROO• + H_2O) . These reactions are known as branching steps of the fatty acid autoxidation process and could produce other secondary products such as aldehydes (RCHO) and ketones (RCOR) Appearance of two new spectra peaks at 990 and 970 cm^{-1} band along with disappearance of peak at 905 and 865 cm^{-1} band is related to formation of dimer carboxylic acid in the oil. The occurrence of this acid is evidently showed that the oxidation proceeds to formed aldehyde and ketone after the branching process. The aldehyde and ketone then undergo further reactions to form carboxylic acids as well as other high-molecular-weight species that thicken the oil.

4. CONCLUSIONS

Autoxidation is considered as main mechanism of jatropha oil oxidation. This process typically attack the double bond site of the jatropha oil fatty acid to produce hydroperoxide, aldehyde and ketone which increase viscosity of the oil

5. REFERENCES

[1] Achten, W.M.J., L.Verchot, Y.J. Franken, E. Mtahijs, VP. Singh, R. Aerts, and B.Muys, "Jatropha Bio-diesel production and use," *Biomass and Bioenergy,* vol. 32, pp. 1063 - 1084, 2008.

[2] Lubis, A.M.H.S., M.B. Sudin, B. Ariwahjoedi, "Investigation of Worn Surface Characteristics of Steel Influenced by Jatropha Oil as Lubricant and Eco-friendly Lubricant Substituent," Journal of Applied Science, vol. 10, pp. 1797 - 1802, 2011

[3] Scrimgeour, C., "Chemistry of Fatty Acids," in *Bailey's Industrial Oil and Fat Products*, F. Shahidi, Ed., 6th ed: John Wiley & Sons, Inc, 2005.

[4] Guebitz, G. M. , M. Mittelbach, and M. Trabi, "Exploitation of the tropical oil seed plant Jatropha curcas L.," *Bioresource Technology,* vol. 67 pp. 73-82, 1999.

[5] Vlachos, N, Y. Skopelitis, M. Psaroudaki, V. Konstantinidou, A. Chatzilazarou, E. Tegou, "Applications of Fourier transform-infrared spectroscopy to edible oils," *Analytica Chimica Acta* vol. 573-574, pp. 459-465, 2006.

[6] Crawford, J., A. Psaila, and S.T. Orszulik., "Miscellaneous additives and vegetable oil " in *Chemistry and Technology of Lubricant*, R. M. Mortier, *et al.*, Eds., 3rd ed: Springer, 2010

[7] Aguilar, G., G. Mazzamaro and M. Rasberger, "Oxidative Degradation and Stabilisation of Mineral Oil-Based Lubricants," in *Chemistry and Technology of Lubricants*, 3rd ed: Springer, 2010.

Stability of nano-oil by pH control in stationary conditions

H. Amiruddin[1,2], M.F.B. Abdollah[1,2,*], A.M. Idris[1], M.I.H.C. Abdullah[1], N. Tamaldin[1,2]

[1)] Faculty of Mechanical Engineering, Universiti Teknikal Malaysia Melaka,
Hang Tuah Jaya, 76100 Durian Tunggal, Melaka, Malaysia.
[2)] Centre for Advanced Research on Energy, Universiti Teknikal Malaysia Melaka,
Hang Tuah Jaya, 76100 Durian Tunggal, Melaka, Malaysia.

[*]Corresponding e-mail: mohdfadzli@utem.edu.my

Keywords: Stability, nano-oil, pH control

ABSTRACT - The purpose of this study is to investigate the stability of nano-oil by pH control in stationary conditions. The nano-oil was prepared by dispersing an optimal composition of 0.5 vol.% 70 nm hexagonal boron nitride (hBN) nanoparticles in SAE 15W-40 diesel engine oil by sonication technique. Hydrochloric (HCl) acid and Sodium Hydroxide (NaOH) were used as a dispersing agent to determine the stability of the dispersion. The dispersion stability was evaluated by using the sedimentation method with the help of Ultra Violet-Visible (UV-Vis) spectrophotometer. It was demonstrated that the suspension in the alkaline region with a pH value of 11 to 13 was stable over the period of 60 days.

1. INTRODUCTION

The study of nanomaterials has attracted a great interest in the recent years, due to their remarkable applications concerning several realms of science. Nanotechnology has the potential to create several fresh materials and devices with a vast range of applications, such as in medicine, electronics, biomaterials and energy production [1]. On the other hand, dealing with nanopowders is a complicated issue and a very difficult one, mainly because of their toxicity and propensity to agglomeration as a result of their high surface area. Therefore, study of the stability of nanoparticles in liquid solution is essential.

Stabilization is achieved through absorption of stabilizing molecules on the pigment surface, so that repulsive forces prevent other particles from approaching close enough for the attractive van der Waals forces to cause agglomeration. There are two principal mechanisms for the stabilization of pigmented dispersions [2]: (a) Electrostatic stabilization (b) Steric stabilization. However, this study only focuses on the electrostatic stabilization. Classic colloidal science explains electrostatic stabilization in terms of an electrical double-layer. A charge is generated on the pigment surface, and a more diffuse cloud of oppositely charged ions develops around it. As two particles approach each other the charge effectively provides a barrier to closer particle interactions. Stabilization increases along with the thickness of this layer.

Even though the stability of nanoparticles is the key issue for its application, there are limited studies on estimating the stability of a suspension. Therefore, the aim of this study is to further investigate the stability of nano-oil by pH control in stationary conditions using both qualitative and quantitative analyses.

2. METHODOLOGY

Nano-oil, used in this study, was prepared by dispersing an optimal composition of 0.5 vol.% 70 nm hBN in SAE 15W-40 diesel engine oil using ultrasonic homogenizer for 20 minutes. The optimal composition was determined from the previous work [3].

The pH of the suspension was adjusted to a desired value of 1 to 13 with the addition of dispersing agent 0.1M HCl or 0.1M NaOH. The dispersion stability was evaluated for 60 days. The stability of the dispersion was determined using the sedimentation method by observing the nanoparticles formed at the bottom of the bottle. Moreover, UV-Vis spectrophotometer measurements were used to quantitatively characterize the colloidal stability of the dispersions. The sample was hold by a glass cuvette with 1 mm thickness. At 200 – 900 nm wavelengths, the UV–Vis spectrophotometer measures the absorption of liquid and is used to analyze various dispersions in the fluid [4]. The degree of absorbance is proportional to the amount of the particles per unit volume, so that it can denote the dispersion stability of the particles in the solution.

3. RESULTS & DISCUSSION

Table 1 shows the sedimentation time during which a white layer of hBN nanoparticles is formed at the bottom of the bottle. Formation of the above mentioned layer is shown in Figure 2, where it was taken after the suspension was kept at room temperature for 2, 3, 30 and 60 days. As can be seen from Figure 2, decreasing the pH value gave rise to the reduction of stability time and hBN nanoparticles formed at the bottom of the bottle over a period of 60 days. However, at pH value of 11 to 13 (alkaline region), the nanoparticles were well dispersed in the oil.

The above qualitative analysis was supported by the absorbency of nano-oil with time using UV-Vis spectrophotometer at 600 nm wavelength, as shown in Figure 3. The absorbency should be greater if the dispersion of nanoparticles is better. After 60 days, the absorbency of nano-oil at pH values of 11 to 13 was still stable. However, below than a pH value of 9, the absorbency decreases about 60 – 80%.

Table 1 Stability time of hBN nanoparticles suspensions with different pH values

pH	1	3	5	*6	7	9	11	13
Stability [day]	2	2	2	2	2	30	60	60

*The pH value of suspension without dispersing agent

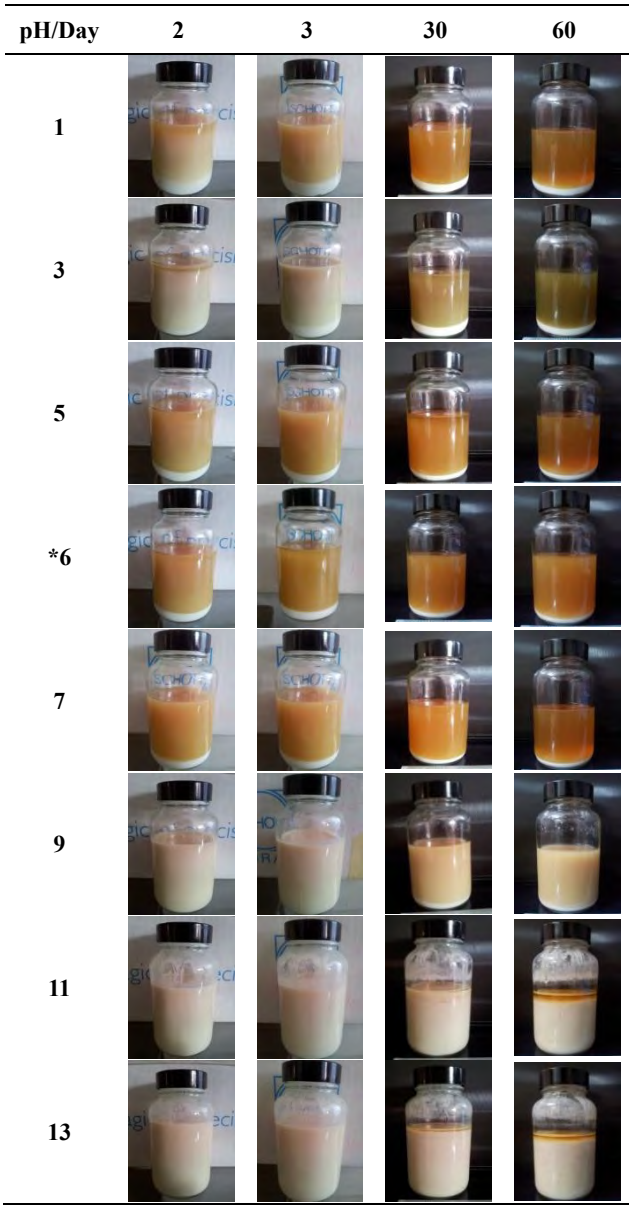

*The pH value of suspension without dispersing agent

Figure 1 Photo of formation of hBN nanoparticles layer over time in different pH values

The higher absorption of UV radiations in suspension stabilized by NaOH, confirmed the higher efficiency of electrostatic repulsive force. This behavior is attributed to the fact that the absorbed ions in electrostatic mechanism form a charged layer around the particles preventing aggregation. Adsorption of OH- ion (in the alkaline region) on the particles surface increases the repulsive force and results in the lengthening of the distance between particles or increases the thickness of the electrical double-layer, which causes an electrostatic stability.

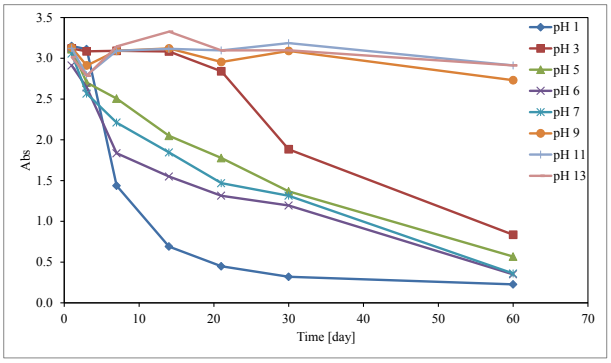

Figure 2 UV-Vis absorption of nano-oil in different pH values (wavelength = 600 nm)

4. CONCLUSIONS

In conclusion, the stability of the hBN nanoparticles in SAE 15W-40 diesel engine oil increases in the alkaline region with pH value of 11 – 13. The suspension was stable over the period of 60 days, as compared with the suspension in the acidic region. This is due to the electrostatic mechanism, which increases the repulsive force and results in thicken the electrical double-layer that provides stability.

5. ACKNOWLEDGEMENTS

The authors also gratefully acknowledge contributions from the members of the Green Tribology and Engine Performance (G-TriboE) research group. This research was supported by grants from the World Academy of Sciences (TWAS) [grant number: GLUAR/2013/FKM(2)/A00003], Ministry of Education Malaysia [grant number: FRGS/2013/FKM/TK01/02/1/F00163], and Universiti Teknikal Malaysia Melaka (UTeM) [grants number: PJP/2012/FKM(40A)/S01044 and PJP/2012/FKM(11A)/S01086].

6. REFERENCES

[1] C. Buzea, I. I. Pacheco, and K. Robbie, "Nanomaterials and nanoparticles: sources and toxicity.," *Biointerphases*, vol. 2, pp. 17–172, 2007.

[2] "Dispersing process." [Online]. Available: http://www.inkline.gr/inkjet/newtech/tech/dispersion/. [Accessed: 01-Jan-2015].

[3] M. I. H. C. Abdullah, M. F. B. Abdollah, H. Amiruddin, N. Tamaldin, and N. R. M. Nuri, "Optimization of Tribological Performance of hBN/AL_2O_3 Nanoparticles as Engine Oil Additives," *Procedia Eng.*, vol. 68, pp. 313–319, 2013.

[4] K. Lee, Y. Hwang, S. Cheong, L. Kwon, S. Kim, and J. Lee, "Performance evaluation of nano-lubricants of fullerene nanoparticles in refrigeration mineral oil," *Curr. Appl. Phys.*, vol. 9, no. 2, pp. 128–131, 2009.

Modeling for assessing the dynamic performance of pneumatic valve

N.S. Osman[1,*], A.Y. Bani Hashim[1]

[1, 2]Faculty of Manufacturing Engineering, Universiti Teknikal Malaysia Melaka,
Hang Tuah Jaya, 76100 Durian Tunggal, Melaka, Malaysia.

*Corresponding e-mail: norsuriyanti.osman@gmail.com

Keywords: Pneumatic valve; control system; MATLAB

ABSTRACT – The fundamental control system for an electro-pneumatic valve is explained where this work discusses of the mathematical model and MATLAB program used in controlling system of pneumatic valve. This paper presents an approach to assessment of the dynamics performance of pneumatic valves.

1. INTRODUCTION

Pneumatic is one of preferred power source in industries due to it is simple, cheap, easy to handle and maintenance and has a high degree of controllability. Within the pneumatic system, valve plays a significant rolein controlling fluid flow into different paths from one or more sources. In getting a good results in pneumatic system operation, users need to monitor and control the valve operating condition. Therefore, this requires the development of suitable control techniques in order to deal with nonlinearities that are common in valve[1].

2. BACKGROUND

Pneumatic valve commonly consists of a body with ports that are connected to internal flow passages by spools inside a cylinder. It is can be controlled either mechanically or electrically controlled. The movement of the spool restricts the flow of fluid. Thus the valve controls the fluid flow. Anothertypical application of this valve is to control the rate of air flow under a given set of pressure condition[2]. The pneumatic valve works when it is actuated either by actuator, followed by movement of spool or end with emission of gaseous.

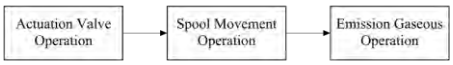

Figure 1 Main working principle of pneumatic valve

3. BASIC CONTROL SYSTEM

The basic mathematical model and control block diagrams will be utilized in modeling control system of pneumatic valve.

3.1 Mathematical Models

Mathematical models relating the various physical parameters may predict and improve the performance of the valve. This paper focuses on electro-pneumatic valve and the mathematical model involved can be separated into three major distinct parts, which are magnetic circuit, mechanical subsystem and air flow path (see Figure 2).

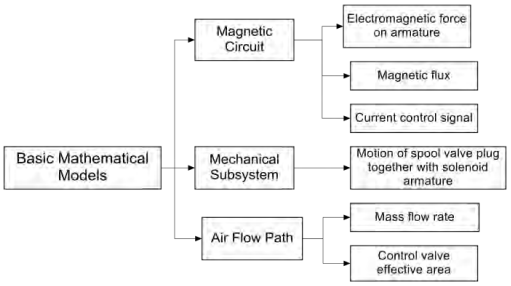

Figure 2 Basic mathematical model

3.1.1 Magnetic Circuit

In general, the mathematical model of the magnetic circuit can be concentrated to the electromagnetic force, magnetic flux and air gap[3]. Below are the mathematical model for the magnetic circuit.

a) Electromagnetic force on the armature

$$FM = \frac{B^2.A_\delta}{2.\mu_A} \quad (1)$$

where

B = the magnetic flux density
A_δ = the cross-sectional area of the air gap
μ_A = the magnetic permeability of air

b) Magnetic flux

$$B = \frac{\emptyset}{A_\delta} \; ; \; \emptyset = \frac{\mu_A.A_\delta.I.\eta_C}{L_M} \quad (2)$$

where

Φ = magnetic flux
A_δ = the cross-sectional area in the air gap
μ_A = the magnetic permeability of air
I = the current of the control signal
n_C = the number of turns in the solenoid coil
L_M = the magnetic circuit length

c) Current control signal

$$FM = \frac{\delta F}{\delta I}.(I - I_I) + \frac{\delta F}{\delta y}\, y \quad (3)$$

where

$\partial F/\partial I$ = the electromagnetic stiffness by a control signal current
$\partial F/\partial y$ = the electromagnetic stiffness by an armature movement
I = the current of the control signal
I_1 = the value of the control signal current when the valve armature begins to move
y = the stroke of the armature

3.1.2 Mechanical Subsystem

The mathematical model of mechanical subsystem can be concentrated on the motion of the valve plug together with solenoid armature.

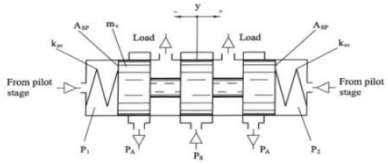

Figure 3 Spool valve schematic diagram (source: [3])

a) Motion of the valve plug together with solenoid armature[3]

$$m_V.\ddot{y} + b_{vv}.\dot{y} + k_{sv}.(y_0 + y) + F_{VF} = (P_1 - P_2).A_{VE} + F_M \quad (4)$$

where

A_{VE} = valve effective area
(P1 – P2) = differential pressure across the plug
m_V = the armature and plug assembly mass
b_{VV}= the viscous friction coefficient
k_{SV} = the valve spring constant
y_0 = the valve spring compression in the valve closed position
y = the valve plug displacement
F_{VF} = the coulomb friction force
A_{VE} = the valve plug effective area
F_M = the solenoid electromagnetic force

3.1.3 Valve Flow Ability

The most important parameters of control valves are their flow ability and control valve effective area[3].

a) Mass flow rate (flow capacity)

$$G = A_V.\beta.P_{in}.\sqrt{\frac{2.k}{R.T_{in}.(k-1)}}.\varphi(\sigma) \quad (5)$$

where

A_V = valve area
β = the degree to which the control valve is open
T_{in} = Test medium air temperature
k = constant
σ = critical value
P_{in} = the upstream pressure

b) Control valve effective area

$$A_V = \frac{G}{\beta.P_{in}.\varphi(\sigma)}.\sqrt{\frac{R.T_{in}.(k-1)}{2.k}} \quad (6)$$

$G = Q_n \times \rho_{an}$,

where

ρ_{an} = the density of air under standard conditions
T_{in} = Test medium air temperature
k = constant
β = the degree to which the control valve is open

3.2 Control System Block Diagrams

The control diagram below represents free body diagram and block diagram of pneumatic valve.

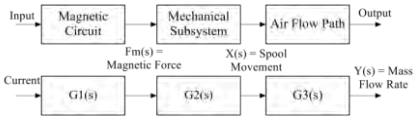

Figure 4 Control diagram of electro-pneumatic valve

4. METHODS

Figure 5 depicts the process flow for identifying result in this project. Begin with identification of the DCV basics. Next, modeling the control system of DCV. Lastly, evaluate response of DCV control system.

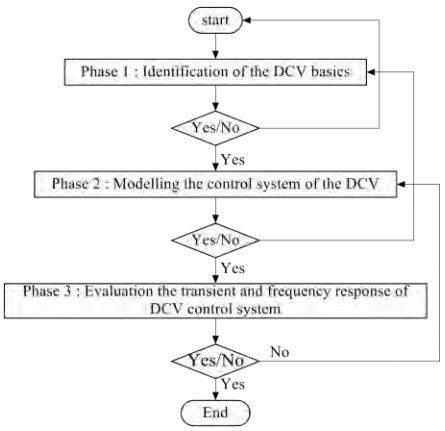

Figure 5 Project process flow

Dynamic performances of electro-pneumatic valve are illustrated below. Graph A represents mechanical part and graph B represents electrical part while graph C represents the air flow rate part.

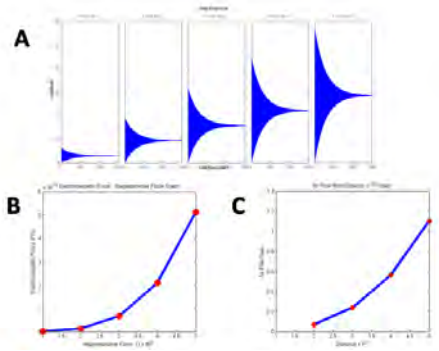

Figure 6 Dynamic performance of electro-pneumatic valve

5. SUMMARY

Mathematical model control system of pneumatic control valve has been identified. To account the control system, we have to analyze the underlying mathematical model with respect to the selected valve. Examining the control system through the mathematical models is the most efficient method whereby this work suggests it is possible to analyze and evaluate the dynamic performance of an electro-pneumatic valve.

6. REFERENCES

[1] S. R. Majumdar, *Pneumatic Systems: Principles and Maintenance*. Tata McGraw-Hill Education, 1996, p. 282.

[2] Lansky, *Industrial Pneumatic Control*. CRC Press, 1986, p. 264.

[3] I. L. Krivts and G. V. Krejnin, *Pneumatic Actuating Systems for Automatic Equipment: Structure and Design*. Taylor & Francis, 2006, p. 368.

Precision control performances of a vertical motion electrostatic actuator stage with locking function

M.M. Ghazaly[1,*], Y.P. Chin[1], K. Sato[2]

[1)] Center for Robotic and Industrial Automation (CeRIA),Faculty of Electrical Engineering, Universiti Teknikal Malaysia Melaka, Hang Tuah Jaya, 76100 Durian Tunggal, Melaka, Malaysia
[2)] Interdisciplinary Graduate School of Science and Engineering, Tokyo Institute of Technology, 4259-G2-17 Nagatsuta Midori-ku, Yokohama 226-8502, Japan

[*]Corresponding e-mail: mariam@utem.edu.my

Keywords: Multilayer electrostatic actuator; locking function; vertical motion stage.

ABSTRACT – The paper validates the effectiveness of the characteristic switching for a vertical motion electrostatic actuator stage with a holding function. The friction forces often deteriorate the response and positioning accuracy of a control system, especially when the lightweight electrode layers in the electrostatic actuator are supported by only lubricating oil. However, the contact condition between the electrodes can be changed by the attractive forces resulting from the driving signal waveforms. In this paper, the driving signal waveforms for switching between two frictional conditions are examined and clarified. The actuator exhibits a positioning error of less than 14 nm.

1. INTRODUCTION

In microscope systems, optical systems and semiconductor manufacturing systems [1]; high response and high positioning accuracy are critical. In microscope systems, samples need to be finely positioned and precisely held in vertical stages for precision motion. Additionally, in micro electric discharge machining large thrust capability and high positioning and tracking accuracy is desired with use of a clamping mechanism with force magnifying structure as a locking function [2].

As a resolution, an electrostatic actuator supported by only lubricating oil has been proposed in this paper that has a locking function without any additional mechanism. The electrode layers of the actuator are lightweight enough to maintain the gap and reduce the frictional force between the layers without applying voltage. In the actuator, the motion characteristics depend on the driving signal since the frictional force is changed by the driving signal. The frictional force exhibited by the electrostatic actuator is used to continuously generate the holding force, which acts as a locking mechanism. The driving signal waveforms for adjusting two types of frictional force have been proposed; i.e. (a) high friction force for the limited working range motion with a large holding force and (b) low friction force for full working motion. Therefore, in this paper, the usefulness of the electrostatic actuator supported by lubricating liquids with a locking function is demonstrated using a vertical motion stage which uniquely contributes to the research originality.

2. VERTICAL MOTION STAGE STRUCTURE

The electrostatic actuator presented in this paper is a variable-capacitance motor type actuator that has two mover layers. Figure 1 shows the structure of the experimental two-layer electrostatic actuator in the vertical stage. To realize bidirectional motion, voltages V_1 and V_2 are applied to Stator A and Stator B, whilst voltage V_3 is set to zero and applied to the mover shown in Figure 2. Stator B is set to be shifted by 500um to Stator A. Table 1 shows the detail specifications of the electrostatic actuator.

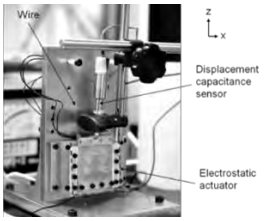

Figure 1 Overall view of the displacement measurement setup in vertical stage.

Table 1 Specifications of the electrostatic actuator.

Parameters	Value
Electrode width and length (mm)	50 × 50
Spacer (mm)	50 × 6.5
Electrode thickness (mm)	0.1
Spacer thickness (mm)	0.4
Mover mass (g)	5.43

In comparison to the horizontal stage [3], the stator is aligned and screwed parallel to the z- axis and spacers are inserted between the stator electrode layers to maintain the gap at each side. Extra film at each side of the laminated stator electrodes is used for fixing the electrode layers of the stator to the base in order to prevent the thin electrodes from bending. The electrodes are laminated with 30μm thickness low density polyethylene flat films as isolation films to reduce the friction between the electrode layers. The lubricating liquid is expected to easily be maintained between the electrode layers using high wettability film in the vertical setup. The nominal silicone oil thickness inserted in the gap is 0.123mm. Figure 2 shows the driving procedures.

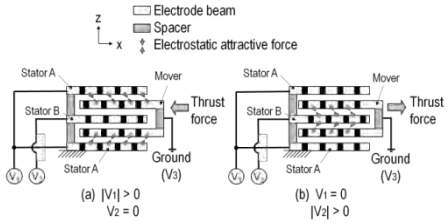

Figure 2 Driving procedures for the bi-directional motion of the electrostatic actuator [3].

3. CONTROL PERFORMANCES WITH LOCKING FUNCTION

In the vertical motion stage, the attractive forces resulting from the driving signal greatly influence the contact condition between the electrode layers (i.e., the frictional effect). The attractive force between the electrode layers causes the mechanical contact which increases the frictional force between them. Although the frictional force deteriorates the positioning characteristics, it is useful as a locking function in the actuator. In order to utilize the characteristics, two driving modes has been proposed and the driving signal profiles for adjusting the frictional effect have been discussed; i.e. (a) fine driving mode for the fine motion with a large holding force and (b) wide driving mode for wide and fast motion. Figure 3 shows the reciprocating motion using applied voltage 1.5kV and the control period, T_{cs}=0.5 ms with the 1kV holding signal.

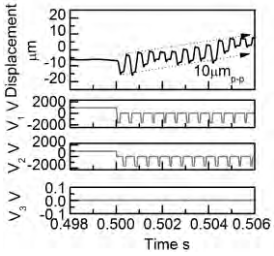

Figure 3 Reciprocating motion characteristics with negative monopulse signal, 1.5kV & 1kV holding signal.

The negative monopulse signal with a duty cycle of 1/5 is used to avoid an increase in the frictional effect and also to ensure the full working range of the actuator. In this paper, the full working range is referred to as the wide working range. The signal is used as the wide driving mode signal to ensure the full working range of the actuator. In order to demonstrate the effectiveness of the electrostatic actuator, the control performances are evaluated. In the vertical setup, gravity will affect motion of the actuator. To maintain the mover position with precision at the desired position, the holding function is vital for that purpose especially during the performance evaluation in the wide motion range. The combination of the wide driving mode and the fine driving mode which is referred to as the dual driving mode is used. The control system was designed based on a PID controller shown in Figure 4. The effect of mass changes on control performances are evaluated as shown in Figure 5.

The vertical motion stage is influenced by the gravity through the movable mass. To evaluate the effect of mass changes, the extra mass of 1.00 g, 2.05 g and 3.12 g is added to the mover. From Figure 5, it can be depicted that the dual driving mode is able to hold the mover with a residual vibration less than 14nm when the mass of the mover increases by 57%. The increased in the mass will increase the positioning time of the actuator; however the mover is still able to be held with precision.

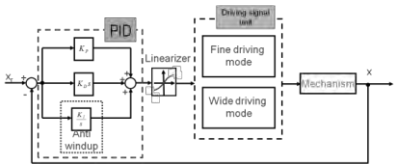

Figure 4 Block diagram of the control system for the dual driving mode

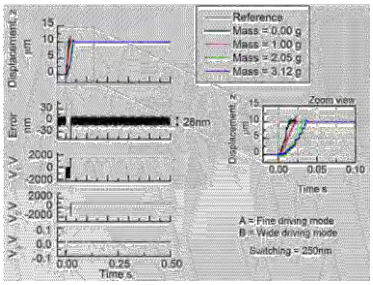

Figure 5 Effect to mass changes using a 10 μm step input under the dual driving mode with 1kV holding signal.

4. CONCLUSIONS

In summary, this paper validates the effectiveness of the holding function for a vertical stage electrostatic actuator maintained by lubricating liquid, which are the main contributions of this paper. In the vertical motion stage, the holding function is crucial for maintaining precise motion due to the influence of gravity.

5. ACKNOWLEDGEMENT

This research and publication is supported by Universiti Teknikal Malaysia Melaka (UTeM) Short Term Grant no. PJP/2013/FKE(4C)/S01170 and Tokyo Institute of Technology, Japan. Authors are grateful to Tokyo Tech. and UTeM for supporting the research.

6. REFERENCES

[1] Y. Ando, "Development of three-dimensional electrostatic stages for scanning probe microscope", *Sensors and Actuators A,* vol. 114, pp. 285–291, 2004.

[2] T. Mineta, N. Kida, S. Nomura, E. Makino, "Pulsation sensor integrated with micro vascular holding actuator for thrombosis monitoring", *Sensors and Actuators A*, vol. 143, pp. 14-19, 2008.

[3] Mariam MG, Sato K., "Characteristic switching of a multilayer thin electrostatic actuator by a driving signal for an ultra-precision motion stage", *Precision Engineering* vol. 37, pp. 107-116, 2013.

Force tracking control of MR damper and controller parameter optimization using sensitivity analysis method

M.F. Md Isa[1], M.H. Harun[1,2], M.A. Abdullah[1,2,*], N.S. Muhammad[1,2]

[1)] Faculty of Mechanical Engineering, UniversitiTeknikal Malaysia Melaka, Hang Tuah Jaya, 76100 Durian Tunggal, Melaka, Malaysia.
[2)] Centre for Advanced Research on Energy, UniversitiTeknikal Malaysia Melaka, Hang Tuah Jaya, 76100 Durian Tunggal, Melaka, Malaysia.

[*]Corresponding e-mail: mohdazman@utem.edu.my

Keywords: magnetorheological damper; inner loop controller; optimization; sensitivity analysis

ABSTRACT - The objective of this paper is to optimize the control parameters of Magnetorheological (MR) damper under harmonic motion. The MR damper is modeled using parametric approach and Bouc-Wen model is chosen to represent MR damper model. Next, a control strategies using continuous state feedback controller is used to track the desired and actual force through B and G parameter. An optimization tool (sensitivity analysis) is used to determine the selection of controller parameter. Lastly force tracking control used to evaluate the performance of control strategies.

1. INTRODUCTION

Magnetorheological (MR) fluid is smart materials that change its behavior due to responds from the applied magnetic field [1]. The ability to change its state reversibly from viscous liquid to semi solid in milliseconds when exposed to magnetic field make it more flexible [2]. Since MR damper can reversibly change its state, therefore MR play an important role in semi-active damper as control device [3][4]. However magnetic field applied need to be suitable with the application. Thus a control parameters need to be design for the system in order to control state of MR fluid inside the MR application as previous study [5][6].

2. METHODOLOGY

In this study, a MR damper (RD-8040-1) manufactured by Lord Corporation has been used in the experiment. The experimental work is conducted to study the characteristic of the MR damper on 5 Hz cranked oscillation motion with stroke 0.05 m. The experiment data collected based six current input levels as 0, 0.2, 0.4, 0.6, 0.8 and 1.0 Ampere. There are several characteristic of MR damper in the experiment such as the relation of damper force against velocity of the movement.

The experimental setup in Figure 1 shows the communication of instrument in the experiment. In the experimental setup, the experiment is used in studying the characteristic of MR damper and power by the propulsion system.

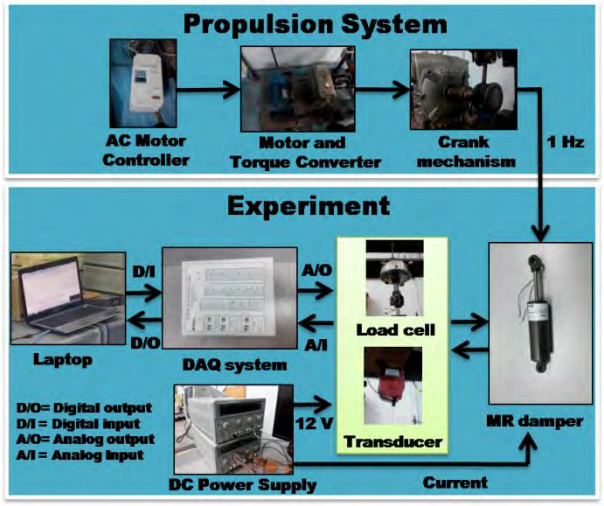

Figure 1 Experimental setup

By using parametric approach, the MR damper model is developed based on Bouc-Wen model [7]. Then, a control strategy is designed by using continuous state feedback controller and the controller parameter is optimized using sensitivity analysis. Lastly, a force tracking control with a different input signal is conducted to evaluate the performance of the controller parameter.

3. RESULTS AND DISCUSSION

From the experimental data, the relation of force and velocity is studied for each current 0, 0.2, 0.4, 0.6, 0.8 and 1.0 Ampere as shown in Figure 2. Figure 2 shows the damper force is increase as the current applied to the magnetic coil damper increase. The maximum and minimum of damper force is 948N and 81N. The MR damper acts as passive damper when there is no magnetic field on the magnetic coil. As the magnetic field increase inside the MR damper, the MR fluids change its state from liquid to semi solid state and make it harder to move the particle of MR fluid inside the MR damper.

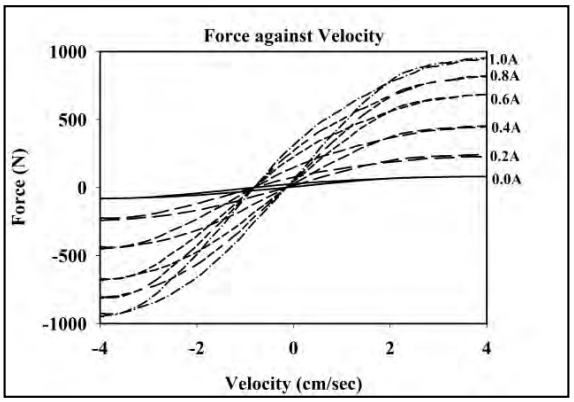

Figure 2 Force against velocity from the experimental data

From the sensitivity analysis in Figure 3 the optimal solution for parameter B and G controller is 0.001026 and 0.027. This is because of the RMS value is the lowest when B and G is 0.001026 and 0.027.

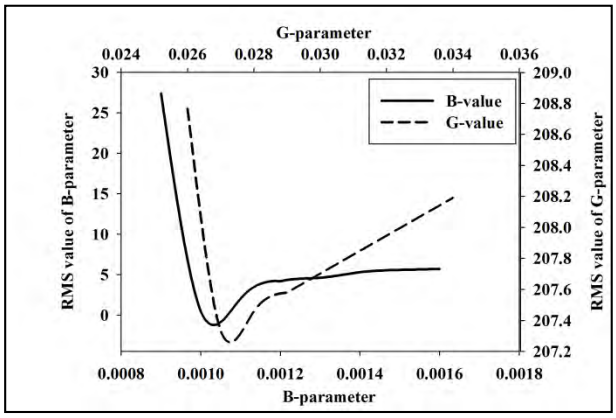

Figure 3 Control parameter of inner loop control system

Figure 4 shows the proposed MR damper model is able to tracking the desired force and produced an actual force by given saw tooth, square and sine input signals.

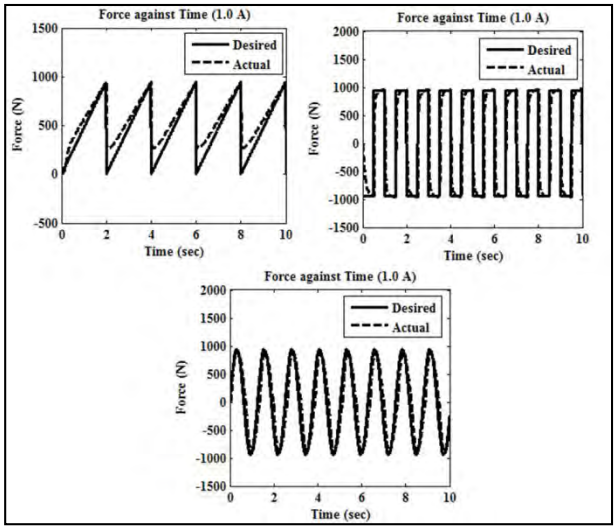

Figure 4 Force tracking control

4. CONCLUSIONS

In conclusion, an experimental work to find the characteristic of MR damper has been conducted in the laboratory. The MR damper model has been developed using a Bouc-Wen model. The tracking ability of the proposed model and control strategy has been investigated in simulation work. The sensitivity analysis method is used to find an optimum value of the MR damper controller. Through this study, it shows the MR damper model is able to track the desired force.

5. ACKNOWLEDGEMENT

The authors gratefully acknowledged the Advanced Vehicle Technology (AcTiVe) research group of Centre for Advanced Research on Energy (CARe), the financial support from Universiti Teknikal Malaysia Melaka and The ministry of Education, Malaysia under Short Term Research Grant, Grant no. PJP/2014/FKM(10A)/S01330 and Fundamental Research Grant Scheme (FRGS), grant no.: FRGS/2013/FKM/TK06/02/2/F00165.

6. REFERENCES

[1] J.D. Carlson and B.F. Spencer, "Magnetro-rheological fluid dampers for semi-active seismic control", Proceedings of the Third International Conference on Motion and Vibration Control, Chiba, Japan, Vol. 3, 1996, pp. 35-40.

[2] T. Katsuda, N. Hiraiwa, S.H. Doi and E. Yasuda, "Improvement of ride comfort by continuously controlled damper", SAE 920276, Vo1.1 01(6), 1992, pp. 356-363

[3] B.F. Spencer Jr. et. al, "Phenomenological model of magnetorheological damper", Journal of Engineering Mechanics, ASCE. Vol. 3, pp. 230-238, 1997.

[4] A.Z. Zainordin, M.A. Abdullah and K. Hudha, "Modelling and validation of Magnetorheological brake responses using parametric approach", IOP Conferences Series: Materials Science and Engineering, Vol.50, No.1, doi:10.1088/1757-899X/50/1/012038, 2013.

[5] M.A. Abdullah, A.Z. Zainordin and K. Hudha, "Validation and experimental evaluations of magnetorheological brake-by wire system", Journal of Engineering and Technology (JET), Penerbit Universiti, Universiti Teknikal Malaysia Melaka Vol. 4, No. 1, January-June 2013, pp. 109-122, ISSN 2180-3811, 2013.

[6] A.Z. Zainordin, M.A. Abdullah and K. Hudha, "Experimental Evaluations on Braking Response of Magnetorheological Brake", Journal of Mining, Metallurgy & Mechanical Engineering (IJMMME) Vol.1, Issue 3, pp.75-77, ISSN 2320-4052 (Online), EISSN 2320-4060, 2013.

[7] S. Talahari et.al, "Parameter Identification of Bouc-Wen model for MR fluid dampers using adaptive charged system search optimization", Journal of Mechanical Science and Technology. Vol. 26, Issue 8, pp. 2523-2534. doi: 10.1007/s12206-012-0625-y, 2012.

Comparative study for material removal rate, surface finish and electrode wear rate on die sinking EDM

H.H. El Grour[1], S. Maidin[1,*]

[1)] Faculty of Manufacturing Engineering, Universiti Teknikal Malaysia Melaka, Hang Tuah Jaya, 76100 Durian Tunggal, Melaka, Malaysia.

[*]Corresponding e-mail: shajahan@utem.edu.my

Keywords: Electrical discharge machining; material removal rate; tool wear rate

ABSTRACT - The electrical discharge machining (EDM) is one of non-conventional machining process where the erosion of the work piece take place based on the thermal energy between the electrode and the work piece. Two different work piece materials (copper and aluminum) was machined using die sinking EDM to study the characteristics of each material using copper electrode. The experiments conducted under the designed full factorial procedure where pulse on-time and pulse current are used as the input parameters. It was found that material removal rate (MRR) increases with increase in current and pulse duration, but MRR is higher during machining of aluminum than that of copper. In term of tool wear rate (TWR) it is found that the TWR resulting of machining copper is lower than aluminum.

1. INTRODUCTION

In case of requiring close tolerance, high precision and surface quality, EDM is one of the best processes that can be used to obtain the desired shape [1]. The erosion of the work piece take place due to thermal energy generated between the work piece and electrode. Both electrode and work piece are immersed in dielectric fluid (ionized water or kerosene usually used). When the high voltage is applied (300 v) in modulated pulses, this cause the free electrons of the tool be subjected to high force which in turn emitting the electrons. These electrons then accelerated toward the work piece via the dielectric fluid. As they are moving quickly from tool to work piece collision with dielectric molecules takes place. Because of this reaction between the free electrons and the molecules more positive ions and electrons will be generated due to the collision. These actions reoccurring again and again till the plasma channel where the temperature approximately 8000 to 10,0000C and because of the very low electrical conductivity that the plasma has, this makes the electrons move from the tool to the work piece whereas the ions move from the work piece to the tool [2]. The material removed from work piece due to the collision of electrode which is known as Material Removal Rate (MRR) which is desired whereas material removed from electrode due to the collision of ions this is known as Tool Wear Rate (TWR) [3].

2. EXPERIMENTAL DETAILS

In this experiment, copper electrode was used to machine aluminum and copper. The properties of those two materials are shown in Table 1. Sodick CNC EDM die sinking was used to machine 100x50x6mm work piece of copper and aluminum. 16 mm a radian and 75.20 high of copper electrode was used to conduct engraves. Pulse current and pulse on time are changed from time to time while keeping other factors such as pulse off time and voltage are constants. The values of these parameters are given in Table 2. In this study, direct polarity was used In order to achieve higher material removal rate and less tool wear rate [4].

Table 1 Properties of Aluminum and Copper work material

Material	Thermal conductivity (W/mk)	Melting point (^oC)	Density (gm. /cm^3)
Aluminum	173	580	2.70
Copper	401	1083	8.92

Table 2 Die sinking EDM conditions

Dielectric fluid	Kerosene
Reference voltage	22
Pulse current (A)	8,12,16 and 20
Polarity	direct polarity
Pulse on time (μs)	50, 100, 150 and 200
Pulse off time (μs)	50

3. RESULTS AND DISCUSSION

Two factors and four levels were used to compare the response values of MRR and TWR.

3.1 Material Removal Rate

The work pieces were weighted before and after machining to calculate the material removed from both aluminum and copper work piece see Equation 1.

$$MRR = (M1 - M2) / T \quad (1)$$

Where M1 and M2 are the weight of workpiece before and after machining (g), respectively. T is the machining time (min). From Fig.1 it is clear that the MRR increased with the increase of pulse currents for both

work when 50 µs is applied. It also shows that MRR is higher when aluminum is machined compared with copper this is due to the fact that aluminum melting point is lower than copper. When the melting point of the work piece is lower than the other this means for the same energy or current applied, more material will be eroded and the machining time will be lower [5].

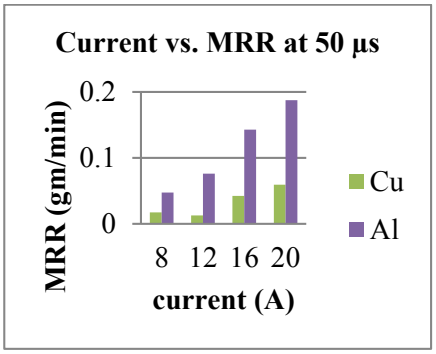

Figure 1 Current vs. MRR at 50 µs

3.2 Wear Rate

Tool wear ratio can be calculated using the Equation 2.

$$EWR\ (\%) = [EWW/WRW] \times 100 \quad (2)$$

Where EWW = Electrode Wear Weight and WRW = Work Piece Removal Weight

It is noticed that machining copper using copper electrode has less TWR value compared to machining aluminum as shown from Fig.2 , this is becuase copper has higher value of thermal conductivity where the heat energy will be diffused easily. In case of using aluminum which has lower thermal conductivity compared with copper, the electrode showed more wear where the thermal energy cannot be diffused easily resulting in higher wear ratio.

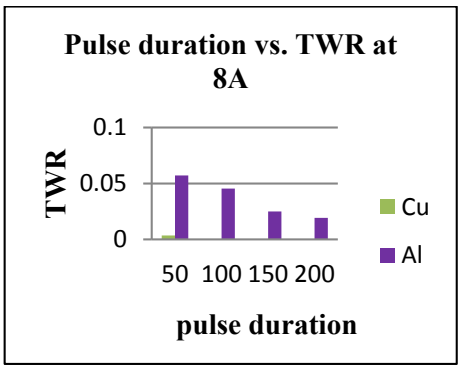

Figure 2 Pulse Duration Vs. TWR At 8A

4. SUMMARY

From the above analysis the following summary can be made:

i. MRR increases with the increase of current. MRR of aluminum is higher than that of copper due to less melting point of aluminum than copper
ii. Pulse duration has a little effect on the MRR
iii. TWR decreases with the increase of pulse duration due to the presence of carbon layer that precipitated on the surface of the electrode and the thickness of this layer increased with the increase of pulse duration and in turn decrease the TWR.
iv. Copper has little TWR when machined using copper electrode, this is because copper has higher thermal conductivity compared to aluminum.

5. REFERENCES

[1] A. Pandey and S. Singh: Current Research Trends in Variants of Electrical Discharge Machining, *International Journal Of Engineering Science And Technology*, 2(6), 2172-2191, 2010

[2] A. Moarrefzadeh and Mahshahr : Study of Work Piece Thermal Profile in Electrical Discharge Machining process, *WSEAS Transaction On Applied And Theoretical Mechanics*, 7(2), 83-92, 2012

[3] A.A. Khan, Electrode Wear And Material Removal Rate During EDM Of Aluminum And Mild Steel Using Copper And Brass Electrodes. *International Journal of Advanced Manufacturing Technology*, vol. 39, p. 482-487, 2008

[4] D.A. Khan: Effect Of Tool Polarity On The Machining Characteristics In Electrical Discharge Machining Of Silver Steel And Statistical Of The Process. *International Journal of Engineering Science and Technology* (IJEST): 3(6), 5001-5010, 2011

[5] A. A. Khan and S. E. Saifuddin, Wear characteristics of copper and Aluminum electrodes during EDM of stainless steel and carbide, *ICME2005*, Dhaka, Bangladesh, 28-30,2005.

Kinematic synthesis of planar, shape-changing rigid body mechanisms for slat design profile

M.H. Ismail[1,2,*], S.A. Shamsudin[1],[2], M.N. Sudin[1,2]

[1)] Faculty of Mechanical Engineering, Universiti Teknikal Malaysia Melaka, Hang Tuah Jaya, 76100 Durian Tunggal, Melaka, Malaysia.
[2)] Centre for Advanced Research on Energy, Universiti Teknikal Malaysia Melaka, Hang Tuah Jaya, 76100 Durian Tunggal, Melaka, Malaysia.

[*]Corresponding e-mail: mohammadhazrin858@gmail.com

Keywords: Kinematic synthesis; shape-changing mechanisms; geometric constraint programming

ABSTRACT – This paper presents a kinematic procedure to synthesize planar mechanisms that are capable of approximating a shape change defined by a set of morphed slat design profiles. This work applies a chain of rigid bodies connected by revolute and prismatic joints that can approximate a general set of design profiles that have significant differences in arc length. To achieve a single degree of freedom (DOF), a building-block approach is employed to mechanize the fixed-end shape-changing chain with the helped of Geometric Constraint Programming technique as an effective method to develop the mechanism.

1. INTRODUCTION

Some mechanical systems function by their capacity to vary between specific shapes in a controlled fashion. Consider the advantages of an aircraft wing that can change between different profiles for loiter versus attack modes. The US military constantly search for exotic technologies that will enable aircraft wings to actively change shapes to achieve a wider range of aerodynamic performance and flight control not currently achievable by traditional wing technology [1].

An alternative to the above technologies is shape-changing rigid-body mechanisms with the advantage of lower cost, greater displacements and higher load carrying capabilities. Additionally, rigid-body linkages have a well-established set of mechanical design principles. The concept has been applied to open design profiles [2,3] and closed design profiles [4].

A new shape-changing slat design is proposed where the profiles are considered to move from loiter to attack modes. The synthesis process is started with a segmentation phase that creates segments, which are optimized in shape and length so that they approximate corresponding portions on each desired profile. To complete the synthesis, a mechanization phase applies building-block approach to a selected segment and adds binary or ternary link in order to achieve a lower degree-of-freedom (DOF) linkage. If possible, a 1-DOF system is preferred for simplicity in control.

2. TARGET PROFILES

The design profiles may be defined by any number of points spaced at various intervals, producing a wide range of c_{j_i}. To proceed with kinematic synthesis, the design profiles are converted to target profiles that have common features. It is important for the target profiles to have common features so comparisons can be made and a chain of rigid-bodies can be formed that when repositioned will approximate all design profiles. In earlier work [3], the design profiles were assumed to be of roughly equal arc lengths, $C_1 \approx C_2 \approx ..... \approx C_p$. In that case, the design profiles could be converted to target profiles that all have the same number of defining points n distributed equally along the design profile so that each segment has roughly the same length, $c_{1_1} \approx c_{1_2} \approx .....c_{1_n} \approx c_{p_n}$.

3. SEGMENTATION

Prismatic joints are introduced among the rigid-bodies to approximate the target profiles in order to change between shapes of different lengths using rigid-bodies. Shamsudin and his colleague [5] show a method in preparing the target profiles to convert into prismatic joint(s). The curvature of target profiles is calculated to identify regions where prismatic joint(s) can be implemented and a scheme is adopted to inspect the target profiles for regions of similar curvature that can be candidate for locating the prismatic joints.

A complete segmentation of shape-changing slat where the revolute and prismatic joints are implemented on the segment is shown in Figure 1. In this design, the prismatic joints are applied into Segment 1 through Segment 3 and Segment 5 with Segment 6.

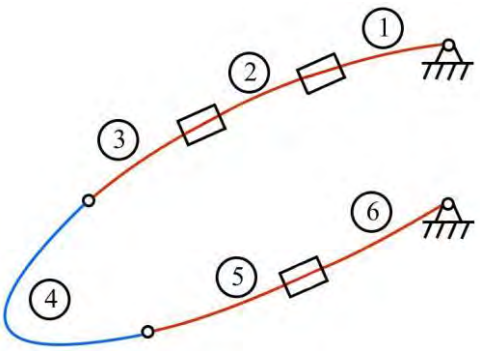

Figure 1 Segmentation of the shape-changing slat that consists of revolute and prismatic joints.

4. MECHANIZATION

Once a set of rigid-body segments has been generated through the segmentation process, these segments are accordingly joined together to form a linkage as the prismatic joints are used to join in between prismatic links while the remainder links are joined together at the end points with the revolute joints. In order to achieve 1-DOF for mechanism with prismatic joint, the application of building-block approach [6] is needed for mechanization stage as it is widely accepted for analysis [7,8] and synthesis [9,10] of planar mechanism. The rigid segments are constructed in the sketching mode of a parametric design software package, and Geometric Constraint Programming (GCP) [11] techniques are employed.

4.1 Mechanism

The development of mechanism of shape-changing slat is based on precision position synthesis. In this approach, the linkage is designed such that the coupler passes through three prescribed positions. Figure 2 represents the movement of slat mechanism in three prescribed positions where the slat deployed from cruise through landing position. Position 1 represents the slat is on cruise state, Position 2 refers to takeoff state while landing state when the slat at Position 3. As the input force is applied, the slat moved to Position 2 as ternary link is rotated at the angle of a. Position 3 is achieved when ternary link is rotated until the angle reached at the angle of b.

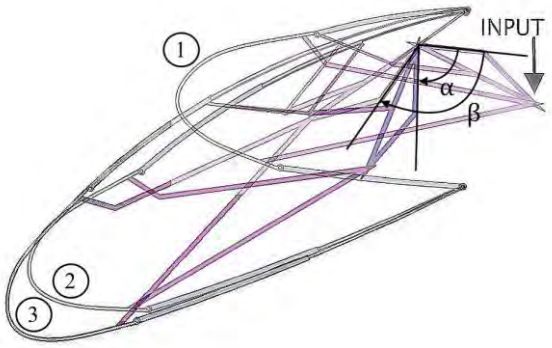

Figure 2 The slat is deployed according to three prescribed positions; Position 1 at cruise state; Position 2 at takeoff state; and Position 3 at landing state.

5. CONCLUSIONS

The work in this article proposes a synthesis procedure to synthesize mechanism compose of combination of rigid links joined together with revolute and prismatic joints to approximate a desired shape change of profiles defined by three prescribed position. By applying prismatic joints into the segments in result the mechanism can be simplified by decreasing the number of link of each segment. To achieve 1-DOF mechanism for the fixed-end changing chain, subchains referred to as building-blocks are assembled, and prismatic joints can be implemented in any of these building blocks except the binary link auxiliary blocks. With the application of GCP technique, the development of the mechanism is easier as GCP gives a comprehensive graphical representation of the large and complex constraint set thus provides a very effective method to design the mechanisms.

6. ACKNOWLEDGEMENT

This work was supported by the Department of Higher Education (Malaysia) under grant No. RAGS/2013/TK01/FKM/04/B0043.

7. REFERENCES

[1] T. A. Weishar, "Morphing Aircraft Technology - New Shapes for Aircraft Design," *Proceedings of the Multifunctional Structures Integration of Sensors and Antennas Meeting*, 2006.

[2] B. P. Trease, Y. M. Moon, and S. Kota, "Design of Large-Displacement Compliant Joint," *Journal of Mechanical Design*, vol. 127, no. 7, pp. 788-798, 2005.

[3] A. P. Murray, J. P. Schmiedeler, and B. M. Korte, "Kinematic Synthesis of Planar, Shape-Changing Rigid-Body Mechanisms," *Journal of Mechanical Design*, vol. 130, no. 3, pp. 1-10, 2008.

[4] B. M. Korte, "The Application of Rigid-Body Kinematics to Shape-Changing Mechanism Design," MSc. thesis, The Ohio State University, Ohio, 2006.

[5] S. A. Shamsudin, and J. P. Schmiedeler, "Kinematic Synthesis of Planar, Shape-Changing Rigid Body Mechanisms for Design Profiles With Significant Differences in Arc Length," *Proceedings of the ASME International Design Engineering Technical Conferences & Computers and Information Engineering Conference*, 2011.

[6] K. Zhao, J. P. Schmiedeler, and A. P. Murray, "Design of Planar, Shape-Changing Rigid-Body Mechanisms for Morphing Aircraft Wings," *ASME Journal of Mechanisms and Robotics*, vol. 4, no. 4, p. 041007, 2012.

[7] G. L. Kinzel, and C. Chang, "The Analysis of Planar Linkages Using a Modular Approach," *Mech. Mach. Theory*, vol. 19, no. 1, pp. 165–172, 1984.

[8] D. H. Myszka, A. P. Murray, and J. P. Schmiedeler, "Singularity Analysis of an Extensible Kinematic Architecture: Assur Class N, Order N-1," *ASME J. Mech. Rob.*, vol. 1, no. 1, p. 011009, 2009.

[9] A. B. Neville, and A. C. Sanderson, "Tetrobot family tree: modular synthesis of kinematic structures for parallel robotics," *Proc. IEEE/RSJ IROS*, 1996.

[10] G. Krishnan, C. Kim, and S. Kota, "An Intrinsic Geometric Framework for the Building Block Synthesis of Single Point Compliant Mechanisms," *ASME J. Mech. Rob.,* vol. 3, no. 1, p. 011001, 2011.

[11] E. C. Kinzel, J. P. Schmiedeler, and G. R. Pennock, "Kinematic Synthesis for Finitely Separated Positions Using Geometric Constraint Programming," *ASME J. Mech. Des*., vol. 128, no. 5, pp. 1070–1079, 2006.

Optimizing PID controller for an electro-hydraulic servo system via gradient descent technique

C.C. Soon[1], R. Ghazali[1,*], H.I. Jaafar[1], S.Y.S Hussien[1]

[1)] Faculty of Electrical Engineering, Universiti Teknikal Malaysia Melaka,
Hang Tuah Jaya, 76100 Durian Tunggal, Melaka, Malaysia.

[*]Corresponding e-mail: rozaimi_85@yahoo.com

Keywords: Electro-hydraulic servo system; gradient descent technique; PID controller

ABSTRACT – This paper presents the basic knowledge in optimizing parameters of PID controller for an electro-hydraulic servo (EHS) system. Based on the Ziegler-Nichols tuning method, the obtained PID controller parameters were implemented in the physical model of EHS system. Then, an optimization technique which known as Gradient Descent is utilized using the MATLAB Simulink library. The findings show significant improvement in EHS tracking performance for both step and sinusoidal reference signal by applying the presented optimization technique.

1. INTRODUCTION

Many studies related to the **e**lectro-hydraulic **s**ervo (EHS) system problems have been conducted to figure out right direction to surmount these problems. The problems such as nonlinearities, uncertainties and disturbances that could degrade the EHS system performance must be solved. One of the ways is by optimizing the system controller performance. As the optimization technique has becoming popular nowadays, it can be utilized to optimize various types of controller such as PID controller that employed in this paper.

In order to optimize the PID controller, the PID parameter is first obtained by using Ziegler-Nichols tuning methods. Ziegler and Nichols published a paper that suggested a rule for tuning PID controller through the experimental step response or by adjusting the value of K_p that results in marginal stability. Ziegler-Nichols rules are helpful when the mathematical models of plant are not known [1]. After the obtained parameter was inserted into the controller, the improvement was caused by using optimization technique to the controller.

Optimization was described as the cognitive operation of researching for the solution that is more useful than several others. Qualitatively, this assertion implicitly recognizes the requirement of selecting among alternatives. This condition implies that an outcome of using optimization technique to the problem or design must yield numbers that will define our solution; in other words, numbers or values that will qualify the particular invention or overhaul. Quantitative description of the solution conducts a quantitative description of the problem itself. This description is called a mathematical model. The application of the optimization methods must be expressed mathematically according to the design and characteristic.

In this paper, the performance of position tracking control for EHS system is investigated using a PID controller with optimization technique. The servo valve and hydraulic actuator integrating with nonlinear dynamics model is derived. Subsequently, the performance of position tracking controller is compared with the optimized controller performance to demonstrate the significant enhancement of the controller through the proposed technique.

2. MODELING EHS SYSTEM

The block diagram of the EHS system is described in Figure 1 below.

By producing mechanical motion of the spool valve, the electrical current is supplied to the coil that connected to the servo valve. The torque motor that received the power source will drive the servo spool valve to the desired position. An electrical signal of the torque motor is given as in equation (1) [2].

$$V = \frac{dI}{dt} L_c + R_c I \tag{1}$$

where *Rc* and *Lc* are the coil resistance and inductance respectively.

The dynamics of the servo valve are represented by a second order differential equation that relates to electric current drive from the torque motor as expressed in (2).

$$\frac{d^2 x_v}{dt^2} + 2\xi\omega_n \frac{dx_v}{dt} + {\omega_n}^2 = I{\omega_n}^2 \tag{2}$$

where ξ is the damping ratio while ω is the natural frequency of servo valve.

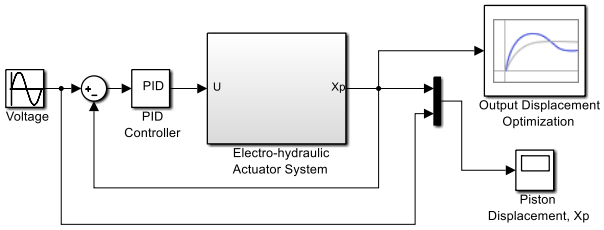

Figure 1 EHS system block diagram.

The flow relation that neglecting the internal leakages in servo valve for each chambers are given in (4) and (5).

$$Q_1 = \begin{cases} K_1 x_v \sqrt{P_s - P_1} & ; x_v \geq 0, \\ K_1 x_v \sqrt{P_1 - P_r} & ; x_v < 0, \end{cases} \quad (4)$$

$$Q_2 = \begin{cases} -K_2 x_v \sqrt{P_2 - P_r} & ; x_v \geq 0, \\ -K_2 x_v \sqrt{P_s - P_2} & ; x_v < 0, \end{cases} \quad (5)$$

The hydraulic actuator volume for each chambers are modelled in (6) and (7).

$$V_1 = V_{line} + A_p(x_s + x_p) \quad (6)$$

$$V_2 = V_{line} + A_p(x_s - x_p) \quad (7)$$

where V_{line} is the volume between hydraulic cylinder and pipeline. Pressure for each chambers can be obtained by defining the relation between bulk modulus, volume, and flow rate as expressed in (8) and (9).

$$P_1 = \frac{\beta}{V_{line} + A_p(x_s + x_p)} \int \left(Q_1 - q_{12} - q_1 - \frac{dV_1}{dt} \right) dt \quad (8)$$

$$P_2 = \frac{\beta}{V_{line} + A_p(x_s - x_p)} \int \left(\frac{dV_2}{dt} - Q_2 - q_{21} - q_2 \right) dt \quad (9)$$

Through the overall dynamics equation of moving mass, damper, and spring, the total force produced from hydraulic actuator can be evinced in (10).

$$F_p = A_p (P_1 - P_2) = M_p \frac{d^2 x_p}{dt^2} + B_s \frac{dx_p}{dt} + K_s x_p + F_f \quad (10)$$

3. RESULTS AND DISCUSSION

The comparison result for the PID controller and optimized PID controller for position tracking performance is shown in Figure 2 and 3. In both figures, step input and sinusoidal input have been fed to the system. The simulation result illustrates better performance through optimized parameter that is fed into the PID controller. Figure 2 depicted that the optimized controller produced a much stable response and eliminated the overshoot effect of the response. Figure 3 shows the position tracking performance which has been enhanced through the optimized parameters that is fed into PID controller. The parameters value was tabulated in Table 1.

Table 1 Parameters value for PID controller and Optimized PID Controller.

PID	Parameters Value		
	Ziegler-Nichols	Optimization	
		Step Input	Sine Input
K_p	1020	289.6602	1487.6219
K_i	0.0150	2.4999	0.0037
K_d	0.0038	0.1015	0.0003

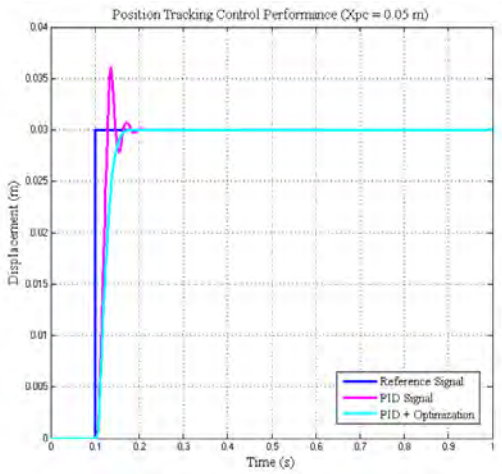

Figure 2 The comparison result for step input.

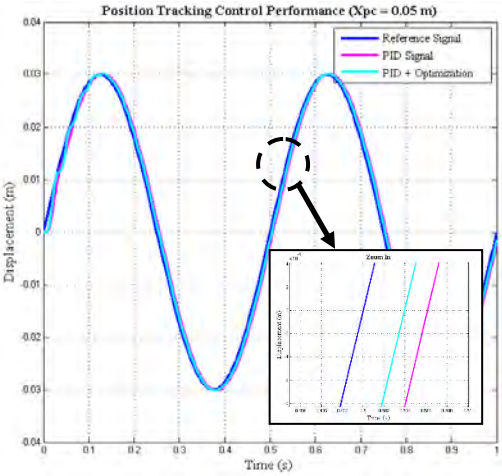

Figure 3 The comparison result for sinusoidal input.

4. CONCLUSIONS

In this paper, mathematical modelling of electro-hydraulic servo system has been derived and impended in the simulation study. The performance of the PID controller is evaluated by considering the Gradient Descent technique that applied to the controller. The numerical simulations show that the optimization technique provides significant improvement to the controller and produced much precise position trajectory tracking.

5. REFERENCES

[1] H. Angue-Mintsa, R. Venugopal, J.-P. Kenné, and C. Belleau, "Adaptive Position Control of an Electrohydraulic Servo System With Load Disturbance Rejection and Friction Compensation," *J. Dyn. Syst. Meas. Control*, vol. 133, no. November, p. 064506, 2011.

[2] R. Ghazali, Y. M. Sam, M. F. Rahmat, A. W. I. M. Hashim, and Z. Zulfatman, "Position tracking control of an electro-hydraulic servo system using sliding mode control," *Res. Dev. (SCOReD), 2010 IEEE Student Conf.*, vol. 4, no. 10, pp. 4749–4759, 2010.

Body to ground improvement at trim and form machine in end-of-line process

M.H. Mohtar[1], S. Maidin[1,*]

[1)] Faculty of Manufacturing Engineering, Universiti Teknikal Malaysia Melaka, Hang Tuah Jaya, 76100 Durian Tunggal, Melaka, Malaysia.

[*]Corresponding e-mail: shajahan@utem.edu.my

Keywords: Body to Ground (BTG); machine yield; jig design

ABSTRACT - The purpose of this study is to make an improvement on the design of the Jig for the Dpak trim and form machine which is one of the End-of-Line (EOL) process at Infineon Technologies (Malaysia) in Melaka. The objective of this research is to improve the design of the Jig so that the trim and form machines number of rejected units could be reduced. The target of improvement is to reduce the Body to Ground (BTG) problem and yield losses from 0.12% to 0.02%. The objective is to achieve an output target of 99.7% as per organization target. The focus of this study is the output track at the off-loading of the machine. The study has made suggestions to improve the track design. The track design has been improved by inserting a jig into the off-loader track. The jig will sort the rejected BTG unit. The cycle time for BTG detection have been improved tremendously into 60 seconds. The redesigned jig has also saved the cost from high rates of rejects.

1. INTRODUCTION

Stabilization is achieved through absorption of stabilizing molecules on the pigment surface, so that repulsive forces prevent other particles from approaching close enough for the attractive van der Waals forces to cause agglomeration. There are two principal mechanisms for the stabilization of pigmented dispersions [2]: (a) Electrostatic stabilization (b) Steric stabilization. However, this study only focuses on the electrostatic stabilization. Classic colloidal science explains electrostatic stabilization in terms of an electrical double-layer. A charge is generated on the pigment surface, and a more diffuse cloud of oppositely charged ions develops around it. As two particles approach each other the charge effectively provides a barrier to closer particle interactions. Stabilization increases along with the thickness of this layer.

1.1 Problem Statement

The auto vision inspection area which is the process after trimming and form is another BTG process which the vision will sort it and send it into the reject tube for lead dimension failure. The BTG problem always happened and it is a continuous problem. Detection at auto vision is already too late as damage already has been done and the unit will be segregated into the reject tube which contributes for 0.2 % yield loss of the overall Dpak product.

2. LITERATURE REVIEW

2.1. Jigs

Jigs have a direct effect upon machining quality, productivity, and the cost of products. Indeed, the costs associated with jig design and manufacture can account for 10 - 20% of the total cost of a manufacturing system [1]. Hence, there are significant benefits to be reaped by reducing the design costs associated with jigs.There are two approaches that have been pursued with this aim. One has concentrated on developing flexible jig systems, the other on simplifying the design process [2].

2.2 Standoff

Li Xun Ping et al., 2010 [3] study the influence of the standoff height, pad size and isothermal aging on the microstructure and shear fracture behaviour of Cu/Sn-3.0Ag-0.5Cu/Cu BGA structured interconnects using the lap-shear test. The experimental results show that the thickness of intermetallic compounds layer at the solder/Cu interface increases with decreasing standoff height of the joints

3. METHODOLOGY

3.1. BTG Jig Design

In order to overcome the problem stated, Figure 1 shows the jig which was implemented at Fico MTF001 machine off loader. Figure 2 shows example of good and bad BTG.

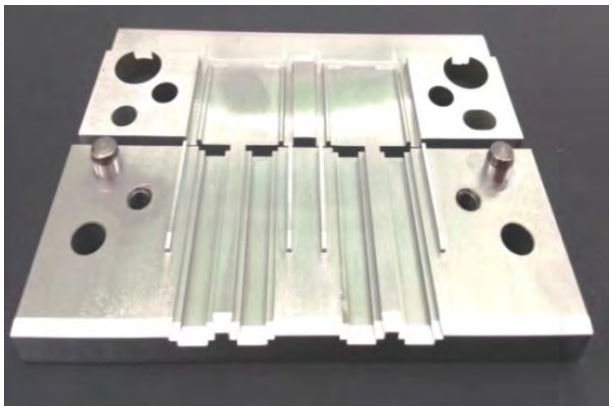

Figure 1 Actual Jig implemented (Inside look of the Jig)

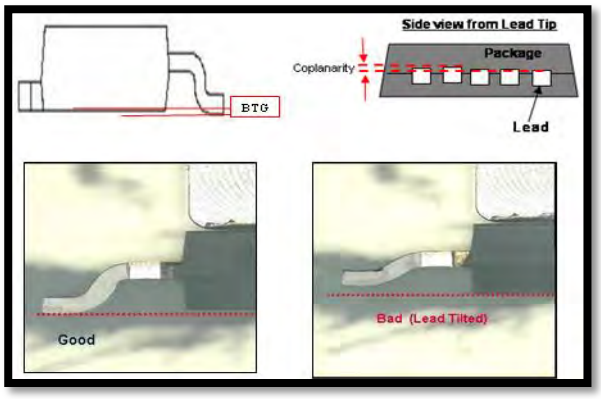

Figure 2 Good and Bad BTG

4. RESULTS & DISCUSSION

4.1 Cycle Time Improvement

Before the jig was implemented, the BTG is detected at auto vision after 2 hours of the trim and form process.

Cycle time = 2 hours X 60 minutes X 60 second
= 7,200 second

After the jig was implemented, the BTG is detected at trim and form itself within 1 minute.

Cycle time = 1 X 60 second
= 60 second

Cycle time Improvement = 7200 – 60
= 7140 second

This is good improvement as the cycle time had been improved to 7140 second.

4.2. Cost Analysis

Table 1 shows the scrap value per unit from week 33 to week 36 from the MTF001 trim and form machine. Week 33 has the highest reject during the study. Week 36 has less rejects after the jig was implemented. Table 2 shows the yearly cost saving after all 9 trim and form BTG jig are implemented.

Table 1 Waste cost analysis

No	Week	Quantity	Price/unit	Waste (RM)
1	33	4689	RM1	4689
2	34	3665	RM1	3665
3	35	2202	RM1	2202
4	36	1432	RM1	1432

Table 2 Cost saving

No	Week 33	Week 36	Qty Saved	Qty Machine	Yearly saved (RM)
1	4689	1432	3257	9	351,756

4.3 Yield Improvement

Table 3 shows that there is a yield loss improvement from 0.23% to 0.08%.

Table 3 Yield improvement percentage

Week	Total btg loss	MTF001	%
W33	20,078	4689	0.23
W34	28,810	3,665	0.13
W35	17,199	2,202	0.09
W36	29,234	1,432	0.08

5. SUMMARY

As a summary the jig design has improved the cycle time for BTG detection tremendously into 60 second. The redesigned jig also shows a significant cost saving yearly. Yield improvement from 0.23 percent to 0.08 percent shows that the target 0.05 percent could be be achieved. The redesigned jig is recommended to be implemented at all the trim and form machine at Infineon Technologies (Malaysia) in Melaka as this can improve yield target and reduce rejects and effective for cost saving.

6. REFERENCES

[1] Z.M. Bi and W.J. Zhang,"Flexible Fixture Design and Automation: Review, Issues and Future Direction", *International Journal of Production Research*, Vol. 39(13), pp. 2867-2894, 2001

[2] F.B. Hazen and P.K.Wright, "Workholding Automations in Analysis, Design, and Planning", *Manufacturing Review*, Vol. 43(4), pp. 224-237, 1990

[3] X.P. Li, J.M. Xia, M.B.Zhou, Ma Xiao, "The Influence of Standoff Height and Pad Size on the Shear Fracture Behavior of BGA Structured Cu/Sn3.0Ag0.5Cu/Cu Interconnects" *11th International Conference on Electronic Packaging Technology & High Density Packaging (ICEPT-HDP),* pp 1118 - 1123, 2010.

Performance on tensile properties of GFRP stacking sequence using Taguchi Method

M.A. Md Ali[1,2,*], A.K. Khamis[1], N.I.S. Hussein[1,2], R.I. Raja Abdullah[1,2], M.S. Kasim[1,2], M.H. Abu Bakar[1,2], E. Mohamad[1], M.A. Sulaiman[1,2]

[1)] Faculty of Manufacturing Engineering, Universiti Teknikal Malaysia Melaka, Hang Tuah Jaya, 76100 Durian Tunggal, Melaka, Malaysia.
[2)] Precision Machining Group (PMG), Universiti Teknikal Malaysia Melaka, Hang Tuah Jaya, 76100 Durian Tunggal, Melaka, Malaysia.

[*]Corresponding e-mail: mohdamran@utem.edu.my

Keywords: GFRP; tensile properties; Taguchi method

ABSTRACT – The performance of glass fibre direction on tensile strength (σ_{TS}) and modulus (E_{TS}) was studied. The GFRP sequence directions of -45°, 0°, 45° and 90° were lay-up in five levels and symmetrical laminated. The specimens follow ASTM D638 type II. Orthogonal arrays design of Taguchi method was applied and the data was analyzed using analysis of variance (ANOVA). It is found that the most GFRP sequence direction affected the tensile properties is fibre layup at direction of 0° while at -45°, 45° and 90° show less significant. Result after validation of optimum parameter for σ_{TS} reduces to 1.59% however E_{TS} value was unchanged after validation process.

1. INTRODUCTION

Composite materials have excellent mechanical property and offer light weight characteristic with high end performance that required in many manufacturing sectors like body boats, aerospace industry, railway coach and automotive application. Various types of reinforcement have been used in polymer composites such as reinforcement made from PTFE fibre [1], fine fibre [2], and natural fibre [3]. Glass fiber reinforced polymer (GFRP) one of the composite materials have been used for many years due to their low cost as compared to other composite materials, chemical or galvanic corrosion resistance, non electrical conductor and offers various types of weaves such as plains, basket, satin, twill, etc. Various investigation on composite materials have been done such as studied the effect of fibre volume fraction [4], different orientation of fibre [5], and fiber aspect ratio [6]. Sharma et al. revealed that fiber orientation significantly influence both mechanical and tribological property. It was found that fiber oriented beyond 45° deteriorated the performance [7]. Tian studied the effects of fiber orientation on the tensile strength of Csf/Mg. They found that the tensile strength of Csf/Mg composites gradually decreased with the fiber orientation angle increasing from 0° to 60° and slightly increased with the fiber orientation angle increasing from 60° to 90° [8]. Recently, design of experimental becomes essential to optimize the responses [9]. Therefore, in this study the effect of GFRP sequence directions is implemented using Taguchi method.

2. METHODOLOGY

Glass fibre reinforce polymer (GFRP) was used as a workpiece material for this study. Temperature 48.8°C and full vacuum at 20"Hg is applied in autoclave machine to prepare the workpiece samples. Then, the specimens were cut using diamond sliding saw which parallel to the warp fiber direction within ± 3° after the curing process. Finally, the specimens were machined according to ASTM D638 type II [10].

Table 1 shows the selected parameters performed for this study with two working levels. The range of experimental parameters value between low and high was decided with sequence directions of -45°, 0°, 45° and 90° at axis direction of tensile test. Five factors with two levels were performed in this experiment and direction of glass fibre was indicated by direction A, B, C, D and E.

Table 1 Stacking sequence of GFRP

Parameters	Low	High
Direction A	0 (|)	45 (/)
Direction B	0 (|)	90 (—)
Direction C	45 (/)	-45 (\ )
Direction D	-45 (\ )	0 (|)
Direction E	-45 (\ )	90 (—)

3. RESULTS AND DISCUSSON

3.1 Analysis result of ultimate tensile strength

Explanation of the result analysis is described by the graph and percentage of contribution value. It is determined that each of selected parameter influenced all the responses based on the percentage of contribution value. S/N ratio for σ_{TS} after analyzed using Minitab software is shown in Figure 1. It is found that parameters A and D are dominant factor affecting σ_{TS}. This result of dominant can be observed from the higher slope created from the graph. Result after validation on combination optimization using Taguchi method of these parameters decreases the σ_{TS} for 1.59%. Some researchers had agreed that the tensile strength decreased when the orientation of fibre increases more than 30° and become more significantly when fibre oriented to 45° [8].

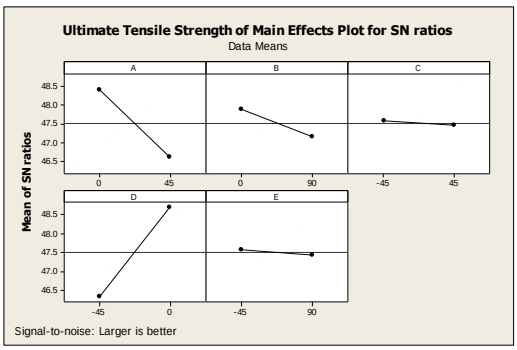

Figure 1 S/N graph for ultimate tensile strength

In order to study the percentage significance of the parameters affected the quality characteristic of interest, ANOVA analysis was performed. The summary of the result percentage is indicated using R-Sq as shown in Table 2. Considering the value of percentage that shows the significant factors influenced σ_{TS}, it can be determined that direction of parameters D is the highest percentage with 59.68%.

Table 2 One way ANOVA for ultimate tensile strength

Level	A	B	C	D	E
Rank	2	3	5	1	4
R-Sq (%)	33.85	5.55	0.13	59.68	0.24

3.2 Analysis result of tensile young's modulus

The S/N response graph of tensile young's modulus (E_{TM}) is shown in Figure 2 with initial setting the larger the better. It shows that the optimum parametric combinations of A, B, C, D & E are 0^o, 90^o, 45^o, 0^o and 90^o respectively. After validation of optimum parameters, the result of validation shows similar with the higher result in the actual experiment.

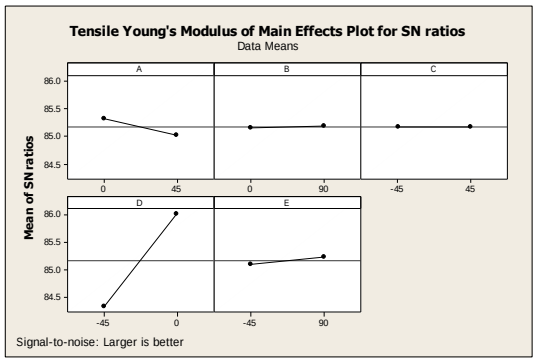

Figure 2 S/N graph for tensile young' modulus

Table 3 shows that direction D is the highest percentage with 80.76% followed by parameter A, E, B and C. Result of this experiment shows that when direction at -45^o and 0^o the higher of E_{TM} can be achieved.

4. CONCLUSIONS

It can be concluded that stacking sequence at 0^o contributes the most significant factor for tensile properties of GFRP. The direction fibre that perpendicular to the acting force developed higher resistant energy to the tensile properties of GFRP.

Table 3 One way ANOVA for tensile young' modulus

Level	A	B	C	D	E
Rank	2	4	5	1	3
R-Sq (%)	2.5	0.04	0.00	80.76	0.51

5. ACKNOWLEDGEMENT

The authors gratefully acknowledge to Universiti Teknikal Malaysia Melaka (UTeM) for supported this project under FRGS/1/2014/TK01/UTEM/02/3.

6. REFERENCES

[1] M.A.M. Ali, S. Nobukawa, and M. Yamaguchi, "Morphology development of PTFE in a PP melt," *Pure Applied Chemistry*, vol. 83, no. 10, pp. 1819-1830, 2011.

[2] M. Yamaguchi, K. Fukuda, T. Yokohara, M.A.M. Ali, and S. Nobukawa, "Modification of rheological properties under elongational flow by addition of polymeric fine fibers," *Macromolecular Materials and Engineering*, vol. 297, no. 7, pp. 654-658, 2012.

[3] M. Amran, R. Izamshah, M. Shahir, M. Amri, and H. Hazwani, "The effect of binder on mechanical properties of kenaf fibre/PP composites using full factorial method," *Applied Mechanics and Materials*, vol. 695, pp. 709-712, 2015.

[4] A. Gupta, H. Singh, and R.S. Walia, "Effect of glass fiber and filler volume fraction variation on mechanical properties of GFRP composite," *Proceedings of the International Conference on Research and Innovations in Mechanical Engineering*, 2014, pp 407-414.

[5] Rahul, S. Sikarwar, R. Velmurugan, and N.K. Gupta, "Influence of fiber orientation and thickness on the response of glass/epoxy composites subject to impact loading," *Composite: Part B*, vol. 60, pp. 627-636, 2014.

[6] K.V. Kumar , P.R. Reddy , and D.V.R Shankar, "Effect of angle ply orientation on tensile properties of bi directional woven fabric glass epoxy composite laminate," *International Journal of Computational Engineering Research*, vol. 3, no. 10, pp. 55-61, 2013.

[7] M. Sharma, R.I. Mohan, and J. Bijwe, "Influence of fibre orientation on abrasive wear of unidirectional reinforced carbon fibre-polyethrimide composites," *Tribology International*, vol. 43, pp. 959-964, 2010.

[8] W. Tian, L. Qi, J. Zhou, and J. Guan, "Effects of the fiber orientation and fiber aspect ratio on the tensile strength of Csf/Mg composites," *Computational Materials Science*, vol. 89, pp. 6–11, 2014.

[9] M. Amran, S. Salmah, R. Izamshah, M. Hadzley, M. Shahir, and M. Amri, "Effect of injection moulding machine parameters on the warpage by applying Taguchi method," *Applied Mechanics and Materials,* vol. 699, pp. 20-25, 2015.

[10] V. Shah, *Handbook of plastics testing and failure analysis*, New Jersey: John Wiley & Sons: 2007.

Design of slanted glass injection mould for flow visualization of molten plastic

M.A. Md Ali[1,2,*], M.F. Khalik[1], S. Subramonian[1], Z. Abdullah[1], R. Jaafar[1], P.J. Liew[1,2], M.S. Abdul Aziz[1,2]

[1)] Faculty of Manufacturing Engineering, Universiti Teknikal Malaysia Melaka, Hang Tuah Jaya, 76100 Durian Tunggal, Melaka, Malaysia.
[2)] Precision Manufacturing Group (PMG), Universiti Teknikal Malaysia Melaka, Hang Tuah Jaya, 76100 Durian Tunggal, Melaka, Malaysia.

[*]Corresponding e-mail: mohdamran@utem.edu.my

Keywords: Slanted glass mould; flow visualization; injection molding

ABSTRACT – A modified two-plate injection plastic mould having a new method of embedded slanted glass at mould cavity side was designed where it can be used to visualize the flow of molten material moving inside the mould cavity. The slanted glass mould was design and fabricated in order to find whether the flow pattern of the molten plastic material fills the cavity area affected the product quality. Through glass observation window, the flow pattern of molten plastics can be detected and the relations between machine parameters and the responses, i.e, weldline, sink mark and air burble, can be investigated in order to produce better quality of plastic products.

1. INTRODUCTION

It is important to understand the polymer flow phenomena in molten stage during mould cavity filling. This is because of economical reason such as reducing the plastic part defects as well as increasing the quality requirements of moulded parts. Therefore, it is useful to carry out research both in visualization [1] and simulation [2] during flow of molten polymer during injection moulding process [3]. Recently, the polymer flow using visualization techniques in plastic injection mould have studied by several researchers. Bociga and Jaruga investigated the polymer melt in the cavity filling with various accesses and found that visualization technique had been able to improve various problems that cannot be seen during simulation [4]. Kanetoh and Yokoi studied the flow fronts of plastics melt using glass insert mould. They used the direct visualization method and found that defect of flow marks was observed at plastic parts where it was closely related to plastic behaviour in the flow front [5]. Result from simulation can be compared with visualization where the parameters of machine injection can be optimized using various optimization method such as using full factorial [6], response surface method [7] and Taguchi method [8].

This project discuses the design mechanism of slanted glass mould that will be used for visualize the molten polymer flow through transparent glass. There are three locations of digital camera to view of the molten polymer, firstly at the surface front view, secondly at surface side view and lastly at the surface top view of the plastic product.

2. METHODOLOGY

Figure 1 shows the flow chart of mould design. To design the slanted glass injection mould, it begins with familiarization the CAD software that is used and in this case is Solidworks™ software version 2013. Injection mould design had been study in order to understand what type of mould suitable for the slanted glass mould and type of components should have in order to make it works. Lastly the mould base is selected and the direction of mould clamping, direction of ejection, water cooling system and suitable view direction for taking of the image of molten polymer were decided.

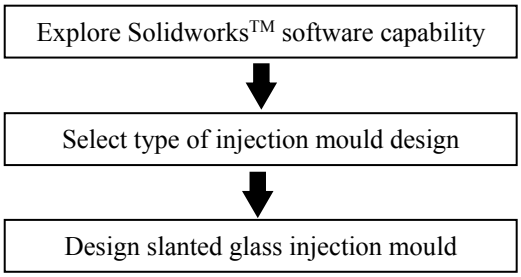

Figure 1 Mould design flow chart

3. SLANTED GLAS MOULD SET-UP

In order to design the slanted glass mould, the main concept and design have been done in a view of a diagram as shown in Figure 2. Front view shows the position of the slanted glass where digital camera no. 1 can capture the flow image from the top view of the product from the deflection of the mirror at the slanted part of the mirror.

Top view in Figure 2 shows the digital camera no. 2 and no. 3 that can capture the flow image from front and side of the product through the glass part. All digital cameras capture the flow image simultaneously during each injection shot.

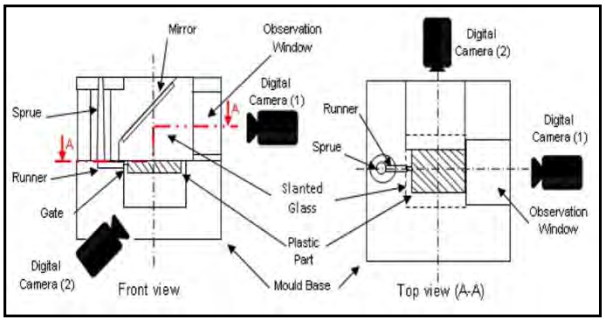

Figure 2 Slanted glass mould diagram

4. STATIONARY / MOVEABLE MOULD DESIGN

The two-plate injection mould design consists of two main plates and that are the core plate and the cavity plate. The cavity plate is known as stationary plate and the core plate known as the moveable plate.

4.1 Stationary Mould Design

Figure 3 shows five main parts in the assembly of stationary part of the slanted glass injection mould. For each process cycle, molten material is shot from the machine through nozzle and go through the sprue. The material is then flow to the cavity side following the shape of the cavity or product. The slanted glass is fixed to the cavity plate by using slot.

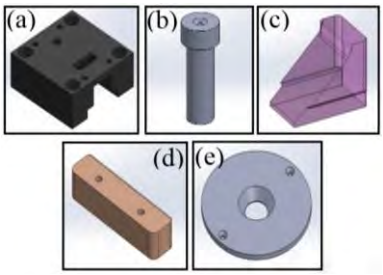

Figure 3 (a) Cavity plate (b) Sprue (c) Slanted glass (d) Slot (e) locating ring

4.1 Moveable Mould Design

Figure 4 shows parts in the assembly of moveable part of slanted glass injection mould. Core plate is the main part where the insert is fixed at the middle of it. The insert decide the shape of the finish product. During the injection process happen, the molten material flow through sprue at the cavity plate. It then flow through the runner and gate at the insert and after that flow inside the cavity space. While the material is filling up the cavity space, digital camera no.1, no. 2 and no. 3 captured the flow material through the slanted glass and the side glass.

5. CONCLUSIONS

The design of slanted glass mould using two-plate of injection mould is designed carefully. Flow of the molten plastic from the gate into the mould cavity can be observed through slanted glass; front and side glass using digital camera and the image of plastic flow taken can be analyzed through the visualization and compared with modeling simulation. The slanted glass injection mould is designed carefully because in actual fabrication of mould need high investment and any error of mould design should be avoided before actual plastic injection is machined and fabricated.

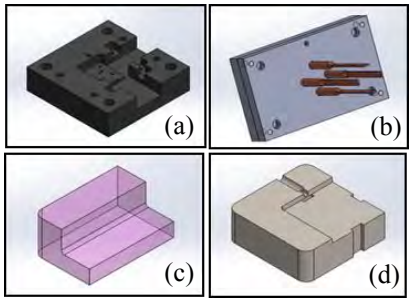

Figure 4 (a) core plate (b) ejector pins and ejector plates (c) side glass (d) insert

6. ACKNOWLEDGEMENT

The authors gratefully acknowledge to Universiti Teknikal Malaysia Melaka (UTeM) for supported this project under FRGS/1/2014/TK01/UTEM/02/3.

7. REFERENCES

[1] A. Ahmadzai, A.H. Behravesh, M.T. Sarabi, and P. Shahi, "Visualization of foaming phenomena in thermoplastic injection molding process," *Journal of Cellular Plastics*," vol. 50, no.3, pp 279-300, 2014.

[2] M.A. Amran, M. Hadzley, S. Amri, R. Izamshah, A. Hassan, S. Samsi and K. Shahir, "Optimization of gate, runner and sprue in two‐plate family plastic injection mould," in *AIP Conference Proceedings,* 2010, pp. 309-313.

[3] T.J. Bress and D.R. Dowling, "Visualization of injection molding," *Journal of Reinforced Plastics and Composites*, vol. 17, no. 15, pp. 1374 -1381, 1998.

[4] E. Bociga and T. Jaruga, "Experimental investigation of polymer flow in injection mould," *Archives of Materials Science*, vol. 28, no. 3, pp. 165-172, 2007.

[5] Y. Kanetoh and H. Yokoi, "Visualization analysis of resin behavior around a flow front using a rotary runner exchange system," *International Polymer Processing*, vol. 3, no. 3, pp. 310-317, 2012.

[6] M. Amran, S. Salmah, M. Zaki, R. Izamshah, M. Hadzley, Sivarao, M. Shahir, and M. Amri, "The effect of pressure on warpage of dumbbell plastic part in injection moulding machine," *Advanced Materials Research*, vol. 903, pp. 61-66, 2014.

[7] Y.T. Jou, W.T. Lin, W.C. Lee and T.M. Yeh, "Integrating the taguchi method and response surface methodology for process parameter optimization of the injection molding," *Applied Mathematics & Information Sciences*, vol. 8, no. 3 pp. 1277-1285, 2014.

[8] M. Amran , S. Salmah, A. Faiz, R. Izamshah, M. Hadzley, B. Manshoor, M. Shahir, and M. Amri, "Effect of injection moulding machine parameters on the warpage by applying taguchi method," *Applied Mechanics and Materials*, vol. 699, pp. 20-25, 2014.

Design of semi-auto line for *gula Melaka* processing

K.A. Azlan[1,*], T. Manoharan[1], H. Zainuddin[1], J. Basiron[1], M.K.M. Nor[1], F.R. Ramli[1, 2]

[1)] Faculty of Mechanical Engineering, Universiti Teknikal Malaysia Melaka, Hang Tuah Jaya, 76100 Durian Tunggal, Melaka, Malaysia.
[2)] Centre for Advanced Research on Energy, Universiti Teknikal Malaysia Melaka, Hang Tuah Jaya, 76100 Durian Tunggal, Melaka, Malaysia.

[*]Corresponding e-mail: khairulazri@student.utem.edu.my

Keywords: *Gula Melaka*; demoulding; production; aluminium, conveyer

ABSTRACT – *Gula Melaka* is broadly used in ASEAN, mainly for cooking. The demands are impressive but the current production capacity is not enough. Hence, a new semi-auto line is design to replace traditional method to shorten its processing time. A thorough study is conducted for improvement and several new design concepts have been put into consideration. The final selected concept operates with manual pouring process and the remaining processes are in automatic mode. Design of mould, cooling time reduction, and automatic transporting and demoulding process enables the production capacity to increase by 500 %.

1. INTRODUCTION

Gula Melaka or Palm Sugar is a nutrient-rich, low-glycemic crystalline sweetener that tastes, dissolves and melts almost exactly like sugar. It is acquired from the flowers growing high on coconut palm trees; liquid flower nectar. In traditional method, the fresh sweet palm neera is boiled down shortly after collection to make palm syrup and *Gula Melaka*. To concentrate the nectar into solid sugar, the fresh juice is boiled down and evaporated before being poured into bamboo sections to form cylindrical shapes [1]. The demands of the *Gula Melaka* are currently very high and the manufacturers which use traditional method must take action to increase their production [2]. Hence, a new modern method are required to increase the capacity

2. METHODOLOGY

2.1 Design

The design processes are according to the engineering design processes proposed by Pahl and Beitz [3] that includes clarification of the task, conceptual design, embodiment design and detail design. In traditional process, we observed that the process arrangements are cooking, pouring, cooling, demoulding and packaging of *Gula Melaka.* Morphological chart is used by listing few possible solutions for the problem. It is to establish any essential aspects that are necessary to the process. Then, we made few concepts as in Table 1. For concept evaluation and screening, we utilize the Pugh Matrix Evaluation [4] and it shows that Concept 2 has the best features, with highest weighted total. The selection criteria are based on the performance, durability, ease of handling, safe to use, feasibility and cost.

Table 1 Concepts Generation

Concept	Process		
	Pouring	**Cooling**	**Demoulding**
1	Nozzle	Fan	Piston
2	Jar Pouring	Cooled Chillers	Piston
3	Injection	Room Temperature	Shaking Motion
4	Injection	Fan	Mould Opening

In traditional method, bamboo moulds need to get wet for easy demoulding process [5]. By eliminating this process, it will prevent water from the bamboo to be absorbed by *Gula Melaka*. Thus, aluminium mould that consists of "mould inserts" with tapered drilled bore hole is suggested as replacement for easy separation of the *Gula Melaka* from the mould by means of gravity as well as easy maintenance and cleaning. In addition, aluminium has a light weight, high strength to weight ratio, corrosion resistance and formability [6]. A set of mould has 36 pieces of standard size mould inserts as illustrated in Figure 1. This enable constant volume for each single piece of *Gula Melaka.*

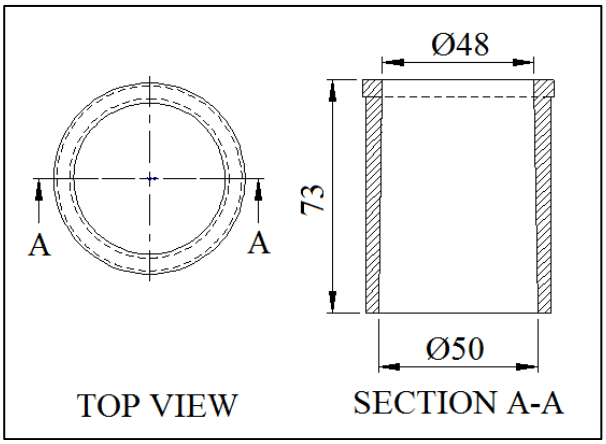

Figure 1 Mould Insert Dimension.

2.2 Process Flow

The overall process flow from pouring to demoulding for the new semi-auto line of *Gula Melaka* is summarize in Table 2 and illustrated in Figure 2.

Table 2 Flow Process of *Gula Melaka* Production

No.	Section	Description
1	Pouring	Manual pouring using a jar.
2	Conveyer	The conveyer will transport the molten *Gula Melaka* to chiller.
3	Chiller	Molten *Gula Melaka* will cool down and solidifies.
4	Conveyer	Transport the solid *Gula Melaka* to demoulding process station.
5	Demoulding	Process started with the pushing down of the *Gula Melaka*.
6	Rolling Conveyer	Transfer mould from demoulding to return conveyor
7	Return	Return empty mould to the pouring work station.

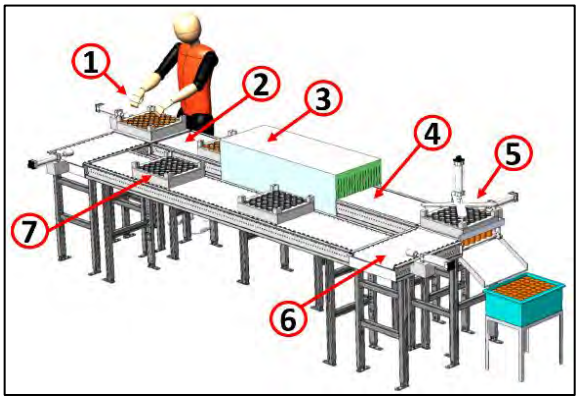

Figure 2 Process Flow of *Gula Melaka* Production

2.3 Cycle Time

In setting the target cycle time for the new semi-auto line, the cycle times for traditional process is use as a benchmark. To achieve the set target of increasing the production capacity by 500%, the new semi-auto line need to be able to produce five time faster. As the new design of mould set consists of 36 cavities, the cycle time for traditional method are also taken for every 36 pieces for reasonable comparison. The cycle time for each process in the traditional method are taken and recorded. The semi-automation ceiling cycle times are calculated for each process by setting the cycle times to be five times lower than the benchmark cycle times.

3. RESULTS AND DISCUSSION

Table 3 tabulate the cycle time comparison between traditional and new semi-automation for each process. The "bottle neck" can be determined from this table and are used to calculate the total line cycle time. The measured cycle time per piece for traditional process and the calculated cycle time per piece for semi-auto line are 37.5 and 7.5 seconds respectively. It also shows that the longest cycle time is the cooling process thus indicates the cooling process as the "bottle neck" which determine total line cycle time. Therefore an analysis have been conducted to determine the required cooling load to ensure the 36 pieces of *Gula Melaka* are able to solidified before it leave the cooling tunnel. For a 3 meters long cooling tunnel, the speed of the conveyor belt need to be set to 11 mm/s for the cooling time of 269 sec. The cooling load required for 36 pieces of *Gula Melaka* to reduce its temperature from 350°C to 24°C and solidified is about 2536 kJ/s. This calculated load is used to select the most suitable cooling tunnel according to its specification.

Table 3 Comparison of Traditional and Semi-Auto

Process	Categories	
	Traditional	Semi-Auto
Mould Arrangement	18 sec	3.6 sec
Pouring	108	21.6 sec
Cooling	1350 sec	269 sec
Demoulding	144 sec	28.8 sec
Total Cycle Time for 36 pieces (Bottle Neck)	1350 sec	269 sec
Cycle Time Per Piece	37.5 sec	7.5 sec

4. CONCLUSIONS

The application of automation control system to the production of *Gula Melaka* is a possible way to increase the food production. The theoretical calculation proves that the new production system can reduce the cycle time per piece from 37.5 seconds to 7.5 seconds. It means that the production of *Gula Melaka* by using the aluminium as a mould material can increase up to 500% compare to traditional method. As a result, the manufactures have enough capacity for the high demand, reduce manpower and therefore improves their productivity.

5. REFERENCES

[1] Ecobuddy. (2011) Gula Melaka. [Online] Available: http://www.chefcristysrawfoods.com/images/Coco%201.pdf

[2] Sarah. (2013) Coconut Sugar: Sustainable and Healthy Sweetener. [Online] Available: http://www.thehealthyhomeeconomist.com/coconut-sugar-a-healthy-and-sustainable-sweetener/

[3] G. Pahl and W. Beitz, *Engineering Design: A Systematic Approach*, 2nd edition, Springer-Verlag, 1996.

[4] N. Cross, *Engineering Design Methods: Strategies for Product Design*, 4th edition, Wiley-England, 2008

[5] R.Naufalin, B. Sustriawan, Sakhidin, K.E. Sularso and T. Yanto, "Mould Design and Packaging to Maintain Palm Sugar Quality," *Journal Lembaga Penelitian dan Pengabdian Masyarakat*, vol. 13, pp.1-8, 2013

[6] R. S. Rana, R. Purohit and S. Das, "Reviews on Influences of Alloying Elements on the Microstructure and Mechanical Properties of Aluminum Alloys and Aluminum Alloy Composites," *International Journal of Scientific and Research Publications*, vol. 2, pp.1-7, June 2012

Integrated recycle system concept for low cost 3D-printer sustainability

F.R. Ramli[1,2,*], M.I. Jailani[1], H. Unjar[3], M.R. Alkahari[1,2], M.A. Abdullah[1,2]

[1)] Faculty of Mechanical Engineering, Universiti Teknikal Malaysia Melaka,
Hang Tuah Jaya, 76100 Durian Tunggal, Melaka, Malaysia.
[2)] Centre for Advanced Research on Energy, Universiti Teknikal Malaysia Melaka,
Hang Tuah Jaya, 76100 Durian Tunggal, Melaka, Malaysia.
[3)] PFCE Ocean Engineering Sdn.Bhd. Lot 1428,Block 3,
Piasau Estate, 98000 Miri,Sarawak,Malaysia

[*]Corresponding e-mail: faiz@utem.edu.my

Keywords: 3D Printer; recycle system; sustainability design

ABSTRACT – Plastic prototypes that are produced by a low cost 3d printing process may contribute to the increases of plastic waste due to its post-process or from the waste from prototype building error. In this paper, with the goal to sustain and reuse the plastic waste, a recycle system which integrated to the low cost 3D-printer was proposed. This system concept which consisted of 13 parts was designed and analyzed by computer modelling and computer aided engineering software. Afterwards, most parts were built by 3D printer before they were assembled together and attached to the low cost 3D printer in order to prove the working design concept. From the result of the analysis, it shows that all parts were safe to produce where the factor safeties were in the range of 3 to 10 and the working concept of the system was proven.

.

1. INTRODUCTION

The popularity and the growth of low cost 3-D printers are in the extreme level. The attraction to build product for concept visualization that is working, reliable and cheap, demands not only the needs of a low cost machine but also the needs of cheaper building materials. Thus, in order to sustain the plastic materials that are produced by low cost 3D printer, a system to recycle the plastic waste and extruding the filament of the 3-D printer is required. This was already initiated by projects and works from RecycleBot and Filamaker [1,2]. These systems utilized the principle of plastic extrusion where it utilizes a screw to move material through a heated barrel, the plastic material was melted, compressed and forced through a die [3]. However these systems are separated from the low cost 3D printer itself, therefore the needs to operate two separate systems are not practical in term of time and cost. Furthermore, these recycle system machine have separated filament extruder and plastic shredder. This lead to the increases of produce time as one process should be complete before another.

In order to overcome this problem, a new concept of recycle system that able to recycle plastic waste into filament and integrated with the 3-D printer was proposed. To reduce the energy used in 3-D printing, the recycle system was developed without the uses of filament. This attempt will reduce the cost of feedstock 3-D printer even further. The system feed directly from the shredded plastic waste during printing using the concept of commercial filament extruder. The recycle system developed and analyzed using computer aided engineering software and the concept was produced by the 3D printing process.

2. METHODOLOGY

The concept design started with the concept generation presented by morphology chart which considered the following criteria; mechanism to decompose plastic materials, mechanism to extrude and draw out the filament, heating element, working mechanism and cooling element. Afterwards, the design concept was assessed by using evaluation matrix that emphasized on the following criteria of cost; ease of use; automation; adaptability to RepRap; quality; and energy use. The final concept design was prepared by solid modeling software and is illustrated in Figure 1. Each of the integrated system part is explained in Table 1. The design was then analyzed using computer aided engineering software by considering forces acted on each part when the system was assembled with the low cost 3D printer. The von Mises Stress and factor safety for each part were obtained.

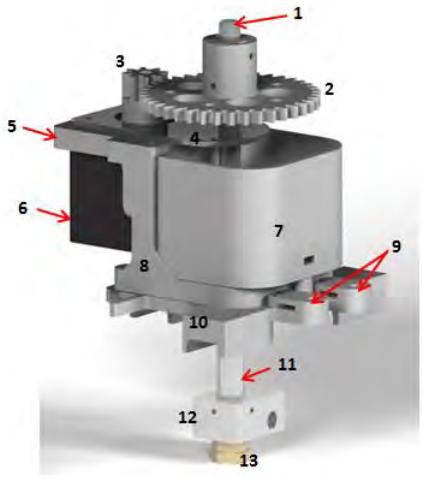

Figure 1 Concept Design of Integrated Recycle System

Table 1 Integrated recycle system parts description

Part No	Part Name	Material	Description
1	Auger drill bit	Steel	To transfer the shredded plastic to the hot end (Ø8 mm)
2	Gear A	ABS	To rotate drill bit (Ø 67 mm, t=38)
3	Gear B	ABS	To rotate Gear A (Ø 17 mm, t=8)
4	Drill bit holder	ABS	To grip the drill bit in fix position
5	Motor mount	ABS	To clench the motor and the auger drill bit holder
6	Motor		To rotate Gear B (NEMA 17)
7	Hopper	ABS	Contain shredded material and to guide their flow to the auger drill bit
8	Body	ABS	To hold the motor mount, hopper and is attached to the slider
9	Bell Mount	ABS	To mount the x-axis belt to the slider
10	Slider	ABS	To move the body, motor, motor mount, hopper, and every parts correspondent
11	Barrel	Aluminum	To transfer the shredded plastic material
12	Hot end	Aluminum	Heating section
13	Nozzle	Brass	To force the molten plastic through

For the assembly purpose, the integrated recycle system part was printed out using Mendel Low Cost 3D Printer Machine and the material used are ABS plastic. The printing process began from the exporting of the STL file of each part to the Sli3er software. The software will slice the parts based on requirement of the wall thickness, density of infill, and the infill pattern of the parts. Then the printed tool path and the temperature of the hot end and the bed which were set to 230°C and 110°C respectively by using the Pronterface software. On the bed surface, acetone was mixed with the ABS filament at the ratio of 3:10 The printed parts were then produced and each parts are assembled together. The assembly fitted on top of the low cost 3D printer and substituted the original extruder. The working concept of the recycle system was then investigated by the smoothness of the movement of the system.

3. RESULTS AND DISCUSSION

The factor safeties of all the analyzed recycling system parts are more than 2 which demonstrate that all of the parts are strong and safe to produce. In addition, most machine component should able to safely operate if they are in range of the recommended or ideal value of 3 to 5. Selected parts of the analysis results were summarized in Table 2 below.

Table 2 Stress analysis of selected recycle parts

Part No	Part Name	Max von mises stress (MPa)	Factor safety
1	Auger drill bit	70.82	3.5
5	Motor mount	4.75	3.4
8	Body	5.4	7.4

The prototype of the recycle system shows that small shredded plastic part was able to extrude smoothly by the auger drill bit. This was because of the hopper design angle transferred the shredded material efficiently. For the system assembly, the integrated system was capable to move in the x-axis direction smoothly. This phenomenon has been observed by the constant speed of the recycle system movement with the speed of motor. Thus, from this result it shows that the working concept of the recycling systems was established.

4. CONCLUSIONS

A new concept of recycle system was developed where the recycle system replaced the extruder head of the 3-D printer. Analysis of the recycle system proved that the component of the systems able to hold the load applied to it and the concept of recycle was working as predicted. In the future, a combination of shredder and extruder will be proposed to speed up the process of recycling of plastic waste.

5. ACKNOWLEDGEMENT

We would like to thanks the Innovative Machine and Mechanism Group of UTeM for all the lab facilities provided.

6. REFERENCES

[1] C.Baechler, M.DeVuono, J.M.Pearce, “Distributed recycling of waste polymer into RepRap feedstock,” *Rapid Prototyping Journal* Vol.19 no.2 pp.118-125, 2013.

[2] B.T.Wittbrodt., A.G.Glover,J. Laureto, G.C.Anzalone, D.Oppliger, J.L.Irwin, J.M.Pearce “Life-cycle economic analysis of distributed manufacturing with open-source 3-D printers,” Journal of Mechatronics Vol.23 pp. 713-726, 2013.

[3] Chase G. G. (2004). “SOLIDS NOTES 10, hopper design”, in “Solids Processing”. The University of Akron.

Forward-chaining approach to expert system for machine maintenance

S.N. Mohamad[1,*], A.Y. Bani Hashim[1]

[1)] Faculty of Manufacturing Engineering, Universiti Teknikal Malaysia Melaka, Hang Tuah Jaya, 76100 Durian Tunggal, Melaka, Malaysia.

[*]Corresponding e-mail: sitinurliza.mohamad@gmail.com

Keywords: Maintenance problems; forward chain; expert system; python programming language

ABSTRACT – This paper is about the machine maintenance of the Square Foiling Machine. Maintenance of the machine relates to the concern of controlling the condition of equipment. Most of the peoples used checklists to store the information but, since technology improved, there is a system that more reliable in maintenance management. There is an expert system that emulates human making decision ability. Knowledge of educated person and the experience of experts will be combined with a particular justification until a perfect decision achieved. Inference Techniques used is forward chaining method to draw the antecedent and consequent of the domain problems. The expert system will be written by using the Python language with graphical user interface (GUI).

1. INTRODUCTION

The Square Foiling Machine (SFM) is a sealing machine that is used for foiling purpose and the model type is BRT-5000SA. It was invented by Boryung Technology (BRT), a Korean-based company [1].

Figure 1 Square foiling machine (Source: [1])

The BRT-5000SA is designed to seal condoms in a square shape by manual loading with four side seals. Sealing process is a process that some heat is applied to the mold to melt a foil for packaging purpose. [1]. Table 1 shows the specification of the SFM.

Table 1 Specifications of square foiling machine (Source: [1])

No	Specifications	Details
1	Model no.	BRT-5000SA
2	Dimension	2200L x 1000W x 1650H mm
3	Power supply	240V. Single-Phase
4	Package size	55 x 57 mm
5	Capacity	About 70 to 100 pieces per minutes
6	Electric power	2~3.0 kWh
7	Automatic Grade	Semi-automated

Operating instructions that produced by BRT clearly stated the symptoms, causes to the symptom and the remedy. Several symptoms are main switch is on and entire electric part not alive, motor does not start, the set point for heating controller cannot be reached in spite of longer time, heater does not work, indicating temperature is unstable, open sealing or air leaking of package, and double sealing. With this available symptoms, causes and remedy, an expert system will be develop with Python Language [1].

2. BACKGROUND

Expert system (ES) is a branch of artificial intelligence. It is extensive use of specialized knowledge to solve problems at the level of human expertise. Human expert is a person who has expertise in a certain field. The expert has knowledge and skill in handling problem efficiently. Thus, expert systems perform reasoning over representations of human knowledge [2].

The fundamental component of an expert system is the knowledge. Human experts will transfer the knowledge and related information to the system to be analyzed. The system, upon having embedded with knowledge, will then respond to a respective situation. The knowledge engineer must communicate with the human experts. Transcribing the knowledge into pseudo codes is performed by the knowledge engineer while extracting the actual knowledge from the human experts. This stage is analogous to the system designer in conventional programming. Once ready, the human experts will then evaluate the ES. This process continues until the human experts satisfy with the system performance. Figure 2 summarizes the process of developing an ES.

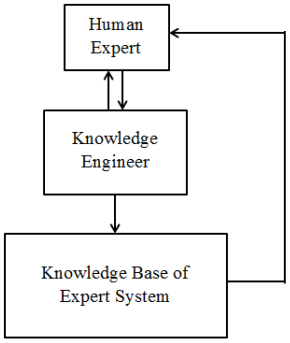

Figure 2 The development process of an ES (Source: [3])

Rule-base ES is the most popular system. It is easy to summarize the knowledge and expand the ES by incremental development as shown in Figure 3. The knowledge base stores expert knowledge as condition action rules. Working memory stores initial facts and generated facts derived by inference engine. Inference engine will matches the condition part of rules against facts stored in working memory. Explanation facility provides justification of solution (reasoning chain). Knowledge acquisition facility helps to integrate new knowledge. User interface act in insert the facts, query the system, solution presentation.

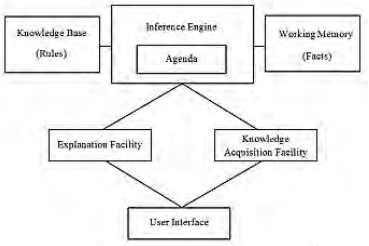

Figure 3 Structure of Rule-based ES (Source: [3])

Furthermore, the rules specified correctly. Rules act as a knowledge representation technique [3]. In any rules, they must consist of two parts. For example, the basic syntax should include at least an antecedent and a consequence.

IF <antecedent> **THEN** <consequent>

An inference is a method to stimulate the antecedent and consequent event. The process helps to draw a conclusion or to derive any starting point to some problem or consequents. This type of technique occurs repeatedly that performing the corresponding actions based on the knowledge base [4].

The objective of this paper is therefore, to discuss the system requirements, then generating the source code that translates the knowledge explicitly into the knowledge base module. A complete set of codes will produce an effective system.

3. METHODOLOGY

The seven symptoms listed in the defect checklist by Boryung Technology will be used in constructing the system. Based on Figure 4, the forward chaining inference technique showed the combination of antecedent and consequent event. The following equations define the rules for ES of the maintenance problem for a square foiling machine.

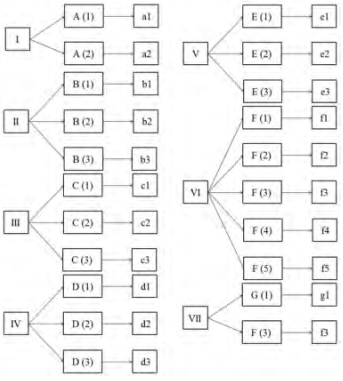

Figure 4: Forward chaining inference technique

Inference techniques used is Forward Chaining Method. Starting from an antecedent that is the problems, it will be a series of consequences that causes and remedy. Capital roman represents the problems, capital alphabet is the causes and the small letter is the remedy.

i) *Rule 0 (Initiation)*
IF Rule 1 **THEN** I
elif Rule 2 **THEN** II
elif Rule 3 **THEN** III
elif Rule 4 **THEN** IV
elif Rule 5 **THEN** V
elif Rule 6 **THEN** VI
elif Rule 7 **THEN** VII

ii) *Rule 1*
IF < I ∩ A(1) > **THEN** < a1 > (Rule 1.a)
IF < I ∩ A(2) > **THEN** < a2 > (Rule 1.b)

iii) *Rule 2*
IF < II ∩ B(1) > **THEN** < b1 > (Rule 2.a)
IF < II ∩ B(2) > **THEN** < b2 > (Rule 2.b)
IF < II ∩ B(3) > **THEN** < b3 > (Rule 2.c)

iv) *Rule 3*
IF < III ∩ C(1) > **THEN** < c1 > (Rule 3.a)
IF < III ∩ C(2) > **THEN** < c2 > (Rule 3.b)
IF < III ∩ C(3) > **THEN** < c3 > (Rule 3.c)

v) *Rule 4*
IF < IV ∩ D(1) > **THEN** < d1 > (Rule 4.a)
IF < IV ∩ D(1) > **THEN** < d2 > (Rule 4.b)
IF < IV ∩ D(1) > **THEN** < d3 > (Rule 4.c)

vi) *Rule 5*
IF < V ∩ E(1) > **THEN** < e1 > (Rule 5.a)
IF < V ∩ E(2) > **THEN** < e2 > (Rule 5.b)
IF < V ∩ E(3) > **THEN** < e3 > (Rule 5.c)

vii) *Rule 6*
IF < VI ∩ F(1) > **THEN** < f1 > (Rule 6.a)
IF < VI ∩ F(2) > **THEN** < f2 > (Rule 6.b)
IF < VI ∩ F(3) > **THEN** < f3 > (Rule 6.c)
IF < VI ∩ F(4) > **THEN** < f4 > (Rule 6.d)
IF < VI ∩ F(5) > **THEN** < f5 > (Rule 6.e)

ix) *Rule 7*
IF < VII ∩ G(1) > **THEN** < g1 > (Rule 7.a)
IF < VII ∩ F(3) > **THEN** < f3 > (Rule 7.b)

4. SUMMARY

The ES will be built based on information listed in the BRT user manual using forward chaining method. The codes will be written in the Python language and used of Graphical User Interface (GUI). Figure 5 shows the expert system of maintenance problem for SFM.

Figure 5 Expert System of Maintenance Problem

5. REFERENCES

[1] Boryung Technology, "Operating Instructions," Seoul, Korea, 2013.
[2] A. Barr and E. A. Feigenbaum, *The Handbook of artificial intelligence, Volume 1*. Addison-Wesley, 1986, p. 428.
[3] J. C. Giarratano and G. Riley, *Expert Systems: Principles and Programming, Volume 1*. Thomson Course Technology, 2005, pp. 1–49.
[4] M. Negnevitsky, *Artificial Intelligence: A Guide to Intelligent Systems*. Addison Wesley/Pearson, 2011, p. 479.

Decoding wrist gesture with combinational logic for the development of a practical EMG electrode sleeve

Z. Fu[1,*], A.Y. Bani Hashim[1], Z. Jamaludin[1], Imran Syakir Mohamad[2]

[1)] Faculty of Manufacturing Engineering, UniversitiTeknikal Malaysia Melaka, Hang Tuah Jaya, 76100 Durian Tunggal, Melaka, Malaysia.
[2)] Faculty of Mechanical Engineering, UniversitiTeknikal Malaysia Melaka, Hang Tuah Jaya, 76100 Durian Tunggal, Melaka, Malaysia.

[*]Corresponding e-mail: zinvifu@yahoo.com

Keywords: EMG, human machine interface, synthetic system

ABSTRACT - One of the reasons why EMG still lags as a machine input signal is because EMG is a physiological signal and differs between individuals. As a result, EMG devices also require training regardless whether it is a single user or multiple users. It is hypothesized that although the EMG signals are different among individuals, they still contain some similar traits that have potential for cross-user reusability. The characteristics of an EMG signal are studied across a sample of subjects. These signals are recorded and analyzed for similarities.

1. INTRODUCTION

An Electromyography (EMG) signal is an electrical signal that is generated when a muscle contracts. The EMG signal is a result of an electrochemical ionic exchange that takes place at the nerve-muscle junction during muscular motion. By using electronic pickups, these signals can be detected and utilized in various forms. Typical applications include motor-neuron medical analysis and more recently, gaining momentum as an input signal for computing and robotic systems.

As neural interfaces for machine input are increasingly studied, the EMG signal is an attractive alternative because EMG signals can be acquired from the skin surface. This form of EMG is known as surface EMG (sEMG) and it can be obtained via non-invasive means.

Although there are many researches on improving the acquisition and decoding of sEMG, commercial productization is still distant. The underlying reason is that sEMG is a physiological signal and variations exist among people. Even for a single subject, the sEMG recorded off the same muscle may deviate due to muscle fatigue, skin condition and also sEMG electrode placement [2]. Due to these reasons, sEMG machine input systems are not cross user applicable and even a single user requires a considerable calibration and training time [3].

2. METHODOLOGY

In order to make the sEMG system viable for everyday uses, it must be practical and user friendly. Unfortunately the sEMG system setup is complicated and the user needs anatomic knowledge of the target muscles, since precise electrode placement is critical [4-6].

The user of the sEMG system should not be burdened with clinical setup. In this research, the approach to the problem is to develop the sEMG system with minimal electrodes. In order to achieve this, fewer but significant forearm muscle were targeted, while maximizing the number of classifiable gestures.

A grid coordinate system was introduced for the lower forearm (Figure 1(a)). The target muscles were clearly mapped. For a single user, this system considerably cuts down initial setup time.

The grid system will be implemented onto a flexible material that would be constructed in the form of a wearable sleeve. This sleeve would stretch with the skin as the forearm rotates (Figure 1(b)).

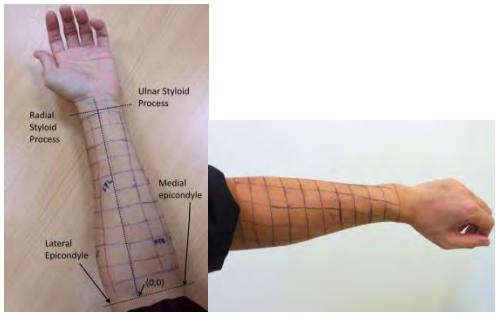

(a) (b)

Figure 1 Coordinate system for locating muscles in the forearm

$$\left.\begin{aligned}
&\text{flex}, w_f = (FCR \cdot FCU) + (FCU \cdot FDS) \\
&+ (FDS \cdot FCR) \\
&\text{extend}, w_e = (ECR \cdot ECU) + (ECU \cdot EDT) \\
&+ (ECR \cdot EDT) \\
&\text{abduct}, w_b = FCR \cdot ECR \\
&\text{adduct}, w_d = FCU \cdot ECU \\
&\text{hand_open}, h_o = F_e = FDS \\
&\text{hand_grasp}, h_g = F_f = EDT
\end{aligned}\right\} \quad (1)$$

Together with the coordinate system, the motion of the wrist and hand muscles was also defined as logical functions. Six gestures were defined and their

algorithms are shown in Equation (1). The gestures are wrist flexion and extension, wrist adduction and abduction and hand open and close. Only major muscles close to the elbow were considered because they are large and less susceptible to shift during forearm rotation.

3. RESULTS AND DISCUSSION

A simple discrete logic relationship has been established for the wrist motion decoding. Based on Equation (1), logic circuits can be built to perform the functions. An example of the circuit to decode wrist flexion is shown in Figure 2. This is however, a simple circuit to serve as the foundation for the ensuing processing stage. The sEMG signals still have to be filtered and processed with feature extraction and classification algorithms to attain a satisfactory precision.

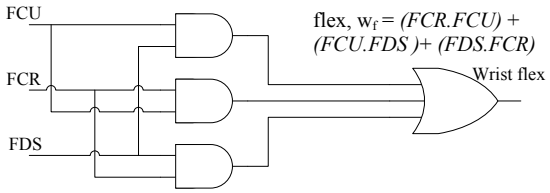

Figure 2 Logic circuit for decoding wrist flexion

The second phase of the will involve the development of a wearable electrode sleeve. The electrode sleeve will be tested on a sample of subjects that represent the target users. Basing on [7], the muscles in Equation (1) will fall in the same proximity. The larger surface size of these muscles will offset the anatomical difference between individuals. We expect the sleeve to speed up setup time for the user whereby the electrodes are already preset, as opposed to having to fix the electrodes individually.

The third phase of the research will focus on recording and analyzing the sEMG signals from the eight muscles listed in Equation (1). The target muscles are listed in Table 1.

Table 1: Major muscles and their functions

	FCU	FCR	FDS	ECU	ECR	EDT
Flex	1	1	1	0	0	0
Extend	0	0	0	1	1	1
Abduct	0	1	0	0	1	0
Adduct	1	0	0	1	0	0
Hand open	0	0	1	0	0	0
Hand Close	0	0	0	0	0	1

The sEMG signal waveform will be acquired with the Noraxon EMG acquisition device. Waveforms from the sample will be compared among subjects and the variations will be recorded. An example of an EMG waveform is shown in Figure 3. Analysis will be done on the power spectrum, frequency, bandwidth and phase to identify possible similar traits that can be used as a platform for cross-user compatibility.

4. CONCLUSIONS

The aim of this paper is to propose an sEMG input system that is practical for real-world appications. The coordinate system proposed as a graphical recording system so users can speed up the setup process. The proposed logic gate decoding system is a conceptual platform for the future development of feature extraction and classification.

Figure 3 Typical waveform of the sEMG signal [8]

Future research will be directed to analyzing the sEMG signals of various individual and also to the construction of the electrode sleeve.

5. ACKNOWLEDGMENT

The Malaysian Ministry of Education supports this research through the research grant—FRGS/2/2013/SG02/FKP/02/2/F00176.

6. REFERENCES

[1] S. Herle, S. Man, G. Lazea, and P. Raica, “Myoelectric Control Strategies for a Human Upper Limb Prosthesis,” *J. Control Eng. Appl. Informatics*, vol. 14, no. 1, pp. 58–66, 2012.

[2] A. Stoica, C. Assad, M. Wolf, K. S. You, M. Pavone, T. Huntsberger, and Y. Iwashita, “Using arm and hand gestures to command robots during stealth operations,” in *Multisensor, Multisource Information Fusion: Architectures, Algorithms, and Applications 2012*, 2012.

[3] S. Bitzer, A. E. M. G. Hardware, and P. van der Smagt, “Learning EMG control of a robotic hand : Towards Active Prostheses,” in *Proceedings of the 2006 IEEE International Conference on Robotics and Automation*, 2006, no. May, pp. 2819–2823.

[4] J. N. A. L. Leijnse, N. H. Campbell-Kyureghyan, D. Spektor, and P. M. Quesada, “Assessment of individual finger muscle activity in the extensor digitorum communis by surface EMG.,” *J. Neurophysiol.*, vol. 100, no. 6, pp. 3225–35, Dec. 2008.

[5] A. Y. Bani Hashim, M. N. Maslan, R. Izamshah, and I. S. Mohamad, “Delivering key signals to the machine: seeking the electric signal that muscles emanate,” *J. Phys. Conf. Ser.*, vol. 546, pp. 1–4, Nov. 2014.

[6] G. J. Tortora and B. Derrickson, *Principles of Anatomy and Physiology*, 12th ed. John Wiley & Sons, 2009, p. 1174.

[7] R. . Northrop, *Noninvasive Instrumentation and Measurement in Medical Diagnosis*. Florida: CRC Press, 2002, p. 113.

Application of defect detection in gluing line using shape-based matching approach

Mohamad Haniff Harun[1,*], Khalil Azha Mohd Annuar[1], Aminurrashid Noordin[1], Mohd Hanif Che Hasan[1], Muhammad Salihin Saealal[1], Mohd Firdaus Mohd Ab Halim[1], Muhammad Fareq Ibrahim[1]

[1)] Faculty of Technology Engineering, Universiti Teknikal Malaysia Melaka, Hang Tuah Jaya, 76100 Durian Tunggal, Melaka, Malaysia.

[*]Corresponding e-mail: haniff@utem.edu.my

Keywords: Shape-based matching; region of interest; matching process; template matching; correlation.

ABSTRACT – This paper investigates various approaches for automated inspection of gluing process using shape-based matching application. A new supervised defect detection approach to detect gap defect, bumper defect and bubble defect in gluing application is proposed. The creation of region of interest for important region of the object is further explained. The Correlation algorithm to determine better image processing result using template matching techniques is also proposed. This technique does not only reduce execution time, but also produce high accuracy in defect detection rate. The recognition efficiency will achieve more than 95% with defect's data for further process.

1. INTRODUCTION

Vision-based inspection of industrial products offers low-cost, high-speed, and high-quality detection of defects. One of the most challenging industrial inspection problems is dealing with the textured of the gluing process. Defects often happen during gluing process. To ensure that only quality units are produced, defects detection and recognition system commonly are installed for segregation of the defects unit. There are many techniques that provide a solution in recognizing image or object in image processing such as region [1], edge-based features [2], feature extraction [3], shape context [4], Gaussian Curve [5] and etc. Other researches were based on HALCON Application for Shape-Based Matching [6-8]. The researches discussed about the process involved in basic shape based matching algorithm together with Extended Region of Interest (ROI) function available in HALCON that fulfils shape based matching to find object based on a single model image with sub pixel accuracy. The basic concept of defect matching using shape-based matching algorithm based on Extended Region of Interest introduced by [9].

In this paper, an improve filter method that uses a computer to automatically recognize the gluing defects is put forward. In this approach, the digital image of the gluing defects is binarized first. Then ROI is further process before. Correlation algorithm refines the image. Once the importance feature of the binarized image has been extracted, the features are trained for defect classification. To better understand this method, in the next section, each kind of defects is elaborated further. ROI is applied to reduce processing time. Then depending on the features classification of the defect, feature extraction and Gaussian smoothing are used.

2. METHODOLOGY

Shape-based matching application is divided into two phases, Training phase and Recognition phase as shown in figure 1. Training phase is important in identifying the defect correctly. If the usage of the specific data are not optimize, the result will not be as accurate as what we desired. Hence, defect matching results with high accuracy and precision depends on the best reference image transformation. Matching phase is used to find similarity between reference images and tested images. Similarity is classified as recognition rate. Higher recognition rate means the systems proposed are effective and optimize. This application is easier to process because it reduce the region known as Region of Interest chosen by the users. Processing time can also reduce apart from producing higher recognition rate.

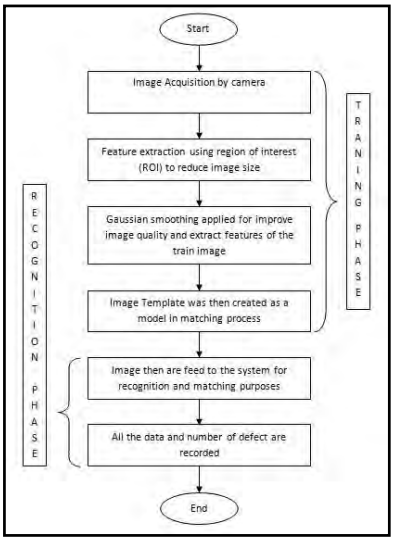

Figure 1 Proposed Vision Algorithm

Correlation is a measure of the degree to which two variables (pixel values in template and source images) agree, not necessary in actual value but in general behaviour. In correlation method, results of combination of differences between template gray level image, x_i with average gray level in the template image, $\dot{x}$ and difference between source image sections, y_i with

the average gray level of source image, ẏ are compared to the square root summation of the pixel differences between two images. Correlation value is between -1 and +1, with larger values representing a stronger relationship between the two images. Figure 2 and equation 1 shows the correlation relationship.

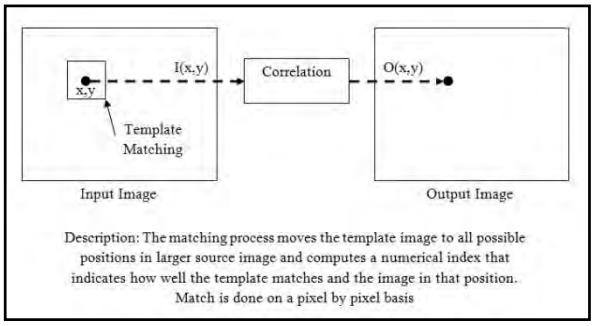

Figure 2 Template Matching Process Evaluation

$$cor = \frac{\sum_{i=0}^{N-1}(x_i - \dot{x}) \bullet (y_i - \dot{y})}{\sqrt{\sum_{i=0}^{N-1}(x_i - \dot{x})^2 \bullet \sum_{i=0}^{N-1}(y_i - \dot{y})^2}} \quad (1)$$

Where N = template image size = column x row

Correlation value totally depends on template creation throughout the system. Without proper contribution on it, may result to poor recognition rate. The important of ROI extraction method that delivers the precise region helps in findings the same object from various types of images.

3. RESULTS AND DISCUSSION

The potential of the proposed visual algorithm system was the flexibility of the program to accommodate changes. 10 images are being tested repeatedly for 10 times for its flexibility in determining all defects occur in the tested images. The tested images are filled with all the three defects models that are already being trained in training phase and fed into the system for recognition purposes.

Table 1 Recognition Rate for Proposed Defect Inspection System

No. of Test	Total Defect	Defect Detected	Average Defect Detected (%)
1	72	69	95.83
2	72	68	94.44
3	72	67	93.06
4	72	70	97.22
5	72	68	94.44
6	72	69	95.83
7	72	67	93.06
8	72	68	94.44
9	72	69	95.83
10	72	70	97.22
Total	720	685	95.14

Table 1 shows the result of defect matching by using 10 tested. According to the results, the recognition rate of the experiment is about 95.14% based on 3 model defects created through the system. This result is compared with [10] where it considered the problem in detecting welding defects in welding lines where the past researchers put an effort on more complex algorithm or limited in efficiency.

Table 2 Comparison of Results

	Weld Defect Detection	Glue Defect Detection (Proposed Method)
No. of Samples	500 samples	720 samples
No. of Types	6 types	3 types
Recognition Rate (%)	94.3%	95.14%
Error Rate (%)	5.7%	4.86%

4. CONCLUSIONS

Auto recognition of gluing defects is a useful research with strong application background. In this paper, a method that is used to extract features of defects and auto recognizes defects are put forward. Experimental results show that the recognition rate achieved about 95.14% which is much better for acquiring defect detection in gluing lines.

5. REFERENCES

[1] L. W. Teck, *et al.*, "Flexible approach for Region of Interest creation for shape-based matching in vision system", 2010, pp. 205-208.

[2] C. Gu, *et al.*, "Recognition using regions," 2009

[3] D. Naso, et al., "A fuzzy-logic based optical sensor for online weld defect-detection," *Industrial Informatics, IEEE Transactions* on, vol. 1, pp. 259-273, 2005.

[4] A. C. Berg, *et al.*, "Shape matching and object recognition using low distortion correspondences," 2005.

[5] X. Xie, "A review of recent advances in surface defect detection using texture analysis techniques," *Electronic Letters on Computer Vision and Image Analysis*, vol. 7, 2008, pp. 1–22.

[6] Sulaiman, M., M. Shah, et al. "A 3D Gluing Defect Inspection System Using Shape-Based Matching Application from Two Cameras." *International Review on Computers & Software* 8(8), 2013, pp. 1997-2004.

[7] Sulaiman, M., H. N. M. Shah, et al. "Defect Inspection System For Shape-Based Matching Using Two Cameras." *Journal of Theoretical & Applied Information Technology* 61(2), 2014, pp. 288-297

[8] L. Teck, *et al.*, "Implementation of Shape–Based Matching Vision System in Flexible Manufacturing System," *Journal of Engineering Science and Technology Review,* vol. 3, pp. 128-135, 2010.

[9] X. Xu, *et al.*, "HALCON application for shape-based matching," 2008, pp. 2431-2434.

[10] J. Peng, "A method for recognition of defects in welding lines," *International Conference on Artificial Intelligence and Computational Intelligence*, pp. 366-369, 2009.

Investigation of sway angle characteristics in gantry crane system by PSD analysis

S.Y.S. Hussien[1], R. Ghazali[1,*], H.I. Jaafar[1], C.C. Soon[1]

[1)] Faculty of Electrical Engineering, Universiti Teknikal Malaysia Melaka, Hang Tuah Jaya, 76100 Durian Tunggal, Melaka, Malaysia.

[*]Corresponding e-mail: rozaimi.ghazali@utem.edu.my

Keywords: Gantry crane system; power spectral density; sway angle

ABSTRACT – This paper attempts the investigation of the 2D-gantry crane system which focused on the sway angle characteristics via Power Spectral Density (PSD) analysis. The dynamic model of the nonlinear gantry crane system is derived by using Lagrange Equation. The system is simulated in MATLAB environment and the result is presented in the form of time and frequency domain. A comparative assessment of the various payload mass and rope length of the system performance is assessed and discussed.

1. INTRODUCTION

Gantry crane is important in the transportation industry for loading and unloading load. The control objective of this system is to move the trolley to a desired position as fast and accurate as possible without causing any immoderate sway at the final target position. In transportation industry, speed is required as the priority issue as it translates into productivity and efficiency of the system. However, controlling the crane manually by human will tend to excite sway angles of the hoisting line and degrade the overall performance of the system. At very low speed, the payload angle is not significant and can be ignored, but not for high speed condition. The sway angle become larger and hard to settle down during movement and unloading [1]. Besides, the effect of increasing the hoisting will degrade the performance of sway angle. This is very severe problem especially in the industries which requires small of sway angle with time taken for the transportation is short and high safety.

2. DYNAMIC MODEL STRUCTURE

In this section, a dynamic model of nonlinear gantry crane is formed. Assuming the dynamic model has the characteristics that the trolley and payload are connected by a massless, rigid link as in Figure 1 and the parameter of the system is shown in Table 1.

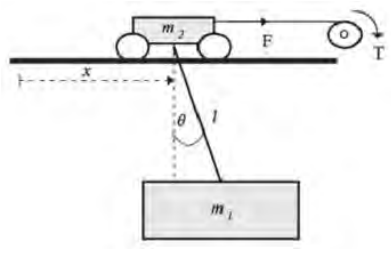

Figure 1 Dynamic model structure of gantry crane [2]

Table 1 Parameters of the dynamic gantry crane model structure [2]

Parameters	Values
Payload mass (m1)	0.5 to 50 kg
Trolley mass (m2)	5 kg
Rope length (l)	0.5 to 1.5 m
Gravitional (g)	9.81 ms^{-2}
Friction (B)	12.32 Nsm^{-1}
Resistance (R)	2.6
Torque constant (Kt)	0.007 NmA^{-1}
Electric constant (Ke)	0.007 $Vsrad^{-1}$
Radius of pulley (rp)	0.02 m
Gear ratio (z)	0.15

From the previous study [2], it shown that Lagrange Equation are frequently used to derive the model of the gantry crane system. Therefore, Lagrange equation is chosen for mathematical modeling of the system where L, T and P represent Lagragian function, kinetic energy and potential energy.

$$L = T - P \tag{1}$$

The kinetic energy and potential energy of the whole system are:

$$T = \frac{1}{2} m_1 \left[\dot{x}^2 + l^2 \dot{\theta}^2 + 2\dot{x} l \dot{\theta} \cos\theta \right] + \frac{1}{2} m_2 \dot{x}^2 \tag{2}$$

$$P = -mgl\cos\theta \tag{3}$$

Constructing Equation (2) and (3) by using Lagrange Equation as in Equation (4) where qi and Qi represent independent generalized coordinate and nonconservative generalized coordinate.

$$\frac{d}{dt}\left[\frac{\partial L}{\partial \dot{q}_i}\right] - \frac{\partial L}{\partial q_i} = Q_i \tag{4}$$

The following equations of motion for trolley position (Equation 5) and payload sway (Equation 6) can be obtained as:

$$\left(m_1 + m_2\right)\ddot{x} + m_1 l \ddot{\theta}\cos\theta + 2\dot{x} l \dot{\theta}\cos\theta + B\dot{x} - m_2 l \dot{\theta}^2 \sin\theta = F \tag{5}$$

$$m_1 l \ddot{x}\cos\theta + m_1 l^2 \ddot{\theta} + m_1 g l \sin\theta = 0 \tag{6}$$

The force in the Equation (7) is derived from the DC motor at the trolley to be substituted in Equation (5).

$$F = \frac{VK_t z}{Rr_p} - \frac{K_e K_t z^2}{Rr_p{}^2}\dot{x} \tag{7}$$

The equation of the position and sway in the overall system is in the equation (8) and (9). In this paper, only sway part will be focused.

$$\ddot{x} = \left(\begin{array}{l} \dfrac{VK_t z}{Rr_p} - \dfrac{K_e K_t z^2}{Rr_p^{\,2}} \dot{x} - B\dot{x} - \\ m_1 l\ddot{\theta}\cos\theta + m_1 l\dot{\theta}^2 \sin\theta \end{array} \right) \left(\frac{1}{(m_1 + m_2)} \right) \quad (8)$$

$$\ddot{\theta} = \left(\frac{1}{m_1 l^2} \right) \left(m_1 l\ddot{x}\cos\theta + m_1 gl\sin\theta \right) \quad (9)$$

3. SIMULATION

Figure 2 shown the design with the development of position and sway as in Equation (8) and (9) respectively in Simulink.

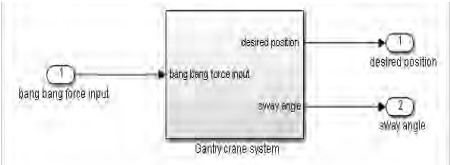

Figure 2 Gantry crane system block model

4. RESULTS AND DISCUSSION

The performances of the sway angle are analyzed in Power Spectral Density (PSD). PSD is a measure of a signal power intensity in the frequency domain to identify oscillatory signals in time series data and verify their amplitude. It is also states at which frequency ranges variation is strong and that might be quite useful for further analysis. There were three sets of mass had been tested in payload section which were 0.5 kg, 1.0 kg and 1.5 kg. The performance of the sway sway is analyzed in PSD. Based on Figure 3, when the payload mass is 0.5 kg, the PSD is at the normalized frequency of 0.2.44 π rad/sample. When the mass is tested with 1.0 kg, it shows that the PSD is at 0.2500 π rad/sample which is higher than 0.5 kg. Then, the test is continued with 1.5 kg of payload mass. It shows that the frequency created at 0.2578 πrad/sample. Table 2 shows the summarize of the response in the frequency domain with various of payload mass.

Figure 4 shows that when the payload mass is 0.5 m, the PSD shows the normalized frequency of 0.2734 π rad/sample. When the rope length is tested 1.0 m, it shows that the frequency is 0.1953 π rad/sample which is lower than 0.5 m. Lastly, when the system is tested to 1.5 m of rope length. It shows that the frequency created at 0.1563 π rad/ sample. Table 3 shows the summarized of the response in the frequency domain with various of rope length.

5. CONCLUSIONS

Investigation of the sway angle characteristic for a dynamic model of gantry crane system with variation of payload mass and rope length has been presented. The model structure of the gantry crane system is developed using Langrage Equation and simulated with bang-bang force input. The response of the sway angle has been obtained and analyzed in both time and frequency domain. From these findings, it is useful and important in the development of controller for 2-D gantry crane system in order to minimize the sway angle and also able for the trolley to reach the target position.

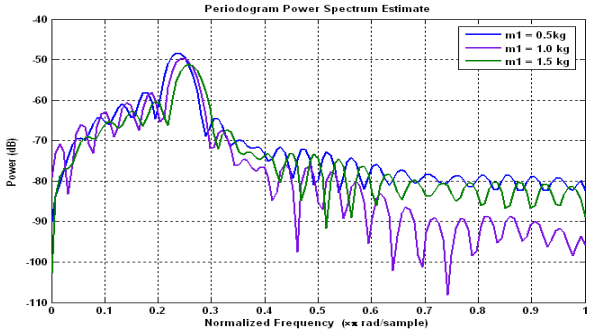

Figure 3 Response in the frequency domain of several of payload mass

Table 2 Summarize of response in the frequency domain with several of payload mass

Payload mass, m1 (kg)	Power, (dB)	Normalized frequency (πrad/sample)
0.5	-48.41	0.2344
1.0	-49.75	0.2500
1.5	-51.23	0.2578

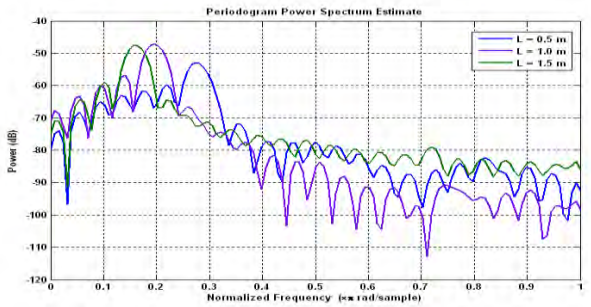

Figure 4 Response in frequency domain of various of rope length

Table 3 Summarize of response in frequency domain with several of rope length

Rope length, l (m)	Power, (dB)	Normalized frequency (π rad/sample)
0.5	-52.89	0.2734
1.0	-47.08	0.1953
1.5	-47.78	0.1563

6. REFERENCES

[1] M. A. Majid, W. S. W. Ibrahim, S. Mohamad, and Z. A. Bakar, "A comparison of PID and PD controller with input shaping technique for 3D gantry crane," in *Systems, Process & Control (ICSPC), 2013 IEEE Conference on*, 2013, pp. 144-148.

[2] M. I. Solihin, M. Kamal, and A. Legowo, "Optimal PID controller tuning of automatic gantry crane using PSO algorithm," in *Mechatronics and Its Applications, 2008. ISMA 2008. 5th International Symposium on*, 2008, pp. 1-5.

Hopping peak height algorithm for a one legged robot hopping height control

A.H. Azahar[1,2*], S.H. Chong[1,2], A.M. Kassim[1]

[1)] Faculty of Electrical Engineering, Universiti Teknikal Malaysia Melaka,
Hang Tuah Jaya, 76100 Durian Tunggal, Melaka, Malaysia.
[2)] Motion Control Research Laboratory (MCon), Universiti Teknikal Malaysia Melaka,
Hang Tuah Jaya, 76100 Durian Tunggal, Melaka, Malaysia.

[*]Corresponding e-mail: rmnhadi_00@yahoo.com

Keywords: One legged hopping robot; hopping height control; hopping peak height algorithm

ABSTRACT – This paper presents the hopping peak height algorithm in controlling the hopping height of a one legged hopping robot. The hopping mechanism produces continuous and rhythmic pattern. The continuous and rhythmic pattern behaviors produce oscillation feedback to the closed loop system and continuously produce oscillation error to the controller. Therefore, hopping peak height algorithm is designed and embedded into the closed loop control system feedback to determine the hopping peak of each produced hopping as a feedback. The existence of the hopping peak height algorithm assists the PI-CPG controller to converge the hopping height error approximately to zero.

1. INTRODUCTION

Hopping mechanism is one of the locomotion dynamic produced by legged robot. Research on one legged robot quite isolated compared to the other types of robot. Most of developed legged robots having difficulties in mechanism and controlling system design. Hopping robots have complex control system in order to calibrate with the one legged mechanical design. Thus, each design of one legged robot has its specific control system.

In controlling the one legged hopping robot, there are three types of problem that have to overcome which are altitude control, horizontal control, and height control. Among the problems, height control problem is the most difficult to overcome. To overcome this problem, Prosser and Kam proposed a vertical control algorithm that differs from previous control algorithm. The first area, the algorithm used a near-inverse of the machine's dynamic. Second, used discrete-time output feedback and a numerical simulation method for height trajectory tracking [1-2]. Naik and Mehrandenz used P, PID, and an inverse dynamics based PID controller to control the hopping height at a desired constant hopping height [3-4]. To achieve the desired hopping height, the feedback is determined via duty cycle of each hopping.

In this paper, the hopping height of a one legged hopping robot is controlled by integrating a hopping peak height algorithm in the closed loop control feedback. The algorithm is designed to determine the hopping peak height for each hopping as a feedback in order to reduce the hopping height error towards reference hopping height.

2. METHODOLOGY

The one legged hopping robot is controlled by using a host target computer and a xPC Target computer. MATLAB & Simulink software is used to design the control system of the one legged hopping robot via Real-time Workshop.

A closed-loop control system with a PI-CPG controller is designed to control the hopping height of the one legged hopping robot. The sampling time, *Ts* is set to 5msec. A hopping peak height algorithm is embedded inside the S-Function and integrated at the closed-loop feedback as shown in Figure 1. The hopping peak height algorithm is designed to determine the hopping peak height for each produced hopping.

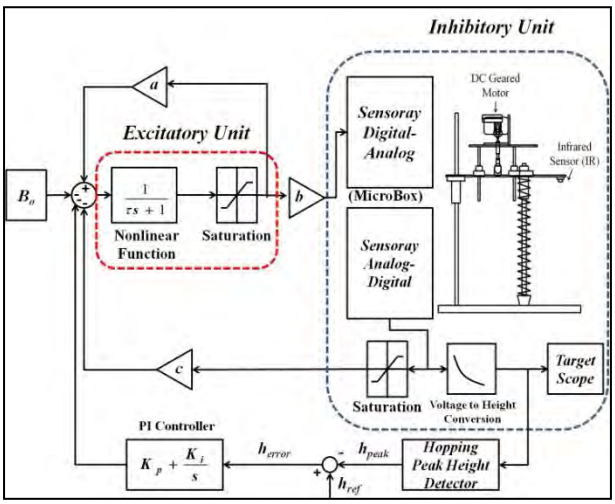

Figure 1 Closed loop system with hopping peak height algorithm

The hopping peak height algorithm is designed based on the rules that can be explained as following conditions:

a. If current value A is lower than the previous value B and the previous value B is greater than the previous value of B which is C, and the previous value B is greater than initial height of the one legged hopping robot, therefore the previous value B will be read out as the output height feedback and will be hold until the next hopping height is

found.

$$If\,(A < B \,\&\&\, B > C \,\&\&\, B > h_i)$$
$$h_{peak(i)} = B,$$

b. If the current value A, previous value B, and previous value of B, C did not meet the rule before the previous hopping peak height value will be read out as the output height feedback of the system.

$$h_{peak(i)} = h_{peak(i-1)}$$

3. RESULTS AND DISCUSSION

This section presents the experimental result of hopping height by one legged hopping robot with and without the existence of hopping peak height algorithm as shown in Figure 2 and Figure 3.

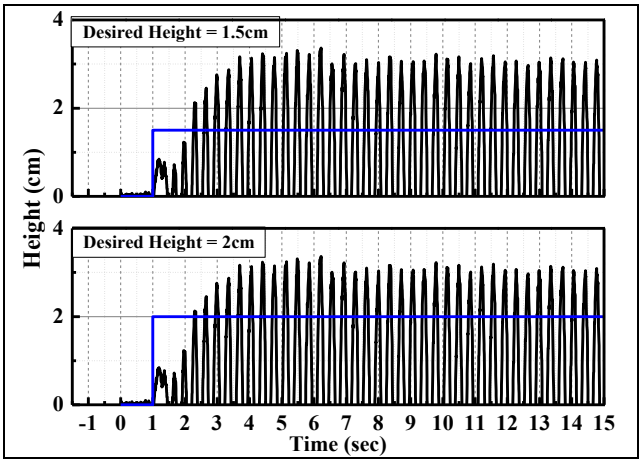

Figure 2 Hopping height without the existence of hopping peak height algorithm

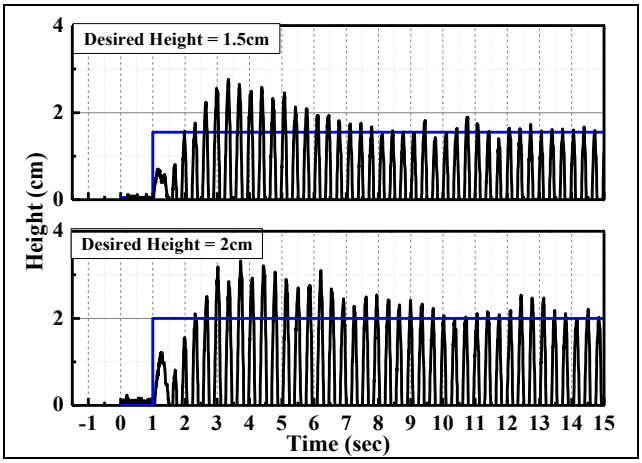

Figure 3 Hopping height with the existence of hopping peak height algorithm

From Figure 2, the hopping height produced by one legged hopping robot without the existence of hopping peak height algorithm demonstrates that there is huge error presents towards reference hopping height given. The huge error occurs caused by the oscillation pattern of hopping height output is directly used as a feedback to the system. According to that situation, the difference of hopping height to reference height keeps changing continuously for every sampling time. Therefore, the controller does not able to compensate the error and directly cannot achieve the reference hopping height.

Meanwhile, the produced hopping height by integrating the hopping peak height algorithm achieves the reference hopping height given as shown in Figure 3. The hopping peak height algorithm determined the hopping peak height for each hopping cycle and used the determined hopping peak height as a feedback to the system. Consequently, the hopping height error towards reference hopping height reduced approximately to zero and the one legged hopping robot achieved the reference height.

4. CONCLUSIONS

As a conclusion, the existence of hopping peak height algorithm in the closed loop control system feedback of a one legged hopping robot reduces the hopping height error towards reference hopping height and demonstrates better performance in achieving the reference hopping height.

5. ACKNOWLEDGEMENT

The authors wish to thank to Universiti Teknikal Malaysia Melaka and Ministry of Education Malaysia for the financial support and for providing the resources for this research.

6. REFERENCES

[1] J. Prosser and M. Kam, "Height Control of a One-Legged Hopping Machine Using a Near-Inverse Model," in *Proceedings 1992 Conference on Information Science and Systems Princeton University NJ*, 1992, pp. 995-1002.

[2] J. Prosser and M. Kam, "Vertical Control for a Mechanical Model of the One-Legged Hopping Machine," in *First Conference on Control Applications*, 1992, pp. 136-141.

[3] K.G. Naik and M. Mehrandezh, "Control of a One-Legged Hopping Robot using an Inverse Dynamics-based PID Controller," in *Canadian IEEE Conference on Electrical and Computer Engineering*, 2005, pp. 770-773.

[4] K.G. Naik, M. Mehrandezh, and J. . Berden, "Control of a One-Legged Hopping Robot using a Hybrid Neuro-PD Controller," in *Conadian IEEE Conference on Electrical and Computer Engineering*, 2006, pp. 1530-1533.

Experimental investigation on the road transmitted vibration on a mountain bicycle

A.Y. Ismail[1,2,*], M.F.A.M. Shukri[1], M.A.A. Johari[1]

[1)] Faculty of Engineering Technology, Universiti Teknikal Malaysia Melaka, Hang Tuah Jaya, 76100 Durian Tunggal, Melaka, Malaysia.
[2)] Applied Mathematics Research Group, Universiti Teknikal Malaysia Melaka, Hang Tuah Jaya, 76100 Durian Tunggal, Melaka, Malaysia.

[*]Corresponding e-mail: ahmadyusuf.ismail@utem.edu.my

Keywords: Road; vibration; mountain bicycle

ABSTRACT – This paper presents an experimental investigation on the road transmitted vibration on a mountain bicycle through a field test. It is purposely to determine the cycling comfort which is commonly represented by the vibration magnitude of the bike. The result shows that the cycling comfort is significantly affected by the roughness condition of the road but on the other hand only small effect is obtained from different tire size.

1. INTRODUCTION

Over decades, bicycle has been become one of the most favorite vehicles in the world. Besides fuel price issue, it is also because people can increase their body health by cycling. Since its presence in eighteen centuries, bicycle technology has been rapidly developed by researchers including the design, materials and also the dimension. One of the most important aspects for the cyclist is comfort issue, represented by the bike vibration. Many researchers have been conducting research concerning on this particular topics. Wenhua *et.al* [1] studies the comfort level of bicycle rider under different surface condition using software simulation. Petrone and Giubilato [2] develop a test method to evaluate the radial structural behavior of a bicycle wheel with respect to the rider's comfort. Holzel *et.al* [3] investigates the effect of surface road condition on the racing bicycle comfort. Similarly, Vanwalleghem [4] studies the dynamic behavior of an instrumented bicycle to see its relation to the comfort level. Currently, Liu *et.al*. conducts a simulation study of a full suspension bicycle to analyze the pedaling force and comfort [5]. Nevertheless, most of the conducted researches are only limited on a road bicycle scope.

This paper, therefore, presents a study on the effect of road transmitted vibration on the mountain bike comfort through field experimental test. The tire size and surface roughness are varied in order to give more comprehensive information.

2. METHODOLOGY

2.1 Experimental Setup

Figure 1 and 2 shows the experimental setup for the bicycle field test. Two accelerometers are placed at the front fork and at the seat post and are connected to the VibPlot dynamic signal analyzer through BNC cables.

Figure 1 Experimental setup.

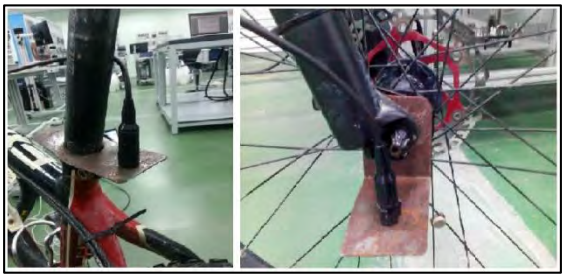

Figure 2 Accelerometer placement: Seat post (left) and front fork (right).

Three different sizes of tire are investigated as depicted in Figure 3. The technical specification of each tire is given in Table 1.

Table 1 Tire specification

Brand	Maxxis Cross Mark	Michelin Wild Racer	Maxxis Larsen TT Exeption
Material	Natural Rubber	Natural Rubber	Natural Rubber
Width (in)	2.1	2.0	1.9
Diameter (in)	26	26	26

Figure 3 Different sizes of tire.

Three different road surface conditions are also investigated as depicted in Figure 4 : cement pavement, soil and soil with uneven rocks.

Figure 4 Different road surface condition:
a). cement, b). soil, c). soil with uneven rocks.

2.2 Measurement Procedure

The measurement is conducted in three different cycling speeds i.e. 5, 6 and 7 km/h. The effect of different tire size and road surface condition is investigated for every speed. Data is taken within 3 seconds on a 6 m track after steady cycling is reached. This is purposely to avoid noise reading data and unwanted shock. The logarithmic value of vibration acceleration is presented against frequency from 0 – 10,000 Hz in order to obtain wide and adequate information of vibrational response from the bicycle.

3. RESULTS AND DISCUSSION

3.1 Effect of Speed

Figure 5 shows the effect of speed on the bicycle vibration. It can be seen that the cycling speed is proportional to the bicycle vibration. As the cycling speed increases, the excitation force form the contact between road and tire is also significantly increased which apparently produce higher vibration to the bike. Apart from this, higher vibration is also produced when the pedaling force of the cyclist is increased during speed increment.

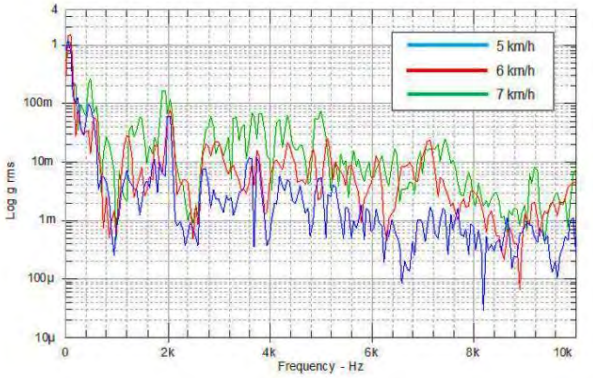

Figure 5 Effect of Speed (2.0”, cement pavement)

3.2 Effect of Road Surface Condition and Tire Size

Figure 6 shows the effect of road surface condition on the bicycle vibration. Smooth road apparently produces the lowest vibration and conversely, rougher surface gives higher vibration. The road roughness affects the force excitation to the bike considerably. The rougher the road, the higher excitation force is produced. While the effect of tire size apparently does not give significant effect to the bicycle vibration. This might be due to the small differences of the size, the force excitation produced by the contact between the road and different tire size is then quite similar.

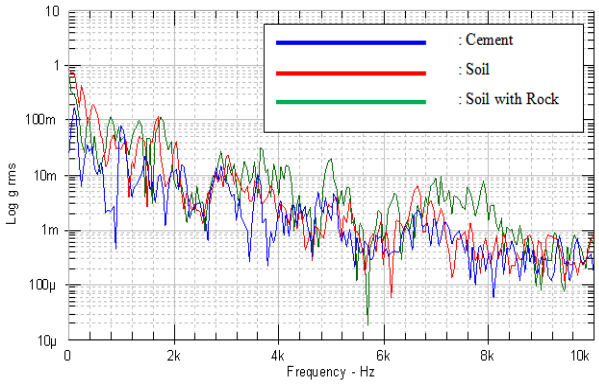

Figure 6 Effect of Surface condition (2.0”, 5 km/h)

4. SUMMARY

The effect of the road transmitted vibration on the bicycle comfort has been studied experimentally. As a conclusion, vibration of a mountain bicycle depends on the road surface condition considerably. On the other hand, different tire size does not give significant effect on the bike vibration.

5. REFERENCES

[1] D. Wenhua, Z. Dawei, Z. Xingyu, “Dynamic modelling and simulation of electric bicycle ride comfort,” in *International Conference on Mechatronics and Automation*, 2009, pp 4339 - 4343.

[2] N. Petrone, F. Giubilato, “Methods for evaluating the radial structural behavior of racing bicycle wheels,” *Procedia Engineering*, vol. 13, pp. 88-93, 2011.

[3] C. Holzel, F. Hochtl, V. Sanner, “Cycling comfort on different road surfaces,” *Procedia Engineering*, vol. 34, pp. 479-484, 2012.

[4] J. Vanwalleghem, F. Mortier, I.D. Baere, M. Loccufier, “Design of an instrumented bicycle for the evaluation of bicycle dynamics and its relation with the cyclist comfort,” *Procedia Engineering*, vol. 34, pp. 485-490, 2012.

[5] Y.S. Liu, T.S. Tsay, C.P. Chen, H.C. Pan, “Simulation of riding a full suspension bicycle for analyzing comfort and pedaling force,” *Procedia Engineering*, vol. 60, pp. 84-90, 2013.

Investigation on reed *Imperata Cylindrica* as sound absorber

F.A. Khair[1], A. Putra[1,2,*], M.J.M. Nor[1], N. Atiqah[1]

[1)] Faculty of Mechanical Engineering, Universiti Teknikal Malaysia Melaka,
Hang Tuah Jaya, 76100 Durian Tunggal, Melaka, Malaysia.
[2)] Centre for Advanced Research on Energy, Universiti Teknikal Malaysia Melaka,
Hang Tuah Jaya, 76100 Durian Tunggal, Melaka, Malaysia.

[*]Corresponding e-mail: azma.putra@utem.edu.my

Keywords: reed, hollow structure, sound absorber

ABSTRACT – The particles from synthetic fiber that are commonly used in sound absorber are very harmful to human health and environment when exposed to the air. Thus, researchers is now focus towards finding the potential of natural materials as alternative sound absorber. This paper presents the use of hollow structure of natural reed as non-fibrous acoustic absorber. Impedance tube method was used to measure the sound absorption coefficient of natural reed. Reed of length 2 cm and 3 cm were arranged in two different configuration: axial and transverse arrangement. The results showed that reed layered with thickness 2 cm in transverse arrangement gives better sound absorption compare to others with absorption coefficient reaches almost 1 at around 1.8kHz. For transverse arrangement, introduction of microholes to the structure of reed only shifts the absorption peak towards lower frequency.

1. INTRODUCTION

The fabrication of sound absorbing materials made of synthetic materials (glass wool, rock wool, asbestos and foam glass) release more carbon dioxide into the atmosphere including issues in environmental pollution and health [1]. Several studies have therefore been conducted on natural materials to investigate their feasibility to be alternative acoustic absorbers. Fouladi et al. [2] studied the utilization of coir fibers as acoustic materials. It is found that the coir fiber with thickness 45 mm can have average absorption coefficient of 0.8 at frequency above 600 Hz. Sugarcane fibers (bagasse) have also been shown to reach average absorption coefficient of 0.7 above 1 kHz with optimum fiber density [3]. The fiber from the paddy waste as sound absorber has also been studied [4,5]. Here, the density of the fiber is found to affect the absorption coefficient and attachment of fabric at the front surface can significantly improve the absorption. The acoustic absorber can also be made into configuration of multiple hollow structures by utilizing the hollow path and gaps between structures to absorb sound. Oldham et al. [6] showed that hollow structures of reed with length of 8.5 cm, arranged with cross-section facing the incident sound can have high normal absorption coefficient reaching almost unity at frequency of 700–900 Hz. This paper also studies the performance of reed, but of different species from those in [6]. The samples were tested for different lengths of stem and also different hollow diameters. The materials were arranged in two different configurations as in [6] such that sound absorption mechanism is possible.

2. METHODOLOGY

2.1 Reed

Reed or cogon grass is categorized as weeds and invasive species because it disturbs ecosystem and reduces other tree seedling growth. However, it also carries some benefits where it can be used as medicine to treat urinary infection and to reduce high blood pressure. Common species of reed are Phragmites australis, *Arundo Donax* and *Imperata cylindrica*. The later is used in this paper as shown in Figure 1(a) and the anatomy of the reed is shown in Figure 1(b).

(a) (b)

Figure 1 (a) The natural reed *Imperata Cylindrica* and (b) anatomy of reed.

2.2 Material Preparation and Experimental Setup

The stem from reeds are utilized here where it was cut into 2 cm and 3 cm and micro-holes of 0.4 mm were introduced to the structure which were expected to allow more sound absorption. The sound absorption coefficient was measured using the impedance tube method according to ISO 10534-2:2001 [7] as shown in Figure 2. The sample was located at the end of the tube while the other end of the tube is a loudspeaker to generate white noise fed into the tube. The tube has diameter of 33 mm and hence the valid frequency range for the measurement is from 500 Hz to 4500 Hz. Two pre-polarized free field microphones were located in front of the sample to record the built-up sound pressure in the tube.

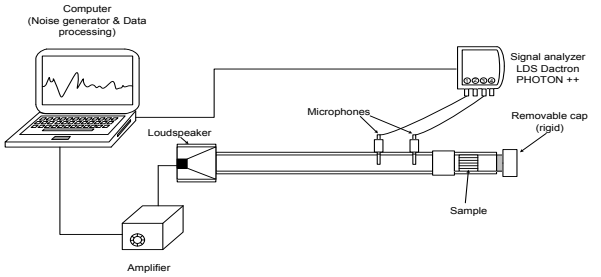

Figure 2 Experimental setup for absorption coefficient test.

3. RESULTS AND DISCUSSION

Result in Figure 4 shows that the reed with small diameter of length 2 cm can absorb more sound energy compared to the reed with large diameter. The absorption coefficient for the reed with small diameter can achieve 0.9 at high frequency around 3.6 kHz. This is because more amounts of reed are required to fit in the impedance tube thus, larger quantity of reed increase the absorption of sound energy.

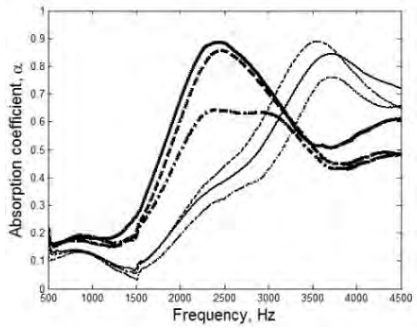

Figure 4 Absorption coefficient of reed in axial arrangement for length 2 cm (thin line) and 3 cm (thick line) length and diameter of : - - - 0.2 cm to 0.4 cm, ── mix diameter and -.-.- 0.5 cm to 1 cm.

Figure 5 and Figure 6 shows reed with introduction of microholes for both configuration (axial and transverse). For axial arrangement, it can be seen that reed of length 2 cm with micro-holes absorbs more sound energy compared to reed without micro-holes. However, the increment of absorption coefficient is not significant with only around 0.05 across the frequency range.

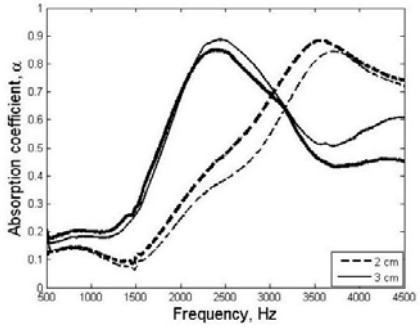

Figure 5 Absorption coefficient of reed in axial arrangement without micro-holes (thin line) and with micro-holes (thick line).

For transverse arrangement, the 2 cm thick layer can be seen to have absorption peak at 1.8 kHz and reaches almost unity. By increasing the thickness, this peak shifts to lower frequency. The introduction of microholes in the structure can also be seen to widen the frequency bandwidth around the absorption peak.

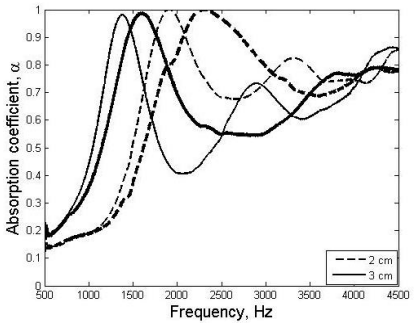

Figure 6 Absorption coefficient of reed in transverse arrangement without micro-holes (thin line) and with micro-holes (thick line).

4. CONCLUSIONS

For axial arrangement, the smaller the diameter of reed, the better the sound absorption but introducing microholes into the structure is found to not give significant improvement of sound absorption. For the transverse arrangement, the sound absorption performance is generally better than that from the axial arrangement where the absorption coefficient can reach unity while introduction of microholes in the transverse arrangement widen the frequency bandwidth around the absorption peak frequency.

5. REFERENCES

[1] F. Asdrubali, “Survey on the acoustical properties of ne sustainable materials for noise control, ” in *Proceedings of the Euronoise 2006, Structure Session Sustainable Materials for Noise Control*, 2006.

[2] M.H. Fouladi, Md. Ayub, M.J.M. Nor, “Analysis of coir fiber acoustical characteristics,”. *Applied Acoustics*, vol. 72, no. 1, pp. 35-42, 2011.

[3] A. Putra, Y. Abdullah, H. Efendy, W.M. Farid, M.R. Ayob, Py.M Sajidin, “Utilizing sugarcane wasted fibers as a sustainable acoustic absorber,” *Procedia Engineering*, vol. 53, pp. 632-638, 2013.

[4] A. Putra, Y. Abdullah, H. Efendy, W.M.F.W. Mohammad, N.I. Salleh, “Investigation on natural waste fibers from dried paddy straw as sustainable acoustic absorber,” in *Proceedings of IEEE First Conference on Clean Energy and Technology*, pp. 311-314, 2011.

[5] A. Putra, Y. Abdullah, H. Efendy, W.M.F.W. Mohamad, N.I Salleh, “Biomass from paddy fibers as sustainable acoustic material,” *Advances in Acoustics and Vibration*, pp. 1-7, 2013.

[6] D.J. Oldham, C.A. Egan, R.D Cookson, “Sustainable acoustic absorbers from the biomass,” *Applied Acoustics*, vol. 72, pp. 350-363, 2011.

[7] ISO 10534-2 “Acoustic determination of sound absorption coefficient and impedance tubes part 2: transfer function method, ” 2001.

Fundamental model of structure-borne vibration transmission in buildings using the portal frame approach

Y.M. Cheah[1], A. Putra[1,2,*], N. Muhammad[1,2], R. Ramlan[1,2]

[1)] Faculty of Mechanical Engineering, Universiti Teknikal Malaysia Melaka, Hang Tuah Jaya, 76100 Durian Tunggal, Melaka, Malaysia.
[2)] Centre for Advanced Research on Energy, Universiti Teknikal Malaysia Melaka, Hang Tuah Jaya, 76100 Durian Tunggal, Melaka, Malaysia.

[*]Corresponding e-mail: azma.putra@utem.edu.my

Keywords: structure-borne, portal frame, 2D analytical model

ABSTRACT – Vibration coming from mechanical services are often the source structure-borne noise sources in buildings. The transmitted vibration waves from these machines can activate the building structures to vibrate and radiate audible low frequency noise inside the building. This paper proposes the development of a generic analytical model of a 2D portal frame structure consisting of column and beam elements. The proposed model is use to predict the structural response of a multi-story portal frame building in order to understand the behavior of the structure with propagating vibration waves. The result is validated using the FE model which gives good agreement.

1. INTRODUCTION

As a number of building service equipment, such as ventilators and air conditioners, cooling tower and mechanical parking tower are installed in buildings, inevitably, the machine's operation induced structure-borne vibration can be a common 'noise and vibration problem' in the building.

Existing studies of the structure-borne transmission in buildings are those due to ground-borne vibration from railway trains [1-2] which proposed finite element (FE) and boundary element (BE) scheme analysis of vibration from railway tunnels. The study concentrates on the structure and acoustic response of a multi-story portal frame office building up to a frequency of 150 Hz to the passage of a Thalys high-speed train at constant velocity. The study presented the modes of the structure and the structure response shown in Figure 1. According to this study, a full three-dimensional FE/BE model takes approximately 1000-2000 times longer than the two-dimensional analysis.

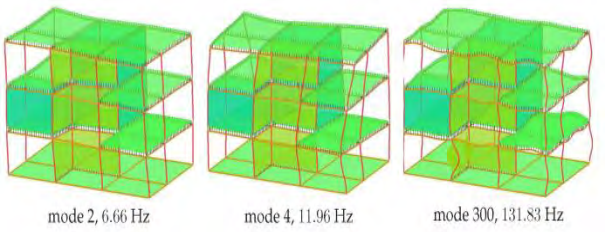

Figure 1 Examples of modes in a multi-storey building model.

Li and Wu [3] presented an analytical model to determine dominant vibration frequencies of a rail bridge. The work was based on the force method to obtain the power flows within a coupled vehicle-track-bridge system, the point mobility of the system and the dynamic interaction forces connecting the various subsystems. A similar analytical method will be used to investigate the structure response in this project, but due to the input from the mechanical service equipment.

2. METHODOLOGY

2.1 Theoretical element

One of the two most important elements in a framework is a column of a building. This type of element has the property of load bearing capability in the axial direction and longitudinal wave travels along the column. According to Thompson (1993) [4], the dynamic stiffness matrix of column is defined as,

$$K = EA\begin{bmatrix} jk_c & -jk_c \\ -jk_c e^{-jk_c Ly} & jk_c e^{jk_c Ly} \end{bmatrix}\begin{bmatrix} 1 & 1 \\ e^{-jk_c Ly} & e^{jk_c Ly} \end{bmatrix}^{-1} \quad (1)$$

where E is the Young's modulus, A is the cross sectional area, L_y is the length of the column in the direction of y, and the wave-number is $k_c = \omega\sqrt{\rho / E}$.

A beam can be assumed as a horizontal structure connecting to the columns and the foundation elements of a floor. For bending in a beam, bending waves are assumed to propagate through the beam. Euler-Bernoulli beam theory is applied [5], the dynamic stiffness matrix is equal to:

$$K = EI\begin{bmatrix} jk^3 & -jk^3 & -k^3 & k^3 \\ k^2 & k^2 & -k^2 & -k^2 \\ -jk^3 e^{-jkLy} & jk^3 e^{-jkLy} & k^3 e^{-kLy} & -k^3 e^{kLy} \\ -k^2 e^{-jkLy} & -k^2 e^{-jkLy} & k^2 e^{kLy} & k^2 e^{kLy} \end{bmatrix} \quad (2)$$

$$\times\begin{bmatrix} 1 & 1 & 1 & 1 \\ -jk & jk & -k & k \\ e^{-jkLy} & e^{jkLy} & e^{-kLy} & e^{kLy} \\ -jke^{-jkLy} & jke^{jkLy} & -ke^{-kLy} & ke^{kLy} \end{bmatrix}^{-1}$$

where I is the second moment of cross sectional area and the wave-number is $k = \sqrt{\omega}\left(\rho A / EI\right)^{1/4}$.

2.2 *One Floor Portal Frame Model*

Figure 2 shows an example of a simple portal frame model representing a building with one floor. This frame is developed in order to explain how the stiffness matrix of each element is assembled into one matrix. The roof top is a combination of two beam elements where the force is applied between element *b* and *c*. The size of the general dynamic stiffness matrix of the connections between elements is 8×8.

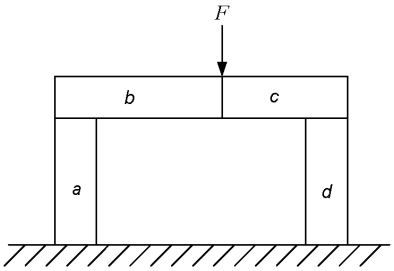

Figure 2 Injection force at the mid-bay of the floor.

The general dynamic stiffness matrix of the element is as follows,

$$\begin{bmatrix} a_{11} & a_{12} & 0 & 0 & 0 & 0 & 0 & 0 \\ a_{21} & a_{22}+b_{11} & b_{12} & b_{13} & b_{14} & 0 & 0 & 0 \\ 0 & b_{21} & b_{22} & b_{23} & b_{24} & 0 & 0 & 0 \\ 0 & b_{31} & b_{32} & b_{33}+c_{11} & b_{34}+c_{12} & c_{13} & c_{14} & 0 \\ 0 & b_{41} & b_{42} & b_{43}+c_{21} & b_{44}+c_{22} & c_{23} & c_{24} & 0 \\ 0 & 0 & 0 & c_{31} & c_{32} & c_{33}+d_{11} & c_{34} & d_{12} \\ 0 & 0 & 0 & c_{41} & c_{42} & c_{43} & c_{44} & 0 \\ 0 & 0 & 0 & 0 & 0 & d_{21} & 0 & d_{22} \end{bmatrix} \quad (3)$$

where the matrix $[a_{11} \;\; a_{12}; \;\; a_{21} \;\; a_{22}]$ is the matrix referring to the component *a* and *a*, *b*, *c* and *d* in Eq. (3) refers to the wave amplitude propagating in the column and the beam.

3. RESULTS AND DISCUSSION

The displacement at any point can be estimated by first finding the wave amplitudes using Eq. (1). The vibration amplitude is described here in terms of velocity and vibration velocity level in decibels is used in this study is $L_v = 20 \times \log_{10}\left(v / v_{ref}\right)$, where L_v is the velocity level in decibels, v is the rms velocity amplitude, and $v_{ref} = 1 \times 10^{-9}\,\mathrm{ms}^{-1}$ is the reference velocity amplitude.

As shown in Figure 3, the result from analytical model is validated using FE model which gives good agreement. In this analytical model, two types of materials are selected to model the beam and column of a building. The properties of the building material used in the model are shown in Table 1.

The analytical is then used to predict the motion of the structure due to the influence of the external force. As show in Figure 4, the operating deflection shapes (ODS) is estimated using the ratio between displacements at all points of the beam with displacement at the mid-bay point where the force is injected, U_{midbay}. The ratio is defined as $\mathrm{X} = \mathrm{real}\left(U(x) \times e^{\,j\varphi} / U_{\mathrm{midbay}}\right)$.

Table 1 Material Properties

	Beam	**Column**
Density, ρ (kg/m^3)	2000	2800
Young's Modulus, E (GPa)	2.6×10^{10}	3×10^{10}
Damping loss factor, η	0.012	0.006

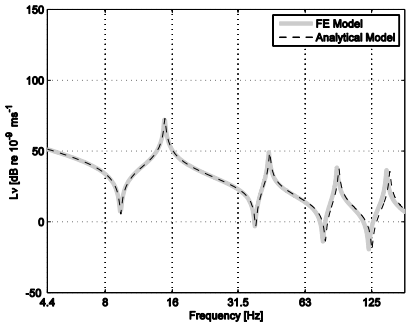

Figure 3 Vibration velocity level at the mid-bay point of the floor.

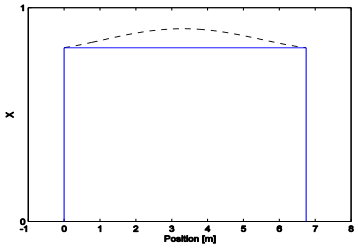

Figure 4 ODS of the structure at 14.8 Hz

4. CONCLUSIONS

A single portal frame model has been proposed to simulate vibration of a one-storey building. The model will be extended to a complex portal frame consisting five floors to achieve a model closest to the real aplication.

5. REFERENCES

[1] P. Fiala, G. Degrande, and F. Augusztinovicz, "Numerical modelling of ground-borne noise and vibration in buildings due to surface rail traffic," Journal of Sound and Vibration, vol. 301, no. 3, pp. 718–738, 2007.

[2] L. Andersen and C.J.C. Jones, "Coupled boundary and finite element analysis of vibration from railway tunnels: a comparison of two and three-dimensional modes," Journal of Sound Vibration, vol. 293, pp. 611-625, 2006.

[3] Q. Li and D. Wu, "Analysis of the dominant vibration frequencies of rail bridges for structure-borne noise using a power flow method," Journal of Sound and Vibration, vol. 332, no. 18, pp. 4153–4163, 2013.

[4] W. T. Thomson, *Theory of vibration with applications*, 4th ed. Prentice Hall; 1993.

[5] M. Petyt, *Introduction to finite element vibration analysis*, Cambridge University Press; 1990.

Preliminary study on sound absorption of natural kenaf fiber

Z.Y. Lim[1], A. Putra[1,2,*], M.J.M. Nor[1,2,*], M.Y. Yaakob[3]

[1)] Faculty of Mechanical Engineering, Universiti Teknikal Malaysia Melaka, Hang Tuah Jaya, 76100 Durian Tunggal, Melaka, Malaysia.
[2)] Centre for Advanced Research on Energy, Universiti Teknikal Malaysia Melaka, Hang Tuah Jaya, 76100 Durian Tunggal, Melaka, Malaysia.
[3)] Faculty of Manufacturing Engineering, Universiti Teknikal Malaysia Melaka, Hang Tuah Jaya, 76100 Durian Tunggal, Melaka, Malaysia.

[*]Corresponding e-mail: azma.putra@utem.edu.my

Keywords: Absorption coefficient; kenaf fiber; air gap

ABSTRACT – The increasing number of researches on utilizing natural fibers for acoustic panel to cater environmental and health problems has led to the study of the natural kenaf fibers. Several parameters such as thickness and air gaps are studied and measurement using impedance tube shows that kenaf fiber are feasible to be used as substitute for synthetic material as the absorption coefficient are found to be greater than 0.5 starting at the low frequency region for most cases.

1. INTRODUCTION

Conventional sound absorption materials used for building acoustic such as glass fiber and foam glass are known to be harmful to both the environment and human. In a comparison done between different sound insulation panel materials including synthetic and natural materials, the data suggests that the fabrication and production of synthetic materials have a positive global warming potential by contributing more carbon dioxide to the atmosphere when compared with natural materials. Besides, the mineral-made synthetic fibers contain a certain amount of toxic and can be a threat to human health if it is inhaled, and if contacted, may lead to skin irritation [1]. Natural fibers, which do not contribute too much on the environmental issue and contain very low toxicity are hence an alternative in sound absorption material. Vegetable fiber panels are found to have compatible and higher performance in indoor noise control comparing with conventional material [2]. Good acoustic performance has been discovered on sugarcane wasted fibers [3] where the absorption coefficient is found to have an average of 0.65 at 1.2 to 4.5 kHz. Whereas the acoustic performance of paddy waste fibers [4] had been studied and the average value of absorption coefficient is found to have reached 0.8 above 2.5 kHz. This paper presents the preliminary studies on the acoustic performance of Kenaf fiber. Kenaf is a hibiscus plant that is related to cotton, okra and hollyhocks, scientifically known as *Hibiscus cannabinus*, it is a member of Malvaceae family [5]. Kenaf is usually used as building materials, organic absorbents, and paper products [6]. Traditionally it is used in ornamentals, food, medicine, musical instruments and superstitious rites.

2. METHODOLOGY

2.1 Preparation of Material

Kenaf fiber sheet in a form of chopped strand mat with thickness of 5 mm is being cut into a disc shape with diameter of 33 mm in order to fit onto the removable cap of the impedance tube. Several disc-shaped kenaf fiber were layered to vary the thickness of the sample as shown in Figure 1.

Figure 1 Raw kenaf fiber (left) and layers of kenaf fiber forming a sample with thickness of 10 mm (right).

2.2 Experimental set up

The impedance tube method was used for the measurement of sound absorption coefficient. Figure 2 shows the experimental set up of the measurement. The data acquisition system used was the RT Pro Photon+v6.34 analyzer.

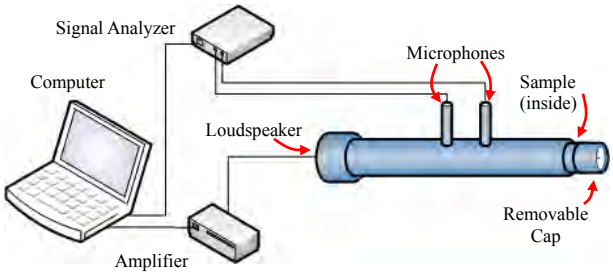

Figure 2 Diagram of absorption coefficient measurement setup.

White noise was the sound source fed by the loudspeaker to the interior of the tube, whereas the sample to be tested was placed in the removable cap at the other end of the impedance tube. The cap can be adjusted to form an air gap behind the sample. The two microphones used were G.R.A.S ½ inch prepolarized

free-field microphone type 40AE and ½ inch CCP preamplifier type 26CA to record the incident sound and the reflected sound from the sample.

3. RESULTS AND DISCUSSION

3.1 Effect of thickness of fiber

Figure 3 shows the sound absorption coefficient of kenaf fiber for different thicknesses. The result shows that sample with thickness of 10 mm has absorption coefficient greater than 0.5 above 3500 Hz. Whereas, for the 30 mm sample, the absorption coefficient is greater than 0.5 above 1000 Hz and approaches unity at around 2000 Hz. The increment of the thickness can be seen to significantly improve the absorption coefficient.

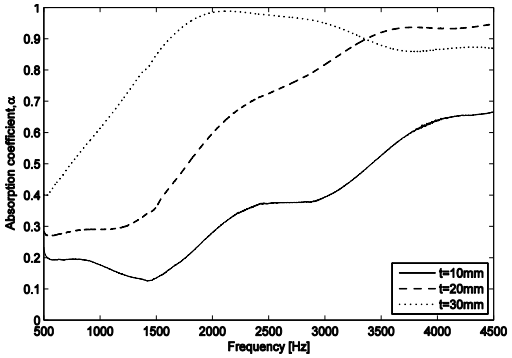

Figure 3 Sound absorption coefficient of Kenaf fiber with thickness of, 10 mm (─), 20 mm (---), 30 mm (···).

3.2 Effect of air gap

Figure 4 shows the sound absorption measured on a 20 mm thick kenaf fiber, with different air gap thicknesses.

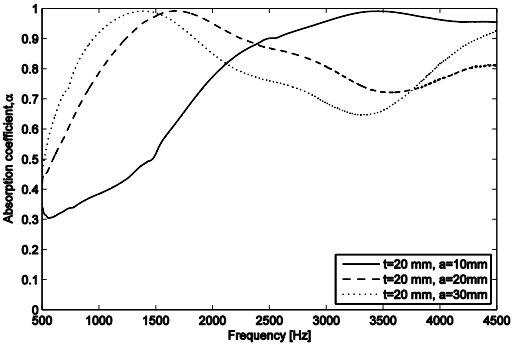

Figure 4 Sound absorption coefficient of 20 mm thick Kenaf fiber with air gap thickness of, 10 mm (─), 20 mm (---), 30 mm (···).

The results show that the peak shifts to lower frequency as the air gap increases, but in consequences, the absorption at high frequencies are reduced. Figure 5 plots the sound absorption coefficient of fiber with thickness of 10 mm, measured with rigid backing, and 10 mm of air gap. This also compared with 20 mm fiber. Comparing the 10 mm without and with air gap backing, the latter has greater absorption coefficient as already shown in Figure 4. However, with identical total thickness, i.e. for 20 mm fiber and 20 mm fiber-air, the performance of air gapped fiber is lower than that from the sample with more fibers.

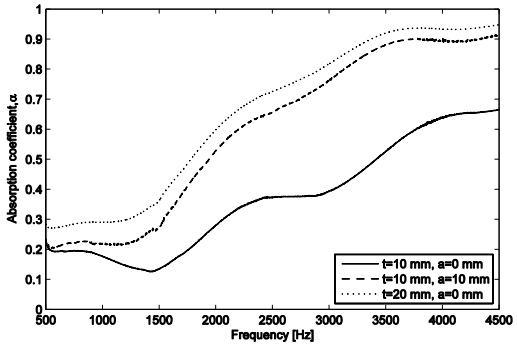

Figure 5 Sound absorption coefficient of kenaf fiber with thickness of 10 mm backed with rigid backing (─), 10 mm with air gap of 10 mm (---), and 20 mm with rigid backing

4. CONCLUSIONS

Measurement on the sound absorption of kenaf fiber shows that kenaf fiber has a potential to be employed as an alternative acoustic material. The experimental results show that for 30 mm thick sample, the performance can closely reach unity above 1.5 kHz. Additional air gap for thinner sample of 20 mm thick is also shown to improve the absorption coefficient close to unity.

5. REFERENCES

[1] F. Asdrubali, "Survey on the Acoustical Properties of New Sustainable Materials for Noise Control," in *Euronoise 2006,* 30, 2006.

[2] L. P. Bastos, G. D. S. V. de Melo, and N. S. Soeiro, "Panels Manufactured from Vegetable Fibers: An Alternative Approach for Controlling Noises in Indoor Environments," *Advances in Acoustics and Vibration*, vol 2012, 2012.

[3] A. Putra, Y. Abdullah, H. Efendy, W. M. Farid, M. R. Ayob and M. S. Py, "Utilizing Sugarcane Wasted Fibers As a Sustainable Acoustic Absorber," in *Procedia Engineering*, 53, 2013.

[4] A. Putra, Y. Abdullah, H. Efendy, W. M. F. W. Mohamad, and N. L. Salleh, "Biomass from Paddy Waste Fibers as Sustainable Acoustic Material," *Advances in Acoustics and Vibration*, vol 2013, 2013.

[5] F. D'Alessandro, and G. Pispola, "Sound Absorption Properties of Sustainable Fibrous Materials in an Enhanced Reverberation Room," in *The 2005 Congress and Exposition on Noise Control Engineering,* 2005.

[6] A. M. Mohd Edeerozey, H. M. Akil, A. B. Azhar, and M. I. Zainal Ariffin, "Chemical Modification of Kenaf Fibers," *Materials Letters*, 61(10), 2023-2025, 2007.

Mobility of rectangular plate with constraint and unconstraint edges

K.H. Lim[1], A. Putra[1,2,*], R. Ramlan[1,2]

[1)] Faculty of Mechanical Engineering, Universiti Teknikal Malaysia Melaka,
Hang Tuah Jaya, 76100 Durian Tunggal, Melaka, Malaysia.
[2)] Centre for Advanced Research on Energy, Universiti Teknikal Malaysia Melaka,
Hang Tuah Jaya, 76100 Durian Tunggal, Melaka, Malaysia.

[*]Corresponding e-mail: azma.putra@utem.edu.my

Keywords: Mobility; vibration; plate

ABSTRACT – Several theories have been established in calculating the mobility of rectangular plate. However, there is still a lacking of discussion on the mobility of plate with various boundary conditions. In this paper, modal summation approach is used to present the mobility of rectangular plates with various constraint and unconstraint edges to discuss their effect on the level of vibration across the frequency range. It is found that at very low frequency (1-20 Hz) that the more constraint the edges the lower the mobility.

1. INTRODUCTION

Concepts of mobility and impedance have been commonly used to investigate the responses of forced structures and power radiated or transmitted by the structures. Over the years, many technique and different approaches have been used to find the mobility of plates with various boundary conditions. The exact solutions available are for plate with simply supported, at least one pair of opposite edges. Extensive study has been carried out by Leissa [1] and presented the mode shape of the plates with various boundary conditions in monograph. Later, Warburton [2] produced a set of approximate frequency formulas derived from Rayleigh method in calculating mobility of the plates with various boundary conditions. The assumption is that the mode shape of the plate is the multiplication of vibrating beam eigenfunctions. The objective of this paper is to calculate and to present the mobility across the frequency of excitation with various boundary conditions using modal summation approach.

2. METHODOLOGY

Consider a plate with dimension l_x and l_y as shown in Figure 1. The reference point is located at the corner of the plate, O.

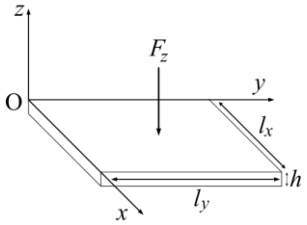

Figure 1 Rectangular plate with dimension l_x and l_y and thickness h.

According to Soedel [3], mobilities of finite plates can be written in terms of a modal summation. The mobility of the plate can be calculated by [3]

$$Y = \frac{v_z}{F_z} = j\omega \sum_{m=1}^{\infty}\sum_{n=1}^{\infty} \frac{\psi_{mn}(x_2, y_2)\psi_{mn}(x_1, y_1)}{\rho h l_x l_y [\omega_{mn}^2(1 + j\eta) - \omega^2]} \quad (1)$$

where v_z is the velocity of the plate in z-direction, F_z is the force excitation, $\psi_{mn}(x_2, y_2)$ is the (m,n) th bending natural mode and ω_{mn} is the (m,n) th natural frequency and η is the loss factor and ω is harmonic circular frequency with implicit time dependence $e^{j\omega t}$.

Mode shape of the plate $\psi_{mn}(x_2, y_2)$ is the product of the characteristic function of beam in *x*-direction and *y*-direction which is

$$\psi_{mn}(x, y) \cong \phi(x) \cdot \phi(y) \quad (2)$$

The characteristic function of the beam can be found in [3]. Natural frequencies for rectangular plates with various boundary conditions given by [2]

$$\omega_{mn} = \sqrt{\frac{Eh^2}{12\rho(1-\nu^2)} \cdot \left(\frac{\pi}{l_x}\right)^2 q_{mn}} \quad (3)$$

where

$q_{mn} = \sqrt{G_x^4(m) + G_y^4(n)(a)^2 + 2(a)^2(b)}$ with

$a = l_x / l_y$ and $b = \nu H_x(m) H_y(n) + (1-\nu) J_x(m) J_y(n)$

for ν is Poisson ratio, E is Young modulus, h is thickness of the plate, and ρ is density of the plate. The coefficient G_x, G_y, J_x, J_y, H_x and H_y for different boundary conditions correspond to the number of mode (m,n) th can be found in [2].

3. RESULTS AND DISCUSSION

Results presented in the paper are calculated for aluminum plate with dimensions of $0.5 \times 0.6 \times 0.003$ m^3, Young modulus of 7.1×10^{10} N/m^2, Poisson ratio of 0.3,

and density of 2700 kg/m^3. Calculation in MATLAB was performed up to 1 kHz with frequency step of 0.005Hz. The notation of the plate boundary condition uses 'S' for simply supported, 'F' for free and 'C' for clamp.

3.1 Validation of Results

The results of each plate with different boundary conditions are validated through finite element method (FEM) using software ABAQUS 6.10. A plate with the same dimension and material properties is created for simulation. The mesh resolution used is 0.01. The result calculated frequency range is up to 1 kHz. Figure 2 show mobility of F-F-F-F plate and C-C-C-C plate calculated from analytical model and ABAQUS 6.10. It can be seen that the result calculated from the analytical model shows good agreement with that compute from the ABAQUS 6.10.

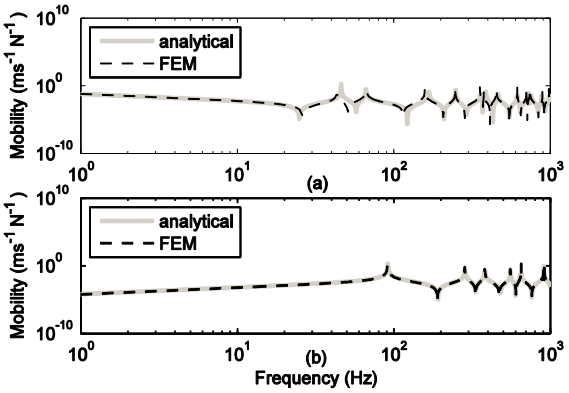

Figure 2 (a) Mobility of F-F-F-F (b) C-C-C-C plate with loss factor of $\eta = 0$.

3.2 Mobility of Plates with All Edges Having Same Boundary Conditions

Figure 3 shows the diagram of plate edges denoted by number. Plate with all edges having the same boundary conditions is indicated by edge-1 = edge-2 = edge-3 = edge-4 in Figure 3.

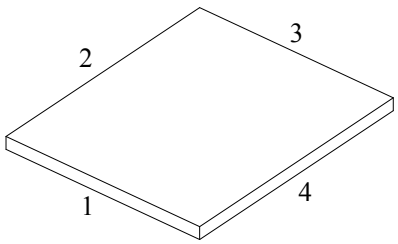

Figure 3 Rectangular plate with numbered edges.

Figure 4 show the mobility for a plate with uniform edges. It can be seen that plate with F-F-F-F edges has a different trend from frequency below 45 Hz compared to all other edges boundary condition. This is due to the even and rock mode. It also shows that F-F-F-F plate has the highest mobility and C-C-C-C plate has the lowest mobility at low frequency (1-20 Hz).

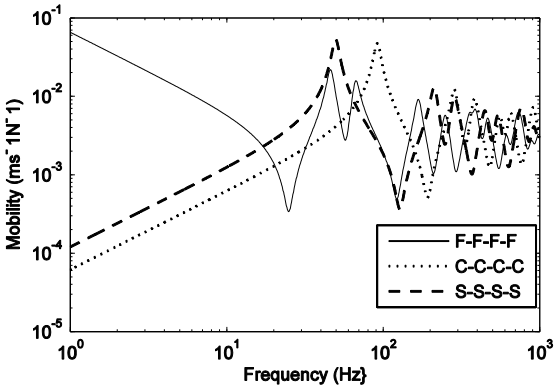

Figure 4 Mobility of plate with same boundary conditions at all edges with loss factor of $\eta = 0.1$.

3.3 Mobility of Plates with Identical Opposite Edges

Identical opposite edges is when edge-1 = edge-2 and edge-3 = edge-4 referring to Figure 3. It can be seen in Figure 5 that the more the edges is constrained, the lower the mobility at low frequency (1-20 Hz). This can be seen for the C-C-S-S plate. Conversely, the plate with less constraint edges has the greatest mobility as seen for F-F-S-S plate at low frequency (1-20 Hz) in Figure 5.

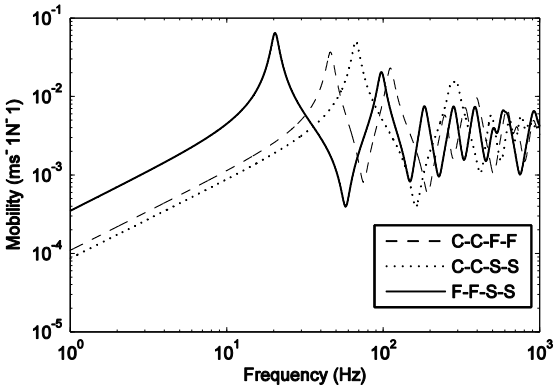

Figure 5 Mobility of plate with identical opposite side boundary condition with loss factor of $\eta = 0.1$.

4. CONCLUSIONS

The mobility of plates with various boundary conditions has been presented. Significant vibration level can be seen at low frequency (1-20 Hz) where the greatest mobility is given by the plate with less constraint edges. At high frequency, average level of mobility is almost similar for all the boundary conditions.

5. REFERENCES

[1] A. W. Leissa, "Vibration of plates," *NASA SP-160,* 1969.

[2] G. B. Warburton, "The vibration of rectangular plates," in *Proceedings of the Institution Mechanical Engineers,* 1954, pp. 371-384.

[3] P. Gardonio, and M.J Brenan, *Advanced applications in acoustics, noise and vibration*, Taylor & Francis; 2004.

Oil palm empty fruit bunch fibers as sustainable acoustic material

K.H. Or[1,2], A. Putra[1,2,*], M.Z. Selamat[1,2]

[1)] Faculty of Mechanical Engineering, Universiti Teknikal Malaysia Melaka,
Hang Tuah Jaya, 76100 Durian Tunggal, Melaka, Malaysia.
[2)] Centre for Advanced Research on Energy, Universiti Teknikal Malaysia Melaka,
Hang Tuah Jaya, 76100 Durian Tunggal, Melaka, Malaysia.

[*]Corresponding e-mail: azma.putra@utem.edu.my

Keywords: Natural fiber; Oil Palm Empty Fruit Bunch; sound absorption coefficient

ABSTRACT – Environmental issues such as pollutions have created awareness among the scientists to find sustainable and 'green' materials as alternative sound absorber to replace synthetic materials. Oil Palm Empty Fruit Bunch (OPEFB) is a biodegradable material and is available in abundance quantity as agricultural by-products. This paper discusses the use of OPEFB fibers as an acoustic absorber. Samples of raw OPEFB fibers with different mass and thickness are fabricated. The effect of fiber density and air gap are investigated through experiment to obtain the sound absorption coefficient. It is found that OPEFB fibers showed good performance as an acoustic material.

1. INTRODUCTION

Acoustic absorber is used to absorb a certain frequency range of sound wave to reduce noise level and to improve the communication between the speaker and audiences. Traditionally, synthetic materials are used widely as acoustic absorber. These synthetic materials such as glass wool, stone wool and foam plastics not only cause pollution and global warming, but can also harmful to human life [1]. Thus, researchers have changed the focus towards natural materials as the alternative way to replace synthetic materials. Nor et al. [2] tested the effect of compression on the sound absorption properties of coir fiber. The compression work on coir fiber can enhance the sound absorption at low frequency. Putra et al. [3] employed the sugarcane wasted fibers as acoustic absorption material and the results show the increase of fiber density improves the sound absorption performance. Experimental work by Putra et al. [4] on paddy waste fibers also show good sound absorption coefficient and is comparable with synthetic glass wool at the same thickness. Traditionally, oil palm empty fruit bunch (OPEFB) fibers are used as burning fuel, fertilizers, mulching material and reinforcement materials in polymer composites [5]. This paper discusses the acoustic performance of OPEFB fibers which according to the author's knowledge has not been investigated by other researchers.

2. METHODOLOGY

The OPEFB fibers were weighted for 1, 2, 3, 4, 5, 6 and 7 grams and fitted into a 33 mm diameter aluminium mold for sample preparation. By using hot compression molding, the OPEFB fibers were compressed into samples with thickness of 10 mm and 20 mm as shown in Figure 1.

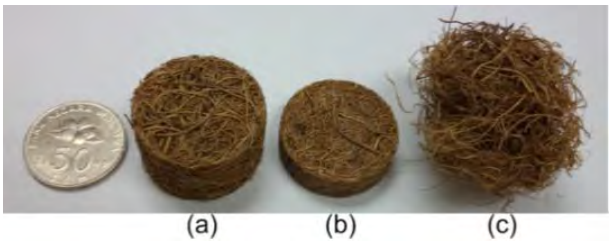

Figure 1 OPEFB: (a) 5 gram of 20 mm thickness sample, (b) 5 gram of 10 mm thickness sample and (c) raw fiber

The measurement of sound absorption coefficient was conducted using the impedance tube as shown in Figure 2 according to ISO 10534-2 [6]. The sample was fitted into the 33 mm diameter tube at one end while the other end was the location of a loudspeaker. White noise was generated from the computer through Audacity 1.3 Beta software and supplied into the tube through the loudspeaker. Two ½" pre-polarized free field microphones with ½" CCP pre-amplifier were located near the sample to record the built-up sound pressure. The two microphones were 22.5 mm apart. The loudspeaker was located 132.5 mm from the first microphone. The distance between the second microphone to the sample was 85 mm. The validity of the result was between frequency of 500 Hz to 4500 Hz due to the diameter of the tube. Range of the frequency was limited by the accuracy of the signal processing equipment and to avoid the occurrence of non-plane wave mode propagation [6].

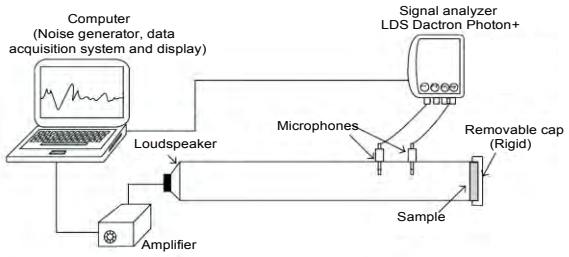

Figure 2 Experimental setup for measurement of sound absorption coefficient

3. RESULTS AND DISCUSSION

Figure 3 plots the absorption coefficient for samples with different densities at 10 mm thickness. At the same thickness, mass of 2, 3, 4 and 5 grams showed good absorption coefficient where $\alpha > 0.5$ above 2 kHz which is a typical frequency range for a fibrous type absorber. It can also be seen that increased the density or mass of the sample improves the absorption at higher frequency range. The increment in density contributes to increase of flow resistivity and tortuosity. Thus, more sound waves can be absorbed. However, too high density can limit the porosity in the sample and thus degrade the absorption performance. As shown in Figure 3, sample with mass of 6 and 7 grams showed absorption coefficient of less than 0.5.

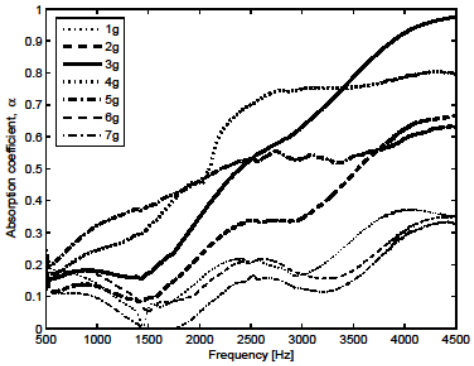

Figure 3 Absorption coefficients of OPEFB fibers with different masses

The effect of thickness can be seen in Figure 4. It is shown that the increase of thickness significantly enhances the absorption coefficient and shifts the peak of the absorption coefficient to the lower frequency region.

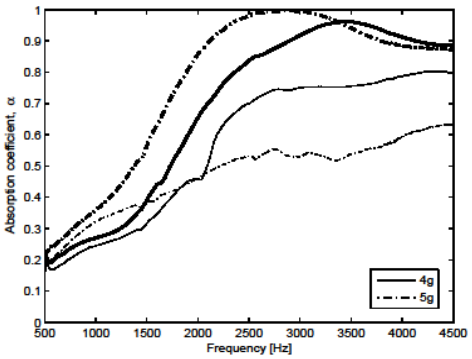

Figure 4 OPEFB fibers with two different masses and thicknesses of: 10 mm (thin line) and 20 mm (thick line)

The absorption coefficient at lower frequency can also be enhanced by providing the air gap behind the fiber sample. As shown in Figure 5, the utilization of air gap shifts the curve to the lower frequency. However, good absorption coefficient at lower frequency region was compromised with the reduction of absorption at high frequency.

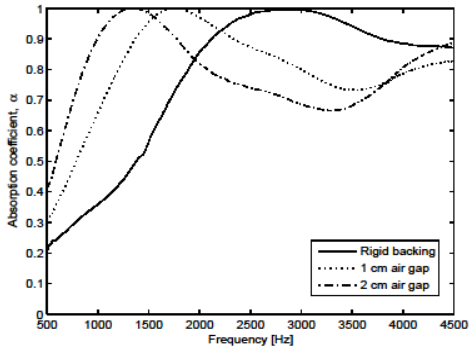

Figure 5 Absorption coefficient of OPEFB fibers with mass of 5 gram and 20 mm in thickness with different air gaps

4. CONCLUSIONS

The oil palm empty fruit bunch fibers are found to be good sound absorber and can be the alternative to the synthetic sound absorber. The increase of mass or density yields high absorption coefficient at high frequency region. For 10 mm samples with 4 grams fibers, the absorption coefficient can reach 0.75 in average above 2.5 kHz. For 20 mm, the average absorption coefficient increase to 0.9. Increment in thickness and application of air gap resulted in increase of absorption coefficient at lower frequency region.

5. ACKNOWLEDGEMENT

Part of this research is supported under the Exploratory Research Grant Scheme No. ERGS/1/2013/STG02/UTEM/02/01 provided by the Ministry of Higher Education Malaysia (MoHE).

6. REFERENCES

[1] F. Asdrubali, "Survey on the acoustical properties of new sustainable materials for noise control," in *Euronoise*, 2006, pp. 1-10.

[2] M.J.M. Nor, M. Ayub, R. Zulkifli, N. Amin, and M.H. Fouladi, "Effect of compression on the acoustic absorption of coir fiber," *American Journal of Applied Sciences*, vol. 7, no. 9, pp. 1285-1290, 2010.

[3] A. Putra, Y. Abdullah, H. Efendy, W.M.F.W. Mohamad, M.R. Ayob, and M.S. Py, "Utilizing sugarcane wasted fibers as a sustainable acoustic absorber," *Procedia Engineering*, vol. 53, no. 1, pp. 632-638, 2013.

[4] A. Putra, Y. Abdullah, H. Efendy, W.M.F.W. Mohamad, and N.L. Salleh, "Biomass from paddy waste fibers as sustainable acoustic material," *Advances in Acoustics and Vibration*, vol. 2013, pp. 1-7, 2013.

[5] R. Mahjoub, J.M. Yatim, and A.R.M. Sam, "A review of structural performance of oil palm empty fruit bunch fiber in polymer composites," *Advances in Materials Science and Engineering*, vol. 2013, pp. 1-9, 2013.

[6] *Acoustics - Determination of sound absorption coefficient and impedance in impedance tubes - Part 2: Transfer-function method*, ISO 10534-2, 2001.

Reciprocity method in a small acoustic space to measure sound radiation from baffled perforated plates

N. Shyafina[1,2], A. Putra[1,2,*], Z.Y. Lim[1,2], N. Muhammad[1]

[1)] Faculty of Mechanical Engineering, UniversitiTeknikal Malaysia Melaka, Hang Tuah Jaya, 76100 Durian Tunggal, Melaka, Malaysia.
[2)] Centre for Advanced Research on Energy, UniversitiTeknikal Malaysia Melaka, Hang Tuah Jaya, 76100 Durian Tunggal, Melaka, Malaysia.

[*]Corresponding e-mail: azma.putra@utem.edu.my

Keywords: sound power; reciprocity; radiation efficiency

ABSTRACT – Reciprocity method has been used widely in vibro-acoustics especially to measure sound power from vibrating structures. One existing method is the measurement under a reverberant condition inside a reverberation chamber. This paper discusses the reciprocity method implemented in a small acoustic box rather than using a proper, large acoustic chamber. The result shows the radiation efficiency of perforated baffled plate with different number of holes and different perforation ratios to have good agreement between the measured data and the theory.

1. INTRODUCTION

The technique of vibro-acoustic reciprocity was based on the theory proposed by Lyamshev [1] where it is stated that the acoustic pressure at a point B due to a vibrating structure subjected to a harmonic mechanical force at a point A is 'equivalent' through a reciprocity relationship with the situation where the vibration velocity is produced at the point A on the structure due to acoustic excitation by a point source located in fluid at the point B. This is illustrated in Figure 1.

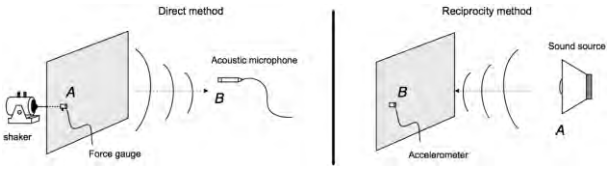

Figure 1 Illustrative diagram of reciprocity method.

From this fundamental theory, several techniques of reciprocity were expanded including to measure noise transmission in an aircraft fuselage [2], to measure sound pressure radiated by a combustion engine [3], to study the tyre induced vehicle interior noise [4] and is also used as noise source characterization [5].

Recently, Squicciarini et. al [6] used reciprocity method in reverberant condition to determine the radiation efficiency of vibrating structures including two components of a railway track test-rig and three different built-up structures. The results using the reciprocity method show good agreement between the direct measurement and those from the finite element model.

In this paper, the same technique in [6] is used, but using a small acoustic chamber and to measure the radiation from baffled plate condition.

2. FUNDAMENTAL EQUATION

The radiation efficiency of a vibrating structure can be determined by means of two measurements: an acoustic measurement (radiated sound power) and the spatially-averaged squared velocity representing by the mobility. This is represented by

$$\sigma = \frac{W / \overline{F^2}}{\rho c S <|Y_t|^2>} \tag{1}$$

where ρ is the air density, c is the speed of sound, S is the surface area of the structure and $<|Y_t|^2>$ is the spatially-averaged transfer mobility.

The normalised sound power $W/\overline{F^2}$ can be conventionally measured using the sound intensity probe. However, using the reciprocity technique, this is defined as [6]

$$\frac{W}{\overline{F^2}} = \frac{\overline{a^2}}{<\overline{p^2}>}\left(\frac{\rho}{4\pi c}\right) \tag{2}$$

where $\overline{a^2}$ is the acceleration response of the structure due to acoustic excitation on the plate and $<\overline{p^2}>$ is the spatially-averaged mean-square acoustic pressure in the test room. Using the measured mobility, the radiation efficiency of the plate can then be obtained from Equation (1).

3. EXPERIMENTAL SETUP

The measurement for plate mobility was first determined by hanging the plate with soft rope to a rigid frame. A miniature accelerometer was attached to the plate to measure the plate vibration when the plate was excited by an impact hammer at ten locations across the plate surface. The acceleration (converted to velocity) from the accelerometer and the force recorded from the impact hammer were used to obtain the spatially averaged squared mobility as required in Equation (1).

In order to measure the radiated sound power using

reciprocity method, the experiment was conducted in a small, fabricated acoustic chamber. The steel chamber is made with non-parallel walls to enhance the development of diffuse field in the chamber for reverberant condition and to fulfill the assumption used in Equation (2). Free-field microphone was used to measure the sound pressure radiated in the small chamber having volume of roughly 0.18 m^3 as seen in the Figure 2.

Perforated plates having dimension of 0.3 × 0.2 m and thickness of 1 mm with varying number of holes and diameters were placed in frame where all the edges are rested on soft foam to simulate free-free conditions. The frame was then laid on the top of the chamber, covering the square opening hole from where the sound from the loudspeaker inside the chamber excited the plate. The arrangement is considered baffled condition as the sound excited the plate from one surface only.

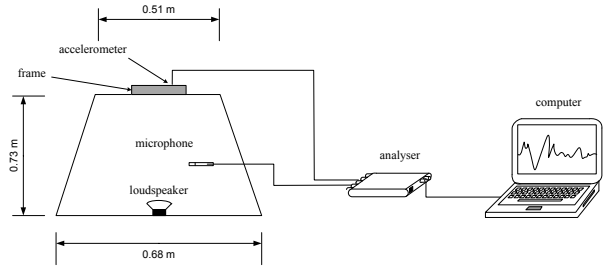

Figure 2. Measurement setup for reciprocity method in a small chamber.

4. RESULTS AND DISCUSSION

Figure 3 shows the measured radiation efficiency for perforated plates with number of holes of $N = 20$ and 34 and perforation ratios of $\tau = 20\%$ and 30%. The measured results show the typical trend expected from radiation efficiency and follows that of the theory [7], starting with low value at low frequencies and increases towards the critical frequency.

Good agreement with the theory can be seen across the frequency except at several frequency ranges for example around 2 kHz in Figure 3(a) and around 500-800 Hz in Figure 3(b). High possibility of error could come from the acoustic measurement where more sound source locations are required to obtain good 'average' of sound field in the chamber and directivity of excitation incidence on the plate.

5. CONCLUSIONS

The reciprocity method has been successfully conducted to measure radiated sound power from perforated baffled plates in a small acoustic chamber. The measured radiation efficiency shows good agreement with the theory. However care should be taken in the future measurement for example by considering several locations of sound source to obtain more representative averaged energy.

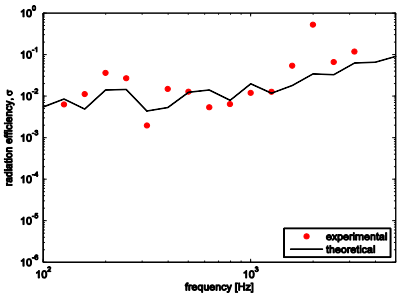

(a)

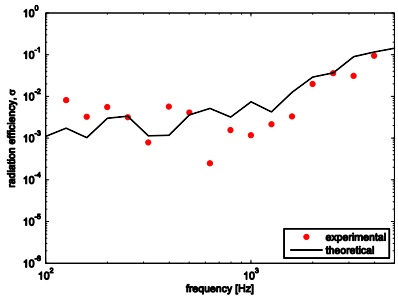

(b)

Figure 3. Radiation efficiency of perforated plate with (a). $N = 20$, $\tau = 20\%$ and (b). $N = 34$, $\tau = 30\%$.

6. ACKNOWLEDGEMENT

The authors gratefully acknowledge the Universiti Teknikal Malaysia Melaka (UTeM) for funding this project under the Short Term Research Grant No. PJP/2012/FKM (5C)/S1007.

7. REFERENCES

[1] L.M. Lyamshev, "A method for solving the problem of sound radiation by thin elastic shells and plates," *Soviet Physic-Acoustic,* vol. 5, pp. 122-124, 1959.

[2] D.G. MacMartin, G.L. Basso, F.W. Slingerland, "Aircraft fuselage noise transmission measurement using a reciprocity technique," *Journal of Sound and Vibration,* vol.187, no. 3, pp. 467-483, 1995.

[3] J. Zheng, F.J. Fahy, D. Anderson, "Application of a vibro-acoustic reciprocity technique to the prediction of sound radiated by a motored IC engine," *Applied Acoustics*, vol. 42, no. 4, pp. 333-346, 1994.

[4] B.S. Kim, G.J. Kim,T.K. Lee, " The identification of tyre induced vehicle interior noise," *Applied Acoustics,* vol. 68, no. 1, pp. 134-156, 2007.

[5] J.W. Verheij, "Inverse and reciprocity methods for machinery noise source characterization and sound path quantification. Part 1: sources", *International Journal of Acoustics and Vibration,* vol. 2, pp. 11-20, 1997.

[6] G. Squicciarini, A. Putra, D.J. Thompson, X. Zhang, M.A. Salim, "Use of a reciprocity technique to measure the radiation efficiency of a vibrating structure," *Applied Acoustics,* vol. 89, pp. 107-121, 2015.

[7] A. Putra. "Sound radiation from perforated plates." PhD Thesis. University of Southampton, United Kingdom 2008.

Double layered micro-perforated panel as acoustic absorber in mosque

D. Hafizah[1], A. Putra[1,2,*], M.J.M. Noor[1,2] and M.S. Py[1,2]

[1)] Faculty of Mechanical Engineering, Universiti Teknikal Malaysia Melaka,
Hang Tuah Jaya, 76100 Durian Tunggal, Melaka, Malaysia.
[2)] Centre for Advanced Research on Energy, Universiti Teknikal Malaysia Melaka,
Hang Tuah Jaya, 76100 Durian Tunggal, Melaka, Malaysia.

[*]Corresponding e-mail: azma.putra@utem.edu.my

Keywords: speech intelligibility; double layered micro-perforated panels; mosque acoustics

ABSTRACT – Poor speech intelligibility in large mosque is still a classical problem in many cases to due to lack of consideration for its acoustic performance in the architectural design of the mosque's interior. This paper presents the assessment of indoor acoustics performance of a mosque by using CATT acoustic software. Double layered micro-perforated panel as the acoustic absorber is introduced. It is aimed at discussing the possibility to utilize the micro-perforated panels, which is new for mosque application instead of the typical porous, fibrous absorbers or the conventional Helmholtz resonator. The results show that the micro-perforated panels successfully reduce the reverberation time at low frequencies which can improve the speech intelligibility in a mosque.

1. ACOUSTICS IN MOSQUE

Mosque is an important house of worship for Muslims. As most activities in a mosque deal with speech, good speech intelligibility is thus important to ensure clear voice are delivered to the congregations. Acoustic performance in mosque therefore becomes topics of interest to be studied. The existing studies using simulation include the effect of the wall geometry [1] and roof/ceiling shape [2, 3]. Some studies also conducted on-site measurements for acoustic characterization [4,5]. Discussion on the utilization of the new generation of non-fibrous absorber, namely the micro-perforated panel (MPP) in a mosque is still lacking. As most acoustic problems in mosque are at low frequencies [6], implementation of the MPP absorber is thus more suitable than the fibrous or porous materials which are best at mid to high frequency range. The MPP performance also resembles that of a Helmhotlz resonator. Simulation for the single MPP, however has been presented in [7] and in this paper, investigation is extended to the double micro-perforated panels (DMPP).

2. SIMULATION MODEL

2.1 CATT Geometry Model

Indoor geometry for the simulation model is developed by using CATT acoustic software version 9. The volume of the mosque is chosen to imitate a mosque having a typical large volume of the main hall area as seen in Figure 1. This geometry of mosque, with a unique inclined ceiling is mostly found in Melaka, Malaysia which follows the architecture a traditional Malay house.

Omni directional sound source is placed in front of the mihrab to simulate the speech coming from this area. The main prayer hall is divided into 16 symmetrical areas; with each of the area contains one receiver of 0.5 m to assume the height of ear of a person sitting on the carpeted floor. The absorption coefficient for the materials in the interior including the concrete wall, plaster ceiling, glass window, solid wooden door and thick carpet are extracted from the software data library.

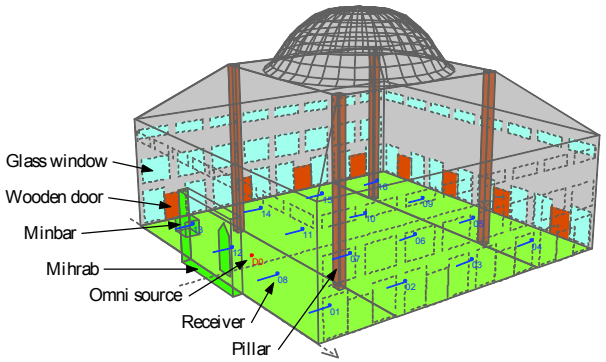

Figure 1 The 3D view of mosque model from CATT.

2.2 Double layered micro-perforated panel (DLMPP)

The theory and design of micro-perforated panel (MPP) were pioneered by Dah You Maa in 1975 [8]. MPP are solid panels with holes of less than 1 mm and perforation ratio between 0.5–1 %. The performance of sound absorption for MPP is usually narrow and is mainly at low frequency. The double layered micro-perforated panel (DMPP) is found to be able to widen the frequency band of absorption. Figure 2 shows the diagram of the DMPP system and the analytical simulation of absorption coefficient for different distances between first MPP, D and between second MPP, L where both distances are from a rigid wall.

3. REVERBERATION TIME RESULTS

The first simulation is run for the CATT model without MPP installed in the mosque. It is found that the RT reaches 6.47 s at 500 Hz and 4 s at 1 kHz. This is used as the baseline result. The second is by assuming the whole inclined ceiling is covered with DMPP (as

seen in Figure 3) with the absorption coefficient of DMPP is as shown in Figure 2(b).

Figure 4 shows the simulation results with DMPP installed on the ceiling. The RT can be seen to reduce to below 3 s at 500 Hz and to below 2.5 s at 1 kHz. The more speech content to the sound, the lower the ideal RT in a room should be. However, by compromising the recitation of Quran as a liturgical music, RT between 2 s to 3 s could still be acceptable [9].

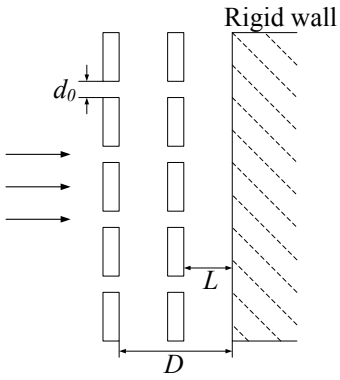

(a)

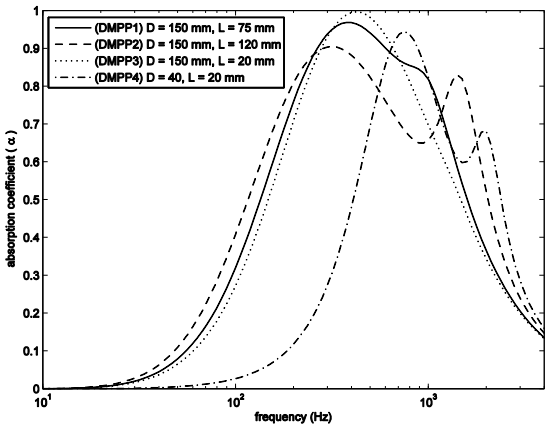

(b)

Figure 2(a) Schematic diagram of DMPP in front of a rigid wall and (b) absorption coefficient of DMPP.

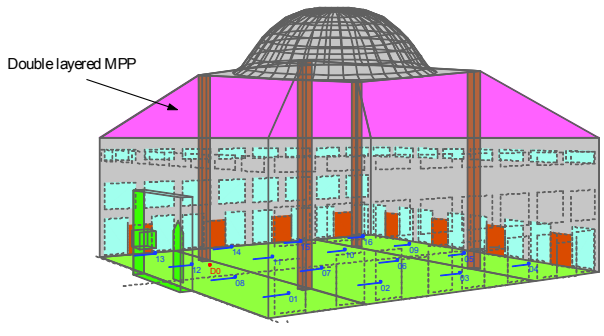

Figure 3 CATT model with DMPP installed on ceiling.

4. CONCLUSIONS

It has been shown from the simulation that use of DMPP in the mosque to improve the acoustic performance is feasible. For the depth of the study in the future, results from real measurement is therefore of interest.

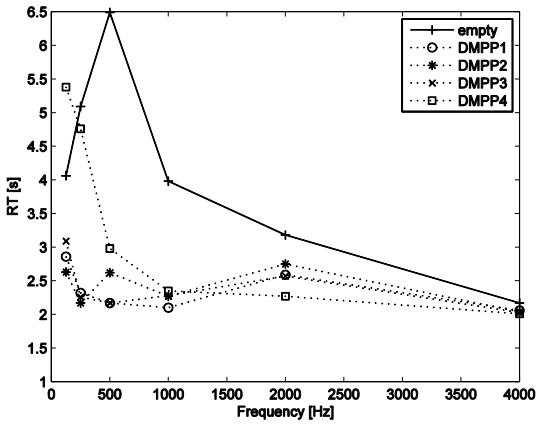

Figure 4 The simulation results of reverberation time.

5. ACKNOWLEDGEMENT

The authors gratefully acknowledge the Universiti Teknikal Malaysia Melaka (UTeM) for funding this project under the Short Term Research Grant No. PJP/2012/FKM(50C)/S01069.

5. REFERENCES

[1] A. A. Abdou, "Comparison of the acoustical performance of mosque geometry using computer model studies", *8th International. IBPSA Conf*erence, Eindhoven, Netherlands, pp. 39-46, 2003.

[2] N. Prodi, M. Marsilo. "On the effect of domed ceiling in worship spaces: A scale model study of a mosque", *Building Acoustics*, vol 10, no. 2, pp. 117-133, 2003.

[3] D.H. Kassim, A. Putra, M.J.M. Nor, N.S. Muhammad, "The effect of pyramidal dome geometry on the acoustical characteristics in a mosque", *Journal of Mechanical Engineering and Sciences*, vol. 7, pp. 1127-1133, 2014.

[4] A.A. Abdou, "Measurement of acoustical characteristics of mosques in Saudi Arabia", *The Journal of the Acoustical Society of America*, vol. 113, no. 3, pp. 1505-1517, 2003.

[5] M. K. Abdelazeez, R.N. Hammad, A.A. Mustafa, "Acoustics of King Abdullah mosque", *The Journal of the Acoustical Society of America*, vol. 90, no. 3, pp. 1441-1445, 1991.

[6] E. Setiyowati, "Strategies to increase the acoustical quality of the mosques without reinforcement system", *Journal of Islamic Architecture*, vol. 1, no. 1, pp. 27–31, 2010.

[7] A. Putra, D. Hafizah, M.Y. Yaakob, M.J.M. Nor, "Study on the use of micro- perforated panel to improve acoustic performance in mosque", *Applied Mechanics and Materials*, vol. 393, pp. 971-975, 2013.

[8] D. Y. Maa, "Theory and design of microperforated panel sound-absorbing", *Scientia Sinica* (in Chineese), vol. 18, no. 1, pp. 55-71, 1975.

[9] D.H. Kassim, A. Putra, M.J.M. Nor,"The acoustical characteristics of the Sayyidina Abu Bakar Mosque, UTeM", *Journal of Engineering Science and Technology* (Accepted in Press).

Noise analysis in Malaysian passenger car cabin

M.A. Abdullah[1,2,*], J.F. Jamil[1,], N. Basrah[1], A. Putra[1,2], M.A. Salim[1,2]

[1)] Faculty of Mechanical Engineering, Universiti Teknikal Malaysia Melaka, Hang Tuah Jaya, 76100 Durian Tunggal, Melaka, Malaysia.
[2)] Centre for Advanced Research on Energy, Universiti Teknikal Malaysia Melaka, Hang Tuah Jaya, 76100 Durian Tunggal, Melaka, Malaysia.

*Corresponding e-mail: mohdazman@utem.edu.my

Keywords: Noise analysis; noise distribution; passenger comfort; vehicle cabin noise.

ABSTRACT - In this paper, experimental study on noise analysis in cabin of a 1.3 cc passenger car is performed. The noise is recorded using sound level meter at 3 different places, namely, at the hand brake, near the drivers' pedals and at the bottom of front passengers' seat. The experimental study is performed at different engine speeds at static and dynamic conditions with and without air conditioner switched on. The data is analyzed and discussed for comparison. The noise distribution in the passenger cabin is generated at 3 locations. From the results, it is shown that, different locations give different density of noise. The passengers' noise comfort level is still achieved with and without air conditioning.

1. INTRODUCTION

There are many sources of noise in passenger car cabin. In previous studies, in order to provide passenger comfort, researchers tried to reduce the noise either by; trouble shooting the source or improving the sound barrier by applying sound absorber. The noise is coming from engine and powertrain, tire, wind and air conditioning system. The road and tire interaction is generally providing low frequency noise depending on speed, road surface and tire configuration. The engine in the powertrain system creates noise even at idle engine operation due to vibration of the components and parts [1]. The noise from wind is affecting the cabin due to aerodynamic surface, speed and sometimes by the side mirror and windows' visors [2]. The air conditioning system however, is always neglected due to the necessity for the passenger comfort inside the cabin.

In this research, noise experimental analysis is performed on a Malaysian passenger car cabin. The data is studied and analyzed at different positions and vehicle conditions. This study is carried out to measure the noise inside the car cabin and justified whether the noise is acceptable for the passenger.

2. METHODOLOGY

A 1.3 cc Malaysian passenger car is used in this experiment. The engine speed is set from 1000 to 3000 rpm at static and dynamics conditions. During dynamic testing, the car is operated at speed from 80 to 120 km/h. The route for dynamic test is shown by Figure 1. RION Sound Level Meter is used in this experiment (Figure 2).

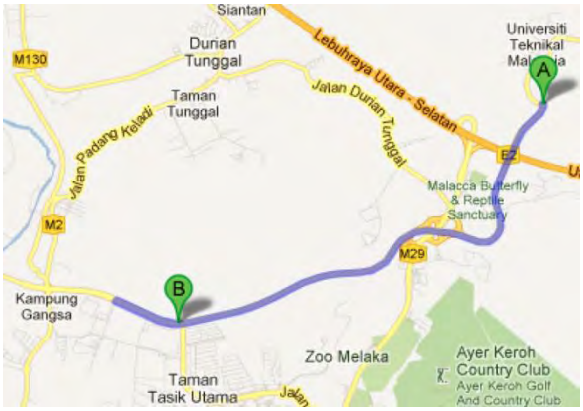

Figure 1 Dynamic test route

Figure 2 Sound level meter

3. RESULTS AND DISCUSSION

The passenger comfort level for noise is around 40 to 50 dB at frequency from 2.5k to 3k Hz [4][5]. Based on this fact, the results of the noise analysis are focused at frequency from 2 to 4 kHz. Figure 3, 4 and 5 show the noise data for 2 kHz, 4 kHz and at 3000 rpm engine speed.

From Figure 3 and 4, it can be observed that the speed of the car affects the noise inside the cabin. The noise inside the cabin is increased as the speed increased. This is due to the fact that as the engine turns faster to provide power for the car to increase speed, more vibration is generated internally. As the speed increased, more interaction between tire and road is happened. These vibrations and interactions cause the

increment of noise inside the cabin of the car. The different between air conditioning systems switched on and off is only about 1 dB.

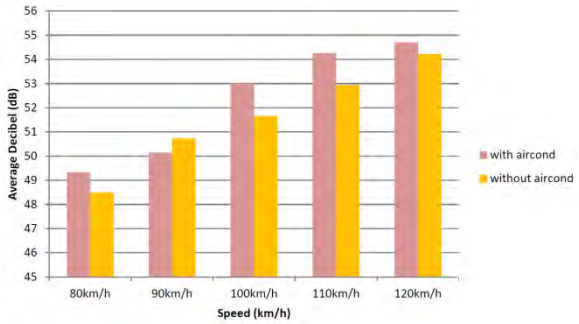

Figure 3 Noise data at 2 kHz

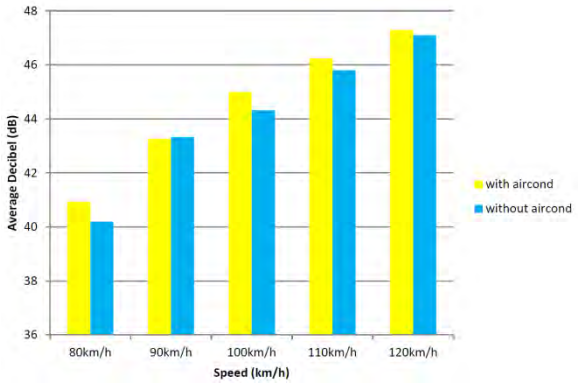

Figure 4 Noise data at 4 kHz

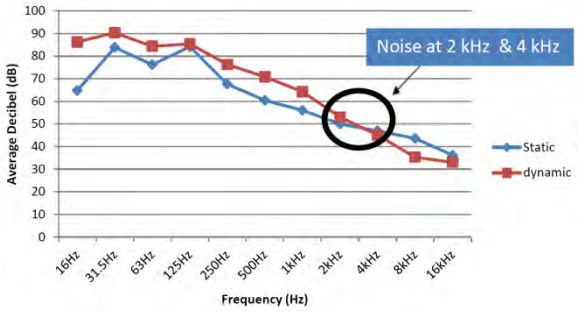

Figure 5 Noise data at 3000 rpm engine speed

4. CONCLUSIONS

The noise inside the cabin of a car is caused by several reasons. The noise is also affected by the speed of the car. For the comfort of passengers, 1 dB different in noise for the car with and without air conditioning system switched on is acceptable. Since human ears can accept noise as high as 50 dB for comfort level and hear 2 to 3 kHz of frequency, the noise generated inside the cabin for all experiments are considered as comfort.

5. ACKNOWLEDGEMENT

The authors gratefully acknowledged the Advanced Vehicle Technology (AcTiVe) research group of Centre for Advanced Research on Energy (CARe), the financial support from Universiti Teknikal Malaysia Melaka and The ministry of Education, Malaysia under Short Term Research Grant, Grant no. PJP/2014/FKM(10A)/S01330 and Fundamental Research Grant Scheme (FRGS), grant no.: FRGS/2013/FKM/TK06/02/2/F00165.

6. REFERENCES

[1] A. Putra, F.A. Munir and C.D. Juis, “On a simple technique to measure the airborne noise in a car interior using substitution source”, Int. Journal of Vehicle Noise and Vibration, Inderscience Publishers, Vol. 8, No. 3, 275-287. 2012.

[2] A. Putra, A.Y. Ismail and M.R. Ayob, “Employing the micro-perforated panel in the vehicle cabin: Is this possible?”. Malaysian Technical Universities International Conference on Engineering & Technology (MUiCET 2011), 674-679, 2011.

[3] Government of South Australia, “Noise in the workplace: what you should know”. SafeWork SA, Last accessed 02/01/2015, Address: http://www.safework.sa.gov.au/uploaded_files/Noise.pdf, 2015.

[4] Noise Help, “Noise dose chart: noise exposure limits”. Noise Help, Last accessed 02/01/2015, Address: http://www.noisehelp.com/noise-dose.html, 2015.

Variability of vibration input power to a beam structure

N. F.Saari[1,*], A. Putra[1,2], H. Bakri[1], R. Md Dan[1,2]

[1)] Faculty of Mechanical Engineering, Universiti Teknikal Malaysia Melaka,
Hang Tuah Jaya, 76100 Durian Tunggal, Melaka, Malaysia.
[2)] Centre for Advanced Research on Energy, Universiti Teknikal Malaysia Melaka,
Hang Tuah Jaya, 76100 Durian Tunggal, Melaka, Malaysia.

[*]Corresponding e-mail: n.farizasaari@gmail.com

Keywords: structure-borne source; vibration; reception plate

ABSTRACT – Structure-borne source which transmits vibration power to the supporting structure especially in buildings plays a major role in contributing the noise pollution and this remains a challenging problem for noise treatment. In practice however, the lack of knowledge of phase of the excitation force from the structure-borne source creates variability in the input power. This paper discusses the quantification of the frequency-averaged mean and variance from the variability in the input power for the case of two excitation point forces to a beam structure. It is found that quantification of the frequency-average variability from a finite beam structure can be approached by using that from the corresponding infinite beam structure.

1. INTRODUCTION

Information of vibration input power from a structure-borne source is important as a preliminary control measure to allow a structural engineer to take preventive action by ensuring the supported structure is strong enough to absorb the potential vibration power. From this case, technique for structure-borne sound characterisation has been proposed [1,2]. Unfortunately, in order to obtain an accurate prediction of the injected input power, there still remains a problem due to the lack of some information for example the phase of the excitation force which creates uncertainties in the input power. This paper simulates the input power to a simple beam structure with harmonic excitation subjected to two forcing contact points similar to the previous work for plate structure [3]. This discusses the quantification of the frequency-averaged mean and variance of the variability in the input power.

2. FUNDAMENTAL EQUATION

2.1 Input Power in Finite Beam Structure

Figure 1 shows on a finite beam having length *a*, thickness *h* and width *b* subjected to two point forces. The input power can be expressed as:

$$P_{\text{in}} = \tfrac{1}{2}\,\text{Re}\{F^H Y F\} \tag{1}$$

where $F = [F_1 e^{j\phi_1} \;\; F_2 e^{j\phi_2}]$ is the vector of the complex time-harmonic forces, Y is the mobility and ϕ is the phase.

In this paper, only translational force perpendicular to the receiver beam is taken into account. Therefore, the mobility matrix for two contact points is written as:

$$Y = \begin{bmatrix} Y_{11} & Y_{12} \\ Y_{21} & Y_{22} \end{bmatrix} \tag{2}$$

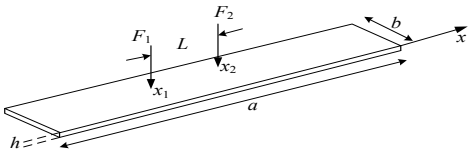

Figure 1 A finite beam with two point forces

where Y_{pq} is the point mobility for mode $p = q$ or transfer mobility for $p \neq q$. For excitation point at x_0 and x, the mobility at frequency ω is given by:

$$Y(x, x_0) = j\omega \sum_{n=1}^{\infty} \frac{\Phi_n(x_0)\Phi_n(x)}{\omega_n^2(1 + j\eta) - \omega^2} \tag{3}$$

where $\Phi_n(x) = (2/M)^{1/2} \sin(n\pi x/a)^2$ is the n-th mass normalised mode with M is the total mass of the beam and $\omega_n = (B/m')^{1/2}(n\pi/a)^2$ is the natural frequency with the bending stiffness of beam $B = Ebh^3/12$, Young's modulus E, mass per unit length m' and the damping loss factor η. The total input power in Eq. (1) in terms of input mobility Y_p is therefore written as:

$$\begin{aligned} P_{\text{in}} &= \tfrac{1}{2}\,\text{Re}\{Y_{11}\}F_1^2 + \tfrac{1}{2}\,\text{Re}\{Y_{22}\}F_2^2 \\ &\quad + \text{Re}\{Y_{12}\}F_1 F_2 \cos\varphi \end{aligned} \tag{4}$$

where $\varphi = \phi_1 - \phi_2$ is the relative phase and note that the transfer mobility $Y_t = Y_{12} = Y_{21}$. For random excitation phase, the probability of relative phase $\varphi_i = 1/2\pi$ is assumed equal and constant. Thus, all the forces can also be assumed to have equal amplitudes. The mean and variance are therefore respectively given by:

$$\mu P_{\text{in}} = \tfrac{1}{2}\,\text{Re}\{\widetilde{Y}_{11}\}F^2 + \tfrac{1}{2}\,\text{Re}\{\widetilde{Y}_{22}\}F^2 \tag{5}$$

$$\sigma^2 P_{\text{in}} = \tfrac{1}{2}\left(\text{Re}\{\widetilde{Y}_t\}F^2\right)^2 \tag{6}$$

2.2 *Input Power in Infinite Beam Structure*

The total input power for an infinite beam subjected to two point forces is also given the same as in Eq. (4). The input and transfer mobilities are given by:

$$Y_{\mathrm{p}} = \frac{\omega}{4Bk^3}(1-j) \tag{7}$$

$$Y_{\mathrm{t}} = \begin{cases} \dfrac{j\omega}{4Bk^3}(-je^{-jkL} - e^{-kL}), & x \geq 0 \\ \dfrac{j\omega}{4Bk^3}(-je^{jkL} - e^{kL}), & x < 0 \end{cases} \tag{8}$$

where $k = \sqrt[4]{m'\omega^2 / B}$. The mean and variance are also the same as in Equations (5) and (6).

2.3 Averaging Over Frequency Bands

The input power can be averaged over the frequency band defined as

$$P_{\mathrm{in}} = \frac{1}{\omega_1 - \omega_2}\int_{\omega_1}^{\omega_2} P_{\mathrm{in}}(\omega)d\omega \tag{9}$$

where excitation frequency lies between two frequencies ω_1 and ω_2. Thus, the frequency-averaged input power in Eqs. (5) and (6) can be calculated numerically using Eq. (9). The relative standard deviation is therefore given by:

$$\gamma_\sigma = \frac{\langle \sigma P_{\mathrm{in}} \rangle}{\langle \mu P_{\mathrm{in}} \rangle} \tag{10}$$

3. RESULTS AND DISCUSSION

Figure 2 shows the frequency-averaged mean power and standard deviation which are averaged over all possible excitation phases and with respect to the non-dimensional force separation distance *kL*. Note that the mean and standard deviation are normalised by the input power to an infinite beam which is also subjected to two point forces. The mean power and standard deviation are seen decay close to the mean power of the infinite beam.

For the same force separation distance *kL*, Figure 3 shows the relative standard deviation between the finite beam and infinite beams which are calculated numerically using Eq. (10) for two different damping loss factors. It can be seen that the result of relative standard deviation from the infinite beam follows the trend of that from the finite beam. Smaller damping gives a better agreement.

4. CONCLUSIONS

The variability of the input power has been modelled for the finite and infinite beam structures for two contact point forces. The quantification of the frequency-averaged mean and the standard deviation represented by the relative standard deviation shows a good agreement for both finite and infinite cases. It is found that quantification of the frequency-average variability from a finite receiver can thus be simply approached by using that from the corresponding infinite structure.

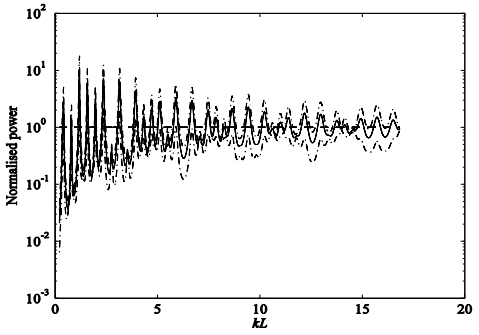

Figure 2 The normalised input power subjected to two harmonic point forces averaged over all possible excitation phases: (—) actual mean and (– - –) actual mean±standard deviation.

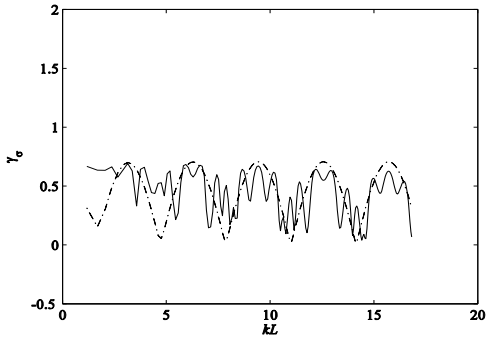

(a)

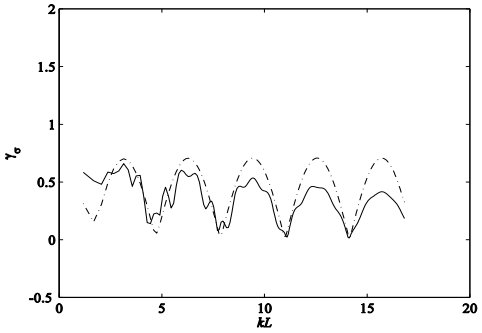

(b)

Figure 3 The relative standard deviation of input power averaged over frequency bands and phases: (—) finite beam and (– - –) infinite beam; (a) η = 0.05 and (b) η = 0.15.

4. REFERENCES

[1] B.A.T Petersson, and B.M. Gibbs, "Towards a structure-borne sound source characterization," *Applied Acoustics*, vol. 61, no. 3, pp. 325-343, 2000.

[2] A. Putra, N.F. Saari, H. Bakri, and R.M. Dan, "Characterisation of structure-borne sound source using reception plate method," *The Scientific World Journal*, vol. 2013, Article ID 742853, 2013.

[3] A. Putra, and B.R. Mace, "The effect of uncertainty in the excitation on the vibration input power to a structure," *Advances in Acoustics and Vibration*, vol. 2013, Article ID 478389, 2013.

Analysis on degree of nonlinearity in hardening nonlinear system of a vibration based energy harvesting device

P.S. Low[1,*], R. Ramlan[1,2], N.S. Muhammad[1], H.A. Ghani[1]

[1)] Faculty of Mechanical Engineering, Universiti Teknikal Malaysia Melaka,
Hang Tuah Jaya, 76100 Durian Tunggal, Melaka, Malaysia.
[2)] Centre for Advanced Research on Energy, Universiti Teknikal Malaysia Melaka,
Hang Tuah Jaya, 76100 Durian Tunggal, Melaka, Malaysia.

[*]Corresponding e-mail: lpeising@gmail.com

Keywords: Energy harvesting; nonlinearity; hardening

ABSTRACT – Analytical analysis is used to quantify the degree of nonlinearity in nonlinear hardening system in order to validate the usage of linear electromechanical coupling on weakly nonlinear hardening system. Approximate solution of harmonic balance method and multiple scales method is applied and both methods show the important effect of higher harmonics on the degree of nonlinearity.

1. INTRODUCTION

An energy harvesting device is modeled as a single degree of freedom mass-spring-damper system which are either mass excited or base excited where the energy harvested by the device is analogous to the energy dissipated by the damper.

The performance of this linear device is optimized when the natural frequency of the device is tuned to match the ambient frequency [1] and a slight mistune will bring a vast deterioration in the device performance. This thus creates a limitation on the linear generator since ambient frequency varies with time.

In order to overcome this limitation, researchers introduce nonlinearity into the system in the form of hardening spring. The theoretical study on the energy harvesting devices engaging a hardening spring has been keenly conducted by Quinn et al. [2] and Ramlan et al. [3]. A hardening spring system has a response that is less sensitive to the change in frequency which makes it fit for applications with varying ambient frequency. The response of the system with such a spring is able to widen the bandwidth to a much frequency range than the linear system, which provides some advantages in harvesting the vibration/mechanical energy from ambient sources since ambient frequency varies with time.

Currently, the degree of nonlinearity of devices employing a hardening spring is considered very weak. Hence, the electromechanical coupling for this weak nonlinear system is assumed to be similar to the one with a linear spring. A conclusive evident is seek theoretically to quantify the degree of nonlinearity in hardening system so that the validity of using linear electromechanical coupling on hardening nonlinear system can be established.

2. METHODOLOGY

Approximate solution of harmonic balance method and multiple scale method is pursued to quantify the degree of nonlinearity of a hardening system. The equation of motion for a base-excited hardening Duffing oscillator is given by [4]

$$m\ddot{s} + c\dot{s} + k_1 s + k_3 s^3 = -m\ddot{y} \tag{1}$$

where $s = x - y$ is the relative displacement between the seismic mass, x, and the housing, y, and $y = Y\cos(\omega t)$, k_1 is the linear spring constant and k_3 is the nonlinear spring constant with $k_3 > 0$ denoting a hardening system. Equation (1) can be expressed in non-dimensional form as

$$\ddot{u} + 2\zeta\dot{u} + u + \alpha u^3 = \Omega^2 \cos(\Omega\tau + \emptyset) \tag{2}$$

where $u = \frac{s}{Y}$, $\zeta = \frac{c}{2m\omega_n}$, $\alpha = \frac{k_3 Y^2}{k_1}$, $\Omega = \frac{\omega}{\omega_n}$, $\tau = \omega_n t$, $\emptyset$ = phase angle between excitation and response

2.1 Harmonic Balance Method

Single harmonic and two harmonic steady state solutions of equation (1) is seek using harmonic balance method as conversed by Hamdan and Burton [5]. The single-mode approximation for the steady state response is assumed to have the solution in the form of

$$u(\tau) = A\cos\Omega\tau \tag{3}$$

where A is the steady state response amplitude. In single-mode solution, only the fundamental harmonic approximation is obtained and the third harmonics is neglected.

Next, the two-mode approximation for the steady state response is assumed to have the solution in the form of

$$u(\tau) = A_1\cos\Omega\tau + A_3\cos 3\Omega\tau + B_3\sin 3\Omega\tau \tag{4}$$

where A_1 is the first harmonic amplitude and A_3 and B_3 is the third harmonic amplitude. In two-mode solutions, the amplitude of first harmonic and third harmonic is acquired.

2.2 Multiple Scale Method

New independent variables is introduced to the Duffing oscillator in equation (2) according to

$$T_n = \varepsilon^n t \text{ for } n = 0, 1, 2, \ldots \quad (5)$$

as shown in [6] and [7] where T_n is the independent time scales and t is a function of these time scales, $t = t(T_0, \ldots T_n)$. This functional form allows the operation of differentiation which is the key step of this method to be expanded as follow

$$\frac{d}{dt} = D_0 + \varepsilon D_1 + \varepsilon^2 D_2 + \cdots, \quad (6a)$$

$$\frac{d^2}{dt^2} = D_0^2 + 2\varepsilon D_0 D_1 + \varepsilon^2 (2D_0 D_2 + D_1^2) + \cdots, \quad (6b)$$

where operators $D_n \equiv \frac{\partial}{\partial T_n}$, ε is small parameter.
Continuing with equating like powers of ε to zero and eliminating secular terms, the amplitude-frequency relation is obtained up to the second order.

3. RESULTS AND DISCUSSION

Frequency response for the Duffing oscillator shown in equation (2) obtained by using single-mode and two-mode harmonic balance method is presented in graph. Comparing single-mode frequency response graph with the two-mode frequency response graph, it is shown that the single-mode approximation did not reveal all of the essential features of the system where higher harmonics have an important effect on the resonance curves. This is presented in the graph where two-mode approximation graph is separated by an island that represents the nonlinear behavior of hardening system while single-mode graph does not.

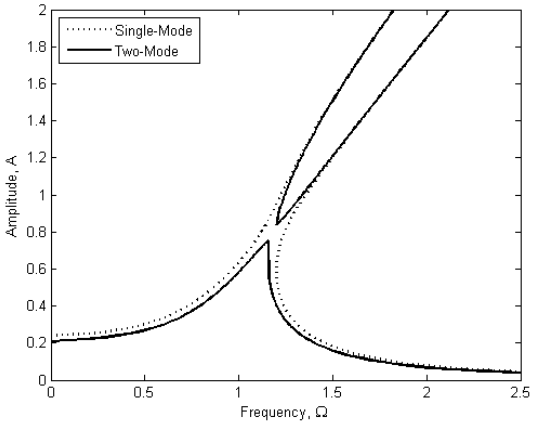

Figure 1 Frequency response obtained by using single-mode and two-mode harmonic balance method

The amplitude-frequency relation obtained for both first order and second order from the multiple scale method is also presented in graph. The relation from the graph shows a similar qualitative behavior with those obtained from harmonic balance method.

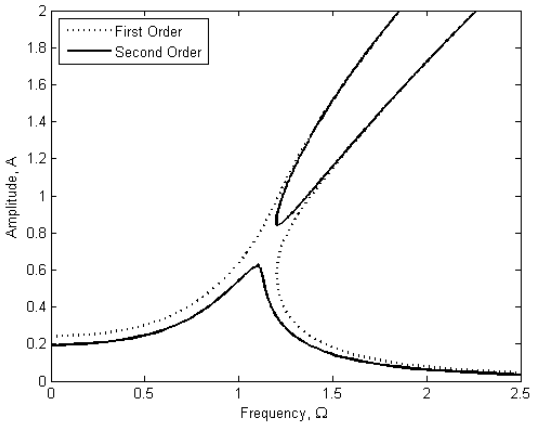

Figure 2 Frequency response obtained by using first order and second order of multiple scale method

4. CONCLUSIONS

Both harmonic balance method and multiple scales method are capable of showing the effect of higher harmonics on degree of nonlinearity of hardening nonlinear system when higher harmonics are taken into considerations. Therefore, the electromechanical coupling of hardening nonlinear system is not preferable to be assumed as similar with linear electromechanical coupling when only first harmonic is being taken into consideration.

5. ACKNOWLEDGEMENT

The authors graciously thank the Higher Ministry of Malaysia for supporting this research under FRGS/2/2013/TK01/FKM/02/2/F00172.

6. REFERENCES

[1] C.B. Williams, and S.P. Beeby, "Analysis of a micro-generator for microsystems," *Sensors and Actuators*, vol. 52, pp. 8-11, 1996.

[2] D.D. Quinn, A.L. Triplett, L.A. Bergman, and A.F. Vakakis, "Comparing linear and essentially nonlinear vibration based energy harvesting," *Journal of Vibration and Acoustics*, vol. 133(1), pp. 1-8, 2011.

[3] R. Ramlan, M.J. Brennan, B.R. Mace, and I. Kovacic, "Potential benefits of a nonlinear stiffness in an energy harvesting device," *Nonlinear Dynamics*, vol. 59(4), pp. 545-558, 2010.

[4] R. Ramlan, "Effects of nonlinear stiffness on performance of an energy harvesting device," *PhD Thesis*, University of Southampton, 2008.

[5] M.N. Hamdan, and T.D. Burton, "On the steady state response and stability of nonlinear oscillators using harmonic balance," *Journal of Sound and Vibration*, vol. 166(2), pp. 255-266, 1993.

[6] A.H. Nayfeh, and D.T. Mook, *Nonlinear oscillations*, New York: John Wiley; 1979.

[7] T.D. Burton, and Z. Rahman, "On the multi-scale analysis of strongly nonlinear forced oscillators," *International Journal of Non-Linear Mechanics*, vol. 21(2), pp. 135-146, 1986.

Study on corrosion features analysis for visual inspection & monitoring system: A NDT Technique

Syahril Anuar Idris[1,*], Fairul Azni Jafar[2], Nurhidayu Abdullah[1]

[1)] Center for Graduate Studies, Universiti Teknikal Malaysia Melaka,
Hang Tuah Jaya, 76100 Durian Tunggal, Melaka, Malaysia.
[2)] Faculty of Manufacturing, Universiti Teknikal Malaysia Melaka,
Hang Tuah Jaya, 76100 Durian Tunggal, Melaka, Malaysia.

[*]Corresponding e-mail: syahrilidris@gmail.com

Keywords: Corrosion; Vision; Non-Destructive Testing (NDT)

ABSTRACT – These days, utilization of camera as inspection tools has been expanded. The flexibility functions of camera fit to get different kind of information. This research work is focusing on developing a robust visual inspection system for NDT corrosion detection that able to detect corrosion in any environment, and the corrosion detection will be using visual data as principal data inspection.

1. INTRODUCTION

Corrosion can cause major losses to industry. One of the industry that has high impact due to the corrosion is oil and gas. This is because, oil and gas use pipeline to transfer goods between places. In a case study, a deteriorated Bar Wrapped Pipe (BWP) due to corrosion was detected by Pure Technology during schedule inspection [1]. However due to the pipe useful life is nearer to the end, the pipes section were replaced. Yet, by replacing BWP earlier then its expiry, the cost compare to the usage is increasing.

Corrosion inspection and monitoring are key activities in ensuring asset integrity and control of corrosion. Management choices on gear condition, expectation of leftover life and necessities for synthetic treating are just in the same class as the information input provided from field experience. Corrosion inspection and monitoring includes assessment of [2]:

a. In-line systems - corrosion coupons, bio-studs
b. On-line monitoring techniques
c. Off-line monitoring - Non-Destructive Testing

Non-destructive testing (NDT) techniques are used extensively to monitor corrosion. One of the advantages is that equipment usually need not be taken out of service. In Cawley review on NDT that presented in 2001, radiography, ultrasonic, eddy current, magnetic particle, and penetrant testing were top five techniques dominating the NDT market [3] yet visual inspection is the most widely applied in NDT technique, but due to the accuracy issues, it is often used together with others method. Meanwhile, this research is discussing the application of visual inspection system to be used as primary equipment for NDT corrosion inspection.

This paper is organized as follow. Section 2 present the current NDT corrosion inspection and monitoring process. In section 3, visual corrosion inspection is introduced, and analyze between other methods of NDT corrosion inspection. In section 4, the corrosion features based on the characterization of corrosion is discussed to identify the profile of each corrosion types. Finally, discussion is concluded in section 5.

2. CORROSION INSPECTION & MONITORING

In the petroleum industry, the internal corrosion in oil and gas production operation is often monitored with hydrogen probes. Hydrogen probes measure hydrogen permeation and provide information on the rate of corrosion [4]. Other on-stream corrosion-monitoring techniques that are used in petroleum and chemical industries include the following:

a. Electrical resistance and linear polarization methods.
b. Ultrasonic thickness measurement.

The costs of corrosion vary considerably from one industry to another industry. However, substantial savings are achievable in most industries. The first step in any cost reduction program is to identify and quantify the present costs of corrosion [5]. Based on this analysis and a review of the present status of corrosion control in the industry, priorities can be determined and the most rewarding cost-reduction projects pursued [6]. Corrosion can be classify based on one of the following three factors [7]:

a. Nature of corrode: either as “wet” or “dry”.
b. Mechanism of corrosion: This involves either electrochemical or direct chemical reactions.
c. Appearance of the corroded metal: either uniform or it is localized

With the ability to classify the corrosion type based on visual, the inspection system able to make suitable decision based on expert system database. Corrosion is either uniform and the metal corrodes at the same rate over the entire surface, or it is localized, in which case only small areas are affected. The detection of the corrosion “areas” will be detected by means of visual sensor, using camera or video that able to determine and analyze the sensed areas. Thus the corrosion detection on the inspection system using visual proves to be validated.

3. VISUAL CORROSION CLASSIFICATION

Classification by appearance, which is particularly useful in failure analysis, is based on identifying forms of

corrosion by visual observation with either naked eye or magnification. The morphology of attack is the basis for classification. Nine forms of wet (or aqueous) corrosion can be identified based on appearance of the corroded metal [5] is shown in Figure 1. However in NDT visual inspection system, macroscopic localized corrosion type is suitable for classification as macroscopic size defect is large enough to be detected in ordinary visible sense.

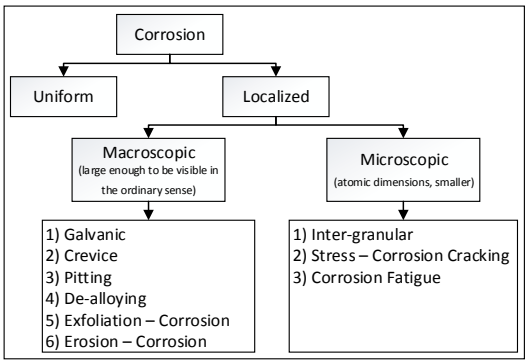

Figure 1 Characterization based on appearance

4. CORROSION FEATURES

In visual inspection, the corrosion level identification requires expert who can clearly determine the corrosion based on experience as well as types of corrosion, with red rust as a common experience. Usually, the corrosion process produces rough surfaces, and image analysis based on textural features can be used for quantification and discrimination of corrosion extent [8]. Additionally, color progression of metallic surfaces is also used for the detection of corrosion because of different metal oxides and other corrosion products [9].

Figure 2 shows the corrosion image features profile identified for localized macroscopic corrosion that able to differentiate various classes of corrosion. Each type has different features that can be differentiate with either texture, color or shape. By enhancing the image capture, the limitation of inspection environment can be lifted and increase the accuracy of the inspection.

5. CONCLUSIONS

This paper discussed the potential of vision system to be used for primary equipment on NDT corrosion inspection. The visual inspection system is to be conducted during monitoring stage in the preliminary inspection. Visual inspection system would be able to gather data and at the same time processed and analyzed the collected data. With the result, the analyzed data is able to classify the corrosion type and by identify the type of corrosion one can understand the pattern of attack, thus early prevention can be done. Using image as inspection data, issue on analogue signal loss due to the communication interference can be eliminated, as the image data able to recover required feature based on other features. Furthermore, the ability of the system, able to adapt the unrefined environment make the proposed system robust and able to use in others application.

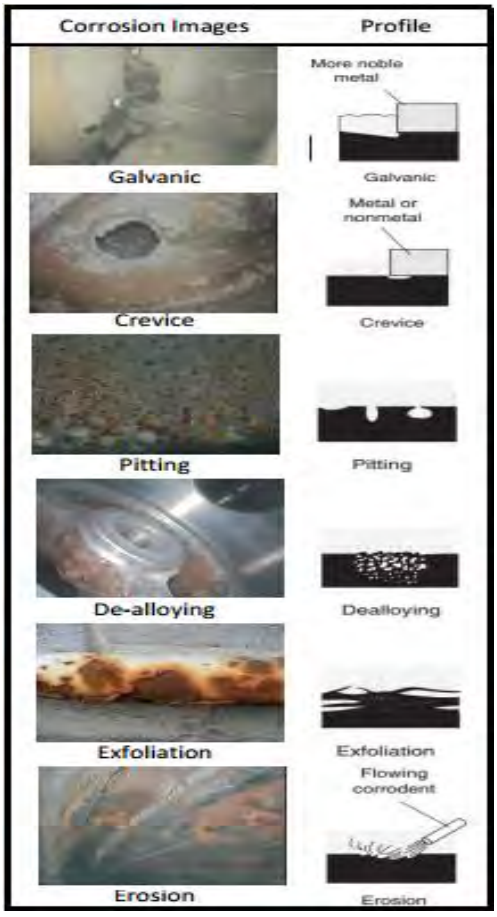

Figure 2 Corrosion image with profile

6. REFERENCES

[1] Pure Technologies, Case Study: City of Calgary - Memorial Feedermain, pp. 2–3, 2013.

[2] S. R. Bowling, "Evaluating the effectiveness of a priori information on process measures in a virtual reality inspection task" Journal Industrial Engineering and Management, vol 3. 2010.

[3] P. Cawley, "Non-destructive testing-current capabilities and future directions," Proc. Inst. Mech. Eng., vol. 215, pp. 213–223, 2001.

[4] Carigali Inspection, "The Art of Pigging." 2013.

[5] J. Davis, "Corrosion: Understanding the basics," p. 574, 2000.

[6] S. Nešić, "Key issues related to modelling of internal corrosion of oil and gas pipelines – A review," Corros. Sci., vol. 49, no. 12, pp. 4308–4338, Dec. 2007.

[7] Z. Liang, L. Hong-yi, Y. Pei-xin, "Study on Image Identification Method of In-service Pipeline Corrosion Fault," 2nd International Conference Information Technology Computer Science, pp. 182–185, Jul. 2010.

[8] S. Livens, P. Scheunders, G. Van De Wouwer, D. Van Dyck, H. Smets, and J. Winkelmans, "A Texture Analysis Approach to Corrosion Image Classification," Microsc. Microanal. Microstructure, vol. 7, no. 2, pp. 1–10, 1996

[9] Medeiros, Fátima NS, et al. "On the evaluation of texture and color features for nondestructive corrosion detection." EURASIP Journal on Advances in Signal Processing, (2010): 7, 2010.

Analytical work of honeycomb based on single ring hexagonal ring subjected to quasi-static lateral loading

M.R. Said[1,2,*], A.J. Chuli[1]

[1)] Faculty of Mechanical Engineering, Universiti Teknikal Malaysia Melaka,
Hang Tuah Jaya, 76100 Durian Tunggal, Melaka, Malaysia.
[2)] Centre for Advanced Research on Energy, Universiti Teknikal Malaysia Melaka,
Hang Tuah Jaya, 76100 Durian Tunggal, Melaka, Malaysia.

[*]Corresponding e-mail: radzai@utem.edu.my

Keywords: Honeycomb, hexagonal ring, quasi-static, lateral loading, energy absorption

ABSTRACT – Over the years, there are many experimental works done in order to investigate the effect of lateral loading on honeycomb. The works however were only validated by using software such as Finite Element Analysis (FEA) and ABAQUS. This paper attempted to validate the result of the experiment by using the single theory on a single hexagonal ring compressed across face which was developed by previous researcher. It is found that the difference between theoretical and experimental value for the compression across faces is 22.46%.

1. INTRODUCTION

Structures that are deformable such as honeycombs as in Figure 1 are often used as an energy absorber. Honeycomb, in particular, is widely used as it has a relatively strong and stiff properties, as well as its good energy absorption characteristics and cost-effective. Previous researcher has found that the energy absorption of tubular structures can be increased by the addition of filler such as foam and wood [1,2,3,4,5,6]. These findings were found in both axial (out-of-plane) and lateral (in-plane) crushing mode. For lateral loading on a single hexagonal ring, it has been found that the collapse load in ring compressed across face is higher than that compressed across corner by a factor of 1.8 [7]. The objective of this paper is to find the energy absorbed by multi-cells honeycomb (hexagonal-shaped) and compare it with the single hexagonal ring theory.

Figure 1 Multi-cell honeycomb

2. METHODOLOGY

Results that presented later used aluminum honeycomb 3003-H18 with the data in Table 1. The basic collapse mechanisms of the hexagonal ring were introduced in [7]. As shown in Figure 2, there are two methods to compress the specimen laterally namely corner and face. By assuming the model to be rigid perfectly plastic, some formulas were derived. The formulas derived by considering the mode of deformation stages. During the compression across faces, the first mode of deformation is known as Mode 1 Phase 1 (M1P1). In the second phase, there are two modes of deformation, namely Mode 2 Phase 1 (M2P1) and Mode 2 Phase 2 (M2P2) is observed and formulated.

Table 1 Data for aluminium honeycomb 3003-H18

Properties	Data
Dimensions	100mm x 100mm x 100mm
Poisson ratio	0.33
Yield Strength	115.8 MPa

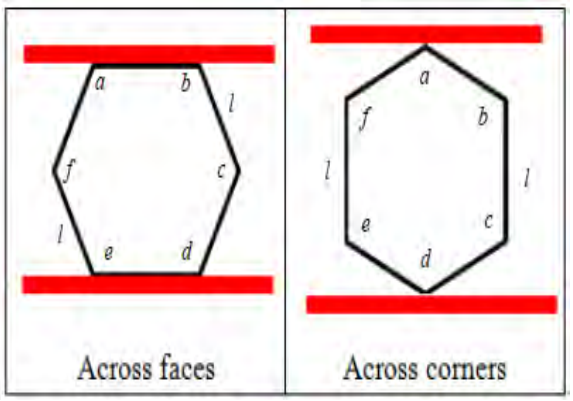

Figure 2 Compression method under lateral loading

Figure 3 shows the basic collapse mode of honeycomb under lateral loading. During compression, all shows a linear-elastic behaviour at the first regime. It is then followed by the second regime in which a plateau of roughly constant stress is observed. In the final regime, a steeply rising stress is detected [7].

Figure 3 Basic collapse mode of honeycomb under lateral loading, where region 1, region 2, and region 3 is Linear-elastic, Plateau and Densification respectively

3. RESULTS AND DISCUSSION

From the experiment conducted, it is found that the collapse behavior of the specimen agrees with the theoretical collapse mode for metal. In addition, there are some distinctive differences between the theoretical and experimental graph for both cases. The specimen are assumed to be in perfect condition (perfect hexagonal shape) either in theory and experiment. Based on this assumption, there are slight differences between the theoretical and experimental graphs for both cases. By referring to Figure 4, the energy absorbed by the specimens is obtained by calculating the area under graph for both theoretical and experimental. The energy absorption value for the theory is 2.73 Nmm whereas 2.23 Nmm for the experiment. These values were differed by 22.46%. In addition, by using a simple empirical formula, it is found that the theoretical graph agrees with the experimental graph by a factor of 3 cells.

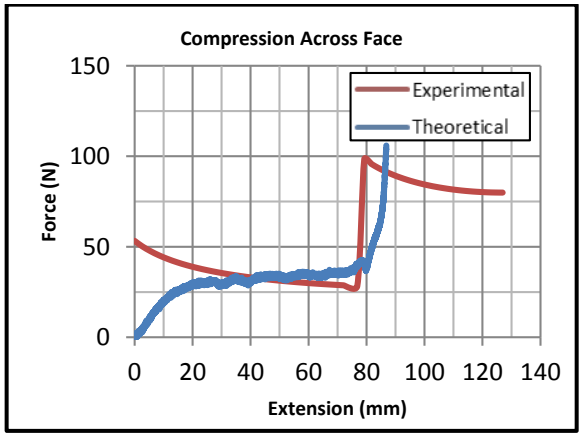

Figure 4 The load against displacement curve for compression across faces

4. CONCLUSIONS

As a conclusion, the results of analytical work agree significantly with the theory of the single ring developed in terms of deformation. For the energy absorbing capacity for the theoretical and experimental work, it is found to be a difference of 22.46%. It is also found that the experimental graph is higher compared to the theoretical graph by a factor of 3 cells.

5. REFERENCES

[1] H. Kavi, A.K Toksoy, M. Guden, "Predicting energy absorption in a foam-filled thin-walled aluminium tube based on experimentally determined strengthening coefficient", *Mater Des*, vol. 27, pp. 263-269, 2006.

[2] Zhang Y., Sun G., Li G., Luo Z., Li Q, "Crashworthiness design for foam-filled bitubal structures for crashworthiness criteria", *Mater Des*. Vol. 38, pp. 99-109, 2012.

[3] S.R. Reid, T.Y. Reddy, M.D. Gray, "Static and dynamic axial crushing of foam-filled sheet metal tubes", *Int. J. Mech. Sci*., vol. 28 (5), pp. 295-322, 1986

[4] T. Wierzbicki, W. Abramowicz, "On the crushing mechanics of thin-walled structures", *Journal of Applied Mechanics*, vol. 50, pp. 727-733, 1983.

[5] T.Y. Reddy, S.T.S. Al-Hassani, "Axial crushing of wood-filled square metal tubes", *Int. J. Mech. Sci*., vol. 35 (3), pp. 231-246, 1993.

[6] L. J. Gibson, M. F. Ashby, *Cellular solids structure and properties*, Cambridge University Press, 1997, pp. 309-343.

[7] M.R. Said, T.Y. Reddy, "Quasi-static response of laterally simple compressed hexagonal ring", *Int. J. Crash*, vol. 7(3), pp. 345-363, 2002.

[8] X. Zhang, H. Zhang, Z. Wen,"Experimental and numerical studies on the crush resistance of aluminium honeycombs with various cell configurations", *International Journal of Impact Engineering*, vol 66, pp 48-59, 2014.

Low-NO_X combustion of biogas from palm oil mill effluent using flameless combustion

Afiqah Hamzah[1,2*], Abuelnuor Abdeen Ali Abuelnour[3], Mazlan Abdul Wahid[3,4]

[1)] Faculty of Mechanical Engineering, Universiti Teknikal Malaysia Melaka,
Hang Tuah Jaya, 76100 Durian Tunggal, Melaka, Malaysia.
[2)] Centre for Advanced Research on Energy, Universiti Teknikal Malaysia Melaka,
Hang Tuah Jaya, 76100 Durian Tunggal, Melaka, Malaysia.
[3)] High-Speed Reacting Flow Laboratory, Universiti Teknologi Malaysia,
Skudai, 81310 Johor, Malaysia.
[4)] Faculty of Mechanical Engineering, Universiti Teknologi Malaysia,
Skudai, 81310 Johor, Malaysia.

[*]Corresponding e-mail: afiqah@utem.edu.my

Keywords: Flameless combustion, biogas, POME

ABSTRACT – An experimental study of flameless combustion in a laboratory-scale furnace using natural gas, simulated biogas and palm-oil-mill-effluent (POME) derived biogas. Flameless combustion regime is achieved for natural gas, simulated biogas and POME biogas. POME biogas flameless combustion has slightly lower average furnace temperature (2.69% reduction) due to increased inert gas in the furnace chamber. Flameless combustion produce larger and more uniform combustion area (R_{tu} = 0.097) compared to conventional flame combustion (R_{tu} = 0.21). NO_X emission measurement has shown reduced NO_X emission in flameless combustion of natural gas, POME biogas and simulated biogas with average of 6 ppm.

1. INTRODUCTION

Flameless combustion is a new technology which has the advantage of high efficiency [1], and low NOx emission [2]. NOx is a dangerous chemical component which causes surface ozone formation and smog. Flameless combustion can also process low calorific value fuel which makes it an ideal candidate for combustion of renewable energy which usually has low calorific value [3, 4]. However, since biofuels', particularly biogas', calorific value is dependent on the raw source, there is a need to study the suitability of biogas derived from POME as fuel for a flameless combustor. In this study, focus is given to flameless combustion of POME derived biogas with a long term aim for industrial application.

2. METHODOLOGY

A readily available laboratory scale furnace is used in this experiment. The flameless combustor was run using three different types of fuels: natural gas, POME biogas and simulated biogas. Natural gas is used to represent commonly used gaseous fossil fuel. The POME biogas is sourced from a biogas capture system in Felda Maokil Palm Oil Mill, Labis, Johor. The simulated biogas is a mix of 75% natural gas and 25% carbon dioxide. During flameless combustion of simulated biogas, CO_2 is added to primary air pathway (green line in Figure 1). For each of the fuel type, the equivalence ratio is varied to see effect of lean, stoichiometric and rich flameless combustion. The equivalence ratio is controlled by changing the air flow rate and keeping the fuel flow rate constant.

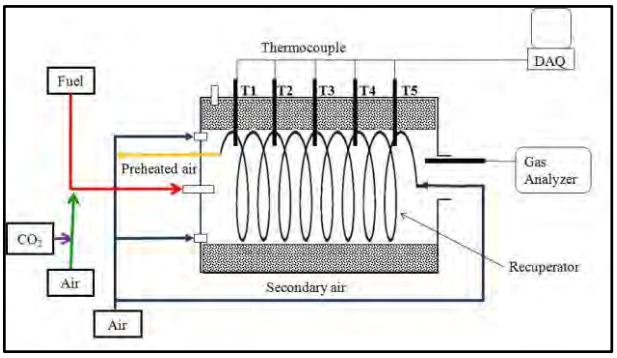

Figure 1 Flameless combustor experimental setup

A preheat time is allowed for about 1 hour before each experiment to heat up the furnace to about 800 ˚C. Temperature is measured at points T1 till T5 as in Figure 1. The data logger is connected to a desktop PC and records the furnace temperature in 1 minute interval. The NOx emission reading is taken using a gas analyzer at every 3-5 minutes time interval. The flameless combustion mode is allowed to run for at least 30 minute in each experiment.

3. RESULTS AND DISCUSSION

3.1 Visual Observation

Figure 2 shows the photographs of furnace chamber in conventional flame and flameless mode. In conventional flame, POME biogas fuel produced the least net radiation flux, which can be attributed to the lower calorific value of POME biogas compared to natural gas and simulated biogas. In flameless combustion mode, simulated biogas combustion produced slightly less net radiation flux compared to natural gas and POME biogas flameless combustion,

due to lower CO_2 temperature in the fuel which slightly cooled the combustion region. In the future, it is recommended to let the CO_2 to reach room temperature before it is combusted for better comparison.

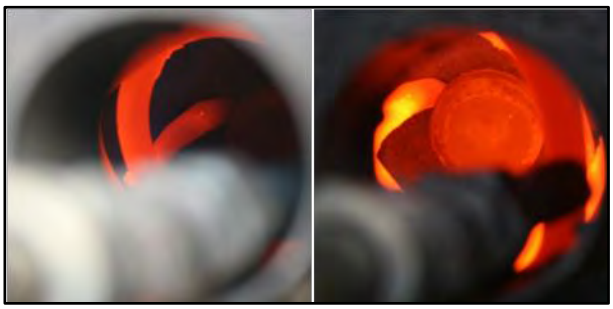

Figure 2 The conventional flame combustion of POME biogas (left) compared to flameless combustion of POME biogas

3.2 Temperature Profile

The average temperature in conventional mode is 796.2 ˚C in natural gas combustion and 782.4 ˚C in POME biogas combustion. For flameless combustion, the average temperature is 811.5 ˚C for natural gas and 789.7 ˚C for POME biogas. The average furnace chamber temperature is lower in POME biogas combustion compared to natural gas combustion in both flameless and conventional flame combustion. The temperature reduction is 2.69% in flameless combustion and 1.73% in conventional flame combustion.

To quantify the degree of temperature uniformity inside the combustion chamber, a temperature uniformity ratio (R_{tu}) is used [5]. In this experimental study, the R_{tu} for flameless combustion for both natural gas (R_{tu} = 0.041) and POME biogas (R_{tu} = 0.097) are less than the R_{tu} for conventional flame combustion using natural gas (R_{tu} = 0.21). The same trend is also seen in [18]. However, R_{tu} for POME biogas is higher than for natural gas, whereas in work by Colorado [6], the R_{tu} for biogas is lower than R_{tu} for natural gas.

3.3 NOx emission analysis

Figure 3 shows the temperature variation and NOx emission during combustion of POME biogas in both conventional flame and flameless mode (separated by red line). The temperature change in flameless mode is slow compared to temperature change in conventional flame combustion. NOx emission is seen to drop drastically when the combustion mode is changed from conventional flame to flameless mode. The drop in NOx emission has been attributed to fewer hot spots in flameless combustion, which inhibits NO formation via thermal mechanism. NO formation via prompt mechanism is also expected to be insignificant. The NO formation in flameless combustion is from N2O intermediate pathway as has been shown in computational simulation of [5].

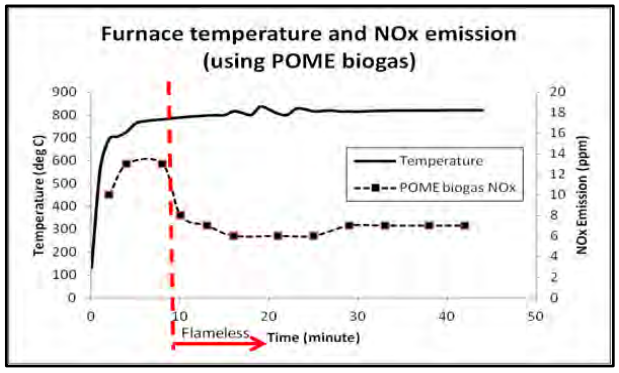

Figure 3 Furnace temperature and NO_X emission for conventional flame (left of red line) and flameless combustion of POME biogas (right of red line)

4. CONCLUSIONS

Flameless combustion method has been used in this study to provide low NOx combustion of POME biogas. It has been found in this study that a flameless combustor can easily function even if the type of fuel is changed.

5. ACKNOWLEDGEMENT

The author, Afiqah Hamzah, gratefully acknowledges the scholarship from UTeM. The authors wish to thank UTM and the Malaysian Government for supporting this research activity. Thanks to the management of Felda Maokil Palm Oil Mill for allowing collection of POME biogas for this research.

6. REFERENCES

[1] M.A. Galbiati, A. Cavigiolo, A. Effuggi, D. Gelosa, and R. Rota, "MILD combustion for fuel-NOx reduction," *Combustion Science and Technology*, vol. 176, no. 7, p. 1035-1054, 2014.

[2] N. Schaffel, M. Mancini, A. Szlek, and R. Weber, "Mathematical modeling of MILD combustion of pulverized coal," *Combustion and Flame*, vol. 156, no. 9, p. 1771-1784, 2009.

[3] B. Danon, W. de Jong, and J.E.M. Roekarts, "Experimental and Numerical Investigation of a FLOX Combustor Firing Low Calorific Value Gases," *Combustion Science and Technology*, vol. 182, no. 9, p. 1261-1278, 2010.

[4] A. Effuggi, D. Gelosa, M. Derudi, and R. Rota, "Mild Combustion of Methane-Derived Fuel Mixtures: Natural Gas and Biogas," *Combustion Science and Technology*, vol. 180, no. 3, p. 481-493, 2008.

[5] W. Yang, and W. Blasiak, "Mathematical modelling of NO emissions from high-temperature air combustion with nitrous oxide mechanism," *Fuel Processing Technology*, vol. 86, no. 9, p. 943-957, 2005

[6] A.F. Colorado, B.A. Herrera, and A.A. Amell, "Performance of a flameless combustion furnace using biogas and natural gas," *Bioresource Technology*, vol. 101, no 7, p. 2443-2449, 2010.

Engineering design on food waste composting bin

S.N. Khalil[1,2,*], K A. Zulkifli[1]

[1)] Faculty of Mechanical Engineering, Universiti Teknikal Malaysia Melaka,
Hang Tuah Jaya, 76100 Durian Tunggal, Melaka, Malaysia.
[2)] Centre for Advanced Research on Energy, Universiti Teknikal Malaysia Melaka,
Hang Tuah Jaya, 76100 Durian Tunggal, Melaka, Malaysia.

[*]Corresponding e-mail: snurhaidakhalil@utem.edu.my

Keywords: Green technology; compost

ABSTRACT – Green technology has been imprinted in our country to gain better future or greener future for our future generations. It is part of our hidden duty to prepare good platform for them to lead on and continually taking care of our earth. Composting is one of the steps towards that greener future. Composting is known as one of the method or solution for wastes around the world. However, it is neither a familiar word nor action in Malaysia and specifically in Universiti Teknikal Malaysia, Melaka. Composting can avoid landfills to be filled with wastes that can be reuse and recycle thus can reduce the usage of incinerator. This research will explain on the benefits of composting and how the process will be done as well as the phases and important parameters. In order to implement it in the University, a conceptual design was made based on the current designs that are already in the market and some new designs were sketched and design using the CATIA software. The material selection for the parts was done using the CES Edupack software and analysis was made as well as the costing of the model to apply the concept according to the University's environment.

1. INTRODUCTION

The main purpose of this research is to conceptually design composting bin that reduces the amount of food wasted in Industrial Café Campus. The Industrial Café Campus located at Faculty of Mechanical Engineering, UTeM, Malacca. In 2012, all cafeteria or café that operates in UTeM was known as Green Café. Green Café is one of the ideas that have been proposed by Vice Chancellor UTeM, Professor Datuk Dr Ahmad Yusof Bin Hassan during the Strategic Plan 2012-2020 meeting at Durian Tunggal, Malacca. This idea was also an initiative from ULDP (UTeM Leadership and Development Program) society. The green concept that was to be applied has its own slogan for the Green Café which is self-service, self-cleaning and saving the earth.

The composting bin method [2] is one of the green technology concepts that have been implemented especially in cafeteria in Europe [4], and home composting has been an economical trend nowadays in Europe. The green technology was created and implemented to minimize the harmful effects[3] on the environment that will lead to global warming in the near future**.**

Food waste is one of the highest rated problems that occur all over the world. People are still finding ways on how to fill up the landfills that are currently full with mostly food disposals. According to (Eco-Business, 2013), Melaka produce between 1,300 tonnes and 1,400 tonnes of waste daily with the cost of disposing them reaching up to RM70,000 daily. Moreover, the Krubong landfill can only last for another three years and the other landfill in Sungai Udang can only last another five years and have to be replaced with new sites. These wastes are coming from houses, apartments, schools, universities and prisons in Melaka. According to the Melaka Chief Minister Datuk Seri Mohd Ali Rustam after being interviewed by Bernama News in 2010[1], an incinerator will help to turn the non-recyclable waste into income and the incinerator can last up to 30 years and is seen as a viable option but the price tag of RM500 million seems to be a stumbling block he said. However, Melaka has prepared an area of 4 hectares in case the incinerator development is approved. Nevertheless, the Melaka Chief Minister has spark awareness around the country to reduce the use of plastic and will be charged 10 to 20 cent for anyone that requests a plastic bag. In regards to this matter, we should still continue to finding ways to solve the problem that will cause our future if we took this important matter for granted.

2. METHODOLOGY

The research will be held by conducting literature review on the broad subject and issues in green technology and narrowed down to composting waste management, composting waste products and lastly composting waste bin design. From the literature the researcher will design the composting bin based on the specifications gathered from literature review. The design shall be held in 3-D CAD software CATIA and analysis of the material used will be held by using CES Edupack software package, highlighting on green materials in both design and material analysis.

3. RESULTS AND DISCUSSION

The design of the composting bin focused on two elements that has critical function during operation i.e. shredder and mixer. The finite element analysis (FEA) results for these two parts are as follows;

Table 1 Shredder and Mixer material properties

Parameters	Properties
Material	Steel
Youngs's Modulus	2e+011N_m2
Possion's ratio	0.285
Density	7800kg_m3
Coefficient of thermal expansion	1.17e-005_Kdeg
Yield Strength	3.05+008N_m2

The design of the composting device is as shown in Figure 1 and Figure 2. In Figure 1, the manual composting device is illustrated. The machine is wall hung and operated by using manual labor. In Figure 2, the proposed automated composting device is illustrated. The design include the body, table door, shredder, mixer and support, transparent glass, service door, wheels and bucket.

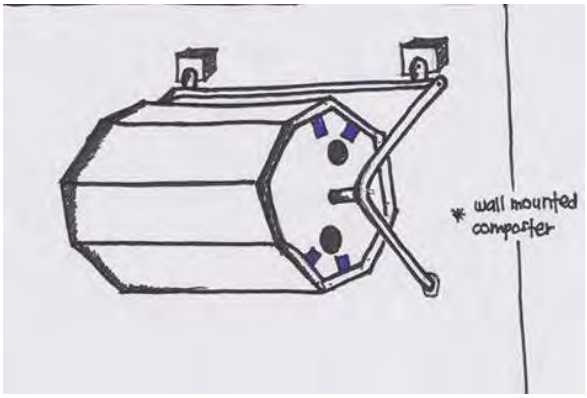

Figure 1 Manual Composting Device

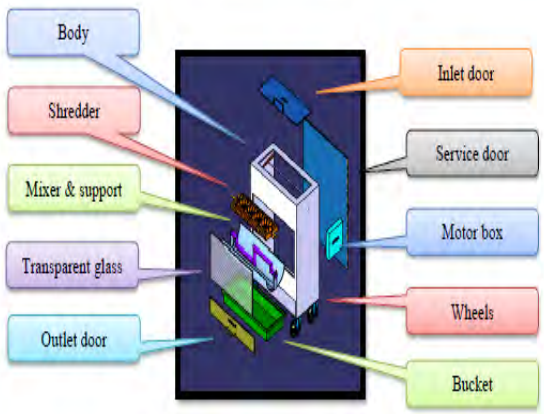

Figure 2 Proposed Automated Composting Device

4. CONCLUSIONS

In this reserach, at the end of the finding, the researcher will be able to understand the composting process and implement the green technology concept by producing a conceptual composting bin. The research also will produce composting bin design that will incorporate processes needed to produce good compost for UTeM's landscaping purposes.

5. ACKNOWLEDGMENT

The researcher would like to thank the University's effort in disseminating green technology awareness through the ULDP project under Green Café theme.

6. REFERENCES

[1] Eco-Business.(2010)." Turning waste into income in Melaka," *Bernama*, [online] 24th November. Retrieved from business.com/news/turning-waste-income-melaka/ [Accessed: 25 Nov 2013].

[2] Ryckeboer, J, Mergaert, J, Coosemans, J, Deprins, K. and Swings, J (2003), "Microbiological aspects of biowaste during composting in a monitored compost bin'," *Journal of Applied Microbiology*, 94 (1), pp. 127—137.

[3] Saheri, S, Mir, M., Basri, N, Begum, R and Mahmood, N (2009), "Solid waste management by considering composting potential in Malaysia toward a green country," *e-BANGI: Jurnal Sains Sosial dan Kemanusiaan*, 4 (1), pp. 48--55.

[4] Smith, A, Brown, K, Ogilvie, S, Rushton, K. and Bates, J. (2001). "*Waste Management Options and Climate Change, "* [report] European Commission, DG Enviroment.

Binary mixture of the decanter cake and fiber from the oil palm industry waste as a potential solid fuel

Mohd Haizal Mohd Husin[1,2,*], Ting Sze Choi[1], Nur Haziqah Mohd Ruzmi[1], Imran Syakir Mohamad[1]

[1)] Faculty of Mechanical Engineering, Universiti Teknikal Malaysia Melaka,
Hang Tuah Jaya, 76100 Durian Tunggal, Melaka, Malaysia.
[2)] Centre for Advanced Research on Energy, Universiti Teknikal Malaysia Melaka,
Hang Tuah Jaya, 76100 Durian Tunggal, Melaka, Malaysia.

[*]Corresponding e-mail: haizal@utem.edu.my

Keywords: Decanter cake; fiber; palm oil waste; solid fuel

ABSTRACT – This study relates to the production of solid fuel using waste products from the palm oil processing industry. Enclosed, the purpose of the study was to produce solid fuel from a binary mixture of decanter cake with the palm fiber. The sample was created based on decanter cake: fiber weight ratio, weight of loading and type of fiber. The sample were shaped into hexagons (radius= 2.34cm and length 8.0 cm). The sample prepared was tested for moisture contents, compression and calorific value. The study found out that the best mixture ratio among all of the sample ratio were decanter cake:fiber (70:30) with the highest compression test (2016 N) and nearest calorific value (4508 cal/g) compared to the commercial solid fuel which the compression test was 2390 N and calorific was 5321 cal/g.

1. INTRODUCTION

The oil palm plantation was being started since 1914 at Malaya before it called Malaysia. The large scale plantation was started around 1960 at all part of the Malaysia. Oil palm was planted for the determination of the crude oil palm. The percentage oil that was been produce from oil palm was only 20% which is the total up of crude palm oil (CPO) and kernel palm oil (KPO). However the percentages of the waste being produced is 80% from the palm oil mill, such as mesocarp fiber, empty fruit bunch (EFB), shell, decanter cake and palm oil mill effluent (POME) [1]. For today, the shell and mesocarp fiber was used to heat up the boiler to produce steam used in the palm oil mill and also produce electricity. Some mill also used the gas trapper to trap the methane gasses from the palm oil mill effluent, to use inside the biogas engine [2]. Malaysian government now had given a lot of attention toward the growth of the oil palm sector in the orchard and the renewable energy from oil palm. Malaysia Palm Oil Berhad (MPOB) was established to increase the palm oil production and quality which this can ensure the development of the oil palm sources will never end and keep growing [3-4]. The purpose of the study was to produce solid fuel from a binary mixture of decanter cake with the palm fiber.

2. METHODOLOGY

The decanter cake (DC) and fiber (F) sample was taken from the Kempas Sime Darby Palm Oil Mill at Malacca. The sample of decanter cake and fiber was weighting (approximately 130 ± 5 g by mass) to the ratio of the mixing. Each of the samples was mixing up well based on the DC:F ratio of 100:0, 90:10, 80:20 and 70:30. The samples was has been shaped into hexagons using pressed molding (radius= 2.34 cm and length 8.0 cm) and dried in oven for 24 hours for moisture contents. All prepared samples were compared with commercial hexagon solid fuel based on coconut shell (Starfire brand) in compression test by Ultimate Tensile Machine (UTM) and calorific values by oxygen bomb calorimeter.

3. RESULTS AND DISCUSSION

3.1 Influence of Moisture toward the Sample

Figure 1 shows the relationship between the percentage of moisture and compression force based on the DC:F ratio. The highest moisture percentage was at the pure 100% decanter cake while the highest compression force was at DC:F ratio 70:30. Meantime with the fiber added into the mixture, compression test drastically increases and the moisture percentages slightly decreasing. It might be the decanter cake only act as the binder to bind the fiber together while the fiber were the reason the sample can withstand a higher force before breakdown.

Figure 2 shows the relationship between the percentage of moisture and calorific value based on the decanter cake and fiber ratio. The highest calorific value was at the DC:F ratio 70:30 which is 4208 cal/g and pure decanter cake, shows the lowest calorific value. This is might be cause of the water contain decanter cake incompletely removed and affected the calorific value. By adding the fiber into the mixture sample, it automatically improve the percentages of the moisture and also the calorific value of the sample.

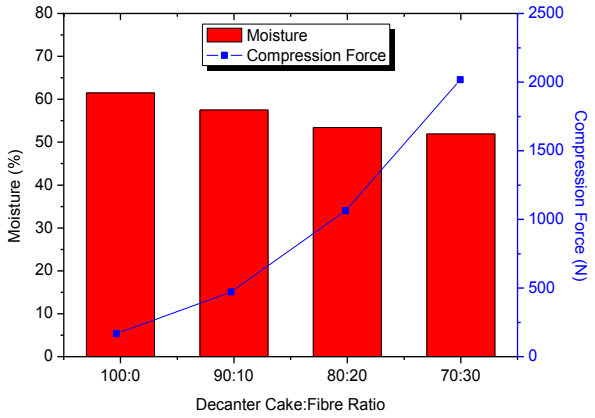

Figure 1 Relationship between moisture and compression force

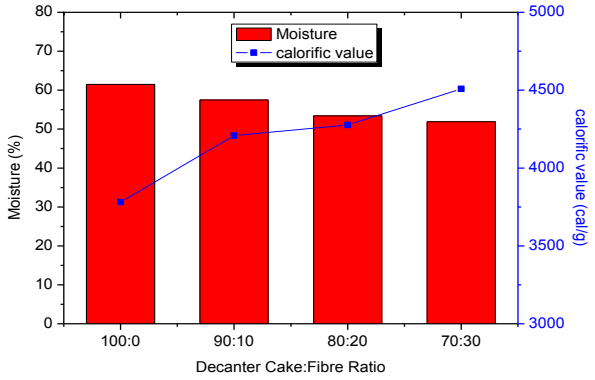

Figure 2 Relationship between moisture and calorific value

3.2 Comparison Commercial and Experimental

Figure 3(A) shows the comparison of compression force between commercial solid fuel and DC: F ratio solid fuel sample. It shows that the compression force for commercial fuel was the highest compression force of solid fuel was the highest compared DC: F ratio solid fuel sample. In term of physical properties, the commercial solid fuel was hard but brittle while the DC:F ratio solid fuel was ductile and elastic. The DC:F ratio 70:30 was the best ratio mixture because the compression force of the sample was nearly closed to the commercial solid fuel compression force.

Figure 3B shows the comparison of calorific value between commercial solid fuel and experimental solid fuel. it show that the calorific value for commercial fuel was highest compared to all DC:F ratio. In term of calorific value, the commercial solid fuel had more carbon contain inside it because of coconut shell based solid fuel compare to the DC:F ratio solid fuel samples. DC:F ratio 70:30 was the best ratio mixture because the calorific value of the sample was nearly closed to the commercial solid fuel calorific value.

4. CONCLUSIONS

For comparison, commercial and DC: F ratio sample solid fuel. The DC: F ratio 70:30 sample of solid fuel has the highest compression and greater calorific value, compared to other mixture ratio. But it is not sufficient potentially, compared to commercial solid fuel. However decanter cake mixing with waste materials can increase the improvement of solid fuels compared decanter cake alone.

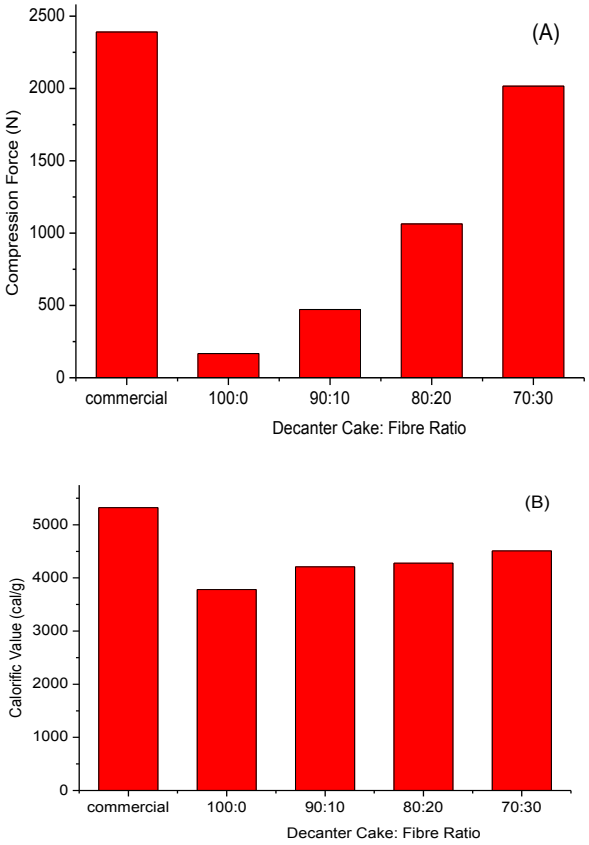

Figure 3: (A) Compression force and (B) calorific value of commercial and DC: F ratio sample

5. ACKNOWLEDGEMENT

The authors would like to thank Sime Darby Palm Oil Mill, Merlimau, Melaka for providing the samples throughout the study.

6. REFERENCES

[1] Y.M. Choo and A.A. Aziz, "Adding Value to Biomass Utilization in the Palm Oil Industry". *in ASMI International Conference (ASMIC) .10-12 July 2012. Royale Chulan Hotel, Kuala Lumpur,* 2012.

[2] R. P. Singh et al. "Management of Biomass Residues Generated from Palm Oil Mill: Vermicomposting A Sustainable Option," *Resource, Conservation and Recycling*, vol. 55, pp. 423-434, 2011.

[3] M.H. M. Husin, et al. "Solid Fuel from Decanter Cake:A Preliminary Study". *Proceedings of MUCEET 2009. Malaysian Technical Universities Conference on Engineering and Technology*, June 20-22, 2009, MS Garden, Kuantan, Pahang, Malaysia.

[4] S.M.Y Sahan, H.Haykiri-Acma, K. Sesen and S. Kucukbayrak, "Production of Fuel Briquettes from Olive Refuse and Paper Mill Waste, *Fuel Process. Technol., vol.* 68, pp.23-21, 2000.

Study the performance of single cylinder spark ignition engine for gasoline and compressed natural gas

M.Z.Yunus[1,*], M.T. Musthafah[1,2], M.Z. Akop[1,2]

[1)] Faculty of Mechanical Engineering, Universiti Teknikal Malaysia Melaka,
Hang Tuah Jaya, 76100 Durian Tunggal, Melaka, Malaysia.
[2)] Centre for Advanced Research on Energy, Universiti Teknikal Malaysia Melaka,
Hang Tuah Jaya, 76100 Durian Tunggal, Melaka, Malaysia.

[*]Corresponding e-mail: zcykko_10@yahoo.com

Keywords: CNG; cylinder pressure; spark ignition engine

ABSTRACT – Due to the unsteady oil prices, shortage continuity of fossil fuel and an emission crisis, automobile manufactured was motivated to find the solution for improve the efficiency of fuel. One of the factors that influence the performance of vehicle engine is the type of fuel used to complete the combustion. In this paper the study about combustion of mixture inside the cylinder is applied. Two types of fuel are tested that is gasoline and compressed natural gas (CNG) in four stroke single cylinder spark ignition (SI) engine. Based on the result, shows that CNG produce 6% lower of pressure compared to gasoline during power stroke. In addition the gasoline also leads in power and torque respectively on average by 15.8% and 16.3 %.

1. INTRODUCTION

Internal combustion engine is most widely used engine in automotive field to convert the chemical energy into the useful mechanical movement to move the vehicle. A lot of alternative fuels have been introduced to replace the usage of current primary fuels that are gasoline and diesel in other to enhance the output performance of the engines. One of the alternative fuels that are most frequently used in automotive industries is a CNG. The increased use of Natural Gas Vehicle (NGV) can be seen through the growth statistics released by the International Association for Natural Gas Vehicles which show an average growth of 22.9 percent for the past decade since 1991 until 2011[1]. Accordingly, the present studies explore about several advantages of CNG applied on the SI engine. Kowalewiez and Wojtyniak [2] in their studies stated that CNG have highest knock resistance due to high octane number that is 130. Moreover, Maji et al. [3] found that CNG delivered 3 to 5 percent higher thermal efficiency and also reduce the specific fuel consumption into 15 percent compared gasoline. Furthermore, according to an investigation by Amitabh et al. [4] it was proved that CNG produced 60% reduction of hydrocarbon and NOx emission also much lowered than gasoline.

The aim of this paper is to show the performance of the CNG fuel in spark ignition (SI) engine compared with the conventional fuel that is gasoline.

2. METHODOLOGY

The study is based on the experimental data collection. The analytical analyses were done by applying appropriate mathematical theories.

2.1 Engine parameter

The experiment was conducted using a modified engine manufactured by Subaru. The engine is rated at 5.0 HP and is suitable for small commercial used. The general specification of the engine is stated in **Table 1.**

Table 1 Engine Specification

Technical Data	Specification
No of cylinder	1
Bore	67.4 mm
Stroke	52 mm
Connecting rod length	91 mm
Compression ratio	6.3
TDC clearance height	0.4 – 0.6 mm

2.2 Experimental Setup

Figure 1 illustrates the setup of the experiment for collecting the data. Two series of experiment are conducted where the speed of the engine is run in range of 2000 rpm until 4000 rpm. For first series it involved of gasoline while the second is CNG. The data of the engine are detected by crank angle sensor and pressure sensor transmitted to data acquisition and collected inside the computer. The combustion analyzer software was applied to manage the data collection and data analysis.

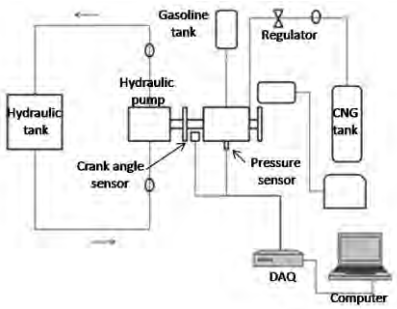

Figure 1 Experimental setup for performance of engine test

3. RESULTS AND DISCUSSION

The performance of the engine is illustrated in Figures 2 to 4 based on the experiment conducted.

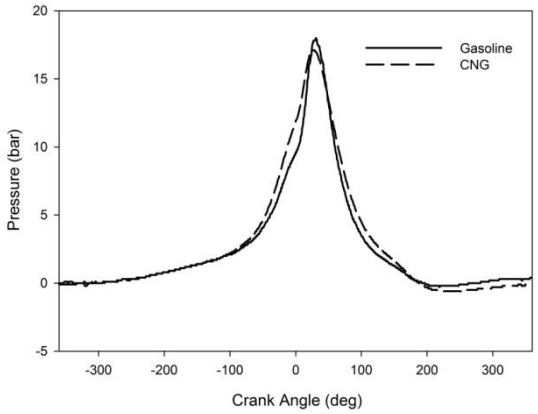

Figure 2 Comparison of cylinder pressure between gasoline and CNG with variation of engine speed

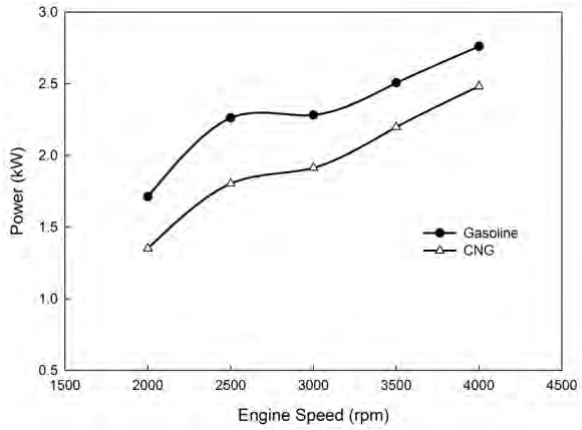

Figure 3 Comparison of power output between gasoline and CNG

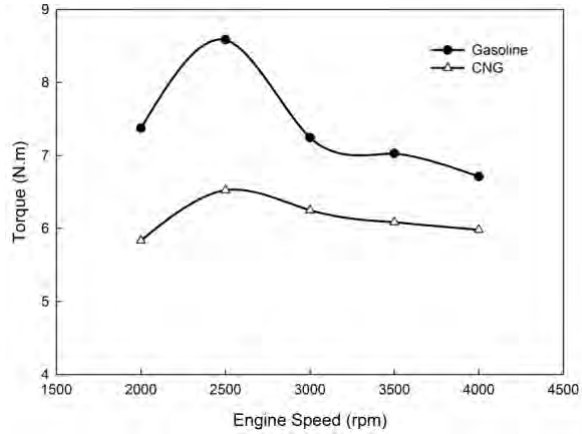

Figure 4 Comparison of torque output between gasoline and CNG

Figure 2 shows the behavior of the pressure inside the cylinder for full cycle process for both fuels. It shows that the highest resulting pressure is with gasoline with value of 18 bar while for CNG, the pressure is only 17 bar. These occurred due to the influence of different fire propagation produced after the ignition of the spark plug.

This situation contributed to the production of higher power output for gasoline as compared to CNG as shown in Figure 3. This happened because the CNG displaced more intake air due to the state of the fuel in gaseous form, as a result more fuel occupied the space during intake system and hence the stoichiometric is not achieved. Moreover, based on Figure 3 it can be stated that the higher the engine speed the higher the power produced by the engine.

The relationship between torque outputs of the two tested fuels is plotted in Figure 4. The curves show that the maximum torque is occurred at 2500 rpm for both fuels and fall back with respect of engine speed. Besides, the great difference between gasoline and CNG occurred at lower speed of engine and same as power graph, the gasoline curve always lead the CNG curve.

4. CONCLUSIONS

Based on the experimental investigation, single cylinder engine that consumes CNG experience lower pressure during power strokes compared to gasoline with a different almost 6 percent. The power output of the gasoline is averagely leading in all range of speed by 15.8 percent. Other than that, the usage of CNG as a fuel shows a cutback from 10 to 24 percent compared to gasoline. Overall, the results of this study provide a reference guide for combustion system design and development of the engine for CNG. Further research should be conducted to enhance CNG performance in order to compete with the gasoline.

5. ACKNOWLEDGEMENT

The author would like to thank the staffs and research group of GTeV in Faculty of Mechanical Engineering of University of Technical Malaysia Melaka for their commitment and support to this study.

6. REFERENCES

[1] NGV Global, “NGV Global 2011 Statistic Show Irrepressible Growth of NGVs,” [online] 2012, http://www.ngvglobal.com/ngv-global-2011-statistics-show-irrepressible-growth-of-ngvs-0704 (Accessed: 10 December 2014)

[2] A. Kowalewicz and M. Wojtyniak, “Alternative fuels and their application to combustion engines,” *J. Automobile Engineering* , vol. 219, pp.103-125, 2005.

[3] S. Maji, P. Sharma and M. Babu, "A Comparative Study of Performance and Emission Characteristics of CNG and Gasoline on a Single Cylinder S. I. Engine," SAE Technical Paper 2004-28-0038, 2004.

[4] A. S. Gautam, R .Garrick. J. H. Lee, C. M. Demico, P. E. Hannum and L. A.Villasmil, “A Comparison of the Emission from Gasoline vs Compressed Natural Gas for an Electronic Fuel Injected Two Cylinder, Four-Stroke Engine” SAE Technical Paper 2012-32-0016, 2012.

Performance and emission characteristics of castor blends biodiesel in single cylinder diesel engine dynamometer

Mohd Zaini Jamaludin[1,2], Safarudin Gazali Herawan[1,2,*], Yusmady Mohamed Arifin[1,2]

[1)] Faculty of Mechanical Engineering, Universiti Teknikal Malaysia Melaka,
Hang Tuah Jaya, 76100 Durian Tunggal, Melaka, Malaysia.
[2)] Centre for Advanced Research on Energy, Universiti Teknikal Malaysia Melaka,
Hang Tuah Jaya, 76100 Durian Tunggal, Melaka, Malaysia.

[*]Corresponding e-mail: safarudin@utem.edu.my

Keywords: Biodiesel; castor oil; engine dynamometer

ABSTRACT – This study presents a preliminary investigation of engine is running on petro-diesel in order to determine the engine's operating characteristics and exhaust emission levels, constituting the base line that is compared with corresponding cases when using second generation biodiesel that used castor biodiesel consists of 5%, 10% and 20% blends. The engine coupled to hydraulic dynamometer through belting connection for load measurement. The same method will be repeated for each fuel blend by keeping the same operating condition. The present studies contribute as an alternative fuel by using biodiesel fuels from non-edible for diesel engines with standard engine parts.

1. INTRODUCTION

Recently, crisis about fossil fuel depletion and environmental pollutants already got a people attraction. Air pollution is one of the most dangerous environmental problems all over the globe. Continuously increasing use of oil will intensify local air pollution and accelerate the global warming problems caused by CO_2. One of the environmental problems are most widespread in the whole world is air pollution. Production of CO_2 gasses accelerates that's global warming and the resulting pollution improving local air from the use of petroleum [1].

Thither is a need to find way by utilizing alternative fuels, which are preferably renewable and also could give off low levels of gaseous and particulate pollutants in internal combustion engine [2].

Nowadays, most researches on biodiesel utilize food based-ingredients as a mixture of the fuel such as palm oil, corn, soy bean and maize, which are also consumed as food. Even though, the effectiveness of those developed biodiesel has been proven to be used as the alternative fuel, it has ignited a conflict between food requirements and fuel necessity. Of this problem, a based non-food ingredient by using Ricinus Communis (Castor) oil is proposed as the blend of the biodiesel. For the purpose of the observation, a direct-injection diesel engine is used to examine the usability and the performance of the proposed biodiesel in term of BSFC, power output, torque and emission produced by the engine[3].

So that, the objectives of this research to studies the direct injection engines performance and emissions of second generation biodiesel of Castor oil and its blends i.e. B5, B10 and B20. As a result the objective this study was to explore the utility of Castor oil as a potential source a biodiesel. Hence, the role of non-edible oils such as Castor would be more sustainable for biodiesel production [4].

2. METHODOLOGY

The experimental was conducted using biodiesel and diesel blends on single cylinder engine. The setup is consists of a single cylinder, air-cooled four stroke direct injection diesel engine KIPOR KM 170F that had power of 2.6 kW at 3000 rpm. The exhaust gas analyzer SV-5Q type was used to measure the concentrations of oxygen (O_2), carbon monoxide (CO), carbon dioxide (CO_2), hydrocarbons (HC) and nitrogen oxides (NOx) of the exhaust gas of engine. Throughout all tests, the engine load was set at 50% load constant while engine speed was varied. Experimental set up was indicated in different blend ratios, these were regular diesel, and then using castor oil blended mixing with diesel at 5% (B5), 10% (B10) and 20% (B20).

Based on values obtained from back pressure, it will allow for obtaining power and torque required. In this case, the engine efficiency was assuming without any losses occurred. Torque and power of engine was determined using equation 1 and equation 2:

Torque of engine:

$$\tau_{th} = \frac{V_D P}{2\pi} \quad (1)$$

where; τ_{th} = torque (Nm), V_D = pump displacement in cc/rev, and P = pump pressure (bar)

Power of engine:

$$P = \frac{2\pi N \tau_{th}}{60} \quad (2)$$

where; P = pump power (W), τ_{th} = engine torque (Nm) and N = rotational speed in round per minute or engine speed (RPM).

3. RESULTS AND DISCUSSION

Fig. 1 show a comparison between a regular diesel and several biodiesel of B5, B10, and B20 at 50% load condition. As illustrated in Fig.1 that graph shows relationship between brake power and engine speed using different blends of biodiesel castor. As the result, the brake power is increasing steadily for diesel and all biodiesel blends. The maximum power of engine was recorded at 3000 rpm, and it was produce about 2.18 kW, 2.07 kW, 2.18 kW, and 2.29 kW for diesel, B5, B10, and B20, respectively. Clearly that castor blends produced a lower value compared than diesel fuel accordingly to lower calorific values and higher viscosities of biodiesel blends that affected in combustion chamber and cause unusual combustion criteria.

The relationship between engine torque against engine speed can be illustrates from Fig. 2. It can be seen that biodiesel blends of B5, B10, and B20 have a similar trends compared to diesel fuel. The diesel produced about 7.29 Nm at 3000 rpm, B5 about 6.95 Nm, B10 about 5.95 Nm and B20 about 5.95 Nm. Biodiesel produced less value of torque because it related to higher calorific value and higher cetane number of blends.

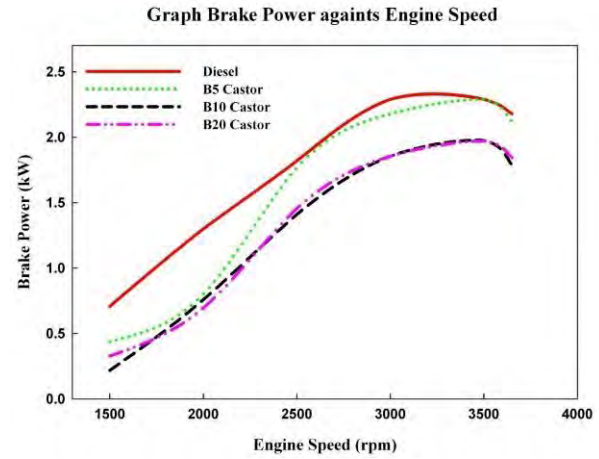

Fig. 1 Variation of Brake Power respect with engine speed

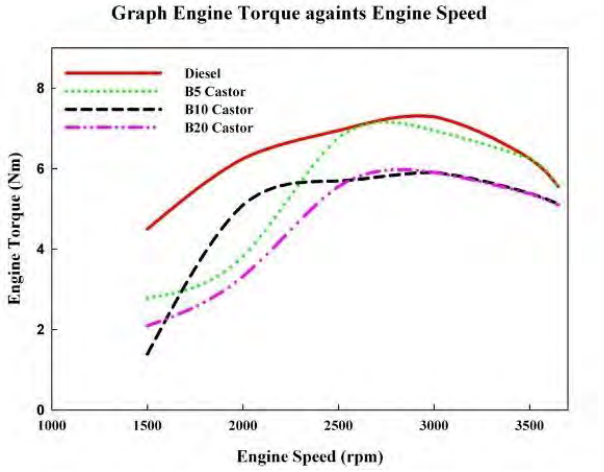

Fig. 2 Variation of Torque of Engine against engine speed

4. CONCLUSIONS

From the experimental works, it can be concluded that biodiesel fuel gives brake power and engine torque, lower than regular diesel fuel due to higher volume flow rate of fuel. Biodiesel castor oil is suitable alternative fuel for diesel engine without major adjustment of engine parts. It suggests that biodiesel from non-edible oil like castor oil could be a full replacement for diesel engine and can play a vital part in the near future particularly for meeting energy requirement in agriculture, industrial and shipping sectors. With comparable engine performance and reduction of Hydrocarbon, CO and with penalty of increased NOx emissions in comparison to regular diesel fuel, it can be concluded that biodiesel derived from castor oil and its blends could be applied in a formal diesel engine without any alteration. Nevertheless, the optimization of suitable blend can be subjected to future work with regard to engine parameters.

5. ACKNOWLEDGEMENT

Research grant provided by MTUN COE RESEARCH GRANT SCHEME project code MTUN/2012/UMP-FKM/3 M00007 under Ministry of Higher Education Malaysia for conducting this research is gratefully acknowledged.

6. REFERENCES

[1] G. Corro, N. Tellez, E. Ayala, and A. Marinez-Ayala, “Two-step biodiesel production from Jatropha curcas crude oil using SiO 2•HF solid catalyst for FFA esterification step,” Fuel, vol. 89, pp. 2815–2821, 2010.

[2] K. K. Radha, A. A. Kumari, S. N. Sarada, E. L. Nagesh, and K. Rajagopal, “Alternative Fuels for a Single Cylinder Direct Injection Diesel Engine,” 2008 First Int. Conf. Emerg. Trends Eng. Technol., 2008.

[3] M. Kousoulidou, G. Fontaras, L. Ntziachristos, and Z. Samaras, “Biodiesel blend effects on common-rail diesel combustion and emissions,” Fuel, vol. 89, pp. 3442–3449, 2010.

[4] B. S. Chauhan, N. Kumar, H. M. Cho, and H. C. Lim, “A study on the performance and emission of a diesel engine fueled with Karanja biodiesel and its blends,” Energy, vol. 56, pp. 1–7, 2013.

Hardware design multi-sources light electric vehicles

F.A. Azidin[1,2,3,*], Z.A. Ghani[1], M.A. Hannan[3], Azah Mohamed[3]

[1)] Faculty of Electronics and Computer Engineering, Universiti Teknikal Malaysia Melaka, Hang Tuah Jaya, 76100 Durian Tunggal, Melaka, Malaysia.
[2)] Centre for Advanced Research on Energy, Universiti Teknikal Malaysia Melaka, Hang Tuah Jaya, 76100 Durian Tunggal, Melaka, Malaysia.
[3)] Department of Electrical, Electronics and System Engineering, Faculty of Engineering and Built Environment, Universiti Kebangsaan Malaysia, 43600 Bangi, Selangor, Malaysia

[*]Corresponding e-mail: faridarafat@utem.edu.my

Keywords: Multi-sources; light electric vehicle, dSPACE

ABSTRACT – Combination of battery, proton exchange membrane fuel cell (FC) and super-capacitor (SC) as energy sources for light electric vehicle (LEV), or better referred to as multi-sources LEV has the purpose to improve vehicle performance and surpass battery drawbacks. Power coordination is designed by implementing intelligent switching hardware in energy management system (EMS) control circuit board. The EMS hardware circuit is integrated with dSPACE/ DS1104 down-scaled model for LEV. The accumulated results show that multi-sources LEV delivered better power efficiency than a single-powered battery LEV. This research could be beneficial to automobile industries in the future.

1. INTRODUCTION

Implementation of renewable energy in EV has becomes an important subject for research and study in both academic and industrial fields. Existing Battery Electric Vehicle (BEV) technology as a single-source EV has flaw to maintain good performance since its electrical characteristics depend heavily on its state of charge (SOC), self-discharge and life cycle [1]. The maximum current limitation differs between a brand-new battery and a battery, which already undergoes many life cycle [2]. Due to this, power performance of LEV will decline over time and thus becoming a hurdle to enter consumer market. Thus as an alternative to deliver acceptable power range, a multi-sources LEV is proposed [3]. Two additional sources that are suggested for implementation in the test bench model are FC and SC.

A small scale test bench model is designed by using dSPACE DSP DS1104 [4]. The hardware is built of EMS control board being connected to multi-sources signals, which is embedded on dSPACE interface signals and then linked to a computer. The output of the EMS control circuit is then linked to dSPACE for data acquisition.

2. HARDWARE DESIGN METHODOLOGY

The Figure 1 illustrated the model of EMS hardware control circuit. Components of the circuit include a voltage regulator, relay SONGLE, power MOSFET, half-bridge driver, speed pedal variable resistor, I/O hex buffers and PWM signal inverters. Additionally, an ampere meter is placed in series due to the fact that current is measured in term of voltage by the current sensor.

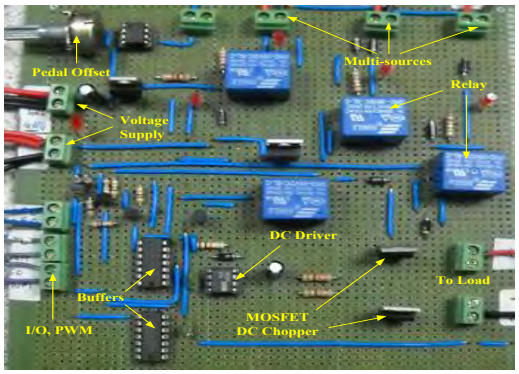

Figure 1 EMS hardware control circuit

2.1 Pedal Sensor through Variable Resistor

The vehicle throttle function is being replaced by a variable resistor. A voltage divider is attached to the variable resistor and its tapped voltage is assumed as pedal offset value.

2.2 Relay Triggered Circuit

SONGLE relay 5 VDC is used for multi-sources power switching. It has capability to hold 24 VDC with maximum current of 10 A. An NPN transistor of type BC184 is used to drive current flow into the coil inside the relay. A buffer is connected to base transistor via a 1 kΩ resistor. At the emitter end of the transistor, a resistor of 47 Ω is connected to the ground. Minimum current flow value to the coil must be greater than 70 mA.

2.3 MOSFET Drive Circuit

Power MOSFET IRL2703 is a fast switching speed of logic gate drive which has capacity of drain to source voltage, V_{DSS} of 30V and drain current, I_D of 24 A. Both pulse width modulation (PWM) signals from dSPACE DSP DS1104 are attached to the gate MOSFET with a series of resistor to avoid short circuit current. A half bridge driver circuit is designed to deliver load current.

2.4 Pedal Sensor through Variable Resistor

Current transducer LTSR-15 is used to measure load

current and battery current for SOC value. The measured current in range of -5A to 5A. The output current is detected in voltage range of 0 - 5V with 2.5V being the 0A point. The output signal is filtered with cut-off frequency, f_c of about 2 Hz.

2.5 Power Efficiency and Dissipated Energy Calculation

The power efficiency is calculated by how accurate the vehicle is able to trail the drive cycle. The under speed LEV from the drive cycle will be deducted. This power efficiency can be calculated as follows:

$$PowerEfficiency = \frac{DriveCyleArea}{TestDriveCycleArea} x100\% \quad (1)$$

The dissipated energy, E_{diss} used to trail drive cycle is calculated from the measured load current, I_L multiplied by rated voltage, V_{rated} and time, t as shown in below equation:

$$E_{diss} = V_{rated} \cdot I_L \cdot t \quad (2)$$

3. RESULTS AND DISCUSSION

The experiment is conducted by executing several test runs under ECE-47 and ECE-15 drive cycles. The speeds of drives cycle are extended to 33% (with ext) from their original speed for better analysis of the vehicle performance. The test runs are applied on both multi-sources (MSLEV) and single-source/battery (BLEV) systems to enable comparison between these two systems. The collected data for vehicle performance and energy consumption are evaluated and presented in Table 1.

Table 1 Test result of BLEV and MSLEV

Drive Cycle	BLEV PE (%)	MSLEV PE (%)	BLEV DS (Ws)	MSLEV DS (Ws)
ECE-47	~98%	~98%	1680	1699.2
ECE-47 ext	92%	97.9%	1940.4	1966.8
ECE-15	70.2%	~98%	2461.8	2700
ECE-15 ext	90.7%	97.2%	2893.6	3040.8

PE-Power Efficiency; DS-Dissipated Energy; Ws-Watt-second

Both BLEV and MS-LEV manage to follow ECE-47 drive cycle with high precision, with both systems achieved power efficiency of 98%. The dissipated energy for both is around 1690Ws. Since maximum speed of ECE-47 is the average power of energy sources, extended speed of 33% is necessary to investigate capabilities of the vehicles. For the extended ECE-47 test, battery condition is no longer new and test runs when battery SOC is at about 70%. BLEV showed a drop in power efficiency to 92% while MSLEV was able to stay at 98%. During the test, SC is triggered in MSLEV to maintain the maximum speed. The consumed energy for MSLEV is 1966.8Ws and BLEV is 1940.4Ws.

The next test executed is for the ECE-15 drive cycle or urban drive cycle. For this test, battery SOC is only at around 50-55%. During this test drive cycle, FC was activated in MSLEV whenever SOC level is below 50%. Meanwhile in BLEV, it is battery powered only when SOC goes beyond 50%. The performances of BLEV dropped to 70.2% while MSLEV still managed to maintain 98%. Less power efficiency of BLEV leads to less energy consumption as well. Therefore, dissipated energy for BLEV is 2461.8Ws while for MSLEV, it is at 2700Ws. The ECE-15 test is included with extended speed of 33%. For this test, battery condition is set at 65% and this condition is better than previous test. At this test drive cycle, BLEV improved its power efficiency to 90.7%, while MSLEV almost maintained its value at 97.2%. The dissipated energy of MSLEV is 3040.8Ws and for BLEV, it is at 2893.6Ws.

The overall results show that battery's electrical characteristics will be decreased by its SOC level and lifecycle numbers. This is obvious to be observed especially when the test was conducted at half of SOC level. During high load current, battery current will be reduced in time until it is maintained at average current. For MSLEV, SC will be triggered to maintain high current load. In the case where battery reaches half of SOC level, FC will take over and continue to power the vehicle.

4. CONCLUSIONS

This paper is concerned in developing hardware and control algorithm for MSLEV. The EMS hardware prepares signals from I/O peripherals of dSPACE DS1104 to select energy source and sensing system. The system performance is evaluated through ECE-47 and ECE-15 drive cycles. The experiment result shows that MSLEV had successfully follow the drive cycle even during low battery condition and urgent power demand. The test result also proves that MSLEV is superior to a BLEV. Thus this system has potential to be implemented in in future vehicle applications.

5. REFERENCES

[1] B.G. Pollet, I. Staffel, J.L. Shang, "Current status of hybrid, battery and fuel cell electric vehicles: From electrochemistry to market prospects," *Electrochimica Acta,* vol. 84, no. 2012, pp. 235-249, 2012.

[2] Y. Tang, W. Yuan, M. Pan, Z. Wan, ", Experimental investigation on the dynamic performance of a hybrid PEM fuel cell/ battery system for lightweight electric vehicle application," *Applied Energy,* vol. 88, no. 1, pp. 68-76, 2011.

[3] S.T. Tie, C.W. Tan, "A review of energy sources and energy management system in electric vehicles," *Renewable and Sustainable Energy Reviews*, vol. 20, no. 2012, pp. 82–102, 2012.

[4] F.A. Azidin, M.A. Hannan, "A dSPACE Test Bench Model of Multi-energy Sources for Light Electric Vehicles," *Engineering International Conference 2013, Semarang,* pp. 105–109, 2013.

On the dynamics of a beam-SDOF energy harvester system

S. Susilo[1,*], A. Putra[1,2], K.S. Leong[3], M.J.M. Nor[1,2]

[1)] Faculty of Mechanical Engineering, Universiti Teknikal Malaysia Melaka,
Hang Tuah Jaya, 76100 Durian Tunggal, Melaka, Malaysia.
[2)] Centre for Advanced Research on Energy, Universiti Teknikal Malaysia Melaka,
Hang Tuah Jaya, 76100 Durian Tunggal, Melaka, Malaysia.
[2)] Faculty of Electronics and Computer Engineering, Universiti Teknikal Malaysia Melaka,
Hang Tuah Jaya, 76100 Durian Tunggal, Melaka, Malaysia.

[*]Corresponding e-mail: sidiksoesilo@student.utem.edu.my

Keywords: Energy harvester, piezoelectric material, vibration

ABSTRACT – Dynamic model of a beam attached at the mass of a single-degree-of-freedom system is presented in this paper. The structural wave propagation method is used leading to solution of complex wave amplitudes across the beam. The proposed model is aimed at characterizing the behavior of the system to study the potential electrical energy harvested from such mechanism where the beam is a piezoelectric material.

1. INTRODUCTION

A conventional piezoelectric energy harvester is a system which consists of a cantilever beam structure. Numerous studies have been published regarding the mathematical modelling and the experimental tests of the electrical energy which can be harvested from this system [1-3].

This paper proposes the beam structure combined with a single-degree-of-freedom system (SDOF) to vibrate the beam from the motion of the SDOF system which is excited by an external harmonic force. Similar model has been by proposed by Wang et. al.[4] using the Hamilton's principle and Rayleigh-Ritz method. Here the structural wave propagation method is implemented where waves in the beam is assumed to consists of propagating flexural and near-field waves. Forces acting at the edge of the beam are determined according to the boundary conditions. The component of the complex wave amplitudes can be obtained through an inverse matrix process.

2. METHODOLOGY

Consider a uniform and thin beam with length L attached with the mass of a single-degree-of-freedom (SDOF) system as shown in Figure 1. The bending waves are assumed to propagate across the length of the beam. The wave amplitude in the beam is assumed for a time harmonic solution of the form [5]

$$u(x,t) = U(x)e^{j\omega t} \tag{1}$$

where the complex amplitude is given by

$$U(x) = a_1 e^{-jkx} + a_2 e^{jkx} + a_3 e^{-kx} + a_4 e^{kx} \tag{2}$$

where $a_{1,2}e^{\pm jkx}$ are the harmonic propagating waves and $a_{1,2}e^{\pm kx}$ are the near-field waves. The wavenumber is defined as

$$k = \sqrt{\omega}\left(\frac{\rho A}{EI}\right)^{\frac{1}{4}} \tag{3}$$

where E, I, ρ, A are respectively the Young Modulus, second mass moment of area, density and cross area of the beam.

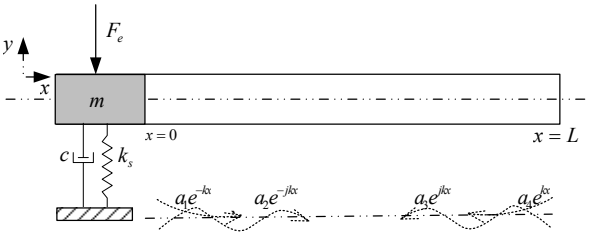

Figure 1 Beam-SDOF energy harvester system model.

The rotational displacement across the beam is defined as

$$\theta(x,t) = \frac{\partial u(x,t)}{\partial x} \tag{4}$$

Based on Eq. (2), the vector of the degrees of freedom is given can be given by

$$\begin{bmatrix} u_1 \\ \theta_1 \\ u_2 \\ \theta_2 \end{bmatrix} = \begin{bmatrix} e^{-jkx} & e^{jkx} & e^{-kx} & e^{kx} \\ -jke^{-jkx} & jke^{jkx} & -ke^{-kx} & ke^{kx} \\ e^{-jkL_x} & e^{jkL_x} & e^{-kL_x} & e^{kL_x} \\ -jke^{-jkL_x} & jke^{jkL_x} & -ke^{-kL_x} & ke^{kL_x} \end{bmatrix} \begin{bmatrix} a_1 \\ a_2 \\ a_3 \\ a_4 \end{bmatrix} \tag{5}$$

Bending moment and shear force are given by

$$M(x) = EI\frac{\partial^2 u}{\partial x^2} \qquad F(x) = -EI\frac{\partial^3 u}{\partial x^3} \tag{6}$$

Substituting Eq. (5) into Eq. (6), the general matrix of the force equal to

$$\mathbf{F} = EI\mathbf{U}\tilde{\mathbf{a}} \tag{7}$$

where $\mathbf{F} = \begin{bmatrix} F_1 & M_1 & F_2 & M_2 \end{bmatrix}^{-1}$ and $\tilde{\mathbf{a}} = \begin{bmatrix} a_1 & a_2 & a_3 & a_4 \end{bmatrix}^{-1}$ with

$$\mathbf{U} = \begin{bmatrix} jk^3e^{-jkx} & -jk^3e^{-jkx} & -k^3e^{-kx} & k^3e^{kx} \\ -k^{2-jkx} & -k^2e^{jkx} & k^2e^{-kx} & k^2e^{kx} \\ jk^3e^{-jkL_x} & -jk^3e^{-jkL_x} & -k^3e^{-kL_x} & k^3e^{kL_x} \\ -k^{2-jkL_x} & -k^2e^{jkL_x} & k^2e^{-kL_x} & k^2e^{kL_x} \end{bmatrix}$$

From Figure 1, at $x = 0$, the shear force at the end of the beam equals to the net force acting on the SDOF system. If the SDOF system is excited with an unit external force $F_e = 1$, the boundary conditions can therefore be written as

$$\begin{aligned} F_1(0) &= (-\omega^2 m + j\omega c + k)\,\mathrm{U}(0) - F_e = F_S - F_e \\ M_1(0) &= 0 \\ F_2(L) &= 0 \\ M_2(L) &= 0 \end{aligned} \tag{8}$$

Equation (7) can then be re-arranged for $x = 0$ to give

$$\mathbf{U} = \begin{bmatrix} jk^3 - F_S & -jk^3 - F_S & -k^3 - F_S & k^3 - F_S \\ -k^2 & -k^2 & k^2 & k^2 \\ jk^3e^{-jkL} & -jk^3e^{-jkL} & -k^3e^{-kL} & k^3e^{kL} \\ -k^{2-jkL} & -k^2e^{jkL} & k^2e^{-kL} & k^2e^{kL} \end{bmatrix} \tag{9}$$

where $\mathbf{F} = \begin{bmatrix} 1 & 0 & 0 & 0 \end{bmatrix}^{-1}$. The amplitude can then be calculated as

$$\tilde{\mathbf{a}} = \frac{\tilde{\mathbf{U}}^{-1}\mathbf{F}}{EI} \tag{10}$$

The results from Eq. (10) can be substituted back to Eq. (2) to obtain the vibration amplitude of the beam.

3. RESULTS DAN DISCUSSION

Simulation is conducted with parameters of the piezoelectric material (PZT) beam and the SDOF system given in Table 1.

Figure 2 shows the response for different mass of SDOF system at location of $x = 0.4L$. It can be seen that there are several significant resonances of the beam which can be a potential source of frequency excitation for harvesting the electrical energy.

4. CONCLUSIONS

Mathematical modeling of the dynamics of a beam-SDOF energy harvester system has been proposed using the wave propagation technique. For future study, it is of interest to investigate the case for vibration energy coming from the base which is more realistic in application where such energy harvester can be used to directly harvest the energy from a vibrating host structure.

Table 1 Parameters of the beam used for simulation

Properties	**Data**
Moment of area, I	5.475×10^{-13} m^4
Young's modulus, E	69×10^{9} N/m^2
Density, ρ	7500 kg/m^3
Mass, m	0.1 kg
Spring stiffness, k_s	100 N/s
Damping constant, c	0.5 kg/s

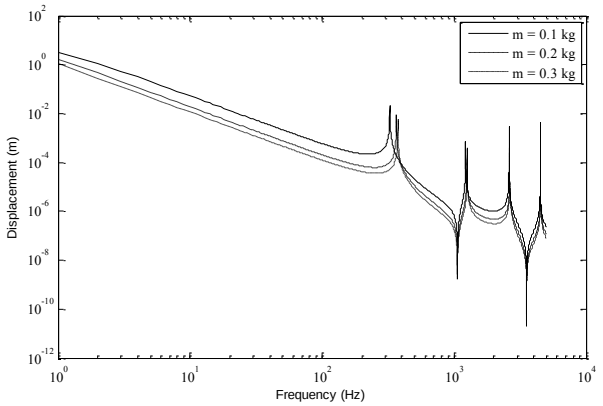

Figure 4 Displacement of the beam at $x = 0.4L$.

5. ACKNOWLEDGMENT

This research is conducted under The Research Acculturation Collaborative Effort Grant Scheme FRGS(RACE)/2012/FKM/TK01/02/1/F00146 from the Ministry of Higher Education Malaysia.

6. REFERENCES

[1] S. Roundy and P. K. Wright, "A piezoelectric vibration based generator for wireless electronics," *Smart Materials and Structures*. 13, pp. 1131-1142, 2004.

[2] S. L. Kok, N. M. White, and N. R. Harris, "A free-standing, thick-film piezoelectric energy harvester," in *IEEE SENSORS 2008 Conference*, 2008, pp. 589-592.

[3] J. Dayou, C. Man-sang, M. C. Dalimin, and S. Wang, "Generating electricity using piezoelectric material," in *Borneo Science*, 2009, pp. 47-51.

[4] H. Wang, X. Shan, and T. Xie, "An energy harvester combining a piezoelectric cantilever and a single degree of freedom elastic system," *Journal of Zhejiang university-SCIENCE A*. 13(7), pp. 526-537, 2012.

[5] D. J. Inman, *Engineering Vibrations,* 3rd ed. New Jersey: Pearson; 2008.

Relationships derived from physical properties of waste cooking oil / diesel blends and biodiesel fuels

M.I. Ali[1,2,*], J. Faezah[1,2]

[1)] Faculty of Mechanical Engineering, UniversitiTeknikal Malaysia Melaka, Hang Tuah Jaya, 76100 Durian Tunggal, Melaka, Malaysia.
[2)] Centre for Advanced Research on Energy, UniversitiTeknikal Malaysia Melaka, Hang Tuah Jaya, 76100 Durian Tunggal, Melaka, Malaysia.

[*]Corresponding e-mail: mdisa@utem.edu.my

Keywords: Waste cooking oil; palm oil biodiesel; mathematical relationships

ABSTRACT – The aim of this study is to estimate mathematical relationships of vital fuel properties of waste cooking oil/diesel blends and biodiesel fuels. The origin of both waste cooking oil (WCO) and biodiesel (BD) are from palm oil to keep the uniformity of this study. To find the fuel properties, experiments are carried out to acquire data for each blend sample. The samples of blends prepared are ranging from 10% to 100% for both WCO and BD blend with diesel respectively. Mathematical relationships for each fuel property for WCO/Diesel and BD/Diesel blends are produced with their respective coefficient of determination denoted as R^2. The results have shown that the properties of the fuel mainly have polynomial relationships.

1. INTRODUCTION

Diesel is a very useful and incredible fuel with diverse use and applications. However, the usage of petroleum when it is at its high demand is actually costly since it is a limited source. With this apparent global energy issue and crisis, scientists have been working towards developing alternate source of energy that is more economical and sustainable in the ecology system of the earth. One of the options for alternative fuel that is often turned to these days is the waste cooking oil. Biodiesel on the other hand is also another alternate source that is too a well-known solution towards petroleum dependency. In addition, biodiesel is renewable and has a positive and less damaging impact on the environment and yet it could be a good substitution of diesel as an engine fuel thus reducing the demand of fossil fuel which is very limited source to cope with the global use.

Biodiesel is given its name because it is made up of variety of ester based oxygenated fuel produced from renewable biological resources [1-2]. As for the production of biodiesel, transesterification is the most common method [3]. This is because it produces and output high yield at low temperature and pressure and has short reaction time.

Waste cooking oil is the oil that is obtained from the fried food. When heated up to 180 °C in order to fry food, the chemical composition of cooking oil tends to change and thus the cooking oil is not advisable to be used over and over again because food will absorb over 5% of the used cooking oil and hence affect human health who consumed the fried food [4]. The global consumption of vegetable oil is increasing every year thus increase the waste oil production and disposal [5]. Waste cooking oil disposal is a problem.

There are numerous study and research made on engine testing and emission that require the input of fuel properties as the pre-requisite condition before applying any fuel in the engine. A study conducted by Liaquat et al. [5] emphasized on the performance of engine and emission nature of diesel engine by using coconut biodiesel blends. Aside from finding the fuel properties to perform engine testing, there is also a research that specify on the study of elemental properties of palm oil biodiesel blends. This study which is mentioned earlier was conducted by Pedro et al. [6] and Donald et al.[7].

In this study, the main fuel properties that are viscosity, density and heating value of diesel blends with respect to WCO and BD are to be determined and to estimate mathematical relationships of vital fuel properties.

2. METHODOLOGY

Sample preparation starts by collecting 4 liters of waste cooking oil (WCO) from local restaurants and purchasing of 4 liters of pure biodiesel (BD) and 6 liters of diesel. The collected waste cooking oil is first filtered by using coffee cloth prior to filtering using 11 micron paper filter. Then the filtered oil is heated at temperature exceeding 100°C so that all the water content in the oil is gotten rid of. The oil is then ready to be blended with diesel and thus prepared to be tested for its properties.

Blending is done to obtain two set of blending sample; one sample set is for BD blended with diesel and the other set is for WCO blended with diesel. The blending is done based on volume percentage ranging from 10% to 100% for both BD and WCO blend with diesel respectively.

The equipments used to measure for the basic properties or fuel characteristics of each blend are summarized in Table 1 as follows:

Table 1 Equipments used for fuel characterizations

Fuel characteristics	Equipment
Heating value	IKA C200 Bomb Calorimeter
Viscosity	Brookfield Viscometer
Density	Hydrometer

3. RESULTS AND DISCUSSION

Figure 1 shows the viscosity of both types of blends increases as the percentage of blend increases as they went from pure diesel to their pure forms of W100 and B100. Commercial diesel has the lowest viscosity of 6.2 cP whilst pure WCO, W100 is the most viscous fuel at viscosity of around 37 cP. It is also indicated that in the graph the pure biodiesel, B100 has slightly higher viscosity than diesel which is at around 6.7 cP.

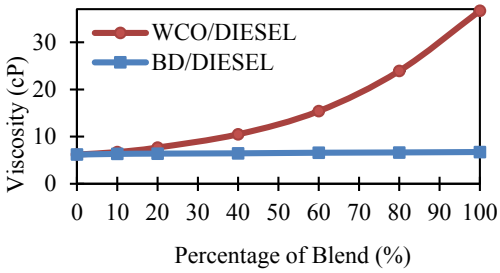

Figure 1 Viscosity against percentage of blend

Figure 2 shows the density for both types of blend is rising as the intensity of the WCO and BD rises. Diesel has the lowest density at 830 kg/m^3 while pure WCO (W100) has the highest density at 905 kg/m^3. Besides that, it is also recognizable that the densities of WCO blends are again greater than that of the BD blends.

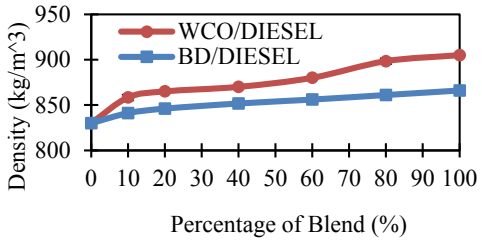

Figure 2 Density against percentage of blend

Figure 3 indicates that the heating value for both types of blend decreases as the percentage or intensity of the blend increases. This phenomenon is happening due to the increase in density of the oils. Heat is an extensive property whereby it is highly dependent on the size of the matter. Study has shown that the relationship between higher heating value (HHV) and density is inversely proportional [7]. This means that as the density of the fuel increases, the heating value of the fuel will continue to decrease.

In summary, the mathematical relationships for WCO/Diesel blends are resulted as follows:

VIS = 0.0035x^2 - 0.0612x + 6.8241

DN = -0.0033x^2 + 0.9687x + 839.84

HV = -3E-05x^3 + 0.0043x^2 - 0.2122x + 46.464

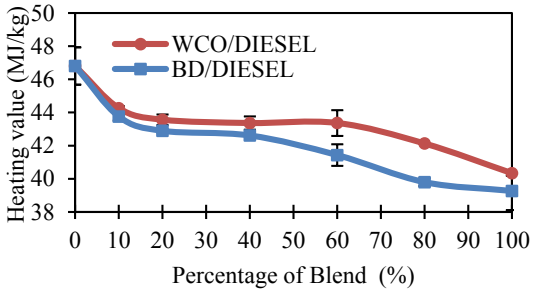

Figure 3 Heating value against percentage of blend

Concurrently, the mathematical relationships of BD/Diesel blends are recorded as follows:

VIS = 0.0048x + 6.2646

DN = -0.0024x^2 + 0.5538x + 833.29

HV = -2E-05x^3 + 0.0029x^2 - 0.199x + 46.23

4. CONCLUSIONS

From the results obtained, BD blends can be concluded as a better fuel in comparison to the WCO blends. This is because transesterification or alcoholyis has brought about positive effects on the properties of the blends. The fuel properties of BD blends especially B20 is compatible to be used in a CI engine on a par with diesel fuel without the need to an engine modification or special handling of the fuel. Besides that, the objective of this study is achieved by the generation of the estimated mathematical relationships of the fuel properties with respect to the blend intensity.

5. REFERENCES

[1] A. Pravin, T. Ashok. Pise and S. Chougule. "Properties of Biofuels and their Diesel Blends as a Fuel for C.I. Engines"in *IEEE-International Conference On Advances In Engineering, Science And Management*, 2012, pp.1-8.

[2] C.B. Daria. "Biodiesel Production from Non-foodstuff" *Chemistry, Catalysis and Engineering*. 2012, pp. 49-51.

[3] M. Mathiyazhagan. M., A.Ganapathi, B. Jaganath, N. Renganayaki, and N. Sasireka. "Production of Biodiesel from Non-edible plant oils having high FFA content". *International Journal of Chemical and Environmental Engineering*, pp. 1-4. 2011.

[4] G.M. Kulkarni and A.K. Dalai. "Waste Cooking Oils - An Economical Source for Biodiesel: A Review." *Ind. Eng. Chem. Res*, pp. 1-13. 2006.

[5] Liaquat A. M., Masjuki H. H., Rizwanul Fattah I. M., Hazrat M. A., Varman M., Mofijur M., Shahabuddin M. Effect of coconut biodiesel blended fuels on engine performance and emission characteristics . *Pro. Eng.* 56, pp. 683-690. 2013.

[6] Pedro Benjumea, John Agudelo, Andre´s Agudelo. Basic properties of palm oil biodiesel– diesel blends. *Fuel* 87, pp. 2069-2075. 2007.

[7] Donald A. Heck, Jordan Thaeler, Steve Howell and Joshua A. Hayes. (2009). Quantification of the Cold Flow Properties of Biodiesels Blended with ULSD, *Iowa Biodiesel Board*, pp.10-15. 2009.

Broadening the bandwidth of energy harvesting devices by using different magnet configurations

H.A. Ghani[1,*], R. Ramlan[1,2], M.J.A. Latif[1,2], P.S. Low[1]

[1)] Faculty of Mechanical Engineering, Universiti Teknikal Malaysia Melaka, Hang Tuah Jaya, 76100 Durian Tunggal, Melaka, Malaysia.
[2)] Centre for Advanced Research on Energy, Universiti Teknikal Malaysia Melaka, Hang Tuah Jaya, 76100 Durian Tunggal, Melaka, Malaysia.

[*]Corresponding e-mail: ahilmiah@yahoo.com

Keywords: non-linear energy harvesting; softening; hardening

ABSTRACT – A nonlinear generator was originally intended to overcome the limitation of a linear resonant generator that is having small bandwidth. This paper presents the experimental results to illustrate the dynamic monostable behaviour of the nonlinear generator using magnetic levitation concept. A device was built to investigate the effectiveness of the different magnets configurations on the dynamics under harmonic excitation. The results show that the softening and hardening behaviours of the system due to the magnetic stiffness produce a broader bandwidth response.

1. INTRODUCTION

The importance of energy harvesting concept has emerged as a prominent research area especially in extracting energy from the ambient sources. Various applications are targeted as power source to power wireless sensor system. Among these ambient power sources, vibration emerges as one of the promising sources.

By applying the mechanical model in a single degree of freedom (SDOF) mass-spring-damper system, the maximum power can be harvested when the device is excited at resonance frequency [1]. However, if the frequency of the device is slightly mistuned from the natural frequency of the system, the performance of the device tends to decrease drastically. Frequency tuning methods (active and passive tuning) are introduced to track the natural frequency for all the time. An active tuning method is reported by Zhu et al. [2], who implemented a tunable electromagnetic vibration to alter its natural frequency. Eichhorn et al. [3] proposed a pre-stress generator to adjust the device natural frequency using passive tuning method.

Another approach to overcome the sensitivity due to mistune is by introducing nonlinearity into the system. The aim of this method is to broaden the bandwidth so that the device is able to function effectively in a wide frequency band. The most common types of nonlinearity used in energy harvesting mechanism are softening and hardening nonlinearity. These two nonlinearities are based on the stiffness nonlnearity. Ramlan et al. [4] implemented the theoretical and experimental studies for hardening behaviour of nonlinear system. Tang et al. [5] proposed a monostable harvester in both hardening and softening behaviours that appear by using two attractive and repulsive magnets. However, the use of magnetic levitation by various configurations magnets in nonlinear generator has not been greatly explored especially involving constant amplitude excitation thus the real benefits of each configurations under similar excitation is yet to be established.

This paper presents an experimental investigation on the use of different magnets configurations under similar excitation. By configuring the magnets under two basic modes (attractive and repulsive), the gap between the magnets are adjusted to investigate the effect on the system's stiffness and the frequency response

2. METHODOLOGY

2.1 Device Configuration

A magnetic levitation method is applied to the device to explore the nonlinearity concept. The masses with a NdFeB magnet (6m x 3 mm) is mounted on an aluminum cantilever beam (30 mm x 0.5 mm x 56 mm) fixed at one end. In this study, three configurations are investigated. This includes a single permanent magnet with a single attractive magnet configuration, double attractive magnet configuration and double repulsive magnet configuration (Figure 1). By altering the axial gap between the moving magnet on the beam and the fixed magnets, the stiffness of the system can be varied accordingly. In this measurement, the axial gaps, *d* are fixed at 1.5 mm, 1.8 mm and 2.5 mm.

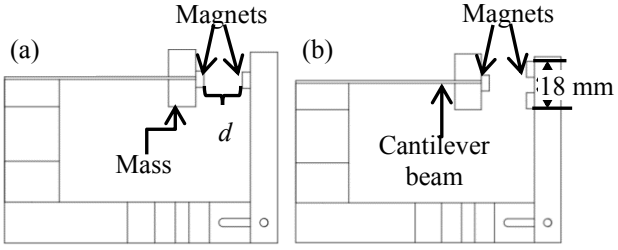

Figure 1: Schematic diagram of the configurations
(a) a permanent magnet with a single fixed magnet
(b) a permanent magnet with the double fixed magnets.

2.2 Experimental Set-Up

Dynamic measurement is implemented to investigate the behaviour of frequency response curve of the proposed configurations. In this measurement, the whole device was placed on the shaker and excited with constant amplitude excitation (2.5 mm) from 4 Hz to 40 Hz and 40 Hz to 4 Hz respectively. Two Dytran accelerometers were used to record the acceleration of the tip mass and the base of the device. All the data were analysed by using Data Physics signal analyser.

3. RESULTS AND DISCUSSION

The responses of the system under different magnet configurations are observed to operate in softening and hardening mode. The gap between the magnets determines the behaviour of the system. In monostable case, the frequency response curve (FRC) of softening and hardening behaviours can be determined by analysing the jump up and jump down in dynamic experiment. The FRC for softening behaviour tends to shift to the left and vice versa.

For two attractive magnets shown in Figure 1(a), with the increase of the gap between magnets, the FRC of the system shifted slightly to the left accordingly. In this configuration, the jump down frequencies are occurred between 14 Hz to 16.5 Hz as shown in Figure 2.

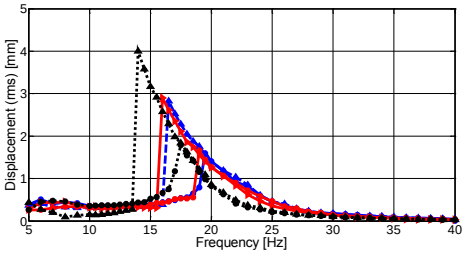

Figure 2: Measured frequency response curve for two attractive magnets with the gaps 1.5 mm [jump up (○- -), jump down (△ -)], 1.8 mm [jump up ○- - --), jump down (-- △--)] and 2.5 mm [jump up (...○..), jump down (..△...)].

For the permanent magnet and two attractive magnets configuration shown in Figure 1(b), when the gaps are fixed at 1.5 mm and 1.8 mm, the system operates in softening mode. However, as the gap is increased to 2.5 mm, the frequency response changes to hardening mode as shown in Figure 3.

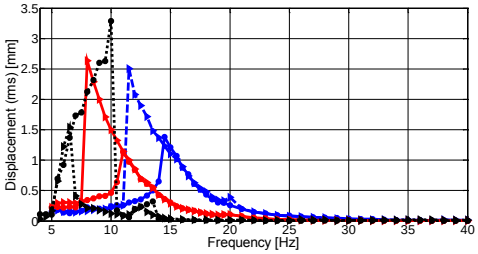

Figure 3: Measured frequency response curve for a permanent magnet with two attractive magnets at 1.5 mm [jump up (○- -), jump down (△ -)], 1.8 mm [jump up (--△--), jump down (--○--)] and 2.5 mm [jump up (...△..), jump down (...○...)].

The response of the system between the permanent magnet and double repulsive magnets (Figure 1(b)) are similar to the two attractive magnets i.e. softening mode as shown in Figure 4. However, the configuration results in a higher jump-up and jump-down frequency

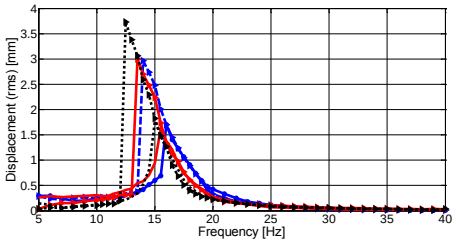

Figure 4: Measured frequency response curve for a permanent magnet with two repulsive magnets at 1.5 mm [jump up (○- -), jump down (△ -)], 1.8 mm [jump up (--○--), jump down (--△--)] and 2.5 mm [jump up (...○..), jump down (... △.)].

4. CONCLUSIONS

This paper presents the experimental results for both softening and hardening behaviours of nonlinear system resulting from different magnetic stiffness. A device using magnetic levitation method was proposed in this study. By applying appropriate magnet arrangements, the gap between the magnets can be altered to change the stiffness of the system so that it can operate in either softening or hardening mode. Either of the nonlinear mode is capable of broadening the bandwidth and improving the response.

5. ACKNOWLEDGEMENT

The authors would like to thank the Ministry of Higher Education Malaysia for funding this work under the Exploratory Research Grant Scheme (ERGS/1/2012/TK01/Utem/02/6-E00006).

6. REFERENCES

[1] C.B. Williams, R.B Yates, "Analysis of a micro-electric generator for microsystem," *Sensors and Actuators A*, vol.52, pp. 8-11, 1996.

[2] C. Eichhorn, F. Goldschmidtboeing, and P. Woias, "Bidirectional frequency tuning of a piezoelectric energy harvester based on a cantilever beam," *Journal of Micromechanics and Microengineering,* vol.19, 2009.

[3] D. Zhu, S. Robert, J. Tudor, and S. Beeby, "Closed loop frequency tuning of a vibration-based micro generator," *Proceedings of PowerMEMS,* pp. 229-232, 2008.

[4] R. Ramlan, M.J. Brennan, B.R. Mace, and I. Kovacic, "Potential benefits of a non-linear stiffness in an energy harvesting device," *Nonlinear Dynamic,* vol.59, no.4, pp.545-558, 2009.

[5] L. Tang, Y. Yang, and C.K. Soh, "Improving functionality of vibration energy harvesters using magnets," *Journal of Intelligent Material Systems and Structures*, vol.23, no.13, pp. 1433-1449, 2012.

The evaluation of machinability and surface roughness in conventional vertical milling machine

M.A.M. Daud[1,2,*], W.T. Ng[1,2] , D. L. Sivakumar[1,2] , M. Z. Selamat[1,2]

[1)] Faculty of Mechanical Engineering, Universiti Teknikal Malaysia Melaka,
Hang Tuah Jaya, 76100 Durian Tunggal, Melaka, Malaysia.
[2)] Centre for Advanced Research on Energy, Universiti Teknikal Malaysia Melaka,
Hang Tuah Jaya, 76100 Durian Tunggal, Melaka, Malaysia.

[*]Corresponding e-mail: ahadlin@utem.edu.my

Keywords: surface roughness; machinability; milling machine

ABSTRACT – The purposes of this research are to analysis the machinability and surface finish of different types of material with high speed steel cutting tool using conventional milling machine and study the effect of machining parameter on quality of surface finish of different types of material. In addition, the materials have been used in this research are aluminum, stainless steel and brass. The machining parameters have been chosen are feed rate and spindle speed. While for the cutting tool in this research is high speed steel end mill. After milling process and surface roughness test have been conducted, the result of each test specimen will be compared and find the optimized machining parameter of each types of material by analyzing the value of surface roughness. The optimized machinability and surface finish is stainless steel at feed rate of 37 mm/min and spindle speed of 1400 rpm.

1. INTRODUCTION

Milling is a cutting process of cutting away material of a work piece by using multiple tooth cutters which is a cutting tool that produces a number of chips in one revolution. It is able to create a variety of features such as holes, pockets, slots and three dimensional contours. Milling process is able to produce different types of surface finish with different machining parameters. Machining parameters such as depth of cut, spindle speed and feed rate. Optimized machining parameters are able to save the production cost and time [1].

Surface finish is surface texture or as known as characteristics of surface. In industries, the quality of surface finish is very important. This is because quality of surface finish is able to affect the quality of product. Therefore optimized machining parameters are able to produce high quality of surface finish of machined workpiece. Surface finish also will affect the production cost in manufacturing industries [2]. Manufacturing industries require high demand on the quality of surface finish but require low machining cost. Yet, better surface finish quality may cause higher manufacturing cost [3]. Therefore, optimized machining parameter is very important in manufacturing industries. Surface roughness influences some functions of work piece such as fatigue resistance, contact causing surface friction, wearing, heat transmission, lubricant distribution plus hold ability and coating [4].

The objectives in the project are to analysis the machinability and surface finish of different types of material with high speed cutting tools using conventional vertical milling machine and study the effect of machining parameter on quality of surface finish of different material.

2. METHODOLOGY

The experiment is carried out with a conventional vertical milling machine and it model is JTM 1050VSE with a high speed steel end mill cutting tool. After the forty five test specimens are prepared, the milling process will be started. There are three machining parameters which are spindle speed, feed rate and depth of cut in this experiment. Spindle speed and feed rate are set as variable machining parameter. The values of spindle speed are 1000 rpm, 1200 rpm, 1400 rpm, 1600 rpm and 1800 rpm. For the values of feed rate are 37 mm/min, 141 mm/min and 240 mm/min. Depth of cut is set as constant machining parameter which is 0.2 mm for three different types of material which are aluminum, brass and stainless steel in this experiment.

Surface roughness test is conducted by using Mitutoyo Surface Tester SJ-301. Mitutoyo Surface Tester SJ-301 is used to measure the parameter of surface roughness of test specimens. Calibration of Mitutoyo Surface Tester SJ-301 needs to be done carefully. Therefore, a mitutoyo precision reference specimen with code 178-602 is used during calibration on the Surface Mitutoyo Surface Tester.

3. RESULTS AND DISCUSSION

From the Figure 1, Figure 2, Figure 3**,** all graphs show the effect of spindle speed to surface finish quality. The increasing of spindle speed results good surface finish quality [5]. Good surface finish quality means low value of surface roughness and vice versa. Meanwhile, spindle speed is inversely proportional to surface roughness. When spindle speed increases, the surface roughness of work piece decreases.

Surface finish quality of a material indicates the machinability of a material. Therefore, the machinability of material increases with increasing spindle speed. This is due to the reduction of built up edge chip formation by increasing the spindle speed. When the feed rate is constant at a certain value, surface roughness decreasing

when the increasing of spindle speed. This behavior can be observed in Figure 1, Figure 2 and Figure 3. However, the value of surface roughness is nearly constant at feed rate of 37 mm/min in Figure 3 for stainless steel. This is because spindle speed does not have much effect on surface finish quality with increment of spindle speed from 1000 rpm until 1800 rpm at feed rate of 37 mm/min.

From the Figure 1 and Figure 2, brass and aluminum have the lowest arithmetic mean surface roughness at spindle speed of 1800 rpm. Besides that, increasing spindle speed is able to improve the surface finish quality. On the other hand, stainless steel has the lowest surface roughness at 1400 rpm.

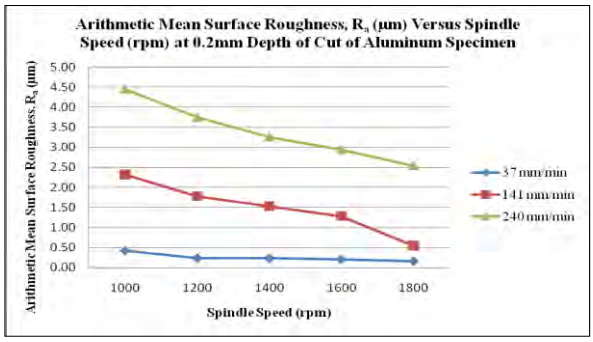

Figure 1 Arithmetic Mean Surface Roughness, R_a (µm) Versus Spindle Speed (rpm) at 0.2mm Depth of Cut of Aluminum Specimen.

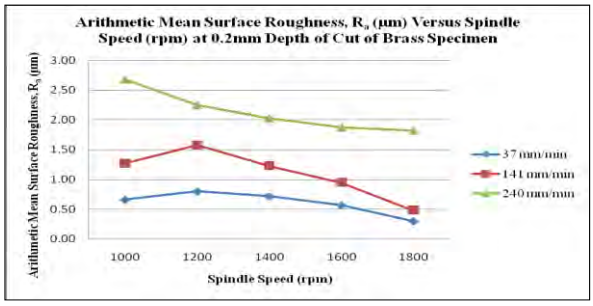

Figure 2 Arithmetic Mean Surface Roughness, R_a (µm) Versus Spindle Speed (rpm) at 0.2mm Depth of Cut of Brass Specimen.

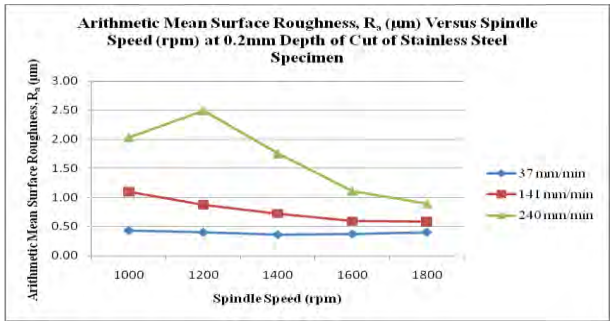

Figure 3 Arithmetic Mean Surface Roughness, R_a (µm) Versus Spindle Speed (rpm) at 0.2mm Depth of Cut of Stainless Steel Specimen.

4. CONCLUSIONS

The objectives in this project have been achieved. The optimized machinability and surface finish of aluminum and brass are at feed rate of 37 mm/min and spindle speed of 1800 rpm. Moreover, the optimized machinability and surface finish of stainless steel is at feed rate of 37 mm/min and spindle speed of 1400 rpm.

5. ACKNOWLEDGEMENT

The author would like to thank to the Centre for Advanced Research on Energy (CARE), Faculty of Mechanical Engineering, University Technical Malaysia Melaka for providing financial, infrastructure and supporting for this research.

6. REFERENCES

[1] S. Kalpakjian & S. R. Schimid "*Manufacturing Engineering and Technology*". 6ed. Singapore. Prentice Hall. 2010.

[2] A. K. Kakati, M. Chandrasekaran, A. Mandal, and A. K. Singh "Prediction of Optimum Cutting Parameters to obtain Desired Surface in Finish Pass end Milling of Aluminium Alloy with Carbide Tool using Artificial Neural Network". *World Academy of Science, Engineering and Technology*. Vol. 57, pp. 56-63, 2011.

[3] B. C. Routara, A. Bandyopadhyay& P. Sahoo Roughness Modeling and Optimization In CNC End Milling Using Response Method: Effect of Workpiece material variation. *Int. J. Adv. Manuf. Technol*. Vol 40, pp. 1166-1180, 2009.

[4] M. S. Lou, J. C. Chen & C. M. Li "Surface Roughness Prediction Technique For CNC End-Milling". *Journal of Industrial Technology*.Vol. 15, pp. 1-6. (1998).

[5] M. T. Hayajneh, M. S. Tahat and J. Bluhm. " A Study of the Effects of Machining Parameters on the Surface Roughness in the End-Milling Process". *Journal of Mechanical and Industrial Engineering*, Vol. 1, pp.15-23. 2007.

Study on surface diffusion of an effective powder-pack boronizing

N.H. Omar[1,*], R. Hasan[1,2], S.M.M. Shahidan[1], N.R. Morjani[1], M.H. Kamaludin[1]

[1)] Faculty of Mechanical Engineering, Universiti Teknikal Malaysia Melaka,
Hang Tuah Jaya, 76100 Durian Tunggal, Melaka, Malaysia.
[2)] Centre for Advanced Research on Energy, Universiti Teknikal Malaysia Melaka,
Hang Tuah Jaya, 76100 Durian Tunggal, Melaka, Malaysia.

[*]Corresponding e-mail: nurulhidayahomar91@gmail.com

Keywords: Boronizing; borided; kinetics

ABSTRACT – Boronizing is a surface treatment which is currently well developed in the industry to produce a super hard and good wear resistant surface layer on the metallic substrate. In this study, 10 mm diameter 316 stainless-steel ball bearings will be used as the specimens. Boronizing treatments will be done for 2, 4 and 6 hours in furnace at temperature 850, 900 and 950 ^{o}C using Ekabor 1. Powder conditions and powder pack surrounding will be studied in these experiments in order to analyze the effective powder usage for the treatment. The boronized surface will be characterized using optical microscope, SEM analysis, and hardness Rockwell indenter. The kinetic diffusion of boron will be determined from activation energy analysis using Arrhenius equation.

1. INTRODUCTION

Boronizing is one of a thermochemical surface hardening process. It is a thermochemical treatment that diffuses boron atoms through the surface of metallic substrates. The boronized steels exhibit high hardness, high wear resistance and high corrosion resistance. There are many types of boronizing processes that have been developed, such as pack boriding, paste boriding, electrolytic boriding and others. Powder-pack boronizing is the most cost-effective compare to other processes besides its simplicity [1]. The objectives of this research is to study the surface diffusion of boronized 316 stainless-steel using powder-pack procedure.

2. METHODOLOGY

2.1 Boronizing of Stainless Steel

10 mm stainless steel ball bearings will be borided and the variables for boronizing process are selected using Taguchi method in order to determine an effective powder pack boronizing conditions. The parameters are boronizing temperature, boronizing time, powder condition, and powder-pack surrounding. All these parameters are shown in Table 1. The different variables will be used to determine the effects of the combinations on the borided layer thickness, kinetic diffusion of boron, as well as surface hardness.

Table 1 The parameters for boronizing 10 mm stainless - steel ball bearing

No.of experiment	Boronizing Temperature (^{0}C)	Boronizing Time (hours)	Powder Condition (%)	Powder Pack Surrounding
1	850	2	100	5mm
2	900	2	60	10mm
3	950	2	30	15mm
4	850	4	60	15mm
5	900	4	30	5mm
6	950	4	100	10mm
7	850	6	30	10mm
8	900	6	100	15mm
9	950	6	60	5mm

2.2 Powder-Pack Boronizing Procedure

The boronizing treatments will be carried out in a solid medium using powder-pack method. For this purpose, the specimen will be buried with boronizing powder in a stainless-steel container with lid as shown in Figure 1. The containers are in different diameters and heights in such a way the samples will be surrounded with different powder thickness.

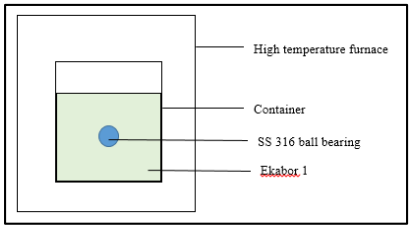

Figure 1 Schematic diagram of powder-pack boronizing in high temperature furnace

3. RESULTS AND DISCUSSION

3.1 Surface Appearance and Cross-Section

Figure 2 shows the outer surface appearance of boronized and unboronized 316 stainless-steel ball bearings. The cross-section of unboronized sample is shown in Figure 3 using optical microscope. It is reported that the cross-sectional surface of borided layer of boronizing stainless steel contains layer rich with iron [2]. The cross-section for boronized 316 stainless-steel ball bearings are shown in Figure 4 and Figure 5 with different parameters.

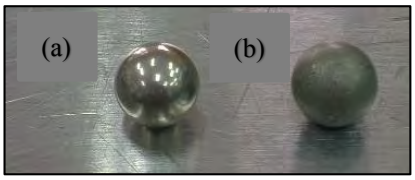

Figure 2 (a) Outer surface unboronized 316 stainless-steel ball bearing (b) Outer surface boronized 316 stainless-steel ball bearing

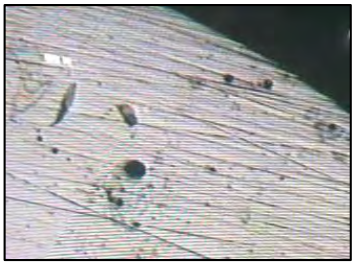

Figure 3 Cross-section of unboronized 316 stainless-steel ball bearing, near the outer surface.

Figure 4 Cross-section of boronized 316 stainless-steel ball bearing with parameters 850 ^{0}C, 2 hours, 10 mm powder surrounding and 100 % powder concentration.

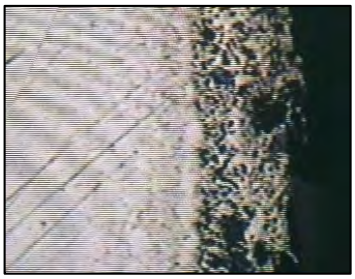

Figure 5 Cross-section of boronized 316 stainless-steel ball bearing with parameters 950 ^{0}C, 2 hours, 10 mm powder surrounding and 100 % powder concentration.

3.2 Hardness values

The initial hardness values for boronized and unboronized is measured using Rockwell hardness tester with load 981 N for each sample. The hardness results are in Table 2. From this initial few samples, it can be seen that the hardness value for boronized 316 stainless-steel ball bearing is greater than the unboronized sample.

Table 2 The hardness values for boronized and unboronized samples

Sample	Temperature	Hardness values
Unboronized	-	56.6 HRD
Boronized	850 ^{0}C	59.9 HRD
Boronized	950 ^{0}C	63.3 HRD

The greater surface hardening effect and the thick diffusion layer are the main cause of this higher hardness. It is possible to claim that the higher boronizing temperature is the cause of the hardness value [1].

3.3 Kinetics of Atoms at Surface Using Arrhenius Equation

The kinetics of layer growth is controlled by perpendicular boron diffusion into the Fe_2B layer. According to Fick's law [3], the squared thickness of the boride layer as a function of boronizing time is described as:

$$X^2 = Kt, \quad (1)$$

where X is the depth of boride layer (cm), t is the process time (s), while K is the diffusion coefficient (cm^2/s) depending on boronizing temperature and is calculated from the slopes of the X^2 versus treatment time graphs. The relationship between diffusion coefficient D, temperature T, and activation energy Q, can be expressed using an Arrhenius equation as follows:

$$K = K_o \exp (-Q / RT), \quad (2)$$

where K is the diffusion coefficient, K_o is called the pre-exponential constant, Q is activation energy (J/mol) required to make the reaction occur, T is the absolute temperature (Kelvin), and R is the universal gas constant (J/mol/K) [3]. The kinetics of atoms is not reported in this paper.

4. CONCLUSIONS

In this present study, with all the parameters combined, it is expected that the kinetics of atoms for boronizing process on stainless-steel material can be analyzed using Arrhenius equation together with the determination of an effective powder-pack procedure. It is also expected the boronization of 316 stainless-steel ball bearing can contribute to a new knowledge in the engineering field especially in the automotive industry.

5. REFERENCES

[1] O. Ozdemir, M.A. Omar, M. Usta, S. Zeytin, C. Bindal, and A.H. Ucisik, "An investigation on boriding kinetics of AISI 316 stainless steel", *Vacuum*, vol. 83, pp. 175 – 179, 2009.

[2] J.H. Yoon, Y.K. Jee, and S.Y. Lee, "Plasma paste boronizing treatment of the stainless steel AISI 304" *Surface and Coatings Technology*, vol. 112, pp. 71 – 75, 1999.

[3] M. Ipek, G. Celebi Efe, I. Ozbek, S. Zeytin, and C. Bindal, "Investigation of boronizing kinetics of AISI 51100 steel," *Journal of Materials Engineering and Performance,* vol. 21, no. 5, pp. 733 – 73, 2012.

Comparative study of surface roughness in milling AISI D2 steel using PVD coated and uncoated tungsten carbide insert

B.I. Redzuwan[1,*], M.S. A. Aziz[1,2], M.F. Ayub [1], M.S. Kasim[1,2], R. Izamshah[1,2], M. Amran[1,2]

[1)] Faculty of Manufacturing Engineering, Universiti Teknikal Malaysia Melaka, Hang Tuah Jaya, 76100 Durian Tunggal, Melaka, Malaysia.
[2)] Precision Machining Group (PMG), Advanced Manufacturing Centre (AMC), Universiti Teknikal Malaysia Melaka, Hang Tuah Jaya, 76100 Durian Tunggal, Melaka, Malaysia.

[*]Corresponding e-mail: bahrinikram5445@gmail.com

Keywords: Surface Roughness; AISI D2 steel; TiAlN/AlCrN PVD coated tungsten carbide insert

ABSTRACT – This paper comparatively investigates the effect of cutting speed and feed rate on the surface roughness of AISI D2 steel using uncoated and PVD coated inserts in milling operation under dry condition. The response surface methodology (RSM) with a Central Composite Design (CCD) was employed in the experiment to determine the optimum control variables which are cutting speed and feed rate. The optimum condition required for obtaining the minimum surface roughness when milling AISI D2 steel was cutting speed of 100.38 m/min, feed rate of 0.1 mm/tooth, axial depth of cut of 1.5 mm and radial depth of cut of 2.5 mm using PVD coated insert which resulted in a surface roughness of 0.129 µm.

1. INTRODUCTION

Nowadays, various manufacturing processes in industry are capable in producing desired shapes of components within the requirements of dimensional tolerances and surface quality. R. Arokiadass et al. [1] stated that one of the most important factors in physical appearance is the surface roughness. Charles A. [2] found that surface finish influences not only the dimensional accuracy of machine parts, but also their properties. Gokkaya H. et al. [3] stated that surface roughness is affected by the cutting tool coating material, cutting speed and feed rate. A good combination of cutting speed and feed rate can provide better surface qualities.

In this research, comparative study between physical vapor deposition (PVD) coated and uncoated tungsten carbide inserts was conducted in terms of surface roughness when milling AISI D2 steel under dry condition, in order to investigate effects of cutting speed and feed rate. Furthermore, Response Surface Methodology (RSM) using Central Composite Design (CCD) was used in the experiment to determine the optimum parameter for obtaining minimum value of surface roughness.

2. METHODOLOGY

2.1 Workpiece

The material used as the workpiece in this research is AISI D2 steel. This material is widely used in mold manufacturing industry. The composition of AISI D2 steel used is described in Table 1 and the hardness is ranged from 54 to 62 of HRC.

Table 1 Composition of AISI D2 steel

Element	C	Si	Mn	Cr	Mo	Ni	V
Composition [%]	1.4 - 1.6	0.5 - 0.6	0.5 - 0.6	11.0 - 13.0	0.7 - 1.2	0.3 (max)	1.1 (max)

2.2 Machining Condition

Two types of round shape tungsten carbide insert were used in this experiment which are TiAlN/AlCrN PVD coated insert and uncoated insert. The machining conditions for the experiment are described in Table 2.

Table 2 Machining condition for the experiment

Workpiece	AISI D2 steel
Tool	TiAlN/AlCrN PVD insert and uncoated insert
Machine	Mazak CNC milling machine
Atmosphere	Dry machining condition

A Response Surface Methodology (RSM) using Central Composite Design (CCD) approach was employed in order to determine the optimum parameter. The parameter range setting was considered based on the tool maker recommendation and setting from the previous studies. Depth of cut is remained constant at 1.5 mm for axial and 2.5 mm for radial as shown in Table 3.

Table 3 Specification of cutting parameter

Control parameter	**Parameter range**	
Level	**-1**	**1**
Cutting speed, V_c	100 (m/min)	150 (m/min)
Feed rate, f_z	0.1 (mm/ tooth)	0.2 (mm/ tooth)
Constant	Axial depth of cut, a_D	1.5 mm
	Radial depth of cut, a_R	2.5 mm

3. RESULTS AND DISCUSSION

In this study, analysis on independent machining variables that includes cutting speed and feed rate was performed in order to evaluate the surface roughness of PVD coated and uncoated tungsten carbide inserts. The Ra data was measured for three points at every single pass along the workpiece. The experiment was repeated for 20 passes. Then, the value of surface roughness was calculated as shown in Table 4 and 5, respectively.

Table 4 Average values of surface roughness using uncoated insert

Run order	Factor A: Feed rate (mm/tooth)	Factor B: Cutting speed (m/min)	Ra(µm)
1	0.10	100.00	0.377
2	0.20	150.00	1.003
3	0.10	150.00	0.475
5	0.22	125.00	0.305
7	0.20	100.00	0.529
12	0.15	160.36	0.447
14	0.15	125.00	0.721
17	0.15	125.00	0.737
19	0.15	89.64	0.925
21	0.15	125.00	0.731
22	0.08	125.00	0.566

Table 5 Average values of surface roughness using PVD coated insert

Run order	Factor A: Feed rate (mm/tooth)	Factor B: Cutting speed (m/min)	Ra(µm)
4	0.10	150	0.359
6	0.08	125	0.092
8	0.15	125	0.144
9	0.15	160.36	0.13
10	0.20	100	0.199
11	0.20	150	0.146
13	0.15	89.64	0.075
15	0.15	125	0.146
16	0.22	125	0.114
18	0.15	125	0.144
20	0.10	100	0.171

3.1 Effect of Feed Rate and Cutting Speed on Surface Roughness

Figure 1 indicates the relationship between surface roughness and feed rate for uncoated and PVD coated inserts using constant cutting speed of 125 m/min. It was found that for both uncoated and PVD coated inserts, the surface roughness values increase as the feed rate increases and compared to uncoated tools, PVD coated insert produced better surface roughness.

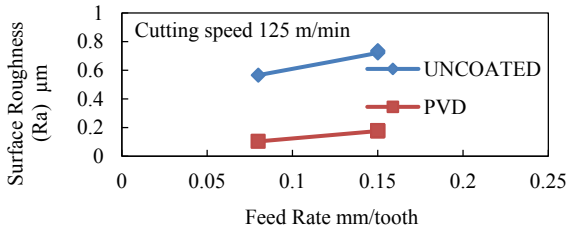

Figure 1 Relationship between surface roughness and feed rate for uncoated and PVD coated inserts

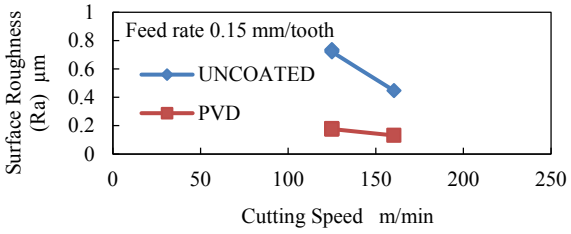

Figure 2 Relationship between surface roughness and cutting speed for uncoated and PVD coated inserts

Figure 2 indicates the surface roughness measured experimentally for uncoated and PVD coated inserts using constant feed rate of 0.15 mm/tooth. It was found that for both uncoated and PVD coated inserts, the surface roughness values decrease as the cutting speed increases and compared to the uncoated insert, PVD coated insert produced better surface roughness.

The relationship between cutting speed and surface roughness is inversely proportional. Increasing the cutting speed decreases the surface roughness. The relationship between feed rate and surface roughness is proportional. Increasing the feed rate increases the surface roughness.

3.2 Optimum parameter for surface roughness

Based on the experiment data and analysis, three cutting conditions predicted to achieve minimum surface roughness are described in Table 6. The optimum cutting condition in milling AISI D2 steel is by using PVD coated insert with cutting speed of 100.38 m/min, feed rate of 0.1 mm/tooth, axial depth of cut of 1.5 mm and radial depth of cut of 2.5 mm, which resulted in a surface roughness of 0.129 µm. For achieving good surface finish on the AISI D2 materials, the lower feed, lower depth of cut and higher cutting speed of machining parameter are preferred.

Table 6 Optimum parameter for surface roughness

No.	Feed Rate (mm/tooth)	Cutting Speed (m/min)	Coating	Surface Roughness (µm)
1	0.1	100.38	PVD	0.129203
2	0.2	150	PVD	0.158406
3	0.1	150	Uncoated	0.678511

4. CONCLUSIONS

Based on the results obtained, the following conclusion can be summarized: (1) Cutting speed and feed rate affect the surface roughness for both PVD and uncoated inserts. (2) The optimum cutting condition in milling AISI D2 steel is by using PVD coated insert with cutting speed of 100.38 m/min, feed rate of 0.1 mm/tooth, axial depth of cut of 1.5 mm and radial depth of cut of 2.5 mm, which resulted in a surface roughness of 0.129 µm.

5. REFERENCES

[1] R. Arokiadass, K. Palaniradja, N. Alagumoorthi, "Surface roughness prediction model in end milling of Al/SiCp MMC carbide tools," Vol. 3, No. 6, 2011, pp. 78-87.

[2] Charles A. Harper, Electronic Materials and Processes Handbook, Third Edition, New York ,McGraw-Hill Professional publication, 2004.

[3] Hasan G¨O KKAYA, "The Effects of Cutting Tool Coating on the Surface Roughness of AISI 1015 Steel Depending on Cutting Parameters," Vol. 30, 2006, pp. 307-316.

Comparison of camera calibration method for a vision based meso-scale measurement system

A.R.K.Anuar[1,*], H. Hanizam[1], S. Mohd Rizal[2], N. Nazrul Anuar[3]

[1)] Faculty of Engineering Technology, Universiti Teknikal Malaysia Melaka, Hang Tuah Jaya, 76100 Durian Tunggal, Melaka, Malaysia.
[2)] Faculty of Manufacturing Engineering, Universiti Teknikal Malaysia Melaka, Hang Tuah Jaya, 76100 Durian Tunggal, Melaka, Malaysia.
[3)] Faculty of Engineering and Built Environment, Universiti Kebangsaan Malaysia, 43600 UKM, Bangi, Selangor, Malaysia.

[*]Corresponding e-mail: khairulanuar@utem.edu.my

Keywords: Meso-scale; camera calibration toolbox; camera calibration

ABSTRACT – This research compared three types of CCD camera calibration techniques namely Bouget's Calibration Toolbox, Zhang's Calibration Toolbox and Heikkilla's Calibration Toolbox. Experimental data for both calibration and optimization were collected to further explain the experimental results. Statistical analyses such as T-Test and ANOVA were conducted on the collected data using Minitab and EXCEL software. The results of this research indicated that the best calibration technique (toolbox) for calibrating Omron F500 CCD Camera for the purpose of measuring dimensions of meso-scale component is the Heikkilla's Calibration Toolbox.

1. INTRODUCTION

Since the contact methods have drawback for the highly advanced manufacturing process that could produce a component smaller than a millimeter size, the non-contact methods that use optical capabilities are mostly focused by recent researchers [1,2]. Based on the survey done by Hibbard and Bono(2003)[3], it is found that current available measuring equipment are focused on components in the size of micrometer or nanometer which requires high investment. There is a gap of measurement size and lack of development being done for the component in the size of meso-scale.

In developing a vision based measuring system, the camera's precision has always been the bottleneck, and often being discussed. As a result none of the existing camera calibration techniques is perfectly suitable for this purpose [4]. The user, need to identify the type of image processing method (i.e edge detection) to be used in their measurement application before deciding which calibration technique to be selected. Furthermore, there is a need to determine simultaneously other parameters such as the image exterior orientation by a process of least squares adjustment.

Ricolfe and Sanchez [5] described that the precision of calibration depends on how accurate the world and image points are located. Studying how localization errors propagate to the estimates of the camera parameters is very important.

2. METHODOLOGY

The experiments were conducted by using Omron F500 Vision System CCD camera. Three samples were identified for this procedure namely checkerboard image pattern, fiducial image pattern and plumb-line image pattern.

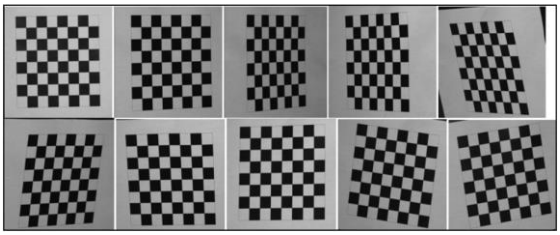

Fig 1 Checkerboard Image Pattern

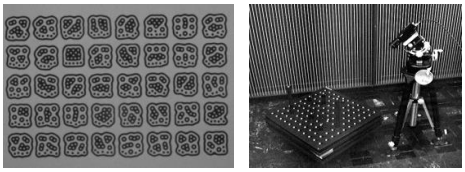

(a) (b)

Fig 2 (a) Fiducial Image Pattern, (b) Plumb-line Image Pattern

Table 1 Table of comparison for calibration method

Calibration Method	Advantages	Disadvantages	Calibration Toolbox
Tsai's Method	This method splits the problem into two steps. It allows use of both planar and non- planar patterns.	This method assumes that optical center is located at image center and that skew is null. In the first step, the distortion is assumed null.	Heikkilla Calibration Toolbox
Heikkilla & Silven's Method	The model uses two coefficients for both radial and decentering distortion, and the method works with single or multiple images and with 2D or 3D calibration grids	Interior Orientation (IO) need to be refined by using Levenberg-Marquardt algorithm	Heikkilla Calibration Toolbox
Batista's Method	This method needs only one image of a planar pattern to calibrate a camera. It is a multistep and iterative method that uses a least squares technique at each step.	Distortion is modeled using only one coefficient	Bouget Calibration Toolbox
Zhang's Method	This method needs at least three different views of a planar pattern. Lens distortion is modeled using two coefficients.	Displacements between these views can be unknown.	Zhang Calibration Toolbox

The camera's parameters were fixed while all the three specimens with different angles were calibrated by the toolboxes.

3. RESULTS AND DISCUSSION

Based on the box-plot chart, each calibration toolbox showed that there are significant differences between the three image patterns used based on the P value which is >0.05. The individual 95% of confident interval (CIs) for each mean also indicates that there is no overlapping and significantly different between the three image patterns means as well. Checkerboard pattern showed the most consistent result : lowest pixel error and low variation(more precise). Comparison results of the three calibration toolboxes showed that Heikkilla Calibration Toolbox give the most precise value in all the three image pattern used. Refer to Table 2.

Table 2 Comparison (pixel error) of camera calibration toolboxes

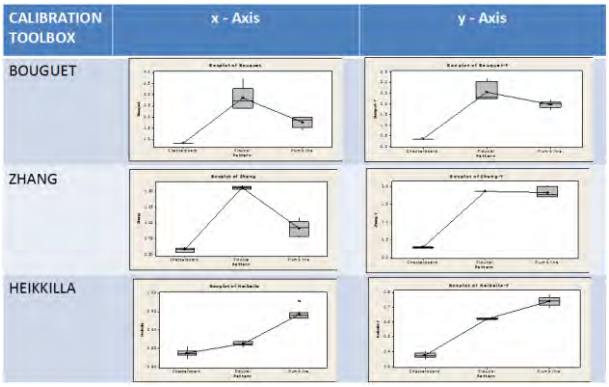

Heikkilla's Calibration Toolbox has the best detection in terms of pixel error at x-axis and y-axis, and can be concluded that the best calibration toolbox required for optical component in non-contact measuring system. This is because the result gathered after experiments, supports the needs and purpose of camera precision in measuring dimensions based on edge detection. Refer to Table 3 and Fig 3.

Table 3 Image pattern vs. camera calibration toolboxes

Pattern / Toolbox	Checkerboard	Fiducial	Plumb Line
Bouquet	0.83213	2.85344	1.76862
Zhang	0.57581	1.55846	0.91260
Heikeila	0.83700	0.86243	0.94181

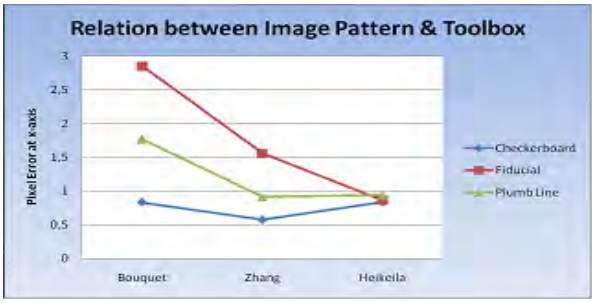

Fig 3 Relation Between Image Pattern and Calibration Toolbox

4. CONCLUSIONS

The research provides a guideline on the selection of calibration technique and calibration toolbox which can be utilized to enhance the precision of CCD camera in order to eliminate error in dimension measurements. The findings have been supported by statistical analysis.

According to this study, Heikkilla's Calibration Toolbox is the most suitable and a good calibration tool to be used in the field of image processing (edge detection). However, the purpose of using the camera, in terms of image processing methods, need to be clarified beforehand in order not to use the wrong calibration tools available.

For future research, the development of meso-scale non-contact method by using CCD camera and image processing shall be applied. The idea is to develop an in-house capability in producing measuring equipment to fulfill the requirement for measuring meso - scale components. If the proposed technique can produce acceptable readings (compared to other non-contact method), the prototype product can be promoted to the industries that require measurement for small components.

5. ACKNOWLEDMENT

Thanks to Universiti Teknikal Malaysia Melaka (UTeM) and fellow researchers and especially to Assc. Prof. Dr. Mohd. Rizal Salleh, for his guidance and support.

6. REFERENCES

[1] Mekid and Ryu. "Rapid Vision-based Dimensional Precision Inspection of Meso-scale Artifacts." *Proceeding of the institution of Mechanical Engineers, Part B: Journal of Engineering Manufacture*, vol. 221, pp 659 -672, 2007

[2] Leach, R., Haycocks, J., Jackson, K., Lewis, A., Oldfield, S. and Yacoot, A. "Advances in Traceable Nanometrology at the National Physic Laboratory." *Nanotechnology,* vol. 12, pp. R1-R6, 2001

[3] Hibbard, R.L. and Bono, M.J. "Meso-scale Tools: A Survey of Relevant Tools and a Discussion of Their Strengths and a Discussion of Their Weakness." in *ASPE Winter Topical Meeting, Gainesville, Florida, USA*. 2003

[4] Ethrog, U. "CCD Camera Calibration based on the Sun's Images." *IAPRS.* vol. XXXVI, Part 5, 2006

[5] Ricolfe-Viala,C and Sanchez-Salmeron, A.J., "Camera Calibration Under Optimal Conditions." *Journal of Optics Express,* vol 19, pp 10769-10775, 2011.

Analysis of body dynamic posture to detect body discomfort by using a webcam and python image histogram

N.S.A Ramdan[1,2,*], A.Y. Bani Hashim[1,] Seri Rahayu Kamat[1], Siti Azirah Asmai[1]

[1)] Faculty of Manufacturing Engineering, Universiti Teknikal Malaysia Melaka, Hang Tuah Jaya, 76100 Durian Tunggal, Melaka, Malaysia.

[*]Corresponding e-mail: sufiah.akmala@gmail.com

Keywords: Image histogram; dynamic posture; metal filing process

ABSTRACT – Nowadays, in factory, manual workers dynamic posture can be recorded by CCTV, but cannot be scientifically analyzed. In this paper, the authors have shown a method to do analysis of human dynamic posture. The purpose of the analysis is to know the sign of body discomfort of the workers after some period of time. The analysis is done by using image histogram and Python software.

1. INTRODUCTION

Dynamic posture is the movement of human that consist of all of the body parts. Body dynamic posture is defined as the movement of every part of the body to produce a dynamic movement. Dynamic posture is how your body is aligned during movement, such as running or walking, according to Lenny Parracino, co-founder of Kinetic Conditioning in Montrose, California. Proper posture ensures that the muscles are optimally aligned in proper length and tension relationships for optimal function. This allows your body to absorb and distribute forces throughout your body evenly [1].

In this paper, the experiment focuses on the dynamic movement of the worker in fitting workstation. In this workstation, one of the processes involved is a metal filing process. Metal filing process is a process where the workers need to file a block of metal, to get the desired shape. It is done by using a suitable file and strength of the worker by hand movements. An example of the posture is as Figure 1. The purpose of the analysis is to know the sign of body discomfort of the workers during working period.

Figure 1 Metal filing process

2. BACKGROUND

2.1 Body discomfort

Body discomfort is the condition where the body of a human experienced a discomfort feeling on their body part such as arms, legs, neck and back bones. There are many researchers that have done their research about body discomfort. Example as Liao MH and Drury CG (2000) did their study on body discomfort. The objective of their study was to demonstrate the interactions between workplace, work duration, discomfort, working posture, as well as performance in a 2-h typing task. While Van Dieen JH and Oude Vrielink HH (1998) did the study on evaluation of work-rest schedules with respect to the effects of postural workload in standing work [2]. Riihimaki H, Tola S, Videman T, Hanninen K. (Et al) (1989), states that Sciatic pain was more common among machine operators and carpenters than among office workers, and also more frequent among machine operators than among carpenters. [2].

2.2 Color histogram

Color histogram is a histogram that has digital image pixel tonality for 24 bit RGB (RED-GREEN-BLUE) color is expressed as a number between 0 and 255. 0 equals pure black and 255 equals pure white. At 127, about the midpoint, would be the equivalent of middle gray in density. Digital image histograms are presented as a bar chart with the horizontal axis being the tonal range of your image. The left side of the graph is 0 and the right side of the graph is 255. The vertical axis is the relative number of pixels in each of the 255 tonal values. The taller the hump of the graph, the more pixels in that particular tonal range [3].

3. METHODOLOGY

Six subjects were selected to do this pilot test. The pilot test was done by following the procedure that has been prepared. The venue takes place at the Fitting workstation, Manufacturing Engineering Faculty, Universiti Teknikal Malaysia Melaka. In this experiment, only one camera is used to record the movements of the subjects. The subject is asked to do the filing process for 15 minutes for non-stop. One of the subjects is assigned to do stand in the position of filing process but without any movement. This is to show the position of mannequin without any movement.

Table 1 Subject's Details

Subject	Age	Height (cm)	Gender
Subject A	24	149	F
Subject B	22	170	M
Subject C	23	165	M
Subject D	22	173	M
Subject E	24	158	F
Subject F	23	171	M

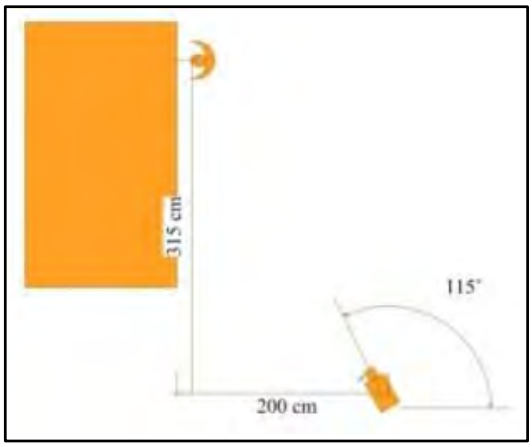

Figure 2 The experimental set up

Figure 2 shows the experimental set-up in the Manufacturing Engineering Faculty, UTeM.

4. RESULTS AND DISCUSSIONS

Table 2 shows that the image analysis for Subject A. In this analysis, three pictures of the frames will be chosen to be analyzed. The frame that has been chosen is (1,2), (1,5), (1,9). From these three pictures, we can see the differences between the position of the neck and head of the subject. This shows that movements are happening and the person has a body discomfort around his neck. This can be proven by the differences of the peaks between the graphs. Figure 3 shows the combination of ten image histograms of Subject C. We can see the differences between each line of the histogram. We can relate the image histogram and the image frames to know the body discomfort by seeing the changes in the picture frame by frame.

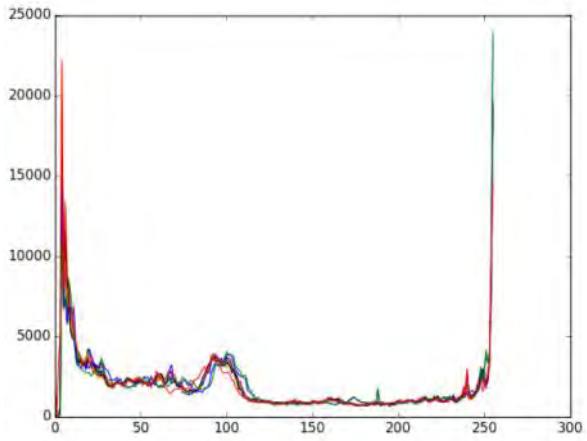

Figure 3 The combination of 10 image histograms of the picture frame

Table 2 Analysis of picture for Subject C

Time (minutes)	Frame picture	Graph
3.00		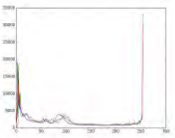
7.30		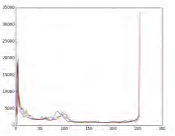
13.30		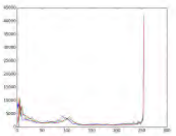

5. CONCLUSIONS

By using the image histogram, we can see that the graph in the respective image is showing some differences in their peak. This shows that there are some differences in the movements of the body within the working period. By relating the picture frame and the graph, we can say that shows body discomfort has happened to the workers.

6. REFERENCES

[1] Nick Ng, "What Is Dynamic Posture?," 2013. [Online]. Available: http://www.livestrong.com/article/180731-what-is-dynamic-posture/. [Accessed: 25-Sep-2014].

[2] L. Mh and D. Cg, "Posture , discomfort and performance in a VDT task . Work posture , workstation design , and musculoskeletal discomfort in a VDT data entry task . vol. 43, no. 1997, 2000.

[3] Steve Hoffmann, "A practical guide to interpreting rgb histograms," 2006. [Online]. Available: http://www.sphoto.com/techinfo/histograms/histograms.htm. [Accessed: 26-Sep-2014].

Development of innovation in Malaysian traditional palm sugar cooking machine

R. Hasan[1,2,*], S.A. Shamsudin[1,2], N. Muhammad[1,2], N. Tamaldin[1,2], H. Ali[1], M.I. Jaafar[1], T.E. Tengku Mansor[1], F.Z. Zainuri[1], N.S.A. Abdul Razak[1]

[1)] Faculty of Mechanical Engineering, Universiti Teknikal Malaysia Melaka, Hang Tuah Jaya, 76100 Durian Tunggal, Melaka, Malaysia.
[2)] Centre for Advanced Research on Energy, Universiti Teknikal Malaysia Melaka, Hang Tuah Jaya, 76100 Durian Tunggal, Melaka, Malaysia.

[*]Corresponding e-mail: rafidahhasan@utem.edu.my

Keywords: innovative cooking; traditional food

ABSTRACT – The research objective is to propose a new method of palm sugar cooking which is more efficient as compared to that of traditional method in Malaysia. Amongst activities in achieving the objective are data collections of traditional process, development of microcontroller and heating element, as well as design of cooking mechanism. In the new method, raw palm sugar is heated by using an electrical heater which is embedded around outer side of cooking pot and temperature is maintained by using a controller in order to produce a more uniform process. A stirrer is equipped in the pot in order to mix the ingredients uniformly. It is found that the new heating process can be used to cook the palm sugar without leaving crust at the bottom part of the pot. A controlled temperature is found beneficial for cooking time estimation.

1. INTRODUCTION

The traditional processing of palm sugar in Malaysia is highly labor intensive, thus producing limited outcome to fulfill consumer demand. Although there are many emerging food technologies, none of them are implemented in the processing of palm sugar [1]. Most of active palm sugar researches worldwide are dealing with the quality and properties of the sugar itself [2-3], and only little of them deals with the processing to enhance the production [4]. The one with the efforts to increase the production is also not specifically meant for the production of pure palm sugar as being consumed in Malaysia and South East Asia, but more towards the derivation of similar product from sugarcane which is called jaggery [4]. Moreover, only small part of the research dealt with modern technology, thus there are many aspects which can be improved especially in cooking process.

The lack of technology implementation in palm sugar production is due to unique characteristics of the cooked material and tedious procedure of the overall process. These factors have not been studied yet. Thus there is a need to do an intensive scientific study in addressing these factors in order to improve the productivity and sustainability of palm sugar production in this country. Study on new processing framework which utilizes potential of modern materials and technologies can be proposed. In initial research, cooking process is studied and reported in this paper.

2. METHODOLOGY

The stages in this research are as follows:

a. Data collection from traditional palm sugar industry
b. Development of microcontroller and heating element for cooking process
c. Design of cooking mechanism and analysis

In data collection, temperature throughout palm sugar cooking process is recorded using thermocouple, while viscosity of the cooked substance is recorded using viscometer. Figure 1(a) shows the traditional palm sugar cooking process while Figure 1(b) shows a data collection procedure of palm sugar sample.

(a) (b)

Figure 1 (a) Traditional palm sugar cooking process; (b) Data collection of palm sugar sample

The collected data is used for selection of electrical heater. Ceramic band heater is selected in this study. The electrical heater is controlled by using an Arduino UNO microcontroller. Figure 2 shows the designed electrical circuit in this study.

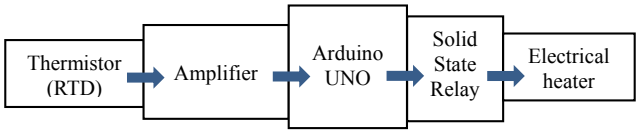

Figure 2 Electrical circuit in this study

A suitable cooking mechanism is designed to suit the proposed heating element. A standard design procedure is applied which consists of concept selection, house of quality, morphology chart, detailed solid modeling design as well as finite element analysis.

3. RESULTS AND DISCUSSION

Temperature and viscosity data for palm sugar cooking process is shown in Table 1.

Table 1 Data taken during palm sugar cooking

Time (minute)	Average temperature (°C)	Viscosity (Pa.s)
0	27	N/A
5	131	N/A
15	247	N/A
35	150	20
45	144	32
55	174	108
75	115	N/A
85	105	212

Controller system for this project is named R6 which consists of various microelectronic components that can save data for automatic control of the cooking process. The system is shown in Figure 3.

Figure 3 Automatic controller R6

Prototype of the innovation for palm sugar cooking mechanism according to the selected concept design is shown in Figure 4.

Figure 4 Prototype of an innovative cooking method for palm sugar

The prototype which is equipped with ceramic band heater and controlled by the automated system R6 shows that the maximum temperature of palm sugar cooking process is sufficient. This is shown in Figure 5. Meanwhile, Figure 6 shows comparison of temperature during both traditional and innovative automated palm sugar cooking processes done in this study.

(a) (b)

Figure 5 (a) Temperature display in R6 system; (b) Cooking pot equipped with ceramic band heater

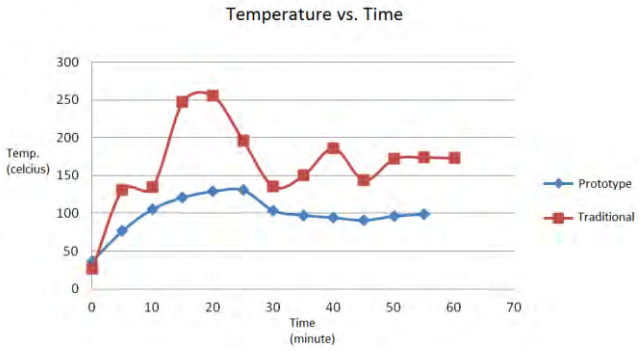

Figure 6 Comparison of temperature for palm sugar cooking processes

4. SUMMARY

From the research, it is found that the new heating process can be used to cook the palm sugar without leaving crust at the bottom part of the pot. A controlled temperature is beneficial for appropriate cooking time estimation. This early stage research concludes that the innovation is applicable in palm sugar industry in Malaysia, with future aim of introducing a more efficient industrial scale process.

5. ACKNOWLEDGEMENT

The authors would like to acknowledge CARe, UTeM for providing research facilities and En. Raidee Baharom of NRB Food Industries Serkam Melaka as industrial partner in the innovation project.

6. REFERENCES

[1] N.P. Mahalik, A.N. Nambiar, "Trends in food packaging and manufacturing systems and technology", *Trends in Food Science and Technology*, vol. 21, no. 3, pp. 117-128, 2010.

[2] D. Karamoko, N.T. Djeni, K.F. N'guessan, K.M.J.-P. Bouatenin, K.M. Dje, "The biochemical and microbiological quality of palm wine samples produced at different periods during tapping and changes which occurred during their storage", *Food Control*, vol. 26, no. 2, pp. 504-511, 2012.

[3] O. Lasekan and K.A. Abbas, "Flavour chemistry of palm toddy and palm juice: a review", *Trends in Food Science and Technology*, vol. 21, no. 10, pp. 494-501, 2010.

[4] J. Singh, R.D. Singh, S.I. Anwar, "Alternative sweeteners production from sugarcane in India: lump sugar (jaggery)", *Sugar Technology*, vol. 13, no. 4, pp. 366-371, 2011.

Proceedings of Mechanical Engineering Research Day 2015, pp. 145-146, March 2015

A humanoid robot for autism rehabilitation: Does IQ influence response in child-robot interaction?

S. Shamsuddin[1,2,*], H. Yussof[2], F.A. Hanapiah[3], S. Mohamed[3]

[1)] Faculty of Manufacturing Engineering, Universiti Teknikal Malaysia Melaka, Hang Tuah Jaya, 76100 Durian Tunggal, Melaka, Malaysia.
[2)] Center for Humanoid Robots and Bio-Sensing (HuRoBs), Faculty of Mechanical Engineering, Universiti Teknologi MARA, Shah Alam, 40450 Selangor, Malaysia
[3)] Faculty of Medicine, Universiti Teknologi MARA Sungai Buloh Campus, 47000 Selangor, Malaysia.

[*]Corresponding e-mail: syamimi@ieee.org, syamimi@utem.edu.my

Keywords: human-robot interaction (HRI); humanoid robot; IQ level

ABSTRACT – Recent advances show that robots have unlimited potential to help the disabled community by providing physical support, social engagement and even co-therapy in collaboration with another human. For children with autism, a robot in human shape might be able to help them to learn better and encourage social-communication skills. To prove this, the key initial step is to explore the initial response of children with autism when they interact with a humanoid robot in an experimental setting. We hypothesize that a robot's presence coupled with specific interplay shall attract the children's attention to engage in robot-based interaction. The initial responses will be utilized to seek association between responses to the robot with the children's intelligence level. Twelve autistic children with IQs between 44 and 107 were exposed to different interactions. Behavior evaluation showed that in the presence of the robot, lower autistic traits were recorded in the subscale of stereotyped behavior and communication. Also, children with IQs higher than 80 were more receptive to robot-based single exposure.

1. INTRODUCTION

The work in this study is motivated by the fact that children with autism are naturally attracted to inanimate, interactive technological devices. Autism is a spectrum disorder characterized by stereotyped behavior and impaired communication and social skills. An individual can be diagnosed with autism as early as before the age of three years. Statistics estimate 1 in every 91 children in the United States [1] and 1 in every 600 children in Malaysia [2] are diagnosed with autism. Thus, there is an urgent need for suitable rehabilitation measures. Early intervention is critical to help children inflicted with autism lead productive lives [3].

Related work in autism intervention has reported positive responses where robots aid the children in areas of social skills [4], communication [5] and even act as playful companions [6] among others. As reported by Baron-Cohen [7] and Pierno et al. [8], people with autism cannot cope with systems of high variance such as social behaviour, conversation and human emotions. Hence, robots with simpler appearance offer minimal variance and stimuli to attract responses during interaction. Next, we seek to find the association between intelligent quotient (IQ) scores and response to robot intervention. IQ scores in autistic children have been recognized as a factor to indicate the success of a particular autism intervention program and also influence the outcome of a particular therapy.

2. METHODOLOGY

Twelve autistic children aged between 7 and 13 years old with IQs on the Stanford Binet between 44 and 107 were exposed to interaction with the humanoid robot NAO. The aim was to investigate the children's initial response a single, first time exposure to a robot and relate this to their intelligence level. As highlighted by Dautenhahn [9], establishing first impressions is important in HRI-based research. The effect of the first encounter between children with autism and a specific type of robot is important before embarking on long-term interactions. Total duration of interaction was 14 minutes and 30 seconds. Interaction contents were decided with advice from experienced clinicians in autism. As fast jerky motions can be dangerous [10], the robot was programmed to keep its movements simple and predictable (Figure 1 (a)).

(a)

(b)

Figure 1 Comparison of interaction with (a) a robot and (b) a familiar teacher, both done at child's school

Comparative observations were carried out on the same 12 subjects during school hours. This was to evaluate their typical behavior (Figure 1 (b)) for the same duration of contact time during the robot observation. The main difference between the two settings is that the robot was not present in the class

setting. A class teacher is present in both situations. The notion to carry out a comparative type of study on HRI has been mentioned in a recent study [9], where in the first setting the participant is exposed to the robot. In the second setting, the condition is different (no robot is involved), but it needs to be comparable to the first one. The purpose is to highlight the added value of robotic presence.

To assess the children's autistic characteristics, a behavior score sheet referenced to known and accepted autistic traits within usual practice parameters were formulated. 24 items of observation were identified and divided into subscales of stereotyped behavior, communication and social interaction [11].

3. RESULTS AND DISCUSSION

3.1 Response to a Robot

Qualitative results from video evaluations showed that 10 children responded positively with reduced autistic behavior in the subscale of stereotyped behavior and communication, compared with 7 children for the social interaction subscale. Technically, we concluded that the interaction scenario was not socially engaging enough for the children. Also, observations showed that during the interaction period with the robot, the children displayed less autistic behavior compared with their regular behavior in the classroom. Furthermore, the presence of the robot did not scare or intimidate the children. Keeping the programmed interaction simple and plausible is important, especially for the first session when the child meets the robot.

3.2 Association with IQ Level

IQ levels were grouped into impaired range (IQ < 80) and normal range (IQ>80). The IQ ranges were analyzed for association between subscales within the robot interaction setting. A paired sample *t*-test showed that children with higher IQ (within normal range) had shown lower autistic characteristics in all 3 subscales. However, the differences in the observed parameters were not statistically significant ($p>0.05$). Further analysis of IQ groups (normal range vs impaired range) in the different settings (robot setting vs classroom setting) showed further pattern of IQ difference after a single exposure. The children with IQ scores of more than 80 fared better in all subscales of autistic characteristics. Thus, autistic children with IQ score between 80 and 109 were found to give encouraging responses to the robot, resulting with less autistic traits across all three behavior subscales. However, this difference was only statistically significant ($p<0.05$) in the stereotyped behavior subscale.

4. CONCLUSION AND FUTURE WORKS

Though promising results were obtained in this experiment, the results of initial exposure requires further investigation involving more subjects and repetitive exposure in the future. Elements of two-way communication will be embedded in the robot scenarios to increase the children's participation. A face recognition algorithm has been developed to enhance the sociability of the robot during the initial interaction.

5. ACKNOWLEDGMENTS

The authors gratefully acknowledge the Ministry of Education Malaysia (MOE) for funding the research project through the Niche Research Grant Scheme (NRGS) [Ref. No 600-RMI/NRGS 5/3 (1/2013)] and Exploratory Research Grant Scheme (ERGS) [Ref. No. 600-RMI/ ERGS 5/3 (14/2013)], Universiti Teknikal Malaysia Melaka (UTeM), Universiti Teknologi MARA (UiTM) Shah Alam, Selangor and The National Autism Society of Malaysia (NASOM) for their support.

6. REFERENCES

[1] M. D. Kogan, S. J. Blumberg, L. A. Schieve, C. A. Boyle, J. M. Perrin, R. M. Ghandour, G. K. Singh, B. B. Strickland, E. Trevathan, and P. C. van Dyck, "Prevalence of parent-reported diagnosis of autism spectrum disorder among children in the US, 2007," Pediatrics, vol. 124, pp. 1395-1403, 2009.

[2] H. Toran, "Experience and Challenges in Setting up a Model Demonstration Classroom for Children with Autism in Malaysia," 2011.

[3] B. Firestone, "Early Identification and Intervention in Autism: Forging the Architecture for Change," presented at the 2006 Reinventing Quality Conference, Alexandria, USA, 2006.

[4] A. Adams and P. Robinson, "An android head for social-emotional intervention for children with autism spectrum conditions," Affective Computing and Intelligent Interaction, pp. 183-190, 2011.

[5] S. Costa, F. Soares, C. Santos, M. J. Ferreira, F. Moreira, A. P. Pereira, and F. Cunha, "An approach to promote social and communication behaviors in children with Autism Spectrum Disorders: Robot based intervention," in RO-MAN, 2011 IEEE, Atlanta, GA, 2011, pp. 101-106.

[6] K. Dautenhahn and A. Billard, "Games children with autism can play with Robota, a humanoid robotic doll," in Universal Access and Assistive Technology, S. Keates, P. Clarkson, P. M. Langdon, and P. Robinson, Eds., ed London: Springer-Verlag 2002.

[7] S. Baron-Cohen, "The hyper-systemizing, assortative mating theory of autism," Progress in Neuro-Psychopharmacology and Biological Psychiatry, vol. 30, pp. 865-872, 2006.

[8] A. C. Pierno, M. Mari, D. Lusher, and U. Castiello, "Robotic movement elicits visuomotor priming in children with autism," Neuropsychologia, vol. 46, pp. 448-454, 2008.

[9] K. Dautenhahn, "Methodology and themes of human-robot interaction: a growing research field," International Journal of Advanced Robotic Systems, 2007.

[10] N. Giullian, D. Ricks, A. Atherton, M. Colton, M. Goodrich, and B. Brinton, "Detailed requirements for robots in autism therapy," in Systems Man and Cybernetics (SMC), 2010 IEEE International Conference on, 2010, pp. 2595-2602.

[11] S. Shamsuddin, H. Yussof, F. A. Hanapiah, and S. Mohamed, "A Qualitative method to analyze response in robotic intervention for children with autism," in RO-MAN, 2013 IEEE, 2013, pp. 324-325.

A Comparative study of concrete strength prediction using fuzzy modeling and neuro-fuzzy modeling techniques.

S.S. Syed Ahmad[1,*]

[1)] Faculty of Information & Communication Technology, Universiti Teknikal Malaysia Melaka, Hang Tuah Jaya, 76100 Durian Tunggal, Melaka, Malaysia.

[*]Corresponding e-mail: sakinah@utem.edu.my

Keywords: Fuzzy modeling; neuro-fuzzy modeling; concrete strength prediction

ABSTRACT – In this study, a comparative study of concrete strength prediction have been carried out by using three different models called type-1 fuzzy model, type-2 fuzzy model, and neuro-fuzzy model. These three models have been applied for concrete strength prediction of ready mix concrete based on its design mix constituents, namely cement, blast furnace slag, fly ash, water, superplasticizer, coarse aggregate, and age. Three different statistical performance measures have been used for evaluating the models. The experimental results show that type-2 fuzzy model give a better performance measures.

1. INTRODUCTION

Concrete is the most important material used in building construction. The modeling of concrete material is a difficult task based on its composite nature [1]. There are various empirical results have been done from experimental studies and are widely implemented in modeling the concrete material. However, these studies do not provide accuracy and predictability where the interactions among the number of variables that are unknown, complex or nonlinear [1]. Fuzzy model is suitable for solving a non-linear problem, especially when the underlying physical relationships are not easy to understand. The framework for a fuzzy model is based on the concepts of fuzzy sets, fuzzy rules-based system, and fuzzy reasoning. The designed fuzzy models are capable of conducting perceptual uncertainties, such as the ambiguity and vagueness involved in a real-world problem [2].

In practice, the expert commonly used standard uniaxial compressive test to determine compressive strength. For example, the coring tests that widely used in the construction field [3]. However, the process is time-consuming and costly. Moreover, there is a practical limit to decide how many samples should be taken for a consideration. Besides that, only small numbers of samples are used, and it will lead to the difficulty in finding the reliable or meaningful statistical conclusions.

In order to overcome the limitation of the existing method, many studies have been done on finding a new approach to predicting concrete compressive strength physically and analytically. In recent years, the used of Artificial Intelligent (AI) as an analytical approach have increasingly been applied to concrete strength prediction [4][5]. Here, the AI techniques such as Artificial Neural Network (ANN) use the basic procedure to predict material behavior by using the training dataset. However, ANN is black box learning approach; the modeling result cannot interpret the relationship between the input and the output data. Besides that, AAN also cannot deal with uncertainties problem. Meanwhile, type-2 fuzzy model is good in handling uncertainties, and we can easily interpret the relationship between the input and output data by producing the rules. In this research, a methodology using type-2 fuzzy model, type-1 fuzzy model, and neuro-fuzzy model is developed to predict the concrete compressive strength. Then a comparative study of concrete prediction has been done based on the statistical performance measures.

2. METHODOLOGY

In this subsection, we discuss the process of constructing the fuzzy model and neuro-fuzzy model for concrete strength prediction. In this study, we implement *Takagi–Sugeno* (TS) fuzzy model for all three variants of fuzzy models.

2.1 Fuzzy Modeling

The *Takagi–Sugeno* (TS) fuzzy model provides a systematic approach for generating fuzzy rules from a given input-output data set. This model is also called the Fuzzy Functional Model, where the rule base is composed by using fuzzy rules, whose consequent parts are a function of the antecedent variables [6]. The consequent rules are represented by either the crisp number or linear functions of the input given. The antecedents' part is represented by a number of fuzzy regions based on the partition of the input space. The format of the TS model provides an effective way to represent the non-linear system by combining a rule-based description with local functional description, for example, in the form of linearization [6][7]. The main process of TSK model can be divided into a two-step procedure of system identification: structure identification and parameter estimation. Here, the structure of the model is identified by using the given input-output data [7].

Consider a function y=f(**x**) being mapped by the TS fuzzy model, in which y is the output variable (dependent variable), and **x** is the input variable (independent variable). The data set is in the form of finite input-output pairs, k=1, 2, …, M, where M is the

total number of the input-output data available for parameter estimation. By considering N number of rules for generating the TSK fuzzy model, the representation of the TSK fuzzy model is:

R_i : if x_1 is $A_{i,1}$ and … x_n is $A_{i,k}$ Then $y_i=\mathbf{a}_i^T \mathbf{x} + a_{i0}$

In this study, we implement two types of fuzzy model called fuzzy type-1 and fuzzy type-2.

2.2 Neuro-Fuzzy Modeling

The neuro-fuzzy model has the learning capability of neural network. Here, the fuzzy inference structure and parameter can be tuned by using the training algorithm in neural network. In this study, Adaptive Neural Fuzzy Inferences System (ANFIS) based on if-then rules of Takagi-Sugeno Fuzzy Model is used for predicting the concrete strength [8].

3. EXPERIMENTAL RESULT

In this section, we elaborate on a set of experiments, in which we used concrete dataset from machine learning repository. The main objective of these experiments is to show the abilities of the developed method and quantify the performance of the predicted concrete compressive strength. A brief summary of the data sets used in the experiment is presented in Table 1.

Table 1The range of training data

Input / Output variables	Minimum data	Maximum data
Cement	0	900.9
Water	118	238
Sand	208	879
Gravel	389	1285
Superplasticizer	0	3.5
Fly ash	0	275
Silica fume	0	90
Slag	0	500
Compressive strength	6.3	107.7

Three models were developed by using eight input variables and one output variable (compressive strength). The comparisons of results are summarized in Table 2. This table emphasizes the comparison performance of the fuzzy models in terms of three different statistical measures. The results show that Fuzzy type-2 model give the best performance compared to the other two models.

Table 2 Comparison of Prediction Models

Model	Root Means Square Error (RMSE)	
	Traning	Testing
Type-1 Fuzzy	0.0715	0.1003
ANFIS	0.0663	0.1038
Type-2 Fuzzy	0.1327	0.0427

Figure 1 show the performance of fuzzy models for training and testing data. Figure 2 show the RMSE for testing data using all three models. Here, the fuzzy type-2 model outperforms the other two approaches.

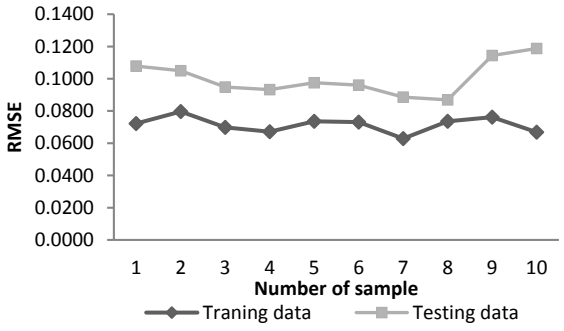

(a)

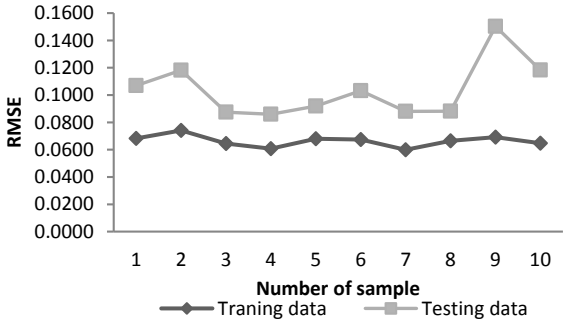

(b)

Figure 1 The performance for training and testing data (a) type-1 fuzzy model and (b) ANFIS

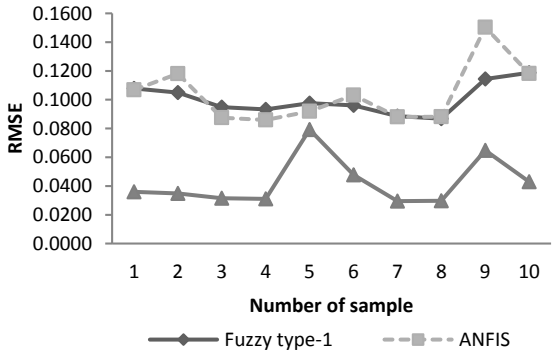

Figure 2 The RMSE for testing data.

4. SUMMARY

The prediction of the best compressive strength of concrete data is not an easy task because it contains highly complex materials. The proposed comparative study of three models helps to improve the prediction that will lead to reducing the waste of physical material and design and time cost.

In this paper, the effect of different fuzzy model on the performance of concrete strength prediction has been studied. The results of fuzzy type-2 model give a better performance compared to fuzzy type-1 and ANFIS models.

5. REFERENCES

[1] V. Chandwani, V. Agrawal, and R. Nagar, "Modeling Slump of Ready Mix Concrete Using Genetically Evolved Artificial Neural Networks," *Adv. Artif. Neural Syst.*, vol. 2014, pp. 1–9, 2014.

[2] L. Zadeh, "Outline of a new approach to the analysis of complex systems and decision processes," *Syst. Man Cybern. IEEE Trans. ...*, no. 1, pp. 28–44, 1973.

[3] M. Q. Feng, L. Chung, U. J. Na, and T. W. Park, "Neuro-fuzzy application for concrete strength prediction using combined non-destructive tests," *Mag. Concr. Res.*, vol. 61, no. 4, pp. 245–256, Jan. 2009.

[4] P. Lande and A. Gadewar, "Application of artificial neural networks in prediction of compressive strength of concrete by using ultrasonic pulse velocities," *IOSR J. Mech. Civ. ...*, vol. 3, no. 1, pp. 34–42, 2012.

[5] M. Neshat, A. Adeli, G. Sepidnam, and M. Sargolzaei, "Comparative study on fuzzy inference systems for prediction of concrete compressive strength," *Int. J. Phys. Sci.*, vol. 7, no. 3, pp. 440–455, Jan. 2012.

[6] M. Sugeno and G. T. Kang, "Structure Indentification on Fuzzy Model," *Fuzzy Sets Syst.*, vol. 28, pp. 15–33, 1988.

[7] A. Tewari, "Prior knowledge based identification of Takagi-Sugeno-Kang fuzzy models for static nonlinear systems," no. May, 2009.

[8] J. Jang, "ANFIS: adaptive-network-based fuzzy inference system," *Syst. Man Cybern. IEEE Trans.* , vol. 23, no. 3, 1993.

Contact us

Centre for Advanced Research on Energy
Faculty of Mechanical Engineering
Universiti Teknikal Malaysia Melaka
Hang Tuah Jaya, 76100 Durian Tunggal, Melaka, Malaysia

Phone : +606 234 6891 | Fax : +606 234 6884
E-mail : care@utem.edu.my
www.utem.edu.my/care